Investigation of High-order, High-resolution methods for Axisymmetric Turbulent Jet using ILES

By

António Filipe Baranda Inok

A thesis submitted to the University of Cranfield
In Partial Fulfillment of the Requirements
for the Degree of
Doctor of Philosophy

University of Cranfield
Department of Aerospace Sciences
Cranfield, UK
September 2011

Typeset in LaTeX 2_ε.

Except where acknowledged in the customary manner, the material presented in this thesis is, to the best of my knowledge, original and has not been submitted in whole or part for a degree in any university.

António Filipe Baranda Inok

Investigation of High-order, High-resolution methods for Axisymmetric Turbulent Jet using ILES

António Filipe Baranda Inok

September 2011

Abstract

This *Philosophiae Doctor* thesis presents the motivation, objectives and reasoning behind the undertaken project. This research, study the capability of compressible **I**mplicit **L**arge **E**ddy **S**imulation (**ILES**) in predicting free shear layer flows, under different free stream regimes (Static and Co-flow jets).

Unsteady flows or jet flows are non-uniform in structure, temperature, pressure and velocity. Turbulent mixing is of particular importance for the developing of this class of flows. As a shear layer is formed immediately downstream of the jet exhaust, an early linear instability involving exponential growth of small perturbations is introduced at the jet discharge. Beyond this development stage, in the non-linear Kelvin-Helmholtz instability region large scale vortex rings roll up, and their dynamics of formation and merging become the defining feature of the transitional shear flow into fully developed regime. This class of flows is particularly relevant to numerical predictions, as the extreme nature of the flow in question is considered as a benchmark; however, experimental data should be selected carefully as some results are controversial. To qualify the behaviour of unsteady flows, some important criteria have been selected for the analysis of the flow quantities at different regions of the flow field (average velocities, Reynolds stresses and dissipation rates). A good estimation of high-order statistics (Standard Deviation, Skewness and Kurtosis) correspond to mathematical steadiness and convergence of results. From the physical point of view, similarity analysis between jet's wake sections reveals physical steadiness in results. Spectral analysis of the different regions of the flow field could be used as a sign that the energy cascade is correctly predicted or efficiently enough since this is where the smallest scales are usually present and which in effect require to be modelled by the different numerical schemes.

The flow solver has been reviewed and improved. The former, a revised version of

the reconstruction numerical schemes (**WENO** 5^{th} and **WENO** 9^{th} orders) has been performed and tested, the correspondent results have been compared against analytical data; the latter, correction of the method to compute the Jacobian of the transformation (singularity correction), by changing from the standard algebraic to geometric method, and augmented with transparent boundary condition, giving mathematical and physical meaning to the obtained results. The flow solver improvements and review have been verified and validated through simulations of a compressible **C**onvergent-**D**ivergent **N**ozzle (**CDN**), and the standard and a modified version of the Shock tube test cases, where the results are gained with minimal modelling effort.

The study of numerical errors associated with the simulations of turbulent flows, for unsteady explicit time step predictions, have been performed and a new formula proposed. Ten different computational methods have been employed in the framework of **ILES** and computations have been performed for a jet flow configuration for which experimental data and **DNS** are available. It can be seen that a numerical error bar can be defined that takes into account the errors arising from the different numerical building blocks of the simulation method. The effects of different grids, Riemann solvers and numerical reconstruction schemes have been considered, however, the approach can be extended to take into account the effects of the initial and boundary conditions as well as subgrid scale modelling, if applicable.

From the physical analysis several observations were established, revealing that differences in terms of jet's core size are not an important parameter in terms of quantification and qualification of predictions, in other words, data should be reduced to the jet's inertial reference system. Moreover, the comparative study has been performed to identify the differences between Riemann solvers (**CBS** and **HLLC**), Low Mach number Limiting/Corrections (**LMC**), numerical reconstruction schemes (**MUSCL** and **WENO**) and spatial order of accuracy (2^{nd}**-order LMC**, 5^{th}**-order LMC** and 9^{th}**-order** schemes) in combination with the most efficient cost/resolution discretization level (*Medium* mesh). The comparisons between results reveals for the Static and Co-Flow jets that the **CBS MUSCL** 5^{th}**-order LMC** and the **HLLC MUSCL** 5^{th}**-order LMC** as the most accurate schemes in predicting this class of flows, accordingly. Furthermore, the selected numerical methods show to be in accordance with the empirical (Static) and experimental (Co-flow) results in terms of resonance frequency and/or Strouhal number; also, the expected behaviour in terms of spectral energy decay rate throughout the jet's central line is observed. To conclude the study of the Static jet case, a possible explanation for the jet's

buoyancy effect is presented.

Acknowledgements

First, I am grateful and thankful to my parents for their economical support throughout the duration of the Ph.D. Words are not enough to show my appreciation and I thank them for the sacrifices they have done towards me. Also my deepest gratitude goes to my relatives for their understanding and always being there for me when in need, in particular to my *Pearl*.

I sincerely thank my supervisor Professor Dimitris Drikakis for his effort, guidance and patience he has invested as well as invited me as his Ph.D. student. His keen advice and expertise guided my Ph.D. from it's beginnings all the way to the very end. It goes without saying, his open mind in terms of being receptive to different approaches in order to achieve a realistic solution, even when we got a five minutes meeting.

Also, I would like to thank Dr Evgeniy Shapiro, Dr. Bowen Zhong, Dr Vladimir Titarev, Dr Ben Thornber and Dr Marco Hahn for the countless inputs, recommendations and guidance. There patience, careful explanations and suggestions have given me the necessary information to improve my work. I am very thankful for there perspective.

I also would like to thank Professor Victor Steinberg for his ability in accept me as his guest student at Weizmann Institute of Science, Department of Physics of Complex Systems and, also, Professor Carvalho Rodrigues, Programme Director of Science and Technology, NATO. Without them advise and support, I was not able to start this endeavour.

I would like to also thank my colleagues for sharing their work and fruitful discussions without whom it would have been impossible to finish my Ph.D.

Last but not least, I would like to thank all the people I have come across and met while in Cranfield that turned my Ph.D. into a unique experience. Further I would like to thank my friends in the FMaCS group, primarily Ioannis Kokkinakis and Matyas Benke, for the good times we had either discussing obscure physics or meta-physical questions,

truly great times that help me to prevent rust or an orthorhombic crystallization of my few survivable brain cells.

Of course my thanks goes to all my friends, who have helped get through my Ph.D. as "sane" as possible.

To all, A big thank you.

Contents

List of Tables

Abbreviations

Acronyms

CBS	Characteristics Based Scheme
CFD	Computational Fluid Dynamics
CFL	Courant-Friedrichs-Levy number
CS	Control Surface
CV	Control Volume
DNS	Direct Numerical Simulation
ENO	Essentially Non-Oscillatory
EOS	Equation of State
FVM	Finite Volume Method
HLL	Harten, Leer, Lax
HLLC	Harten, Leer, Lax Contact
HWA	Hot Wire Anemometry
ILES	Implicit LES
LDA	LASER Doppler Anemometry
LES	Large Eddy Simulation
LMC	Low Mach Number Treatment/Correction
MM	Minimod **MUSCL** slope limiting method
MUSCL	Monotone Upstream-Centred Schemes for Conservation Laws
M3	Third order **MUSCL** slope limiting method
M5	Fifth order **MUSCL** slope limiting method
NSE	Navier Stokes Equations
PIV	Particle Image Velocimetry
RANS	Reynolds Averaged Navier Stokes
RK	Runge-Kutta
RMS	Root Mean Square
SGS	Sub Grid Scale
TVD	Total Variation Diminishing
TW	Time Window
VA	van Albada **MUSCL** slope limiting method
VL	van Leer **MUSCL** slope limiting method
WENO	Weighted Essentially Non-Oscillatory

Greek Symbols

α	speed of sound
β_j	**WENO** smoothness indicator
γ	specific heat ratio
γ_j	**WENO** linear weights
δ_{ij}	Kronecker symbol
ϵ	dissipation rate
$\lambda_{0,1,2}^{\xi,\eta,\zeta}$	eigenvalues of the advective fluxes
μ	dynamic viscosity coefficient
ν	kinematic viscosity or natural frequency
ξ, η, ζ	computational domain spatial coordinates
ρ	density
σ	standard deviation
τ	computational domain time coordinate
$\bar{\bar{\tau}}$	shear stress tensor
τ_{ij}^{sgs}	**LES** modelled stress tensor
$\tau_{x,y,z}$	stress components
ϕ	phase
ϕ^{lim}	slope limiter function
ω	angular velocity
ω_j	**WENO** non-linear weights
Ω	vorticity

Latin Symbols

A	area
$\mathbf{B}$	distribution of field forces
c	speed of sound
c_p	specific heat at constant pressure
c_v	specific heat at constant volume
dA	elemental surface area
dV	elemental volume
e	internal energy
E	total energy
$E_k(\nu)$	spectral kinetic energy
$E_k(t)$	temporal kinetic energy
$\mathbf{F}$	contact forces
k	thermal conductivity coefficient
$\mathbf{M}$	contact momentum
$\mathbf{n}$	unit normal vector
p	pressure
$\mathbf{p}_j(x)$	**WENO** interpolating orthogonal polynomial
q	heat flux
r	non-inertial distance
$r_i^{lim,R/L}$	**MUSCL** ratio of slopes
R	inertial non-inertial frames of reference distance
$\overline{R}$	specific gas constant
S_u	Sutherland temperature
t	Real time
T	absolute static temperature
$u'_{x,y,z}$	fluctuating velocity components
$\mathbf{U}$	generic advective fluxes or domain velocity field
$\mathbf{U}_{Jet}$	Jet exhaust velocity
$\mathbf{U}_{Ref}$	Reference velocity
$\langle U_{x,y,z} \rangle$	Favre average velocities
V	Volume
$\mathbf{V}$	velocity vector

Non-dimensional Numbers

Ma	Mach Number
Pr	Prandtl number
Re	Reynolds number
St	Strouhal number

Subscripts and Superscripts

$*_{i\pm1,j\pm1,k\pm1}$	computational domain cell faces coordinates
$*_{i\pm\frac{1}{2},j\pm\frac{1}{2},k\pm\frac{1}{2}}$	computational domain cell center coordinates
$*^{n}$	time step number or **RK** stage number

Introduction

1 Introduction

This thesis is concerned with the study of different methodologies to predict a jet flow issuing into a free stream. Fluid dynamics of jets and plumes constitute an omnipresent phenomena in nature. Some of these phenomena are obvious to even the most casual observer, e.g. jets which exit from one's mouth when exhaling on a cold morning, astrophysical jets at distances of light years away visible only through telescopes. These mechanisms are highly non-linear, indeterministic and inherently unsteady, leading by consequence to regions dominated by mixing, vortical structures and turbulence. Therefore, a generic representation of turbulence behaviour and intensity plays an essential role in predicting this class of flows [1]. By improving the efficiency of turbulent jet mixing several performance enhancements for jet/rocket engines can be achieved, e.g. decreased jet noise, lower exhaust temperatures, increased combustion efficiency and reduced pollutant emission. The main focus of this work is to improve the understanding of the different numerical methods in predicting the physical behaviour and its correspondent characteristics for this class of flows, jet flows.

The existence of turbulence has been well-established from the past and it is one of the most studied phenomena, also despite great efforts, an unified theory has not emerged. Its

non-linearity character, without mention the importance to every natural system led many scientists and researchers to dedicate themselves to this challenging topic. Notoriously, an accurate measure of turbulence is difficult to obtain in a natural or experimental environment; however, from the work done on turbulence some contributions were made in ideas and tools of lasting value to neighbouring areas of science (e.g. negative temperature, anomalous diffusion, the concept of power law scaling in many body problems, the notions of scale invariance and universality, just to name a few) [1, 2]. With the rapid development of computational hardware and performance (Moore's Law), numerical simulations have increased in significance and are currently used as a tool to predict uncertainties that arise from turbulence phenomenology. As a possible futuristic scenario, when quantum computers become effectively available, the current demands in computational power and hardware could be easily fulfilled, in order to accurately predict the turbulence behaviour.

The remaining of this chapter will briefly illustrate the current physics and computational or numerical techniques behind fluid dynamics, as well as the nature and the characteristic features of turbulence and jet flows.

1.1 Jet Flows

The technology of jets dominate our lives, from propelling engines through the exhaling of chimneys which spew the waste products of industry. Controlling the mixing of the jet (or plume) with its surroundings is the focus of active research [3–9]. Typical practical applications demand enhanced combustion between injected fuel and background oxidizer, rapid initial mixing and submergence of effluent fluid, or improved mixing of a hot exhaust with the surroundings to affect after-burning [10–12]. In this context, there is a crucial interest in recognizing and understanding the local nature of the jet instabilities and their global non-linear development in space and time [13]. On the other hand, purely academic research in this area is also exciting since it deals with the many challenging unresolved scientific issues of non-linear fluid dynamics and turbulence [14–17].

In aerodynamics, jet flows can be defined as the exhaust fluid from a rocket or jet engine moving through another fluid [18]. This flow is non-uniform in structure, temperature, pressure and velocity [19]; however, the jet dynamics is entirely controlled by the vorticity ($\Omega = \nabla \times \mathbf{v}$) defined in terms of the velocity field $\mathbf{v}$, which gives a local measure of the rotation of the fluid [20]. Normally the flow of jet engines or rockets exhausting

into quiescent air, that changes dramatically in size and shape with the surrounding and engine conditions [21, 22], exhibit a range of complex physical phenomena including shock-waves, expansion fans, free shear layers and their interactions, multi-species flow, mixing and chemical interactions. In the simplest conceptual jet description (free laminar jet emerging from an axisymmetric nozzle) a shear layer is formed immediately downstream of the jet exit between jet stream and surroundings. As one moves downstream, there is an early linear instability jet regime, involving exponential growth of small perturbations introduced at the jet exit. Beyond this development stage, in the non-linear Kelvin-Helmholtz instability regime [23], large scale vortex rings roll up, and their dynamics of formation and merging become the defining feature of the transitional shear flow [24]. Figure 1.1, hydrodynamics experimental Kelvin-Helmotz instability, it can be observed the evolution and behaviour of the flow field.

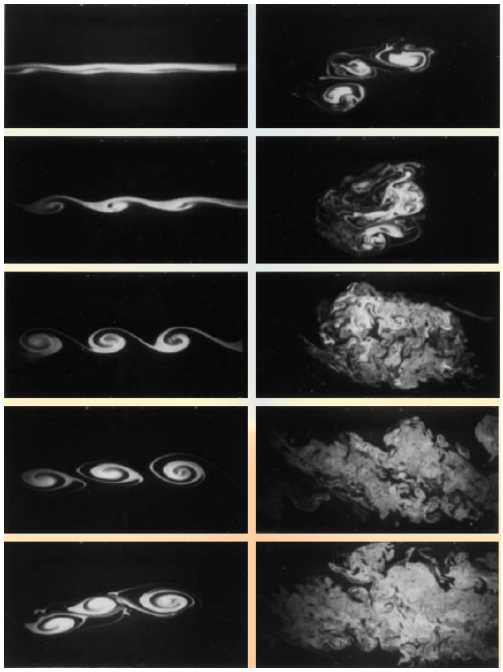

FIGURE 1.1: Experimental visualization of the Kelvin-Helmotz instability. [1]

Laboratory studies show that azimuthal effects can be important fairly close to the jet exit [25], so that the simple axisymmetric vortex-ring picture of the circular jet becomes less realistic as one moves downstream from the jet exit. Sufficiently far downstream, three-dimensionality is the crucial feature of the jet and the stream-wise vorticity component (along the jet axial direction) is the more efficient one in entraining fluid from the surroundings. In addition to the important role of azimuthal instabilities contributing to the

breakdown of the vortex rings, mechanisms such as self-induction, vortex stretching, and vortex reconnection are the main fluid dynamical processes involved in the transition to the turbulent jet regime [26]. The most important new element introduced in the jet by three-dimensional instabilities is that now in addition to the shear vorticity production, vorticity can now also be generated locally through other mechanisms (e.g. by stretching and turning of old vorticity), and there are interesting new possibilities for how the jet flow develops, depending on which types of unsteady vortex interactions are initiated. They are coherent over distances comparable to and often longer than the jet diameter in the axial direction. The characterization of jet flows through the longitudinal axis can be divided in three different fields, near-field, transition and far-field. Figure 1.2, a schematic representation of the different fields and regions that can be observed on a jet flow. The near-field consists in the exhaust fluid that has not yet been mixed with the free stream flow and with residual fuel enriched parts that start to burn randomly with the free stream oxidizer in the outer layer. The transition field, the $3D$ break down of the mixing and jet's vortical rings region occurs. In the far-field (jet's wake), the jet flow is mixed with the free stream flow and the influences of the engine discharge are negligible (fully developed jet). [27]

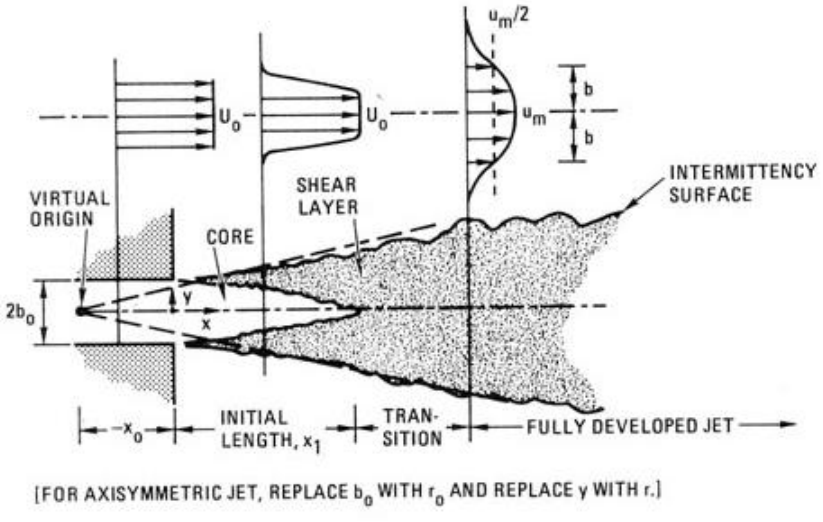

FIGURE 1.2: Schematic representation of a jet flow. [28]

1.1.1 Axisymmetric Jets

A survey concerning jet flows has been performed in the past by Birch [21]. This subsection is a summary of its conclusions. It has been pointed out the enormous difficulty in achieving uniformity and consistency in terms of results, as they are not as readily available as might be supposed and some of the basic characteristics of this class of flows are still surprisingly controversial. Because of this, it is often difficult to clearly identify the best data to use for code validation, or to accurately assess what uncertainty may exist in the data selected.

In axisymmetric jets, there are two regions that approximate standard self-similar flows. The first is the turbulent mixing region in the near-field, and the second is a region far downstream of the end of the jet potential core where the jet becomes fully self-similar. Furthermore, from the survey [21], two significant conclusions can be made from the observation of turbulent mixing layers. These conclusions are that:

- under normal experimental conditions, the mixing in these flows is not a function of either Reynolds number or Mach number (for $Ma \leq 1.0$);
- at sufficiently large downstream distances, the mixing reaches an asymptotic state that is, within data accuracy, independent of initial conditions.

The first observation implies that if differences exist between jets, these must be due to differences in the initial conditions. This is strictly true if the boundary layers at the nozzle exhaust are turbulent; if the boundary layers are laminar, the jet mixing may also depend on a variety of external and internal sources of disturbance, hence the importance of carefully documenting the initial conditions. The second observation suggests that, for sufficiently thin or no initial wall boundary layers, the jet mixing should be essentially independent of initial conditions.

Laminar initial conditions

It has been found, when the boundary layer at the nozzle exhaust is laminar, there is strong and unpredictable variations in the jet core size, for different nozzle exit velocities, and these results differ significantly from facility to facility, as it is extremely difficult to exactly replicate the same conditions/experiments with different equipments, measuring techniques and instruments that behave differently [29]. By tripping the boundary layer,

if it exists, seemed to stabilize the mixing and led to a core length that can be relatively independent of the nozzle exit velocity.

Turbulent initial conditions

For many nozzle flows, however, even if the nozzle's internal boundary layer is turbulent it may not be fully developed. Unfortunately, there are no detailed studies of how this might change the development of a mixing layer. Based on the available data, if a broad band turbulence spectrum is established with an amplitude of about $0.1 \times U_{Jet}$, these changes are probably small [30–32].

The Reynolds number enters the problem because the thickness of the initial wall boundary layer does depend on the Reynolds number. Therefore, while a Reynolds number criterion may be a useful guide in designing a nozzle test, it is important to remember that it is the characteristics of the initial boundary that are the controlling factors, not the Reynolds number. In addition, this Reynolds number estimate applies only to cold jets, since the core of a hot jet is shorter than that of a cold jet.

However, the thickness of the initial boundary layer can have a large effect on the development of a jet and on how well the flow data will scale. A minimum requirement for a jet to be only weakly dependent on initial conditions is that the initial mixing layer becomes fully developed within the potential core. If this is achieved, then the flow at the end of the jet core will not depend on initial conditions and this, presumably, will also apply to the rest of the jet development.

The transition region

Until recently, detailed experimental mean flow and turbulence data for axisymmetric jets has been largely limited to low speed flows, primarily because of the difficulty of interpreting hot-wire data in compressible flows. The accuracy of the data at available, however, varies greatly and so needs to be viewed with caution. Nevertheless, the best of these studies are already proving to be very valuable [33–36]. In spite of some differences, the mean velocity data is in excellent agreement. This, however, is not true for the turbulence data. The mean flow data from Lau et al. [33] were obtained using a **LDV** system.

The shear stress measurements are important because one can check their consistency with the measured mean velocity profiles. The expected value for the shear stress in this region of the jet have also shown and it is known from numerical calculations, that

measured values must fall within this region over most of the length of the jet's core for the turbulence measurements to be consistent with the measured length of the jet's core. Only the [33] data fall within this band. Hot-wire measurements, however, are limited to cold, low speed flows, while **PIV** measurements can be taken in hot compressible flows. One of the very interesting results that emerged is that, while the mean velocity starts to drop at an $\frac{X}{D} \approx 5$, the peak shear stress drops much slower. This is more pronounced for the normal stress.

In an axisymmetric jet when the flow becomes fully developed, the turbulence levels are almost twice those in a fully developed mixing layer. Therefore, at the end of the jet core, the flow starts to transition from something that resembles a mixing layer to an axisymmetric jet. Since the turbulence level, normalized by the local center-line velocity, in a fully developed jet is much larger than in a mixing layer, there is an initial fast increase in this quantity downstream of the end of the jet potential core. However, the center-line velocity itself starts to decrease rapidly in this region of the jet. Furthermore, turbulence measurements are not all that useful indicator of the behaviour of the flow through the center-line; within the core, these measurements provide almost no useful information about the development of the jet. Although these are the measurements that are often compared with numerical predictions, to evaluate the accuracy of measurements. These measurements are more meaningful farther downstream, but the jet mixing is still driven mainly by the shear stress, which is zero on the center-line. If one must look at just one quantity, the peak shear stress is probably the most meaningful quantity to be selected as reference.

1.2 Nature of Turbulence

The nature of a flow field is determined by its ability to cope with small perturbations which are ever present in all real flows. Above a critical value of the Reynolds number, these instabilities propagate and result in a breakdown of the steady character of the flow. The motion then becomes random in nature, the velocity at all points in the flow field fluctuating with time. In spite of this irregularity, the flow is amenable to mathematical treatment, statistically distinct average values can be obtained for its properties. The period over which the averaging is considered must be large compared with the time scale of the turbulence and yet small compared with the period of any slow external variations in the flow field. If the averaged properties do not vary significantly with time, the flow

may be described as 'steady'.[2, 37]

The two hypothesis from Kolgomorov work [38, 39] are that the turbulence is isotropic in the universal equilibrium range, and there is a range of frequencies called the inertial sub-range where no viscous dissipation occurs. The existence of an universal equilibrium range states that turbulent structures that have a scale in this range have the same 'universal' turbulent properties, and the division of larger eddies into smaller ones occurs in the same way for all the concerning scales in this range. Kolgomorov states that they could thus only depend on the energy dissipation ϵ and the kinematic viscosity ν. The dimensionless length scale built from this two quantities is known as the Kolgomorov scale:

$$\eta = \left(\frac{\nu^3}{\epsilon}\right)^{1/4}.$$

At this small scale, viscous effect are predominant and the eddies kinetic energy is dissipated. Under these hypothesis, it can be proven that in the inertial sub-range where isotropy occurs, the energy spectrum decreases with a power law of coefficient $-\frac{5}{3}$ with respect to the frequency (or wave number) and C is a universal constant,

$$E(k) = C\epsilon^{\frac{2}{3}}k^{-\frac{5}{3}}.$$

In other words, turbulence consists of many superimposed periodic motions. Mixing or production occurs predominantly in the largest eddies, those of low wave number which obtain energy from the mean flow. This energy is passed to successively smaller eddies by means of inertial interactions amongst the turbulence. The energy "cascades" from eddies of low wave numbers to those of high wave numbers, or alternatively from low frequencies to high frequencies. The upper size limit of the eddies is determined mainly by the size of the system in which the flow occurs and the lower size limit is governed by the effects of viscosity. Within the smallest eddies the flow is no longer turbulent but viscous, and molecular effects are dominant. The high fluctuating viscous shear stresses that arise in the smallest eddies result in a conversion of the turbulent kinetic energy into heat, this process is termed 'viscous dissipation'. If there is no continuous external source of energy, turbulence will dissipated into heat. However, energy may be generated by interaction between the turbulent stresses and velocity gradients in the mean flow to maintain the supply through the wave number spectrum. This process is termed "production" and the ratio of the production of energy to its dissipation by viscosity is a useful measure of

the state of equilibrium of the flow. To distinguish the spectral regions a phase diagram is associated to the energy spectrum by means of phase distribution. When production exists the value of phase is "random", while a steady phase value ($\pm\frac{\pi}{2}$) identifies the inertial scales.

Isotropic turbulence is said to exist when the statistical properties of the turbulence have no preference for direction. In such a situation, the turbulent kinetic energy is equally divided amongst its components in three orthogonal directions, arbitrarily located within the flow. Isotropic turbulence also implies the absence of any shear stress arising from turbulent fluctuations. Although isotropic flow fields are of little practical concern, the concept has wide implications regarding the process of viscous dissipation of energy. If the smallest eddies are spectrally far removed from those eddies which receive energy from the mean flow and govern the turbulent mixing, then it seems plausible to assume that the dissipative motions occurring in the small scales are independent of the large scale processes. Hence a region of "local isotropy" is postulated to exist at the high wave numbers end of the spectrum where the dissipation rate is equal for the three components of the turbulent kinetic energy, irrespective of the mean flow structure.

1.3 Numerical Approaches

Although many experimental studies in the past decades have significantly increased the current physical understanding of the flow physics, simulations accurately and reliably predict turbulent flows, for the pass decades, and complement the experimental data and results [40–46]. From the evolution of Computational Fluid Dynamics (**CFD**), different modelling techniques appeared. In the context of **CFD**, there are generally three standard techniques:

- Reynolds-Averaged Numerical Simulation (**RANS**),
- Large-Eddy Simulation (**LES**) and Implicit Large-Eddy Simulation (**ILES**),
- Direct Numerical Simulation (**DNS**).

The applicability of these standard numerical approaches to turbulent flows, as well as their general advantages and disadvantages, will be briefly discussed in this section. A more detailed explanation of the these numerical approaches can be found in some text books [47, 48].

1.3.1 Reynolds Averaged Numerical Simulation

The most common approach to calculate a problem in engineering is the Reynolds Averaged Numerical Simulation. Reynolds averaging is based on the idea of decomposing the exact solution of the flow into a statistical average and a fluctuating turbulent component. The averaging procedure cannot be uniquely defined because it depends on the type of problem, e.g. it could be a time average for a statistically steady flow, a spatial average for essentially two-dimensional flows, or an ensemble average for a family of similar flows.

In case of engineering applications, the controlled conditions or free-stream conditions rarely change in time, thus a time-averaging is preferred. With this approach, the resolved mean flow can be considered free of fluctuations and all the unsteadiness is contained in the unresolved turbulent scales that need to be modelled. Modelling is necessary because the averaging procedure introduces additional unknown terms in the governing equations that cannot be computed exactly from the mean flow variables. As a result, the averaged equations are always complemented by additional turbulence models that mimic the effects of the unsteady motions.

For unsteady flows, the time-scale associated with the organised unsteady motion exists and must be well separated from the time-scale of turbulent motion. The exact solution, for unsteady flows, can be seen as the sum of three contributing terms:

- time average,
- conditional average of the coherent motion,
- random fluctuation due to turbulent motion.

However, the time-scales should differ by several orders of magnitude, but in engineering and geophysical applications very few flows satisfy this condition. [47]

The function of turbulence modelling in **RANS** is to devise approximations for the unknown correlations between mean flow and fluctuating component, Reynolds stresses, in order to close the system. However, these quantities are not able to completely represent the complex physical structures and interactions inherent to turbulent flows; hence, it seems unlikely that any single model will successfully predict all types of turbulent flows with any degree of certainty. For this reason, numerous turbulence models have been developed over the past decades, algebraic and turbulence energy (e.g. $k-\epsilon$ and $k-\omega$)

models, all introducing a number of unknown coefficients. In order to adjust the models to particular flows, the unknowns are usually determined empirically by calibration against existing experimental results. Therefore, the existing turbulence models should be regarded as approximations of reality. [49]

1.3.2 Large Eddy Simulation

The development of Large Eddy Simulations is motivated by the limited applicability of **RANS** to turbulent flows and it can be regarded as an intermediate approach between accuracy and computational cost. However, the closure problem in the averaged form of the Navier-Stokes equations, i.e. averaging of the equations leads to additional unknown correlations (22 unknown correlations, in total, accounting for all symmetries) do not arise within the **LES** formulation, as the large scales are explicitly resolved and therefore modelling of the unknown stresses, τ_{ij}^{sgs}, is expected to be more straightforward. Moreover, in contrast to **RANS**, standard **LES** model only the small-scale turbulent motions whereas the larger turbulent structures are directly resolved. Since the smaller structures are only slightly affected by the boundary conditions, they exhibit a more common character for different types of flows. Thus, the models employed in **LES** tend to be more universal and require fewer adjustments to the specific flow compared to a similar **RANS** model. [47]

As it will be presented, on the next subsection, the grid requirements for **DNS** strongly depend on the smallest scales present in the flow, but most of the turbulent kinetic energy is contained in the larger structures. Therefore, while resolving the large-scale dynamics of the flow directly, **LES** significantly reduces the total computing cost by modelling the less energetic small scales. Ideally, the computational cost of **LES** is independent of the Reynolds number, given that the reference length distinguishing the resolved, large scales from the modelled, small scales lies in the inertial sub-range.

Formally, in standard **LES** the governing equations are filtered by convolving all dependent variables with a predefined filter. The filtering operation decomposes the flow field into the sum of a filtered, resolved component and a residual, subgrid-scale component. The spatial and temporal evolution of the filtered component representing the large scales is fully described by the filtered equations. The unknown subgrid scale (**SGS**) stress tensor arising from the unresolved residual motions needs to be modelled. This system is normally closed by **SGS** models that are primarily concerned with reflecting the dissipation of energy cascading down from the larger scales, in a statistical sense. When deriving

the standard **LES** equations, it was implicitly assumed that differentiation commutes with the convolution. However, this is not valid at solid boundaries and for a variable filter operator. Furthermore, like in all numerical approaches, errors in standard **LES** arise from the approximation of the variables on a finite basis and numerical discretization. The dissipation terms are responsible for the numerical diffusion, especially near discontinuities. Drawbacks of conventional **LES** also arise from **SGS** modelling. The possible masking of the **SGS** terms by the leading order truncation error and the difficulties in devising **SGS** models for complex high Reynolds number jet flows.

1.3.3 Implicit Large Eddy Simulation

The Implicit Large Eddy Simulation approach is based on a similar manner to the standard **LES**, in terms of filtering operator. However, it is assumed that the numerical discretization on a computational grid implicitly separates large and small scales; thus, no explicit filtering is necessary and the subgrid scale stress tensor, found for standard **LES**, is absent in **ILES**. Furthermore, the unresolved motions need to be accounted for by the numerical method. This is generally achieved through adaptive, non-linear regularisation of the solution to the governing conservation laws. In Figure 1.3 a detailed idea of the basic principles and numerical differences between **LES** and **ILES** can be seen, where the numerics and the model are "merged" in **ILES**.

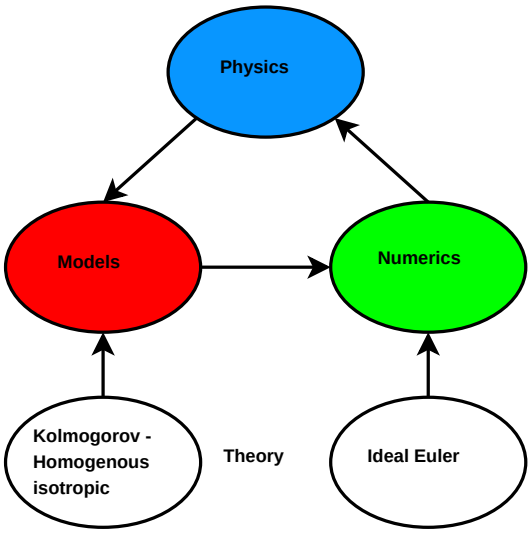

(a) Standard **LES**.

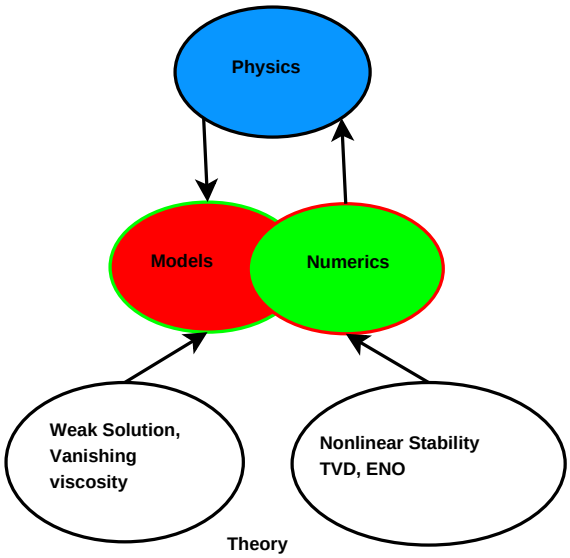

(b) Implicit **LES**.

Figure 1.3: **LES** and **ILES** numerical concepts.[47]

1.3.4 Direct Numerical Simulation

The **DNS** approach provides a complete time-dependent solution for turbulent flows. It provides superior accuracy because all scales of motion and time are resolved, given it is free of significant numerical or other errors. In order to represent all scales numerically, the discretization of the governing equations has to be at least as fine as the exact solution. As a result, the step-size of the discretized problem in time and space must be smaller than

the characteristic time and the characteristic length of the smallest eddies present in the flow. Additionally, the duration of the simulation and the size of the computational domain are determined by the characteristic time and the characteristic length of the largest, energy-containing eddies, which can differ substantially from the size of the time/space step. Since the range of scales observed in turbulent flows increases with progressively higher Reynolds number, the resolution criterion limits the applicability of **DNS** to low Reynolds number turbulent flows.

The number of grid points required for a numerical simulation depends on the spatial resolution and the size of the flow field. Turbulent flows are inherently three-dimensional, thus the number of grid points required for a fully three dimensional **DNS** is proportional to $Re^{\frac{9}{4}}$. In case of **DNS**, every scale has to be resolved, hence the distance between the nodes cannot exceed the Kolmogorov scale and, consequently, the computational domain should ideally have an extent of several times the characteristic length of the largest eddies present in the flow. This estimate underlines the limitations of **DNS** due to a very rapid increases of its computational cost with the Reynolds number.

1.4 Closing Remarks

One of the most important criteria that qualify the behaviour of unsteady flows are the analysis of the flow quantities (average velocities, Reynolds stresses and dissipation rates) at different regions of the flow field. Furthermore, a good estimation of high-order statistics, for this class of flows by employing numerical predictions, correspond to mathematical steadiness and convergence of results; also, the similarity analysis, between jet's wake sections, reveals physical steadiness in results. The spectral analysis of the different regions of the flow field could be used as a sign that the energy cascade is correctly predicted or efficiently enough since this is where the smallest scales are usually present and which in effect require to be modelled by the different numerical schemes.

In **LES**, no "explicit" turbulence model is used since this class of numerical schemes provide a built-in **SGS** model that may offer a better approach than explicit treatments. Otherwise, one can argue the reason of using an explicit turbulence model altogether due to the much larger dissipation introduced by the numerical methods themselves. With **ILES**, the implicit ability of high-resolution methods to model turbulent flows arises from the truncation error of the wave-speed dependent terms (which are responsible for generating numerical dissipation), when applying Godunov-type discretization methods. It

is essential to improve the current understanding of the mechanisms that add dissipation to the flow through the truncation error and avoid over dissipative numerical solutions by triggering entropy production where and when required.

1.5 Objectives and Outline

The main objective of this thesis is to investigate the ability of different solution strategies for the governing equations, based on high-resolution methods, in predicting free shear layers flows with different free stream conditions, by using a compressible flow solver. The objectives can be summarised as follows:

- Understanding, reviewing and improving (when and where is needed) the flow solver numerical methods to improve predictions with physical meaning, discretized control volumes with singularities and **WENO** numerical reconstruction scheme;
- Explore the concept of an error bar, in the context of time explicit and unsteady simulations;
- To assess the accuracy of different high resolution methods against detailed **DNS** and experimental data for turbulent jet flows, this includes, comparisons between different Riemann solvers, comparisons of the effects in augmenting a numerical schemes with **LMC**, comparisons between different limiters/reconstruction schemes and high resolution/higher order schemes;
- Investigate the applicability and turbulence predictions capability of the selected numerical schemes;
- Explicative analysis of the jet wake behaviour (buoyancy).

Outline

The thesis is organised as follows:

- Chapter 1: Here, the introduction to the Ph.D. and literature survey is presented as part of the general description of the investigations conducted in the pass;
- Chapter 2: This chapter describes the necessary theoretical and numerical backgrounds of the numerical methods used to obtain the results in the present thesis. Also, a brief description of the improvements done in the flow solver is presented;

- Chapter 3: The analysis presented in this chapter, show the numerical results from the different improvements done in the flow solver, by using the **C**onvergent-**D**ivergent **N**ozzle and the two and three dimensional Shock tube test cases;

- Chapter 4: In this chapter, the comparative analysis of the different numerical variants is studied from the mathematical point of view, Static and Co-flow Jet cases. Also, the conceptual introduction of an error bar for unsteady simulations with explicit time steeping;

- Chapter 5: The quantitative and qualitative analysis of the different numerical variants is studied from the physical point of view, for the Static Jet case. It is also presented, a possible and realistic explanation for the jet's buoyancy;

- Chapter 6: The quantitative and qualitative analysis of the different numerical variants is studied from the physical point of view, for the Co-flow Jet case. It is also presented, a possible and realistic explanation for the jet's buoyancy;

- Chapter 7: In conclusion, the analysis of the results is presented here, enhancing the main observations. A few recommendations and guidelines are made for future work.

In addition, complementary material to the theoretical and numerical backgrounds, and results presented in this thesis, are included in the appendices, accordingly.

Theory

2
Numerical Methods

In this chapter, a brief description of the flow solver (**CNS3D**) with the different methodologies contained in its library, correspondent improvements and different tools developed in this research will be presented.

The computational study is based on the **ILES** approach, e.g, see reviews [50–52]. The computational fluid dynamics code **CNS3D** [51, 53, 54] has been employed, which has been previously applied to a wide range of flows featuring shock waves and turbulence [51, 55–62]. The code solves the governing equations using a finite volume Godunov-type methods [47, 63, 64]. The inter-cell numerical fluxes are computed based on the solution to the Riemann problem using the reconstructed variables at the left and right of the cell interface. The computational code includes a library of different Riemann solvers [57]. In the present study the **C**haracteristics-**B**ased **S**cheme (**CBS**) [57, 65] and **HLLC** approximate Riemann solver of [64] have been employed.

Higher order of accuracy is achieved using **MUSCL** extrapolation [66], with the fifth-order limiter proposed of [67, 68]; also, the second-order limiter [66] have been employed. The standard **MUSCL** extrapolation has been augmented using a low-Mach number limiting scheme [69], which involves an additional stage in the reconstruction

process for the velocity vector. It ensures uniform dissipation of kinetic energy in the limit of zero Mach number (Ma), extending the validity of the Godunov method to at least $Ma \approx 10^{-4}$, via a progressive central differencing of the velocity components. The formulation of the underlying governing equations is not changed, and monotonicity of the density and scalar field is maintained. Furthermore, numerical simulations have been performed using the fifth- and ninth-order weighted essentially non-oscillatory (**WENO**) methods [70], which have been implemented into **CNS3D** and tested for a wide range of problems[58, 59, 61, 71]. The time integration has been obtained using a three-stage total variation diminishing (**TVD**) Runge-Kutta method [47].

2.1 Jacobian of the Transformation and Transparent Boundary Condition

A modification of the flow solver's Jacobian of the transformation has been performed (Singularity treatment). The algebraic method, previously in use, has been changed into the geometrical method; also, a new boundary condition has been implemented in order to close the transformed computational domain (Transparent Boundary condition). The following relation, presents the corrected Jacobian of the transformation:

$$J = \frac{\partial (x, y, z)}{\partial (\xi, \eta, \zeta)} = \begin{vmatrix} \frac{\partial x}{\partial \xi} & \frac{\partial y}{\partial \xi} & \frac{\partial z}{\partial \xi} \\ \frac{\partial x}{\partial \eta} & \frac{\partial y}{\partial \eta} & \frac{\partial z}{\partial \eta} \\ \frac{\partial x}{\partial \zeta} & \frac{\partial y}{\partial \zeta} & \frac{\partial z}{\partial \zeta} \end{vmatrix} + EPS, \tag{2.1}$$

where EPS is an infinitesimal number with value 10^{-15}, only being used when the product of the partial derivatives of the Jacobian determinant is 0. However, this value in physical terms correspond to the same length scale of sub atomic particles/waves. The pattern created by this improvement over the singularity line is in star (*) pattern. Moreover, the transformation form the physical into the computational domain's, reduces or expand each discretized cell into a computational cell of volume 1. Figure 2.1, shows the mathematical concept of the Jacobian of the transformation and its correspondent effects by changing from the algebraic to the geometrical method.

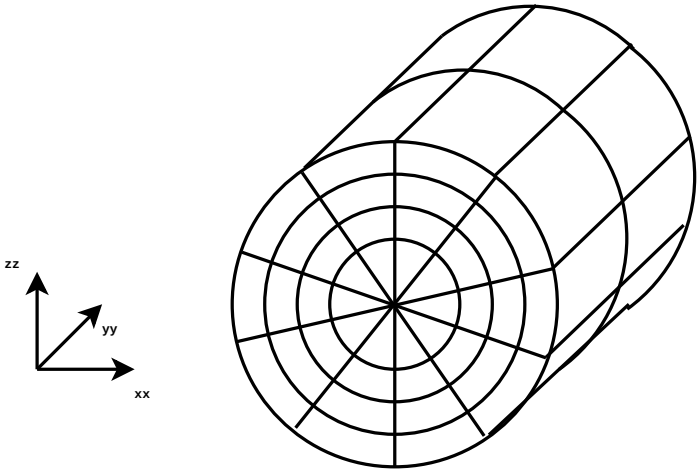

(a) Physical domain.

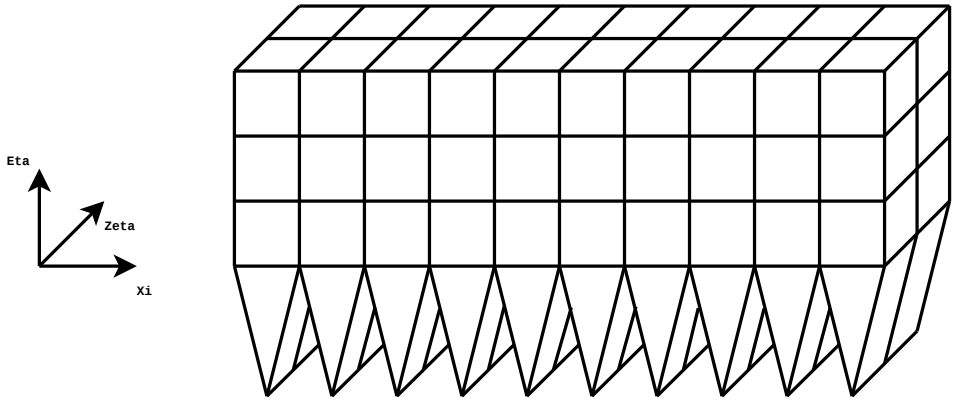

(b) Computational domain, without corrections.

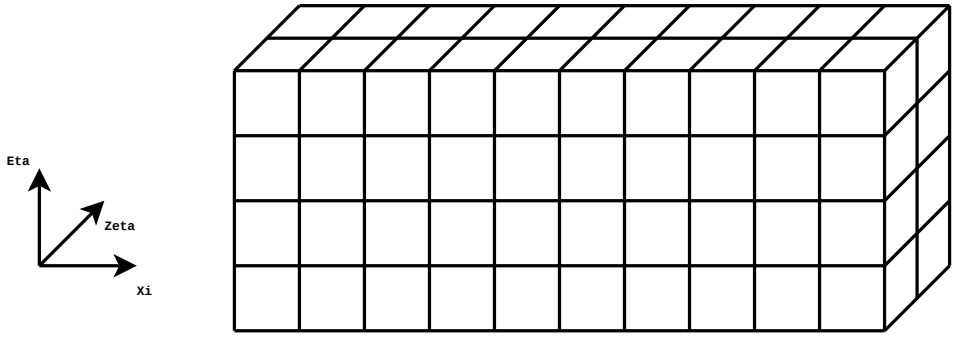

(c) Computational domain, with corrections.

FIGURE 2.1: Concept of coordinates transformation and singularity correction.

The augmentation of this treatment is done by a transparent boundary condition, where the auxiliary cells of the computational domain are going to store the values of the correspondent physical domain cells by 180^o apart. This can be better visualized in Figure 2.2.

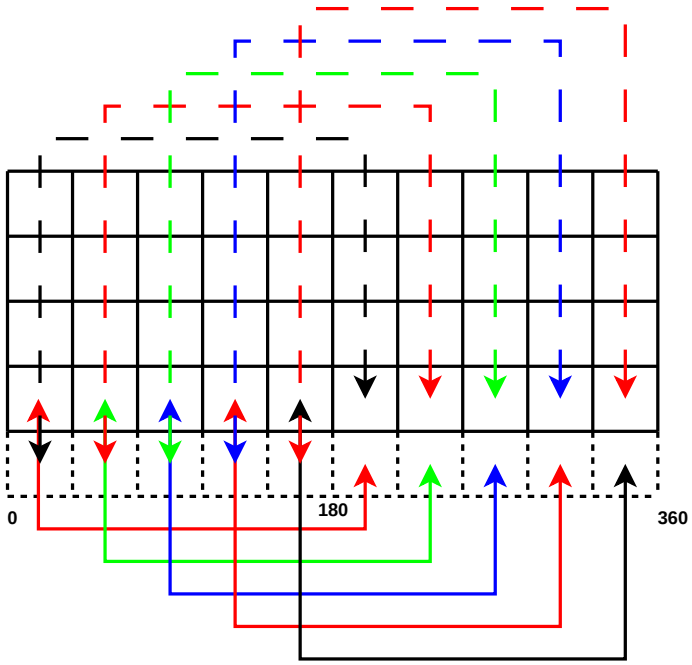

Figure 2.2: Transparent boundary condition concept, computational domain. Dotted squares, auxiliary cells.

This correction do not change the mathematical characteristics of the flow solver and the results have physical meaning. This observation will be proved by the results from the next part of this thesis.

2.2 Governing Equations

The three dimensional compressible Navier-Stokes equations system implemented in the flow solver, for a generalised co-ordinate system is written in conservative variables as:

$$\frac{\partial \mathbf{U}}{\partial t} + \frac{\partial \mathbf{E}}{\partial x} + \frac{\partial \mathbf{F}}{\partial y} + \frac{\partial \mathbf{G}}{\partial z} = 0 \tag{2.2}$$

where, the matrix vectors **U**, **E**, **F** and **G** are:

$$\mathbf{U} = \begin{bmatrix} \rho \\ \rho u \\ \rho v \\ \rho w \\ \rho e \end{bmatrix} \qquad \mathbf{E} = \begin{bmatrix} \rho u \\ \rho u^2 + p - \tau_{xx} \\ \rho uv - \tau_{xy} \\ \rho uw - \tau_{xz} \\ u(\rho e + p) - u\tau_{xx} - v\tau_{xy} - w\tau_{xz} + qx \end{bmatrix}$$

$$\mathbf{F} = \begin{bmatrix} \rho v \\ \rho uv - \tau_{yx} \\ \rho v^2 + p - \tau_{yy} \\ \rho vw - \tau_{yz} \\ v(\rho e + p) - u\tau_{yx} - v\tau_{yy} - w\tau_{yz} + qy \end{bmatrix} \quad \mathbf{G} = \begin{bmatrix} \rho w \\ \rho uw - \tau_{zx} \\ \rho vw - \tau_{zy} \\ \rho w^2 + p - \tau_{zz} \\ w(\rho e + p) - u\tau_{zx} - v\tau_{zy} - w\tau_{zz} + qz \end{bmatrix}.$$

Applying Equation (2.1) to Equation (2.2), it is possible to be seen the effects of the singularity treatment over the Navier-Stokes equations system.

$$\overline{\mathbf{U}} = J\mathbf{U}, \tag{2.3}$$

$$\overline{\mathbf{E}} = J(\mathbf{E}\xi_x + \mathbf{F}\xi_y + \mathbf{G}\xi_z), \tag{2.4}$$

$$\overline{\mathbf{F}} = J(\mathbf{E}\eta_x + \mathbf{F}\eta_y + \mathbf{G}\eta_z), \tag{2.5}$$

$$\overline{\mathbf{G}} = J(\mathbf{E}\zeta_x + \mathbf{F}\zeta_y + \mathbf{G}\zeta_z), \tag{2.6}$$

were J is the new Jacobian of the cell volume under consideration. The subscripts $_{x,y,z}$ indicate a partial derivative with respect to x, y, z. The system of equations is completed with the specification of an equation of state, which for an ideal gas is

$$p = \rho i\,(\gamma - 1)\,, \tag{2.7}$$

and

$$e = \rho i + \frac{1}{2}\rho(u^2 + v^2 + w^2), \tag{2.8}$$

where, ρ, i, u, v and w are, density, internal energy and Cartesian velocity components respectively.

2.3 Discretization Methods

In this section, the numerical background in discretization methods, in which the flow solver (**CNS3D**) is based, is briefly described. A more detailed explanation can be founded in [72, 73].

2.3.1 Finite Volume Method

Based on the control volume formulation, the Finite Volume Method (**FVM**) presents a flexible discretization technique in which its extensive application is used into **CFD** flow solvers. In its formulation applied to analytical fluid dynamics, the splitting the domain into a number of control volumes, as a first step, the variables of interest are stored at the geometrical center of the correspondent control volume. In the second step, an integration of the differential form of the governing equations (similar to the control volume approach) is performed over each cell element. The conservation laws are integrated across a control volume and to describe the variation of the concerned variables, between centroids, interpolation profiles are assumed. The resulting equations are then discretized, allowing a digital handling by computers. In this manner, the discretized equations expresses the conservation principle for the variables inside the control volume. [74]

The resulting solution of **FVM** satisfies the conservation of quantities such as mass, momentum and energy and approximation is done during this procedure. Because the flux entering a given cell is identical to that leaving the adjacent cell, this method is conservative. Moreover, values for the cell faces can be reconstructed by interpolation or extrapolation of the cell averages. In comparison with other methods, like finite differences or finite element, the **FVM** can be consider as an exact method.

2.3.2 Godunov Method

From the methodology of the previous subsection, the governing equations are then solved using the Godunov method [63]. In his proposed first order method, a one dimensional form can be summarized as:

$$\mathbf{U}_j^{n+1} = \mathbf{U}_j^n + \frac{\Delta t}{\Delta x}\left(\mathbf{F}_{j-1/2} - \mathbf{F}_{j+1/2}\right), \tag{2.9}$$

where the numerical flux at the cell face ($\mathbf{F}_{j+1/2}$) is calculated based on the solution to the Riemann problem by using $\left(\mathbf{U}_j^n, \mathbf{U}_{j+1}^n\right)$, and in a similar manner $\mathbf{F}_{j-1/2}$ is calculated by

using the solution of the Riemann problem at $\left(\mathbf{U}_j^n, \mathbf{U}_{j-1}^n\right)$.

2.3.3 Total Variation Diminishing and Monotonicity

Total Variation Diminishing (**TVD**) methods were developed based on the notion of the *total variation* of the flowfield variable oscillations in the solution, this concept was introduced by Ami Harten [75].

Considering just the one-dimensional in space direction x of variable array $\mathbf{U}$, thus becomes $\mathbf{U}_i(x)$, has a total variation defined by:

$$TV(\mathbf{U}) = \int \left|\frac{\partial \mathbf{U}}{\partial x}\right| dx. \tag{2.10}$$

When considering the full system of equations then the $\mathbf{U}$ is also time dependent, $\mathbf{U}(x,t)$, in which case the total variation is defined at a fixed time t. In a discretized domain, like that of a **FVM**, $\mathbf{U}$ is a function of the mesh and its total variation at a time instant t at iteration level n is given by:

$$TV(\mathbf{U}^n) = \sum_{i=-\infty}^{+\infty} \left|\mathbf{U}_{j+1}^n - \mathbf{U}_j^n\right|, \tag{2.11}$$

where the function $\mathbf{U}(x,t)$ is assumed to reach a zero or constant value as it reaches the infinity boundaries in order to obtain a finite total variation. A scheme is regarded as a **TVD** method when the following constraint is met:

$$TV\left(\mathbf{U}^{n+1}\right) \leq TV(\mathbf{U}^n). \tag{2.12}$$

It can be said that a system is monotonicity preserving (Equation (2.12)) if the following properties are maintained as a function of time:

- No new local extrema can be created within the solution spatial domain.
- The value of a local minimum is non-decreasing, and the value of a local maximum is non-increasing.
- A monotone scheme is **TVD**.
- A **TVD** scheme is monotonicity preserving.

In engineering and scientific problems, monotone schemes are preferred because they provide solutions with physical meaning. Moreover, Godunov's theorem proves that only

first order linear schemes are monotone preserved and by consequence are **TVD**. Higher order linear schemes, although more accurate for smooth solutions, in the presence of discontinuities or shocks tend to introduce spurious oscillations. To surpass these characteristics, various high-resolution, non-linear techniques have been developed, often using flux/slope limiters. [76]

2.4 Time Integration

Several time stepping methods are coded within the flow solver, the second-order dual time stepping scheme proposed by Jameson [77] and four fully explicit Runge-Kutta (**RK**) time step methods, second-order method, second-order **TVD** version [78], third-order Total Variation Diminishing (**TVD**) [79] and third-order extended stability method. The third-order **TVD** method has been employed in this project and can be written as:

$$\mathbf{U}_j^1 = \mathbf{U}_j^n + \frac{\Delta t}{\Delta x} f\left(\mathbf{U}_j^n\right), \tag{2.13}$$

$$\mathbf{U}_j^2 = \mathbf{U}_j^n + \frac{1}{4}\frac{\Delta t}{\Delta x}\left[f\left(\mathbf{U}_j^n\right) + f\left(\mathbf{U}_j^1\right)\right], \tag{2.14}$$

$$\mathbf{U}_j^{n+1} = \mathbf{U}_j^n + \frac{1}{6}\frac{\Delta t}{\Delta x}[f\left(\mathbf{U}_j^n\right) + f\left(\mathbf{U}_j^1\right) + 4f\left(\mathbf{U}_j^2\right)]. \tag{2.15}$$

where Δt, is the global time step applied to all the cells. The global time step value is computed based on the Courant-Friedrichs-Levy number(**CFL**)[65], in this research **CFL** = 0.5 for all the case studies. The global time stet is defined as:

$$\Delta t = min\left(J\frac{CFL}{max(|\lambda_0^\xi|, |\lambda_1^\xi|, |\lambda_2^\xi|, |\lambda_0^\eta|, |\lambda_1^\eta|, |\lambda_2^\eta|, |\lambda_0^\zeta|, |\lambda_1^\zeta|, |\lambda_2^\zeta|)}\right), \tag{2.16}$$

where J denotes the Jacobian determinate and $\lambda_l^\xi, \lambda_l^\eta, \lambda_l^\zeta$ $(l = 0, 1, 2)$ are the eigenvalues of the advective fluxes $\overline{\mathbf{E}}$,$\overline{\mathbf{F}}$ and $\overline{\mathbf{G}}$ respectively.

2.5 Higher-order Spatial Accuracy

This class of methods are used in high-resolution schemes, such as the **MUSCL** and **WENO** schemes, to avoid the spurious oscillations that would otherwise occur with high

order spatial discretization schemes due to shocks, discontinuities or sharp changes in the solution domain. They can be understood as a process of reversing digital data to its analogue counterpart.

For Higher-order spatial accuracy, the flow solvers library is based in two different methodologies, the van Leer's Monotone Upstream-centred Schemes for Conservation Laws (**MUSCL** [66]) technique, and Weighted Essentially Non-Oscillatory (**WENO**) methods [80].

2.5.1 MUSCL

In the study of partial differential equations of the conservation laws, the **MUSCL** scheme is a finite volume method that provides highly accurate numerical solutions for a given system, even when the solutions exhibit shocks, discontinuities, or large gradients. The acronym **MUSCL** stands for Monotone Upstream-centered Schemes for Conservation Laws, and the term was introduced by Bram van Leer in a sequence of papers where he constructed the first high-order, **TVD** scheme where second order spatial accuracy was obtained. [66, 81–85]

The idea is to replace the piecewise constant approximation of Godunov's scheme by reconstructed states, derived from cell-averaged states obtained from the previous time-step. For each cell, slope limited, reconstructed left and right states are obtained and used to calculate fluxes at the cell faces. These fluxes can, in turn, be used as input to a Riemann solver, following which the solutions are averaged and used to advance the solution in time.

The base range of standard extrapolation methods in existence in the flow solver library are:

- Second-order: van Leer (**VL**), Minmod (MM), and van Albada (VA) [47, 64]
- Third-order: (**M3**) [55],
- Fifth-order: (**M5**) [67].

For **MUSCL** extrapolation, the left and right states of the conservative (or primitive) variables at the cell faces are computed as:

$$\mathbf{U}^{L}_{i+1/2} = \mathbf{U}_i + \frac{1}{4}\left[(1-c)\,\phi^{lim}\left(r_i^{lim,L}\right)(\mathbf{U}_i - \mathbf{U}_{i-1}) + (1+c)\,\phi^{lim}\left(\frac{1}{r_i^{lim,L}}\right)(\mathbf{U}_{i+1} - \mathbf{U}_i)\right], \quad (2.17)$$

$$\mathbf{U}^R_{i+1/2} = \mathbf{U}_{i+1} - \frac{1}{4}\left[(1-c)\,\phi^{lim}\left(r_i^{lim,R}\right)(\mathbf{U}_{i+2} - \mathbf{U}_{i+1}) + (1+c)\,\phi^{lim}\left(\frac{1}{r_i^{lim,R}}\right)(\mathbf{U}_{i+1} - \mathbf{U}_i)\right], \tag{2.18}$$

$$r_i^{lim,L} = \frac{\mathbf{U}_{i+1} - \mathbf{U}_i}{\mathbf{U}_i - \mathbf{U}_{i-1}} \tag{2.19}$$

$$r_i^{lim,R} = \frac{\mathbf{U}_{i+1} - \mathbf{U}_i}{\mathbf{U}_{i+2} - \mathbf{U}_{i+1}}, \tag{2.20}$$

where $\mathbf{U}$ is the vector of cell averaged conserved (or primitive) variables, c is a free parameter which is set to $\frac{1}{3}$ for the third-order limiter, and the cells are labelled by the integer i. It should be noted that the parameter c does not influence the accuracy of the second-order limiters considered here as they are symmetric.

In this research the second-order limiter (**VL**) and fifth-order (**M5**) are considered. The second-order limier is presented:

$$\phi^{lim}_{VL} = \frac{2r_i^{lim}}{1 + r_i^{lim}}. \tag{2.21}$$

The ϕ^{lim}_{VL} limiter is constrained in the normal fashion to first-order accuracy at local maxima and minima. The fifth-order **MUSCL** scheme (**M5**) is slightly different in structure [67]:

$$\phi*^{lim}_{M5,L} = \frac{-2/r_{i-1}^{lim,L} + 11 + 24r_i^{lim,L} - 3r_i^{lim,L}r_{i+1}^{lim,L}}{30} \tag{2.22}$$

$$\phi*^{lim}_{M5,R} = \frac{-2/r_{i+2}^{lim,R} + 11 + 24r_{i+1}^{lim,R} - 3r_{i+1}^{lim,R}r_i^{lim,R}}{30}, \tag{2.23}$$

where the ratio of the slopes are defined as:

$$r_i^{lim,L} = \frac{\mathbf{U}_{i+1} - \mathbf{U}_i}{\mathbf{U}_i - \mathbf{U}_{i-1}} \tag{2.24}$$

$$r_i^{lim,R} = \frac{\mathbf{U}_i - \mathbf{U}_{i-1}}{\mathbf{U}_{i+1} - \mathbf{U}_i}, \tag{2.25}$$

and monotonicity is maintained by limiting the above extrapolations using:

$$\phi^{lim}_{M5,L} = max(0, min(2, 2r_i^{lim,L}, \phi*^{lim}_{M5,L})) \quad (2.26)$$

$$\phi^{lim}_{M5,R} = max(0, min(2, 2r_i^{lim,R}, \phi*^{lim}_{M5,R})). \quad (2.27)$$

2.5.2 (W)ENO

(W)ENO schemes are a recent method of reconstruction based on the Essentially Non-Oscillatory (**ENO**) concept originally proposed by [86, 87]. The difference between **ENO** and **MUSCL** schemes is the way each on deals with the slopes that are obtained. **ENO** schemes employ a different principle to achieve this while still managing to obtain a order of accuracy higher than one. It achieves this by simply choosing the smoothest of all the slopes obtained in its stencil, be that second or even higher order method.

The **WENO** scheme implemented in the flow solver is primarily based on the work done in [70, 80, 88]. As the name implies, **WENO** schemes *weigh* each slope based on some criteria (such as smoothness following **ENO** schemes) and uses the obtained slope by the combination of all the slopes, depending on the order of the method, instead of employing just the smoothest one. This results in a convexly weighted average of polynomial interpolated slopes according to the smoothness of each slope. Because of considering all slopes calculated, **WENO** schemes can reach higher orders of accuracy than **ENO** methods, which on the contrary achieve lower orders of accuracy since they discard most of the slopes.

Motivated by the previous results obtained with the flow's solver **WENO** schemes, a revised version have been implemented, in particular the way the non-linear weights are calculated, the adjustment of ϵ to a more realistic value ($\epsilon = 10^{-7}$) and give mathematical correctness to the expression of the non-linear weights.

The **WENO** methodology takes a weighted average of several possible stencils to choose the 'smoothest' option [70, 80, 87, 89]. This is an extension of the Essentially Non-Oscillatory (**ENO**) scheme presented by Harten [86]. Both **ENO** and **WENO** schemes use the idea of adaptive stencils in the reconstruction procedure based on the local smoothness of the numerical solution to automatically achieve high-order accuracy and non-oscillatory property near discontinuities. By combining the stencils in this manner very high order accuracy can be achieved; in smooth flow field regions the order of accuracy is $2j - 1$, where j is the number of total stencils needed. Hence, a fifth order method

requires a set of six stencils. The following numerical schemes are implemented into the flow solver library:

- **WENO** fifth- and ninth- orders numerical schemes.

1. Reconstruct k^{th} degree orthogonal polynomial $\mathbf{p}_j(x)$ (Equation (2.35), Equation (2.36) and Equation (2.37) for the fifth order scheme), associated with each of the stencils $S_j \quad j = 0, \cdots, k$, and $(2k)^{th}$ degree orthogonal polynomial $\mathbf{Q}(x)$ (Equation (2.38) for the fifth order scheme), associated with the larger stencil, such that:

$$\mathbf{U}_{i+l} = \frac{1}{\Delta x_{i+l}} \int_{I_{i+l}} \mathbf{p}_j(x) dx \quad , l = -k + j, \cdots, j \tag{2.28}$$

$$\mathbf{U}_{i+l} = \frac{1}{\Delta x_{i+l}} \int_{I_{i+l}} \mathbf{Q}(x) dx \quad , l = -k, \cdots, k. \tag{2.29}$$

2. Find linear weight $\gamma_0, \cdots, \gamma_k$:

$$\mathbf{Q}\left(x_{i+1/2}\right) = \sum_{j=0}^{k} \gamma_j \mathbf{p}_j\left(x_{i+1/2}\right) \tag{2.30}$$

3. Compute the smoothness indicator, denoted by β_j , for each stencil S_j , which measures how smooth the function $p_j(x)$ is in the target cell I_i. The smaller this smoothness indicator β_j, the smoother the function $p_j(x)$ is in the target cell:

$$\beta_j = \sum_{l=1}^{k} \int_{I_i} \Delta x_i^{2l-1} \left(\frac{\partial^l}{\partial x^l} \mathbf{p}_j(x) \right)^2 dx \tag{2.31}$$

4. Compute the non-linear weights based on the smoothness indicators:

$$\omega_j = \frac{\overline{\omega_j}}{\sum_j \overline{\omega_j}}, \tag{2.32}$$

$$\overline{\omega_j} = \frac{\gamma_j}{\sum_j \left(\epsilon + \beta_j\right)^2}. \tag{2.33}$$

5. The final **WENO** approximation is then given by:

$$\mathbf{U}^{-}_{i+1/2} \approx \sum_{j=0}^{k} \omega_j p_j \left(x_{1+1/2}\right) \tag{2.34}$$

From the previous equations, the result for a 5^{th} order method can be performed. The **WENO** reconstruction for the left side ($\mathbf{U}^{-}_{i+1/2}$) is presented, the right side reconstruction ($\mathbf{U}^{+}_{i+1/2}$) is mirror symmetric with respect to "central" cell i of the following procedure. To demonstrate the concept, the fifth order **WENO** reconstruction has $j = 3$ and $k = 2$.

- Considering the "central" cell i.
- The stencils and correspondent polynomial:

$$\mathbf{p}_0 \left(x_{i+1/2}\right) = \frac{1}{3}\mathbf{U}_{i-2} - \frac{7}{6}\mathbf{U}_{i-1} + \frac{11}{6}\mathbf{U}_i \tag{2.35}$$

$$\mathbf{p}_1 \left(x_{i+1/2}\right) = -\frac{1}{6}\mathbf{U}_{i-1} + \frac{5}{6}\mathbf{U}_i + \frac{1}{3}\mathbf{U}_{i+1} \tag{2.36}$$

$$\mathbf{p}_2 \left(x_{i+1/2}\right) = \frac{1}{3}\mathbf{U}_i + \frac{5}{6}\mathbf{U}_{i+1} - \frac{1}{6}\mathbf{U}_{i+2} \tag{2.37}$$

$$\mathbf{Q} \left(x_{i+1/2}\right) = \frac{1}{30}\mathbf{U}_{i-2} - \frac{13}{60}\mathbf{U}_{i-1} + \frac{47}{60}\mathbf{U}_i + \frac{9}{20}\mathbf{U}_{i+1} - \frac{1}{20}\mathbf{U}_{i+2} \tag{2.38}$$

- The linear weights:

$$\gamma_0 = \frac{1}{10}; \gamma_1 = \frac{6}{10}; \gamma_2 = \frac{3}{10} \tag{2.39}$$

- In the actual numerical implementation the smoothness indicators β_j are written out explicitly as quadratic forms of the cell of $\mathbf{U}$ in the stencil:

$$\beta_0 = \frac{13}{12}\left(\mathbf{U}_{i-2} - 2\mathbf{U}_{i-1} + \mathbf{U}_i\right)^2 + \frac{1}{4}\left(3\mathbf{U}_{i-2} - 4\mathbf{U}_{i-1} + \mathbf{U}_i\right)^2 \tag{2.40}$$

$$\beta_1 = \frac{13}{12}\left(\mathbf{U}_{i-1} - 2\mathbf{U}_i + \mathbf{U}_{i+1}\right)^2 + \frac{1}{4}\left(3\mathbf{U}_{i-1} - \mathbf{U}_{i+1}\right)^2 \tag{2.41}$$

$$\beta_2 = \frac{13}{12}\left(\mathbf{U}_i - 2\mathbf{U}_{i+1} + \mathbf{U}_{i+2}\right)^2 + \frac{1}{4}\left(\mathbf{U}_i - 4\mathbf{U}_{i+1} + \mathbf{U}_{i+2}\right)^2 \tag{2.42}$$

For systems of conservation laws, such as the **NSE** system of fluid dynamics, the reconstructions from $\mathbf{U}_i$ to $\mathbf{U}^{\pm}_{i\pm 1/2}$ are performed in the local characteristic directions to avoid oscillations.

2.6 Low Mach Number Corrections

The standard **MUSCL** extrapolation has been augmented using the **L**ow **M**ach-number **L**imiting (**LMC**) [69], where at limit of zero Mach number uniform dissipation of kinetic energy is ensured. A further understanding of the development and reasoning of this augmentation can be found in [90]. The Godunov method validity is further extended to at least $Ma \approx 10^{-4}$. This is achieved by a progressive central differencing of the velocity components, without changing the formulation or discarding monotonicity of the underlying governing equations or the density field.

In [69] has been shown, that the kinetic energy dissipation rate leading order is proportional to $\frac{u^3}{\Delta x}$, similar in form to that proposed by [38] for decaying turbulence. The subgrid model in the **ILES** framework is associated to this dissipation rate. Moreover, comparisons to standard Godunov methods [69] show significantly improved high wave-number performance. This methodology works by enhancing the left and right values obtained from the reconstruction. No further dissipation is introduced as the local Mach number progressively decreases. This is achieved by the following formulae, as introduced in [69]:

$$\overline{u}^R_{i+1/2,j,k} = \frac{\overline{u}^L + \overline{u}^R}{2} + z\frac{\overline{u}^L - \overline{u}^R}{2} \tag{2.43}$$

$$\overline{u}^L_{i+1/2,j,k} = \frac{\overline{u}^L + \overline{u}^R}{2} + z\frac{\overline{u}^L - \overline{u}^R}{2}, \tag{2.44}$$

where z is defined as:

$$z = \min\left(Ma_{total}, 1\right) \tag{2.45}$$

$$Ma_{total} = \max\left(Ma_L, Ma_R\right) \tag{2.46}$$

and Ma_L is the local Mach number to the left of the cell face and Ma_R similarly but to the right. The modified velocity "jump" is modified by the function z, at the cell interface. This show to be a simple solution to the excessive numerical dissipation [69, 90].

2.7 Riemann Solver

As mentioned before, the Riemann solver is used to compute the flux through all the faces of a **CV** given a value for either side of the face. This class of solvers are a mathematical equivalent to the physical experience concerning the second law of thermodynamics (Entropy Law), they also ensure a physical meaning to the solution at any time instant.

However, solving the Riemann problem exactly is not always necessary due to the demanding requirements in terms of numerics, so approximate Riemann solver is used instead. One of the most popular approximate Riemann solver is the Harten, Leer, Lax Contact (**HLLC**) [47, 64, 91] which is an extension of the Harten, Leer, Lax (**HLL**) Riemann solver [92] by taking into consideration the existence of the contact surface. Other Riemann solver that is implemented into the flow solver is the Characteristic Based (Riemann) Solver (**CBS**) [65, 93, 94].

2.7.1 CBS

The Characteristic Based Scheme (**CBS**) is a linearised Riemann Solver. It was first developed and presented in [65] for the compressible Euler equations and extended further by [52, 94]. The conservative variables are defined along the characteristics as functions of their own characteristic values. A recent derivation of the scheme can also be found in [93] and results in the following linear system to compute the flux. The cell $\mathbf{U}_{i-1/2,j,k}$ can now be calculated using the **CBS** Riemann solver by the following relation:

$$\mathbf{U}_{i-1/2,j,k} = \begin{pmatrix} \rho \\ (\rho u) \\ (\rho v) \\ (\rho w) \\ \rho E \end{pmatrix} = \begin{pmatrix} \rho_0 + r_1 + r_2 \\ (\rho u)_0 + (u+\alpha)\, r_1 + (u-\alpha)\, r_2 \\ (\rho v)_0 + v r_1 + v r_2 \\ (\rho w)_0 + w r_1 + w r_2 \\ (\rho u)_0 + (H+\alpha c_0)\, r_1 + (H-\alpha c_0)\, r_2 \end{pmatrix}, \tag{2.47}$$

where r_1, r_2 and H (total enthalpy) are given by:

$$
\begin{aligned}
r_1 &= \frac{1}{2\alpha^2}\left((\rho_0-\rho_1)\left(\alpha c_0-\frac{\hat{\gamma}}{2}\hat{u^2}\right)+\left[(\rho u)_0-(\rho u)_1\right](\hat{\gamma}u-\alpha)+\right. \\
&\quad \left.\left[(\rho v)_0-(\rho v)_1\right]\hat{\gamma}v+\left[(\rho w)_0-(\rho w)_1\right]\hat{\gamma}w-(e_0-e_1)\,\hat{\gamma}\right) \qquad (2.48)\\
r_2 &= \frac{1}{2\alpha^2}\left(-(\rho_0-\rho_2)\left(\alpha c_0-\frac{\hat{\gamma}}{2}\hat{u^2}\right)+\left[(\rho u)_0-(\rho u)_2\right](\hat{\gamma}u-\alpha)+\right. \\
&\quad \left.\left[(\rho v)_0-(\rho v)_2\right]\hat{\gamma}v+\left[(\rho w)_0-(\rho w)_2\right]\hat{\gamma}w-(e_0-e_2)\,\hat{\gamma}\right) \qquad (2.49)\\
H &= \frac{\alpha^2}{\hat{\gamma}}+\frac{\hat{u^2}}{2}, \qquad (2.50)
\end{aligned}
$$

where the values of the velocities u, v, w and α (speed of sound) are the average of their left and right states while $\hat{u^2} = u^2 + v^2 + w^2$ and $\hat{\gamma} = \gamma - 1$. The advective flux $(F_c)_{i-1/2}$ for the **CBS** is calculated by:

$$
(F_c)^{CB}_{i-1/2} = F\left(\mathbf{U}_{i-1/2}\right). \qquad (2.51)
$$

2.7.2 HLLC

In order to calculate the numerical fluxes in this method, the speed of the five waves have to be initially estimated. Note that from [64] it is known that the characteristic speed waves $c_{2,3,4}$ are equal, this meaning $c_2 = c_3 = c_4$, and from now on, the Riemann problem will be approximated by a three wave structure. The following nomenclature is considered:

$$
S_L = c_1, \quad S_R = c_5, \quad S_\star = c_{2,\ldots,4}. \qquad (2.52)
$$

The methodology used to obtain the characteristic wave speed estimates for $S_{L,\star,R}$ is based on a pressure-velocity coupling as detailed in [47, 64] by the following formulae

$$
S_L = \vee_L - \alpha_L q_L, \quad S_\star = u_\star \quad S_R = \vee_R + \alpha_R q_R \qquad (2.53)
$$

where

$$q_K = \begin{cases} 1 & if \quad p_\star \leq p_K \\ \left[1 + \frac{\gamma+1}{2\gamma}\left(p_\star/p_K - 1\right)\right]^{1/2} & if \quad p_\star > p_K \end{cases} \quad K = R \; or \; K = L \tag{2.54}$$

The wave relations used are exact but the pressure ratio across a shock is approximated. The pressure in the star region $p_\star$ is thus obtained by [95]

$$p_\star = \frac{1}{2}\left(p_L + p_R\right) - \frac{1}{2}\left(\vee_R - \vee_L\right)\bar{\rho}\bar{\alpha}, \tag{2.55}$$

where $\bar{\rho}$ and $\bar{\alpha}$ are the local mean values given by

$$\bar{\rho} = \frac{1}{2}\left(\rho_L + \rho_R\right), \quad \bar{\alpha} = \tfrac{1}{2}\left(\alpha_L + \alpha_R\right), \tag{2.56}$$

and the characteristic speed $u_\star$ in the star region is then given by

$$u_\star = \frac{1}{2}\left(U_L - U_R\right) - \frac{1}{2}\frac{\left(p_R - p_L\right)}{\bar{\rho}\bar{a}}. \tag{2.57}$$

The last parameter required is the speed of the characteristic in the star region $S_\star$. This can be obtained by

$$S_\star = \frac{p_R - p_L + \rho_L \vee_L \left(S_L - \vee_L\right) - \rho_R \vee_R \left(S_R - \vee_R\right)}{\rho_L\left(S_L - \vee_L\right) - \rho_R\left(S_R - \vee_R\right)}. \tag{2.58}$$

Finally, the flux F_c for the **HLLC** approximate Riemann solver is then given by

$$\left(F_c\right)_{i+\frac{1}{2}}^{HLLC} = \begin{cases} \left(F_c\right)_L & if \quad 0 \leq S_L, \\ \left(F_c\right)_{\star L} & if \quad S_L \leq 0 \leq S_\star, \\ \left(F_c\right)_{\star R} & if \quad S_\star \leq 0 \leq S_R, \\ \left(F_c\right)_L & if \quad S_R \leq 0, \end{cases} \tag{2.59}$$

2.8 Post-processing

During this research, different post-processing tools have been developed to work in tandem with the flow solver computations. Despite the previous implementations of [96], the results where only valid as the final assemble of the different averages for the complete domain. With the developed tools, the former limitation had been removed, now temporal

follow up of the statistical variables is possible in an inexpensive manner; it is then possible to follow the variation of the statistical variables in time and space, simultaneously. The auxiliary tools have been codified according with the following formulae:

$$\langle U_{x,y,z} \rangle = \frac{\int\limits_{TW} \rho_{x,y,z}(t) U_{x,y,z}(t) dt}{\int\limits_{TW} \rho_{x,y,z}(t) dt}, \tag{2.60}$$

$$u'_{x,y,z} = U_{x,y,z} - \langle U_{x,y,z} \rangle, \tag{2.61}$$

$$\sigma(U_{x,y,z}) = \sqrt{\frac{1}{TW} \sum_{TW} (U_{x,y,z} - \langle U_{x,y,z} \rangle)^2}, \tag{2.62}$$

$$\textbf{Skewness}(U_{x,y,z}) = \frac{\sum\limits_{TW} (U_{x,y,z} - \langle U_{x,y,z} \rangle)^3}{\left(\sum\limits_{TW} (U_{x,y,z} - \langle U_{x,y,z} \rangle)^2 \right)^{\frac{3}{2}}}, \tag{2.63}$$

$$\textbf{Kurtosis}(U_{x,y,z}) = \frac{\sum\limits_{TW} (U_{x,y,z} - \langle U_{x,y,z} \rangle)^4}{\left(\sum\limits_{TW} (U_{x,y,z} - \langle U_{x,y,z} \rangle)^2 \right)^{2}}, \tag{2.64}$$

$$\textbf{RMS} u'_{x,y,z} = \sqrt{\frac{1}{TW} \sum_{TW} (u'_{x,y,z})^2}, \tag{2.65}$$

$$\tau_{x,y,z} = \frac{\langle u'_{x,y,z} u'_{x,y,z} \rangle}{U^2_{Ref}}. \tag{2.66}$$

To compute the spectral results, an extra tool has also been developed. Different numerical recipes are wildly available, but some detail should be attended to the algorithm which they are based. The current algorithm is based in [97, 98], the main advantage of this formulation to **CFD** resides in the fact that the time vector do not need to be modified in order to fulfil the criteria of having a temporal data string with length of 2^n, with $n = 1, \cdots, \infty$; moreover, the power spectral density amplitude and argument of $E_k(\nu)$ are easily computed. The following formulation has been employed:

$$E_k(\nu) = \sum_{n=1}^{N} E_k(t) e^{-\imath 2\pi k \frac{n}{N}}, \qquad k = 0, \ldots, N-1, \tag{2.67}$$

$$\mathbf{PSD}(E_k(\nu)) = |E_k(\nu)| = \sqrt{\Re(E_k(\nu))^2 + \Im(E_k(\nu))^2}, \tag{2.68}$$

$$\phi = arg(E_k(\nu)) = \arctan 2\left(\Im(E_k(\nu))^2, \Re(E_k(\nu))^2\right). \tag{2.69}$$

Simulated Cases and Results

3

Converging Diverging Nozzle and Shock Tube

3.1 Converging Diverging Nozzle

The **C**onverging **D**iverging **N**ozzle (**CDN**) is a simple test case involving the flow of inviscid, non heat conducting air through a converging diverging nozzle. This is a classic quasi-one dimensional, steady, compressible flow problem discussed in most compressible flow textbooks, such as [48]. This case allow us to see the results of the improvements and changed done in the flow solver on the following manner:

- Comparison with analytic solution.
- Consistency of axisymetric and three-dimensional flow domains.

This study consists on the simulation of unsteady, viscus, non heat conducting flow through a converging diverging nozzle. From the methods contained in the flow solver's library, the **CBS MUSCL** 5^{th} augmented with **L**ow-**M**ach number **L**imiting (**LMC**), in

conjunction with the third-order **TVD** Runge-Kutta method and **CFL** = 0.5, has been selected to perform this analysis. The nature of the flow field is determined by the exit conditions, in this case, the exit static pressure. The flow is accelerated out of the nozzle and a shock wave will be generated on the diverging region of the domain. The plenum total pressure and temperature are assumed as constants. The initial conditions used are prescribed in Table 3.1.

Plenum Total Pressure	6894.757 (Pa)
Plenum Total Temperature	55.556 (K)
Exit Static Pressure Ratio	0.75

Table 3.1: CDN Flow conditions.

The geometry is an axisymmetric converging diverging duct with a general shape and an area given by Equation (3.1) [99]. The domain is discretized with $(132 \times 33 \times 33)$ cells (Figure 3.1) and the boundary conditions were set up as fixed and laminar inflow, non-reflective outflow, non-slip solid surface (inside surface) and transparent (singularity line), respectively.

$$\begin{aligned} A(x) &= 1.75 - 0.75 * \cos((0.2 * x - 1.0) * \pi); 0 \leq x \leq 5 \\ A(x) &= 1.25 - 0.25 * \cos((0.2 * x - 1.0) * \pi); 5 \leq x \leq 10 \end{aligned} \tag{3.1}$$

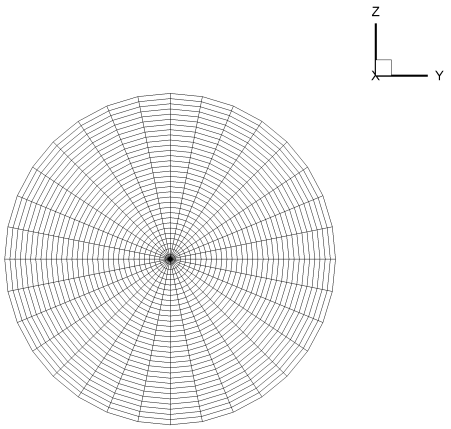

(a) Section $\odot YZ$.

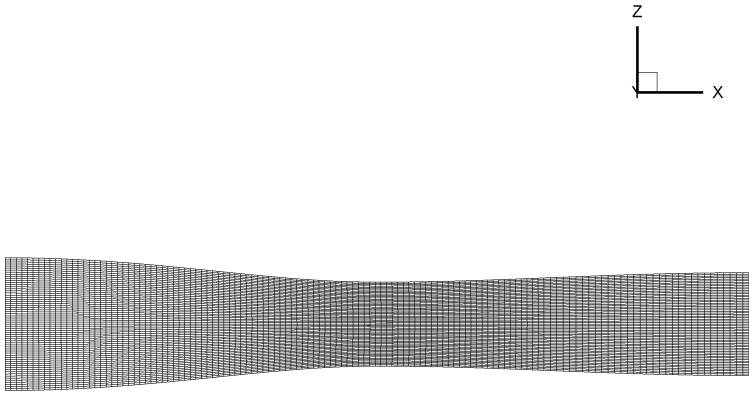

(b) Section $\odot XZ$.

FIGURE 3.1: CDN axisymmetric mesh.

The predicted result is compared, quantitatively, against the analytic solution. Figure 3.2, frame *a*, shows the Mach Number distribution along the center line of the nozzle. The predicted result accurately follow the analytical solution, with the exact position of the shock and velocity ratios, being observed; a slightly undershot in the first cell down stream of the shock can be observed, this can be explained by the mathematical characteristic of the employed method in the presence of sharp flow discontinuities, as it will be seen in the next section. Frame *b*, an instantaneous snapshot of the central radial plane, where it can be observed the uniformity of the flow field trough the central region of the

plane.

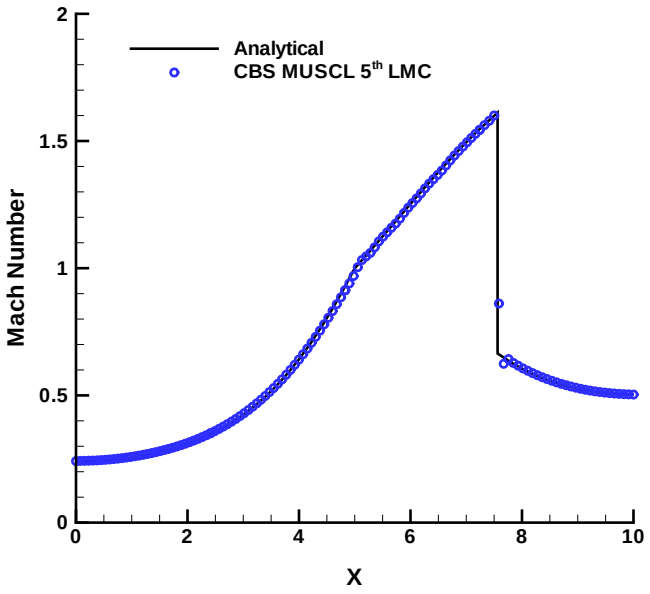

(a) Central line distribution.

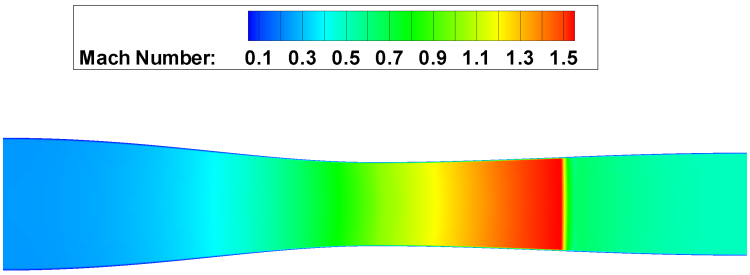

(b) Instantaneous snapshot.

Figure 3.2: Mach Number results.

3.2 Shock Tube

To demonstrate that the geometrical singularity does not affect the ability of the flow solver numerical schemes in capturing shock waves and contact surfaces, the standard Sod Shock Tube problem [100] and a modified version, $3D$ test case, have been analysed.

With the initial discontinuity been placed at half of the domain's length, the following initial conditions have been applied to both cases:

$$(\rho, u, p)_L = (1, 0, 10),$$
$$(\rho, u, p)_R = (0.125, 0, 1).$$

For the standard shock tube problem, a grid convergence or h-study is preformed, with the following discretization levels:

- h1, 100 cells,
- h2, 200 cells,
- h3, 400 cells,
- h4, 800 cells.

On the h-study, the different methods of the flow solver's library, that are going to be used on the jet flow cases, are employed. This allow us to observe the behaviour of each individual method with the different grid refinements and manufacture a benchmark solution to be used, as numerical reference, for the $3D$ cases.

For the $3D$ cases a p-study has been performed. The domain has a discretization level of (300×33×33) cells, which correspond to an intermediary level of $h2$ and $h3$, Figure 3.3. Also, all the methods employed on the h-study were used in the p-study.

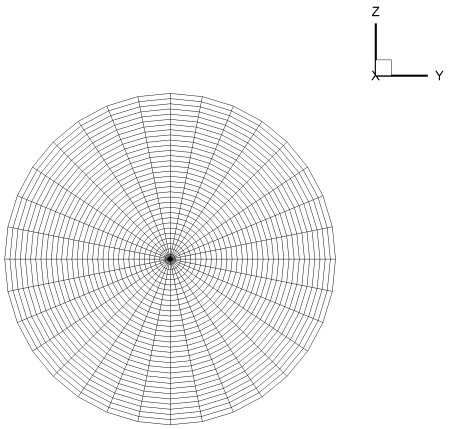

(a) Section $\odot YZ$.

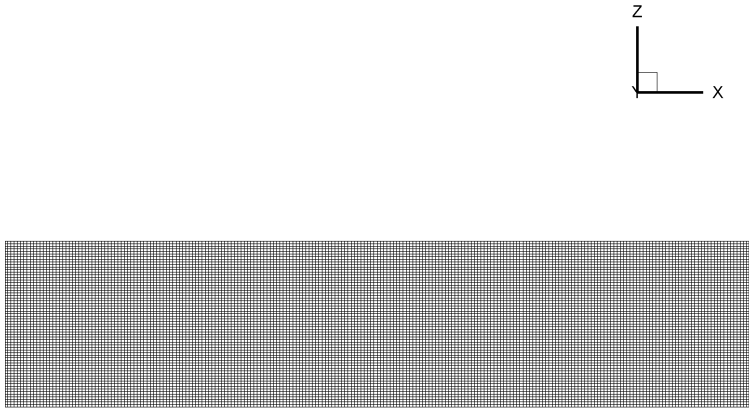

(b) Section $\odot XZ$.

Figure 3.3: Shock Tube, $3D$ axisymmetric mesh.

On the h-study, the flow field is assumed to be steady and inviscid in order to confirm the accuracy of each method. For the $3D$ case, a viscous and unsteady flow field is assumed, with the same initial conditions as the p-study.

The results presented in this section, Figure 3.4 and Appendix B, were taken for the same computational time span ($t = 0.114$). Since the time span of the unsteady flow is short, the waves and fans never reach the end walls. The tube is closed at the ends, thus all boundaries of the computational domain are solid walls. The inside surface of the tube is assumed as non-slip surface. At the domain's geometrical singularity it is applied the

transparent boundary condition.

The presence of discontinuities in the flow field, like shock waves, the maximum error value is half of the shock strength. To go around this characteristic, the maximum error is computed by using the following relation:

$$\varepsilon_{rror}(\rho, u, p) = \left| 1 - \frac{\int_x (\rho(x), u(x), p(x))_{Simulated} dx}{\int_x (\rho(x), u(x), p(x))_{Analytical} dx} \right|. \tag{3.2}$$

With Equation (3.2), it is possible to estimate the error in the presence of sharp discontinuities in the flow field, for each combination of numerical schemes and meshes. The reduced data from these studies, Table 3.2 to Table 3.7, is compared against an analytical solution from [100].

From the following tables, it can be observed the accuracy in results for each combination of numerical schemes with the correspondent meshes. For the standard cases or h-studies, the errors in the analysed variables (density, Mach number and pressure) associated to each numerical combination is only a factor of the discretization levels. The proportional decrease in error has a linear order of convergence for all numerical schemes and variables; with the exception of the Mach number on all the **HLLC MUSCL** and **HLLC WENO**5^{th} schemes, where the order of convergence is sub-linear. As the $3D$ cases are concerned, the error in density is equal to all numerical schemes, as in the standard cases combinations. In terms of pressure, the error value has a negligible difference and can be associated with round off errors in calculations. The Mach number error shows to be dependent of each numerical scheme. Moreover, it can be observed that the error values ($3D$) are lower then the maximum value of the standard results ($h1$ case), accordingly. The Mach Number error has been further reduced in the $3D$ mesh then the $h4$ mesh result, this for the **HLLC MUSCL**5^{th} **LMC** method.

CBS			
Grids	Density	Mach Number	Pressure
h1	0.0609	0.0112	0.0699
h2	0.0022	0.0085	0.0036
h3	0.0008	0.0065	0.0015
h4	0.0002	0.0060	0.0005
HLLC			
Grids	Density	Mach Number	Pressure
h1	0.0609	0.0074	0.0701
h2	0.0022	0.0062	0.0034
h3	0.0008	0.0057	0.0014
h4	0.0002	0.0056	0.0005

Table 3.2: Reduced numerical error reduction with grid refinement, **MUSCL** 2^{nd} **LMC**.

CBS			
Grids	Density	Mach Number	Pressure
h1	0.0609	0.0101	0.0699
h2	0.0022	0.0083	0.0036
h3	0.0008	0.0065	0.0015
h4	0.0002	0.0057	0.0005
HLLC			
Grids	Density	Mach Number	Pressure
h1	0.0609	0.0071	0.0702
h2	0.0022	0.0059	0.0034
h3	0.0008	0.0053	0.0014
h4	0.0002	0.0052	0.0004

Table 3.3: Reduced numerical error reduction with grid refinement, **MUSCL** 5^{th}.

CBS			
Grids	Density	Mach Number	Pressure
h1	0.0609	0.0109	0.0698
h2	0.0022	0.0085	0.0037
h3	0.0008	0.0071	0.0016
h4	0.0002	0.0061	0.0005
HLLC			
Grids	Density	Mach Number	Pressure
h1	0.0609	0.0079	0.0699
h2	0.0022	0.0065	0.0035
h3	0.0008	0.0057	0.0015
h4	0.0002	0.0056	0.0005

Table 3.4: Reduced numerical error reduction with grid refinement, **MUSCL** 5^{th} **LMC**.

CBS			
Grids	Density	Mach Number	Pressure
h1	0.0609	0.0120	0.0698
h2	0.0022	0.0088	0.0036
h3	0.0008	0.0069	0.0015
h4	0.0002	0.0061	0.0005
HLLC			
Grids	Density	Mach Number	Pressure
h1	0.0609	0.0098	0.0699
h2	0.0022	0.0071	0.0035
h3	0.0008	0.0062	0.0015
h4	0.0002	0.0058	0.0005

Table 3.5: Reduced numerical error reduction with grid refinement, **WENO** 5^{th}.

CBS			
Grids	Density	Mach Number	Pressure
h1	0.0609	0.0155	0.0696
h2	0.0022	0.0089	0.0037
h3	0.0008	0.0073	0.0016
h4	0.0002	0.0062	0.0005
HLLC			
Grids	Density	Mach Number	Pressure
h1	0.0609	0.0123	0.0697
h2	0.0022	0.0079	0.0036
h3	0.0008	0.0067	0.0015
h4	0.0002	0.0059	0.0005

Table 3.6: Reduced numerical error reduction with grid refinement,**WENO** 9^{th}.

Method	Density	Mach Number	Pressure
CBS MUSCL2^{nd} **LMC**	0.0048	0.0072	0.0041
HLLC MUSCL2^{nd} **LMC**	0.0048	0.0059	0.0043
CBS MUSCL5^{th}	0.0048	0.0068	0.0042
HLLC MUSCL5^{th}	0.0048	0.0058	0.0043
CBS MUSCL5^{th} **LMC**	0.0048	0.0074	0.0041
HLLC MUSCL5^{th} **LMC**	0.0048	0.0051	0.0042
CBS WENO5^{th}	0.0048	0.0074	0.0042
HLLC WENO5^{th}	0.0048	0.0066	0.0042
CBS WENO9^{th}	0.0048	0.0081	0.0041
HLLC WENO9^{th}	0.0048	0.0073	0.0041

Table 3.7: Reduced numerical error, $3D$ cases.

Figure 3.4, compares the Riemann solvers results for the **MUSCL** 5^{th} **LMC** schemes, $3D$ cases. It can be observed that both solver's resolve the flow field properties accurately, with a small over/under shot for all the variables at $X = 5$ (**CBS**). This can be explained by the physical property (velocities) of the **CBS** solver as a response function to inertia of the fluid, while the same response function (Pressure) for the **HLLC** solver smooths the flow field for the same region. The same pattern can be observed for the remaining results (Appendix B), with the exception of the **WENO** 9^{th} methods, where the same over/under shot occurs for both Riemann solvers. Furthermore, in the presence of sharp discontinuities in the flow field the **WENO** schemes have an oscillatory pattern. This effect occurs by a locally reduction to the first order of accuracy in the reconstruction schemes, in accordance to [70].

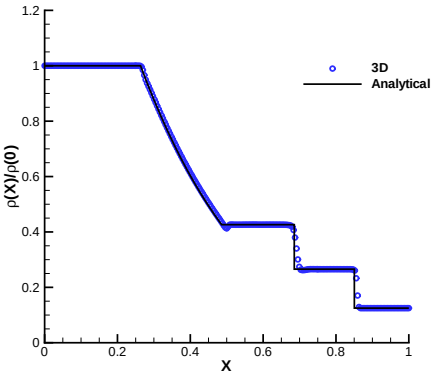

(a) Density, **CBS**.

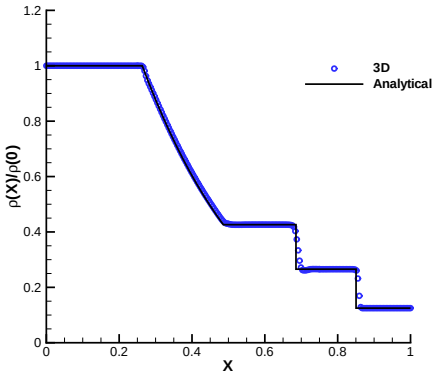

(b) Density, **HLLC**.

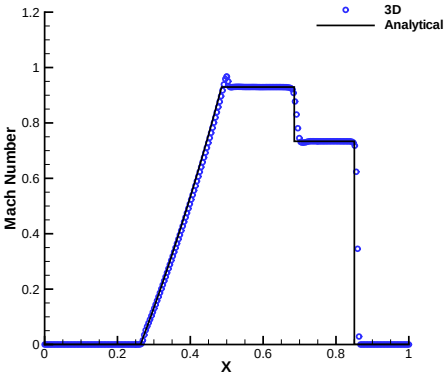

(c) Mach Number, **CBS**.

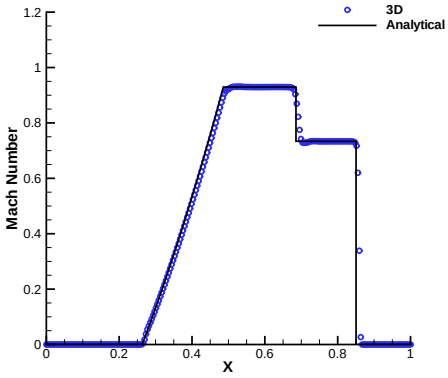

(d) Mach Number, **HLLC**.

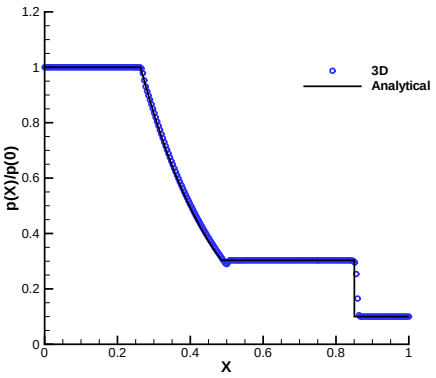

(e) Pressure, **CBS**.

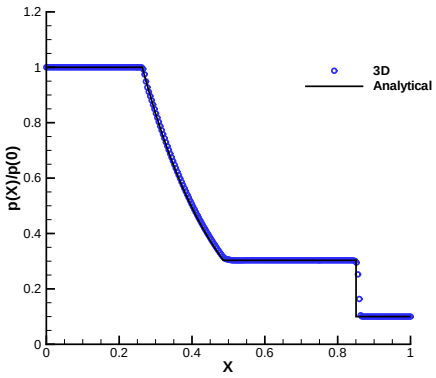

(f) Pressure, **HLLC**.

Figure 3.4: Density, Mach Number and Pressure results, **MUSCL** 5^{th} **LMC**, $3D$ cases. Analytical [100].

3.3 Discussion

Although this chapter does not intend to completely verify or validate the flow solver, it demonstrates that the reviews of the **WENO** schemes and implementation of a new boundary condition (transparent) in association to the change from the algebraic to geometrical method (Jacobian calculation), have mathematical and physical meaning. By doing so, the robustness and accuracy of the flow solver has been increased and enhanced, allowing the solution of problems where the domains discretization demands a singularity point or line. Moreover, from the **CDN** case, it can be concluded that the improvements, coordinate transformation and boundary condition, done in the flow solver accurately capture the physical behaviour of the flow field at different regimes (sub-sonic, sonic and super-sonic), with an accurate prediction (position and intensity) of the correspondent shock wave. Furthermore, the study of the shock tube problem shows that all the combinations, of numerics with the corresponding meshes, concur with the associated though experience of the Second Law of Thermodynamics (Entropy).

Concluding, from the previous observations and results, the most accurate numerical method ($3D$ case) is the **HLLC** 5^{th}**-order LMC**, as the analysed variables (density, Mach number and pressure) show the lowest error. With this conclusion, it is possible to start the study of the jet flow cases (Static and Co-flow), employing the respective numerical scheme in a h-study.

4

Numerical Uncertainties and Error Bar

4.1 Introduction

Computational uncertainty is present in every system, mainly in those who encompass non-linearities and it also appears in many different domains of mathematics, physics and engineering [101, 102]. In the context of computational fluid dynamics for turbulent flows, the uncertainty is associated with the non-deterministic nature of turbulence, which poses numerical modelling challenges with respect to the definition of initial and boundary conditions as well as the design of numerical methods for solving the fluid flow equations [103]. Different ways to quantify numerical uncertainties in **CFD** have also been discussed in the past [104].

Modern numerical methods such as high-resolution and high-order schemes, consist of several numerical components (building blocks) for achieving better convergence and high-order order of accuracy in complex flows [105]. For example, high-resolution schemes [47] encompass several steps in the discretization of the partial differential equations, which include a Riemann solver and a numerical reconstruction scheme. The latter also contains slope/flux limiters which are used for adjusting the order of accuracy in the

computational domain by taking into account the flow gradients on the local stencil. The conventional wisdom is that as the grid is further refined the results will converge to the same solution regardless the numerical schemes employed, as the numerical error will tend to zero. However, in turbulent flow simulations such as in **L**arge **E**ddy **S**imulation (**LES**), there is no explicit verification that the solution is grid-converged, because the computations are always under-resolved. One could argue that this may also be the case with respect to **D**irect **N**umerical **S**imulations (**DNS**) at least with reference to high-order statistics. Discussion on Policy Statement on the Control of Numerical Accuracy can also be found in previous discussion documents [106–108], including the notion of a numerical error bar [107].

Numerical errors in the context of **LES** have also been discussed previously by other authors [109] and in a general **CFD** context [106]. Specifically, a turbulent jet flow [33, 110–117] has been chosen as the benchmark case for different Riemann solvers, high-resolution and high-order methods and different levels of grid refinement, in order to comparatively demonstrate the effects of the above numerical components on the accuracy of the simulations. Comparisons are presented against experimental [33, 111, 115, 116] and **DNS** [110] data. Jet flows are pertinent to many engineering applications, including propulsion, noise radiation, mixing effectiveness among others [4, 6, 10, 27, 117–120].

4.2 Methodology and Results

In order to calculate the numerical value of the error bar, an assemble Favre average (Equation (2.60)) and standard deviation (Equation (2.62)) values are computed over the time window. Furthermore, the analysis of the physical and numerical components of uncertainty, of each numerical scheme, will determine the error bar value. It is then proposed the following equation to compute the error bar value, for computations of unsteady flows with explicit time stepping:

$$\varepsilon_{rrorbar} = \frac{|U_{Exp} - U_{Num}|}{U_{Exp}} + \frac{\sigma(U)}{\sqrt{N}}, \tag{4.1}$$

with U_{Exp}, U_{Num} and U as the reduced velocities values and N ($N \geq 2, \cdots, \infty$) the number of instantaneous results that have been outputted during the time window computations. On the right hand side of Equation (4.1) the first term represents the physical error and the second term is associated with the numerical uncertainty predictions or numerical error

[121], respectively. As the iterations (N) reach infinity the value of the numerical error reach zero, making the error bar value only dependent of the physical component.

The evolution, in time, of the convergence/steadiness level is analysed through the standard deviation, domain's maximum value, for each mesh and methods. Also, the mathematical convergence/steadiness analysis is further extended by using high-order statistics, Skewness (Equation (2.63)) and Kurtosis (Equation (2.64)), which are good indicators of steadiness for unsteady flows (Appendix F). The results were computed for the following central line points:

- $\frac{X}{D} = (20, 25, 30, 35, 40)$.

The domain used in this study is based on the geometry of [110, 119] and clustered using the method of the characteristics [122, 123]. Appendix C presents a brief description of the clustering method and the refinements levels for each h-mesh. Velocities along the jet axis become non-dimensional with reference to the axial velocity of the jet at the geometrical center of the inflow, U_{Ref} (Static case), and ΔU_{Ref} (Co-flow case) with $\Delta U_{Ref} = U_{Jet} - U_{\infty}$, accordingly.

The boundary conditions were set up as inflow for the jet discharge (laminar profile) and upstream of the jet exit; no-slip at the wall of the engine's nozzle (outside), transparent for the domain geometrical singularity and outflow (non-reflective boundary conditions) for the rest of the domain. Table 4.1 presents the initialization values for both jet cases.

Static Jet		Co-Flow Jet	
γ	1.4	γ	1.4
Ma_{Jet}	0.9	Ma_{Jet}	0.9
Ma_{∞}	0	Ma_{∞}	0.243
P_j/P_{∞}	1	P_j/P_{∞}	1
T_j/T_{∞}	1	T_j/T_{∞}	1

Table 4.1: Initial conditions, Static and Co-flow Jets.

Both jet cases, Static and Co-flow, have been developed by 1500 time units, allowing the flow field to become steady. The time window covers, another, 1500 units of time.

Simulations were performed, for the Static and Co-flow jets, using the **HLLC** Riemann solver with the 5^{th}-order **MUSCL** scheme and (**LMC**), h-studies. Comparisons are presented with the **DNS** [110] and experimental data from Hot Wire Anemometry [111] and LASER Doppler Anemometry [33], over the central line. The predicted results

were further reduced to the jet coordinate system (Appendix D). For the *p*-studies a selection of the different methods from the solver's library have been selected. This selection reflects the influence of the Riemann solvers, spatial order of accuracy, **LMC** and reconstruction/limiting schemes. In the *p*-study subsection a selection of three methods will show the Riemann solvers and spatial resolution differences. The remaining results are presented by Riemann solver in Appendix E. In both studies and test cases, the time integration employed was the Runge-Kutta third order **TVD** with $CFL = 0.5$. The following numerical variants were applied for these studies:

- The **CBS** and **HLLC** Riemann solvers with the 2^{nd}-order **MUSCL** scheme and **L**ow-**M**ach **L**imiting, henceforth labelled as '**CBS MUSCL** 2^{nd} **LMC**' and '**HLLC MUSCL** 2^{nd} **LMC**'.
- The **CBS** and **HLLC** Riemann solvers with the 5^{th}-order **MUSCL** scheme, henceforth labelled as '**CBS MUSCL** 5^{th}' and '**HLLC MUSCL** 5^{th}'.
- The **CBS** and **HLLC** Riemann solvers with the 5^{th}-order **MUSCL** scheme and **L**ow-**M**ach **L**imiting, henceforth labelled as '**CBS MUSCL** 5^{th} **LMC**' and '**HLLC MUSCL** 5^{th} **LMC**'.
- The **CBS** and **HLLC** Riemann solvers with the 5^{th}-order **WENO** scheme, henceforth labelled as '**CBS WENO** 5^{th}' and'**HLLC WENO** 5^{th}'.
- The **CBS** and **HLLC** Riemann solvers with the 9^{th}-order **WENO** scheme, henceforth labelled as '**CBS WENO** 9^{th}' and'**HLLC WENO** 9^{th}'.
- The average from all the methods employed, henceforth labelled as '**CNS3D**'.

4.2.1 *h*-study

The reduction in the absolute error and standard-error-of-the-mean with the grid refinement results are presented in Table 4.2, also the ability of each mesh in capturing the jets core length. This ability will be discussed in the next chapters, Chapter 5 and Chapter 6. Moreover, the numerical maximum standard-error-of-the-mean is in the same order of magnitude for all the correspondent cases; in the Static case an improvement with mesh refinement is observed, while on the Co-flow case, the correspondent improvement is negligible.

Computational grid	Maximum error	Standard-error-of-the-mean	X_0
Static Jet			
Coarse	0.265	0.0160	3
Medium	0.190	0.0150	0
Fine	0.189	0.0109	0
Co-Flow Jet			
Coarse	0.391	0.0098	10
Medium	0.108	0.0090	6
Fine	0.245	0.0090	3

Table 4.2: Numerical error reduction with grid refinement, *h*-study.

Figure 4.1, frames *a* and *c*, shows the evolution of the domains maximum standard deviation, for the different grid resolutions, statistical convergence is only achieved for the $Coarse$ and $Medium$ cases, however, all the cases results have converged asymptomatic to a statistically steady state solution. Frames *b* and *d* shows the results for the axial average velocity for all grid resolutions. Here, it can be observed the effects of the grid refinement over the central line velocity distribution. In the Static case, both $Medium$ and $Fine$ cases give similar results in terms of core length size and velocity distribution, making the $Medium$ mesh the most suitable to perform a *p*-study; the Co-flow case, the jet's core length value improves with grid refinement, as it can be observed. Reduction to the jet's coordinates system reveals an increase on the maximum error for the $Fine$ mesh (Co-flow case) and the break down of the jet's core that is approximately steady in space, originating an increase of the oscillating pattern observed on frame *d*; however, the central line velocity distribution follow the same trend as the experimental result. From the Static case observations, also the Co-flow case reveals the $Medium$ mesh as the most suitable to be employed for the *p*-study. Furthermore, in both cases, despite the fact of existing an under prediction in all cases, for the transition and far-field regions, the envelope created by the error bar encompasses the **DNS** and experimental results.

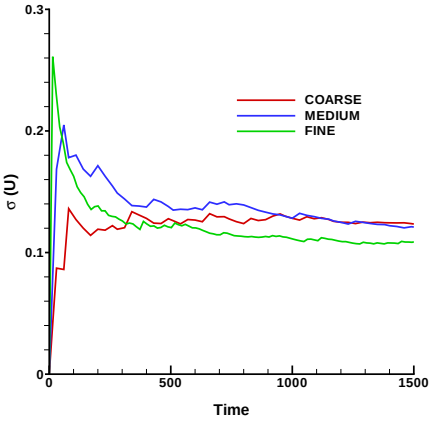

(a) Domains Maximum σ, Static Jet.

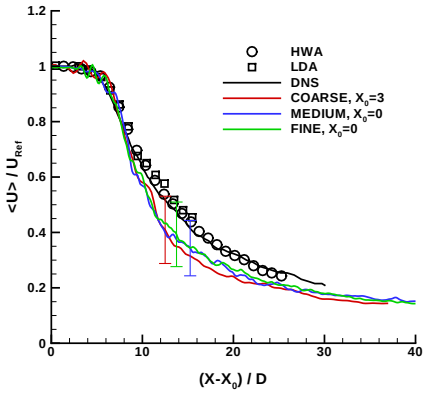

(b) Central Line velocity distribution, Static Jet.

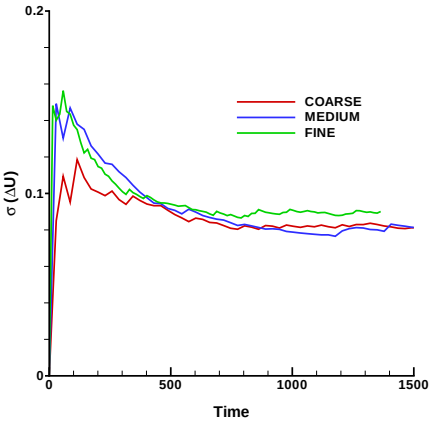

(c) Domains Maximum σ, Co-Flow Jet.

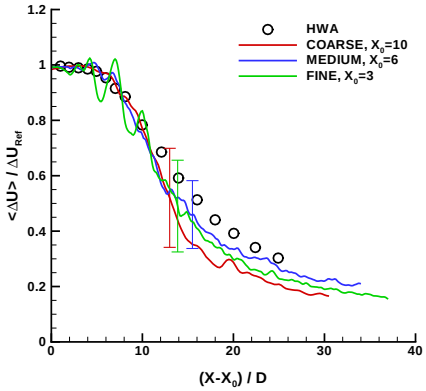

(d) Central Line velocity distribution, Co-Flow Jet.

Figure 4.1: *h*-study. **HWA**[111], **LDA**[33] and **DNS**[110]

Figure 4.2 and Figure 4.3 present snapshots at different time instants of the axial velocity profile of the jets for the *Fine* mesh. The unsteadiness of the flow field can be observed, as well the different structures at the jet's flow field regions. The *Fine* mesh of Co-flow case was chosen because of the core length size value being close to the experimental/analytical value. It can also be observed the influence of the singularity treatment over the domain's geometrical central line.

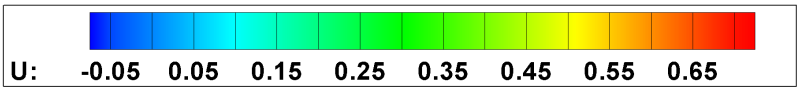

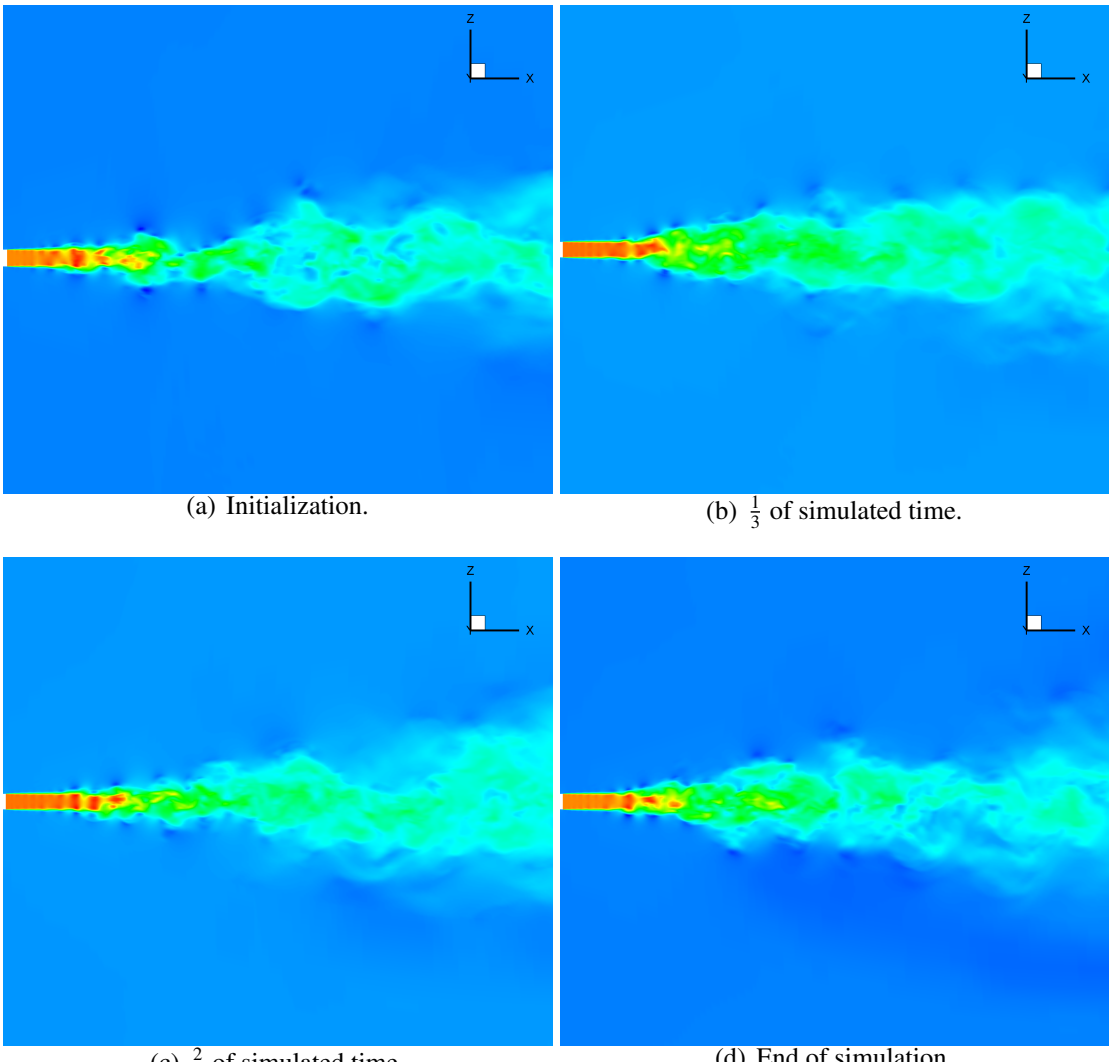

(a) Initialization.

(b) $\frac{1}{3}$ of simulated time.

(c) $\frac{2}{3}$ of simulated time.

(d) End of simulation.

Figure 4.2: Instantaneous axial velocity profiles of the static jet flow, Fine mesh.

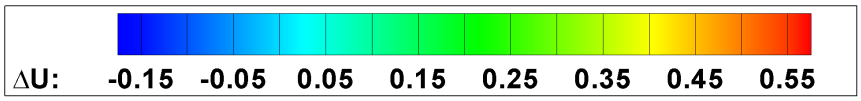

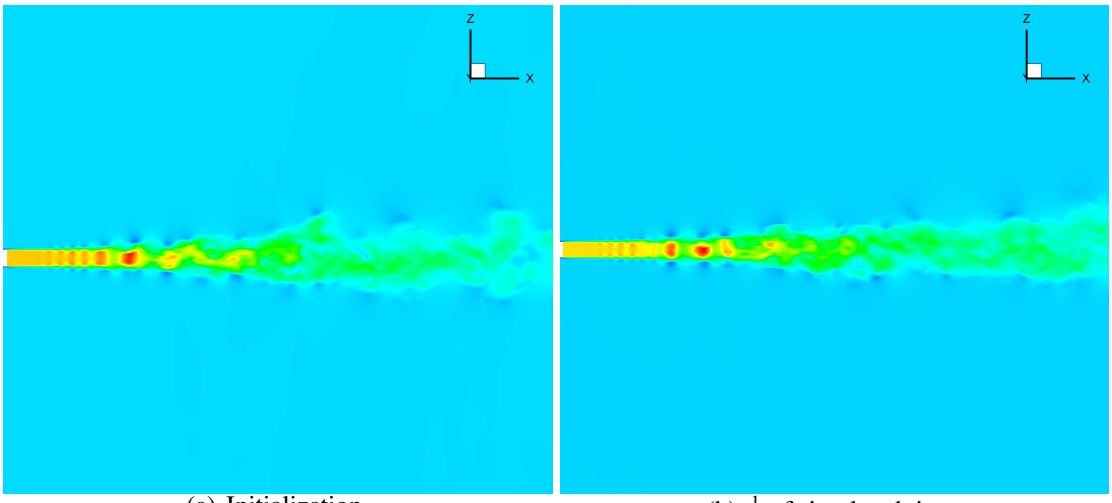

(a) Initialization.

(b) $\frac{1}{3}$ of simulated time.

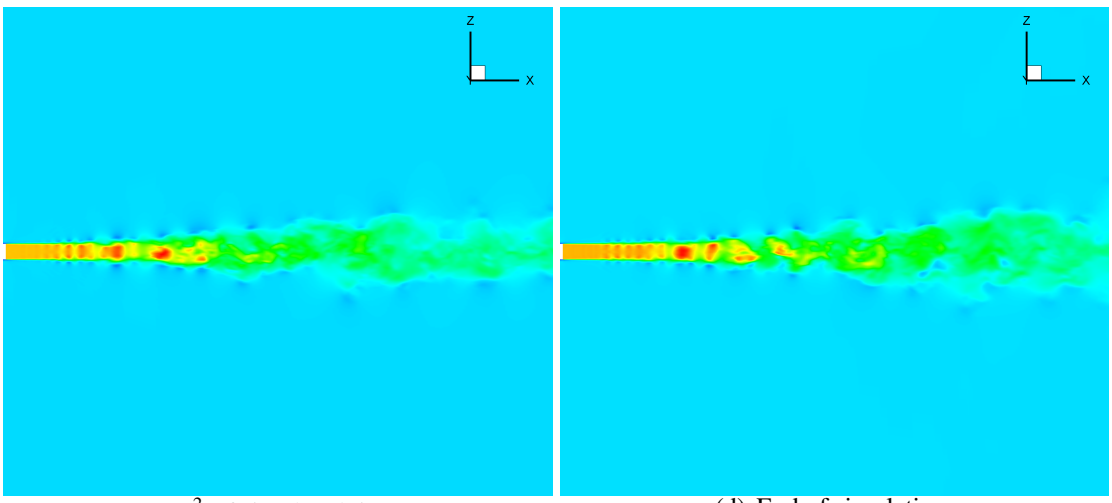

(c) $\frac{2}{3}$ of simulated time.

(d) End of simulation.

Figure 4.3: Instantaneous axial velocity profiles of the co-flow jet, Fine mesh.

4.2.2 *p*-study

Assuming that the total error can be represented by the sum of the estimated maximum error and the maximum standard-error-of-the-mean, a numerical error bar can be defined with respect to an averaged solution. For example, one possibility, including but not not limited to, is to obtain an average of all numerical predictions and put on top of it the numerical error bar, which represents a measure of the numerical uncertainty.

Numerical Variants	Maximum error	Standard-error-of-the-mean	X_0
Static Jet			
CBS MUSCL 2^{nd} **LMC**	0.297	0.0177	2
HLLC MUSCL 2^{nd} **LMC**	0.331	0.0175	2
CBS MUSCL 5^{th}	0.217	0.0167	1
HLLC MUSCL 5^{th}	0.190	0.0170	1
CBS MUSCL 5^{th} **LMC**	0.154	0.0146	0
HLLC MUSCL 5^{th} **LMC**	0.190	0.0150	0
CBS WENO 5^{th}	0.238	0.0140	1
HLLC WENO 5^{th}	0.244	0.0158	1
CBS WENO 9^{th}	0.234	0.0164	0
HLLC WENO 9^{th}	0.269	0.0145	0
CNS3D	0.159	0.0148	0
Co-Flow Jet			
CBS MUSCL 2^{nd} **LMC**	0.422	0.0155	8
HLLC MUSCL 2^{nd} **LMC**	0.440	0.0106	8
CBS MUSCL 5^{th}	0.263	0.0111	6
HLLC MUSCL 5^{th}	0.269	0.0095	6
CBS MUSCL 5^{th} **LMC**	0.404	0.0110	4
HLLC MUSCL 5^{th} **LMC**	0.108	0.0090	6
CBS WENO 5^{th}	0.280	0.0108	7
HLLC WENO 5^{th}	0.299	0.0158	7
CBS WENO 9^{th}	0.361	0.0105	2
HLLC WENO 9^{th}	0.335	0.0114	2
CNS3D	0.225	0.0095	4

Table 4.3: Numerical error reduction, *p*-study.

Table 4.3 shows the effects on the absolute error and standard-error-of-the-mean with the numerical variants, also the ability of each method in capturing the jets core length. This ability will be discussed on the next chapters, Chapter 5 and Chapter 6. Furthermore, the numerical maximum standard-error-of-the-mean is approximately in the same order of magnitude for all the correspondent cases, revealing for the Static and Co-flow cases the

CBS MUSCL 5^{th} **LMC** and the **HLLC MUSCL** 5^{th} **LMC** as the best numerical schemes to be employed, accordingly. It can be observed that the 9^{th}-order schemes under predict the velocity distribution even with the exact (Static case) and closer (Co-flow case) size of the jet's core length. The results of the 2^{nd}-order schemes are comparable to the *Coarse* mesh predictions in terms of errors and size of the jet core length.

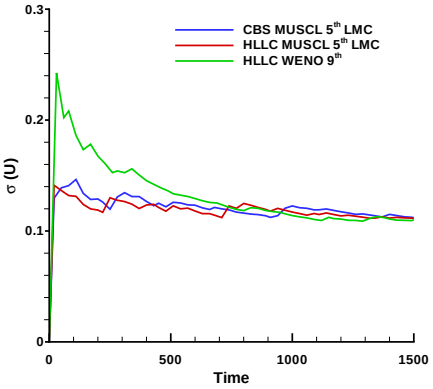

(a) Domains Maximum σ, Static Jet.

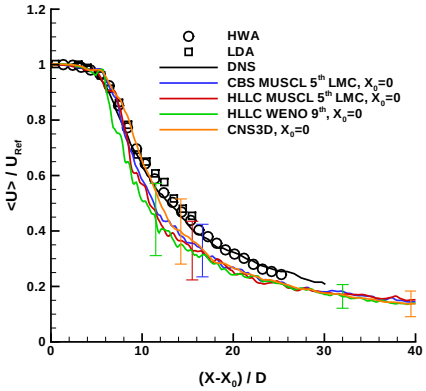

(b) Central Line velocity distribution, Static Jet.

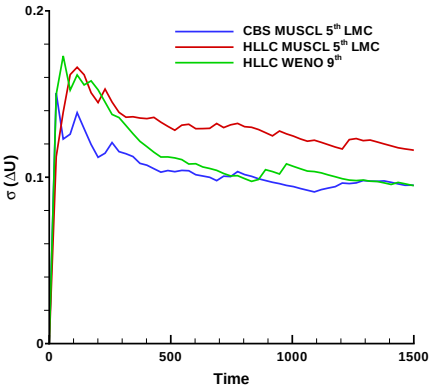

(c) Domains Maximum σ, Co-Flow Jet.

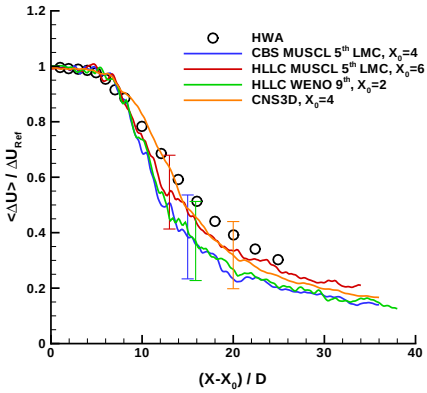

(d) Central Line velocity distribution, Co-Flow Jet.

FIGURE 4.4: *p*-study. **HWA**[111], **LDA**[33] and **DNS**[110]

Figure 4.4, frames *a* and *c*, shows the evolution of the domains maximum standard deviation, for the different selected methods, converging asymptomatic to a statistically converged solution (Static case) and a steady state solution (Co-flow case). Frames *b* and *d* shows the results for the axial average velocity distribution for same selected methods. Here, it can be observed the effects of the Riemann solver and spatial resolution, as well,

over the axial velocity distribution. On the Static case, the selected methods capture exactly the core length size, the velocity distributions follow the same trends as the **DNS** and experimental results. On the Co-flow case, it can be observed the improvement of the core size with the schemes resolution and the difference between Riemann solvers; also, the velocity distributions follow the same trend as the experimental result. Furthermore, the selected results as well the results in Appendix E, for both cases, show to be inside of a numerical envelope that represents an achievable solution, $CNS3D$ averaged result.

4.3 Discussion

Although this chapter does not aim to provide an exhaustive account of the possibilities for defining the numerical error bar, it demonstrates that quantification of the numerical uncertainty requires appropriate amalgamation of the effects of all numerical building blocks that can potentially affect the numerical solution. By doing so, a numerical error bar can be defined, which provides the envelope of an achievable solution.

The results show that effects of the grid refinement can be comparable to the effects of the Riemann solver and numerical schemes (spatial accuracy). Moreover, it is suggested that a numerical error bar approach could be adopted in time explicit, turbulent flow simulations, which takes into account an envelope of results obtained by different methods and subgrid scale models, if applicable.

Concluding, Figure 4.4, frames *c* and *d*, and Appendix E shows the average velocity distributions for all simulation methods (in the medium grid) demonstrating the effects of the Riemann solver and numerical reconstruction schemes on the central line velocity distribution.

The following observations can be made:

Static case

- The **CBS** Riemann solver gives (slightly) better results than the **HLLC**.
- The **MUSCL** 5^{th}**-order** gives slightly better results than the **WENO** 9^{th}**-order**, as the error value is lower with the former numerical method.
- The numerical uncertainty with respect to the errors associated with the numerical reconstruction schemes is of the same order of magnitude with the uncertainty associated with the grid size, *Medium* vs *Fine* grid (Table 4.2 and Table 4.3).

- The size of the jets core length is predicted exactly for the *Medium* and *Fine* meshes, and for the 5^{th}**-order** augmented with **LMC** and 9^{th}**-order** methods. Also, the average result, **CNS3D** captures the exact value.

Co-flow case

- The **HLLC** Riemann solver gives a much better result than the **CBS**.
- The **CBS MUSCL** 5^{th} **LMC** result is in the same order of magnitude than the **WENO** 9^{th}.
- The numerical uncertainty with respect to the errors associated with the numerical reconstruction schemes is of the same order of magnitude with the uncertainty associated with the grid size, $fine$ grid (Table 4.2 and Table 4.3), except the **HLLC MUSCL** 5^{th} **LMC** scheme.
- The size predictions of the jets core length converges with the grid refinement (spatial accuracy) and with the order of the reconstruction methods. Moreover, the average result, **CNS3D**, is lower then the best result **HLLC MUSCL** 5^{th} **LMC**.

From the previous observations and results, it can be concluded the best cost effective scheme to be employed is the **CBS MUSCL** 5^{th} **LMC** (Static case) and **HLLC MUSCL** 5^{th} **LMC** (Co-flow case). Also, that all the methods and grid refinements have converge statistically and the results from the employed methods have mathematical meaning. With this conclusions, it is possible to continue the study of the different methodologies from the physical perspective. Moreover, we can see that the geometrical method of treating the singularity gives meaningful results, in contrast to the traditional algebraic method.

5 Static Jet

5.1 Introduction

As it has been showed on the previous chapter (Chapter 4) all the methodologies have reached a statistical converged and steady state levels, giving mathematical meaning to the obtained results. In this chapter, predictions are made of a jet issuing into stagnant surroundings. This case will be analysed from the physical point of view (velocity, energy and elasticity/plasticity) for the jet's central line and the far-field wake's planes, extending the validity of the previous results. The behaviour of the flow in the near-field region is influenced not only by the initial turbulence profiles, usually not known adequately and for this reason not used, but also by the possible formation of orderly structures in the mixing layers at the edges of the potential jet's core and vortical rings that break down as chaotic structures. The existence of these structures, a non-turbulence phenomenon and not accounted for, may affect the jet development for a significant distance downstream, as it will be seen. Moreover, the energy partition between the normal components of the Reynolds stresses trough the jet's central line and sections is an indicator of an isotropic flow; concluding the physical analysis, the energy decay rate is presented for each selected

method, spectrograms. The linear grow of the wake's spreading size, trough the section profiles, indicates jet's self-similarity. As it will be seen, the normal and cross stress components show the flow field ability to deform. Accordingly, comparisons between the different methodologies with experimental and numerical data will identify the most efficient and accurate method to simulate a high subsonic turbulent jet under a static free stream. To conclude the analysis of the static jet flow, a brief study of the jet buoyancy will be performed and a possible reason for such phenomena will be discussed.

5.2 Methodology and Results

Simulations have been performed for an isothermal, round jet into a static free stream at a Reynolds number of 10000 based on the jet's outlet diameter and velocity ($Ma_{Jet} = 0.9$) at standard sea level, temperature and pressure (Table 4.1). The grids employed, as on the previous chapter, where based on the grids of [110, 119] and clustered according to [122, 123], a brief description can be seen in Appendix C.

The velocities and stresses along the jet axis and radial sections become adimensional with reference to the axial velocity of the jet at the geometrical center, U_{Ref}, accordingly. The reduced data comparisons are referenced to the jets inertial coordinate system (Appendix D). The boundary conditions were set up as inflow for the jet discharge (laminar profile) and upstream of the jet exit, $Ma_{\infty} = 0$; no-slip at the wall of the engine's nozzle, transparent for the domain geometrical singularity and outflow (non-reflective boundary conditions) for the rest of the domain.

The time averaging starts after developing the flow for approximate 1500 time units, and covers 1500 time units, with $\frac{1}{5}$ of the time window spam allocated to the spectral analysis. The h-study is performed with the **HLLC** Riemann solver with the 5^{th}-order **MUSCL** scheme and augmented with **LMC**. For the p-study (*Medium* mesh), a selection of the methods used on the previous chapter (Chapter 4) is employed according to the comparisons to be performed. These comparisons reflect the differences between the **CBS** and **HLLC** Riemann solvers, effects of low-Mach number limiting augmentation (**LMC**), limiters and reconstruction schemes (**MUSCL** and **WENO**) and spatial resolution (**Order**). Moreover, the h and p studies use a Runge-Kutta **TVD** third order time integration, with **CFL**= 0.5. The comparisons results are presented against the **DNS** [110] and experimental data from Hot Wire Anemometry (**HWA**) [111, 116] and LASER Doppler Anemometry (**LDA**) [33, 115].

The average velocities and Reynolds stress profiles results, Central Line and Sections, in this chapter are compared in the following subsections, h-study and p-study. In order to indicate the relative width of each prediction, the radial distances have been normalized with the downstream inertial distance. The scale in the stresses figures is chosen to facilitate a better comparison between components. An observation should be made for the case of the cross stresses components, the experimental and numerical data available from the literature is in absolute values, hiding the possible directions of the flow field's deformation. Three different radial sections have been selected to show the behaviour of the jet's wake. As an indicator of physical convergence, self-similarity should be achieved trough the jet's wake planes, these results are presented in Appendix F. The normal inertial sections are located at:

- Sections $\frac{X - X_0}{D} = (15, 20, 25)$.

Furthermore, the temporal power spectral density of the Total Kinetic Energy ($E_k(\nu)$) is analysed. The frequency domain (ν) is related to the inverse of the adimensional computational time, with a maximum value proportional to the computational time steep; the scale of the power spectrum density is arbitrary and the position of all the different curves have been faithfully reproduced. The probe points encompasses the jet's near-field, transition and far-field regions, over the central line. The location of the probe points are domain's referenced and have the following coordinates:

- $\frac{X}{D} = (0, 5, 10, 15, 20, 25, 30, 35, 40)$.

Moreover, the central line axial velocity intensity data is augmented with an error bar. The error bar values have been computed and discussed on the previous chapter(Chapter 4) for all the different methodologies and grid resolutions.

5.2.1 h-study

In this subsection, the ability of each mesh in capturing the physical properties of the flow field is analysed. Self-similarity results, (Appendix F, Figure F.3), show that the three grids refinements have converged to a physical steady state, reinforcing and confirming the mathematical conclusions for the statistical steady state.

Central Line

Figure 5.1 show the ability of each mesh in capturing the variations of the axial velocity trough the jet's central line. It can be observed for the laminar and transition regions that the jet velocity predictions correspond to the experimental and numerical references ($0 \leq \frac{X - X_0}{D} \lessapprox 8$). The far-field back pressure or blockage effects over the jet's size can be explained by the ability of each mesh, in combination with the correspondent numerical method, in resolving locally the flow field for the vortex ring break down region. As it can be seen in Table 5.1, the results for the *Medium* and *Fine* cases agree exactly with the experimental and numerical results while a small difference exist on the *Coarse* case (jet's core size); also, the jet's induced entrainment effects, by consequence, can be considered correctly balanced out, giving a velocity gradient similar to the reference ($14 \lessapprox \frac{X - X_0}{D} \leq 30$).

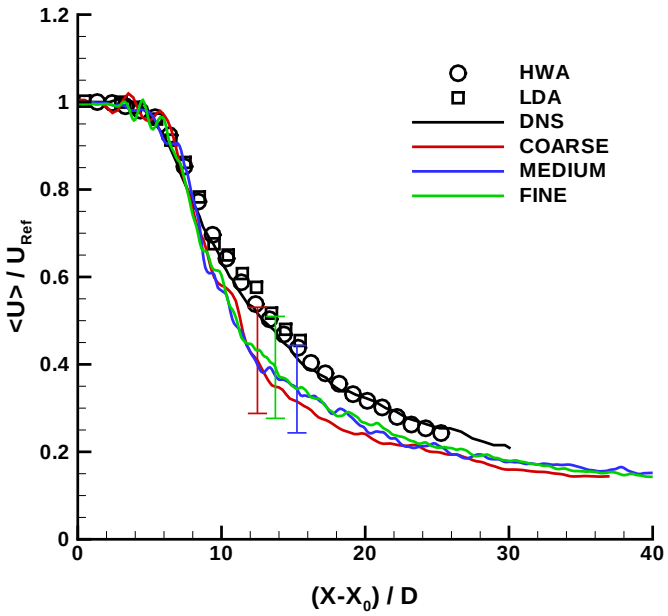

Figure 5.1: Central line velocity results. **HWA**[111], **LDA**[33] and **DNS**[110]

Figure 5.2, frame *a*, show the effective value of the turbulence intensity for all the meshes, with the same peak location for the *Medium* and *Fine* cases. The remaining frames (*b*, *c* and *d*) presents the central line normal components of Reynolds stresses, from the inertial point of view. Comparisons with experimental data reveal an over prediction for all the three normal components in the three meshes. The experimental trends are observed in the three cases, with the peak values being close to the references, down

stream distance. The partition of energy between the normal stress components, axial and radial, is markedly different in intensity, but approximately similar between each case (Table 5.1, *Medium* and *Fine* cases) revealing a quasi-isotropic turbulence behaviour with a polarization towards the axial component, as expected. Furthermore, the higher value of $\langle w'w' \rangle$ component in relation to $\langle v'v' \rangle$ component shows the curling tendency of the flow, after the break down of the vortical rings. The differences in the downstream peak locations shows the uncertainty or the non-deterministic nature of the flow field. Moreover, the energy partition for the *Medium* case is proportional equivalent to the reference ones.

Physical quantities	**Coarse**	**Medium**	**Fine**	**LDA**
X_0	3	0	0	0
Maximum error	0.265	0.190	0.189	*n.a.*
u'_{RMS}	0.120	0.117	0.109	*n.a.*
$\langle u'u' \rangle$	0.039	0.038	0.033	0.022
$\langle v'v' \rangle$	0.021	0.024	0.026	0.013
$\langle w'w' \rangle$	0.031	0.029	0.033	0.013

Table 5.1: Central line results, peak values. **LDA**[33]

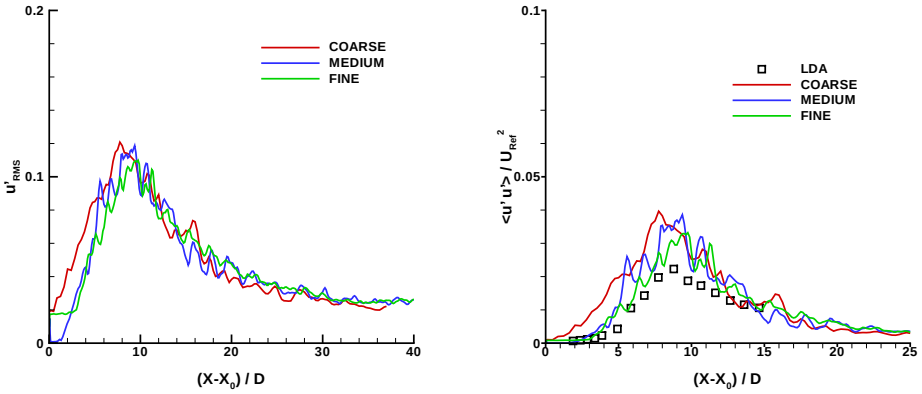

(a) Turbulence intensity effective value.

(b) $\langle u'u' \rangle$ component.

(c) $\langle v'v' \rangle$ component.

(d) $\langle w'w' \rangle$ component

Figure 5.2: Central line turbulence intensity and normal stresses results. **LDA**[33].

Sections

Figure 5.3, Figure 5.4 and Figure 5.5, frames *a*, shows the cross sections average axial velocity values, where the gradient's and intensities' are mesh dependent, with the *Medium* case results revealing a good comparison with the experimental and **DNS** data. The remaining frames (*b*, *c*, *d*, *e* and *f*) compare the predicted Reynolds stresses components with the available data. It can be observed that all the cases follow the reference trends, showing the predicted flow field physical characteristics. From the three sections analysed, Table 5.2, a proportional partition of energy trough the axial and radial components is observed for all the cases, with a polarization towards the axial component; in section $\frac{X-X_0}{D} = 20$ of the *Coarse* case, the flow field is polarized towards $\langle w'w' \rangle$ radial component with the remaining components values being partitioned proportionally. The

radial components results of the *Medium* and *Fine* cases show this partition to be in the same order of magnitude over the analysed sections. In accordance with the reference values and expected flow field behaviour, a quasi-isotropic turbulence with polarization towards one direction is observed for all the cases. Moreover, the difference in direction of the cross components shows the uncertainty and the non-deterministic nature of the flow field, in particular the $\langle u'v' \rangle$ component. Furthermore, the shearing forces or the flow field curl ability has been predicted with confidence for the *Medium* and *Fine* cases.

Physical quantities	**Coarse**	**Medium**	**Fine**	**LDA**	**HWA**	**DNS**
Section $\frac{X-X_0}{D}$ = 15						
$\langle u'u' \rangle$	0.124	0.105	0.092	0.086	0.064	0.053
$\langle v'v' \rangle$	0.089	0.065	0.071	0.047	0.035	0.032
$\langle w'w' \rangle$	0.105	0.064	0.067	0.048	0.035	0.032
$\langle u'v' \rangle$	0.018	0.016	-0.017	0.023	0.019	0.018
$\langle u'w' \rangle$	0.039	0.024	0.025	0.023	0.019	0.018
Section $\frac{X-X_0}{D}$ = 20						
$\langle u'u' \rangle$	0.077	0.071	0.103	0.086	0.064	0.045
$\langle v'v' \rangle$	0.065	0.056	0.068	0.047	0.034	0.030
$\langle w'w' \rangle$	0.094	0.051	0.061	0.048	0.034	0.030
$\langle u'v' \rangle$	0.024	-0.009	0.013	0.023	0.019	0.018
$\langle u'w' \rangle$	0.021	0.029	0.026	0.023	0.019	0.018
Section $\frac{X-X_0}{D}$ = 25						
$\langle u'u' \rangle$	0.078	0.077	0.097	0.086	0.064	0.048
$\langle v'v' \rangle$	0.061	0.067	0.072	0.047	0.035	0.035
$\langle w'w' \rangle$	0.051	0.061	0.068	0.048	0.034	0.030
$\langle u'v' \rangle$	0.016	0.022	-0.014	0.023	0.019	0.018
$\langle u'w' \rangle$	0.026	0.022	0.036	0.023	0.019	0.018

Table 5.2: Sections results, peak values. **HWA**[116], **LDA**[115] and **DNS**[110].

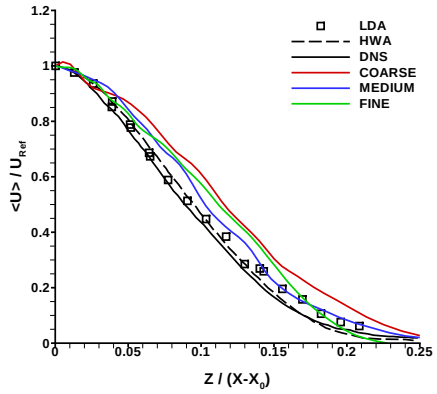

(a) Velocity distribution, axial component.

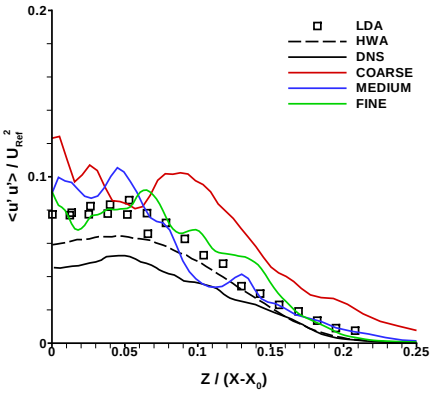

(b) $\langle u'u' \rangle$ component.

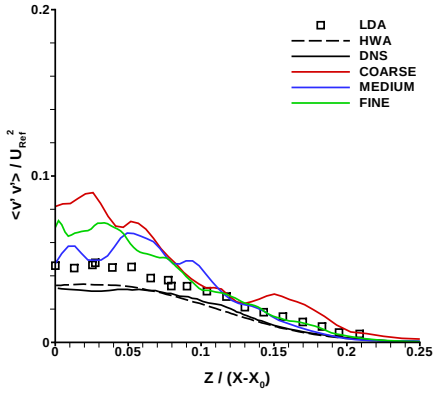

(c) $\langle v'v' \rangle$ component.

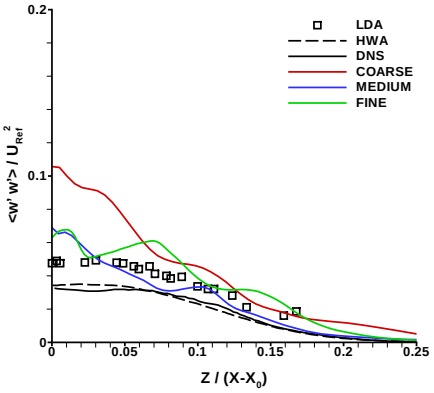

(d) $\langle w'w' \rangle$ component.

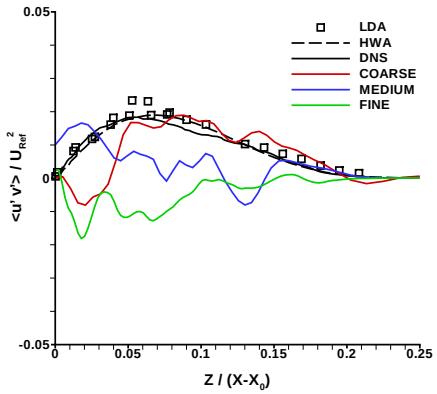

(e) $\langle u'v' \rangle$ component.

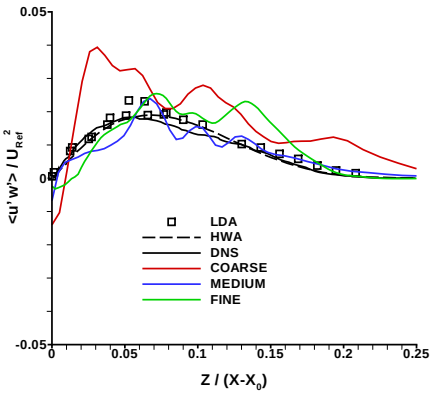

(f) $\langle u'w' \rangle$ component.

Figure 5.3: Section $\frac{X - X_0}{D} = 15$ results. **HWA**[116], **LDA**[115] and **DNS**[110].

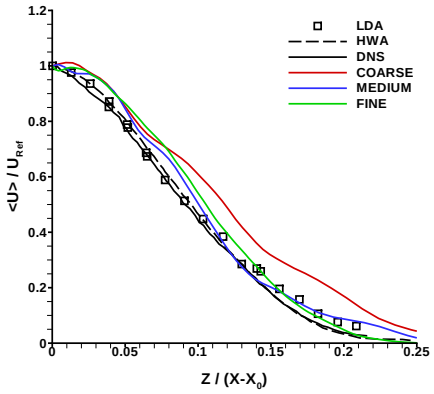

(a) Velocity distribution, axial component.

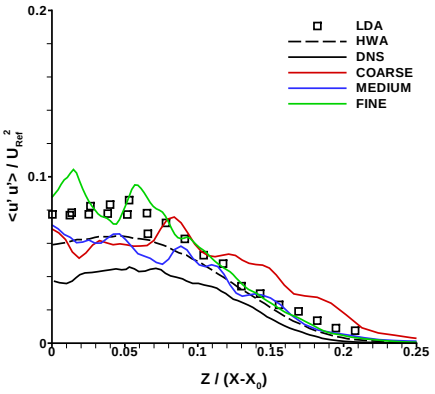

(b) $\langle u'u' \rangle$ component.

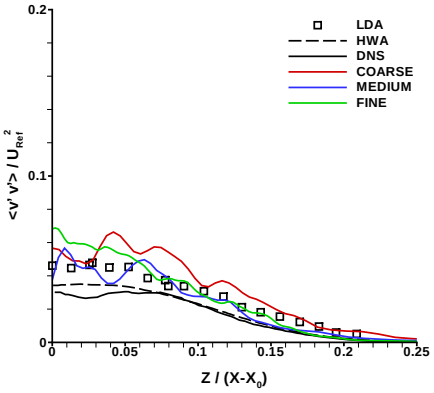

(c) $\langle v'v' \rangle$ component.

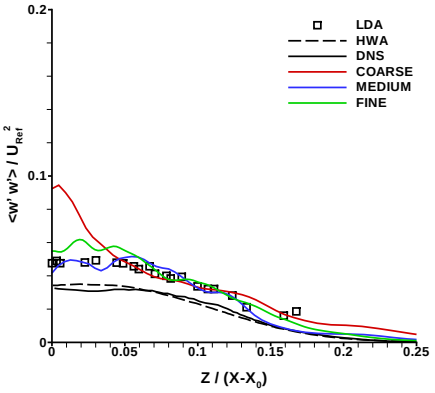

(d) $\langle w'w' \rangle$ component.

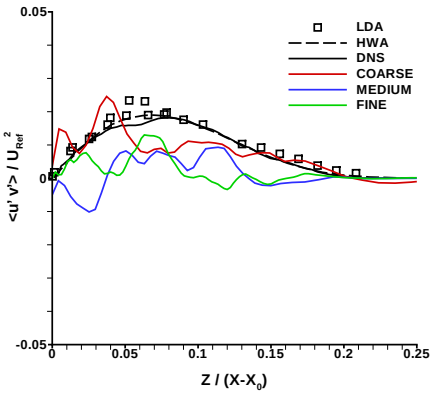

(e) $\langle u'v' \rangle$ component.

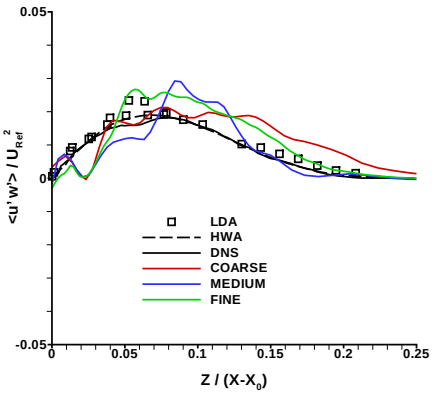

(f) $\langle u'w' \rangle$ component.

Figure 5.4: Section $\frac{X - X_0}{D} = 20$ results. **HWA**[116], **LDA**[115] and **DNS**[110].

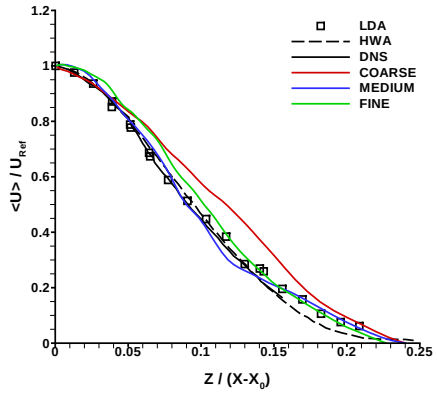

(a) Velocity distribution, axial component.

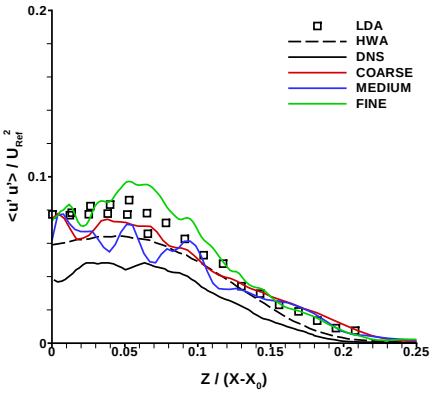

(b) $\langle u'u' \rangle$ component.

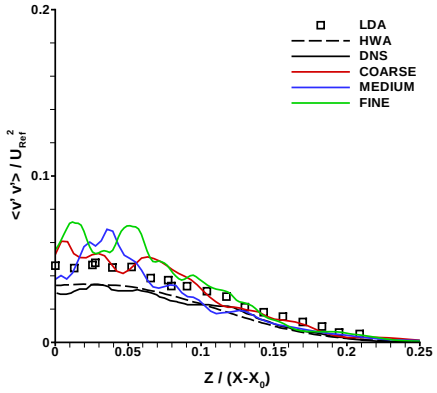

(c) $\langle v'v' \rangle$ component.

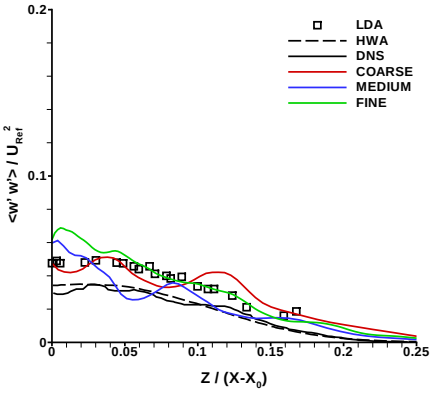

(d) $\langle w'w' \rangle$ component.

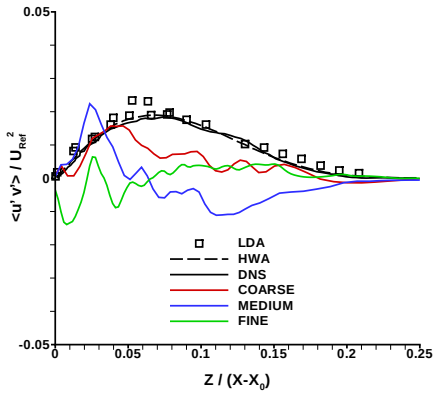

(e) $\langle u'v' \rangle$ component.

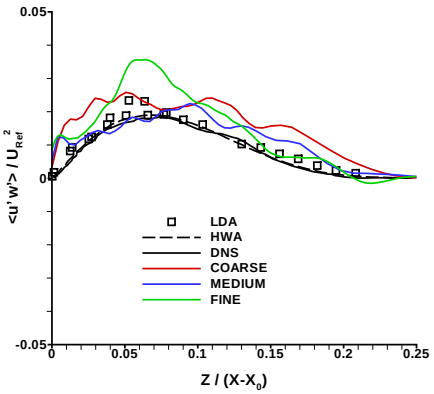

(f) $\langle u'w' \rangle$ component.

Figure 5.5: Section $\frac{X - X_0}{D} = 25$ results. **HWA**[116], **LDA**[115] and **DNS**[110].

Summary

The results of this subsection give strong evidence that the grid and numerics used in the simulations predict the developed turbulent jet (i.e., after the $3D$ breakdown and full flow chaotization) with accuracy, the comparison of the mean flow characteristics and Reynolds stresses in this study reveals the *Medium* and *Fine* cases as the closest to the reference data. For instance, according to the simulations, the center line velocity intensity comes out with some discrepancies (under prediction) from the reference values but with very similar results between the *Medium* and *Fine* meshes, the central line velocity gradient's is observed. The analysed sections average velocity (axial component) is very close to their counterpart (experimental/numerical values), showing almost equal gradients in the three cases, the velocity intensity is well predicted for the *Medium* mesh. Moreover, the stresses analysis reveals similarities between the *Medium* and *Fine* cases, with the results of the *Medium* mesh as the closest to the experimental/numerical sets of data. Therefore, as far as physics is concerned (velocity, energy partition and stresses), the *Medium* case captures with confidence the flow field properties (e.g., from the turbulence point of view, the energy containing motion is captured). With this study, the *Medium* mesh has been selected to perform the *p*-study where the different employed methods will be compared. Furthermore, the predictions of this study show that the azimuthal discretization do not affect the ability to capture the flow field's physical quantities.

5.2.2 *p*-study

From the previous subsection, *h*-study, the medium grid has been selected to perform the *p*-study. The same developed jet initial and boundary conditions have been applied in this study. The previous detailed analysis has been mimicked over the flow field and an extended analysis of the power spectrum density for the central line reference probe points, the results will be presented in the following subsection. From all the methodologies used in Chapter 4, a selection will be used to represent the differences between each numerical method/scheme. The following numerical variants employed in this study are:

- The **CBS** Riemann solver with the 2^{nd}-order **MUSCL** scheme and **L**ow-**M**ach **L**imiting, henceforth labelled as '**CNS3D** 2^{nd} **ORDER**'.
- The **HLLC** Riemann solver with the 5^{th}-order **MUSCL** scheme and **L**ow-**M**ach **L**imiting, henceforth labelled as '**CNS3D HLLC**'.

- The **CBS** Riemann solver with the 5^{th}-order **CBS** scheme, henceforth labelled as '**CNS3D** 5^{th} **ORDER**'.
- The **CBS** Riemann solver with the 5^{th}-order **WENO** scheme, henceforth labelled as '**CNS3D WENO**'.
- The **CBS** Riemann solver with the 9^{th}-order **WENO** scheme, henceforth labelled as '**CNS3D** 9^{th} **ORDER**'.
- The **CBS** Riemann solver with the 5^{th}-order **MUSCL** scheme and **L**ow-**M**ach **L**imiting, henceforth labelled as '**CNS3D CBS**, **CNS3D** 5^{th} **ORDER LMC**, **CNS3D MUSCL** and **CNS3D** 5^{th} **ORDER**', accordingly.

As previously mention, the selected methods have reached a self-similar state (physical steadiness) and a statistical steady state. The former state can be observed in Appendix F (Figure F.7, Figure F.11, Figure F.15, Figure F.19 and Figure F.23). This enhances and extend the mathematical steady state conclusions of Chapter 4.

Riemann Solver

In this analysis, two methods have been selected to compare the differences between the library's Riemann solvers, the **CBS** and **HLLC** 5^{th}-order **MUSCL** augmented with **LMC**, respectively. The comparative study has been performed over the jet's central line and wake sections, as previously mentioned.

Central Line

Figure 5.6 show the ability of each Riemann solver in capturing the variations in the axial intensity velocity trough the jet's central line. It can be observed for the laminar and transition regions the jet velocity predictions correspond to the experimental and numerical references ($0 \leq \frac{X - X_0}{D} \lessapprox 8$). The far-filed back pressure or blockage effects over the jet's size can be explained by the ability of each Riemann solver's in predicting locally the flow field for the break down of the jet's vortical rings region. As it can be seen in Table 5.3, the results for both Riemann solvers agree exactly with the experimental and numerical results (jet's core length); also by consequence, the jet's induced entrainment effects are correctly balanced out, giving a velocity gradient similar to the references, **CNS3D CBS** ($11 \lessapprox \frac{X - X_0}{D} \leq 30$) and **CNS3D HLLC** ($15 \lessapprox \frac{X - X_0}{D} \leq 30$).

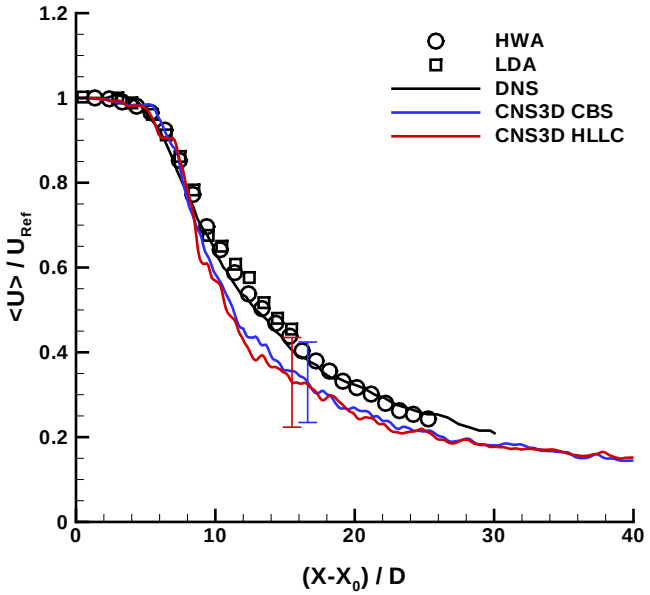

Figure 5.6: Riemann Solver, central line velocity. **HWA**[111], **LDA**[33] and **DNS**[110].

Figure 5.7, frame *a*, show the effective value of the turbulence intensity for the **CNS3D CBS** and **CNS3D HLLC** cases, with very similar results in magnitude and a small difference at the correspondent peak location. The remaining frames (*b*, *c* and *d*) present, from the inertial point of view, the central line Reynolds stresses normal components results. Comparisons with experimental data reveal an over prediction for all the three component in both cases; however, the experimental trends can be observed, with the down stream peak values distance being close to the references. The partition of energy between the normal stress components, axial and radial, are similar in intensity, with a proportional equal partition between the axial and radial components revealing a quasi-isotropic turbulence behaviour with a polarization towards the axial component, as expected. The uncertainty or the non-deterministic nature of the flow field can be observed by the differences in location of the peak values of the stresses components, as this is the vortical ring break down region. Moreover, the energy partition for both Riemann solvers cases is proportionally equivalent to the reference ones.

Physical quantities	**CNS3D CBS**	**CNS3D HLLC**	**LDA**
X_0	0	0	0
Maximum error	0.154	0.190	*n.a.*
u'_{RMS}	0.110	0.117	*n.a.*
$\langle u'u' \rangle$	0.030	0.038	0.022
$\langle v'v' \rangle$	0.026	0.024	0.013
$\langle w'w' \rangle$	0.024	0.028	0.013

Table 5.3: Riemann Solver central line results, peak values. **LDA**[33].

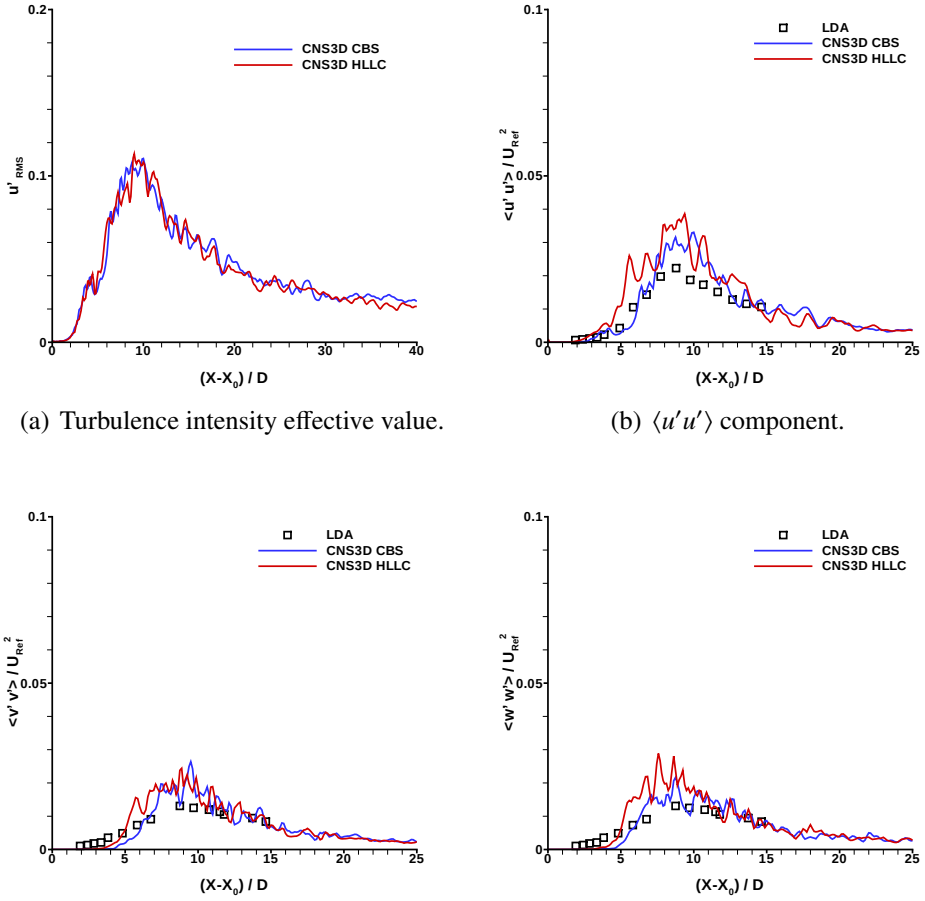

(a) Turbulence intensity effective value.

(b) $\langle u'u' \rangle$ component.

(c) $\langle v'v' \rangle$ component.

(d) $\langle w'w' \rangle$ component.

Figure 5.7: Central line turbulence intensity and normal stresses results. **LDA**[33].

Sections

Figure 5.8, Figure 5.9 and Figure 5.10, frames *a*, shows the cross sections average axial velocity values, where the intensities' are different between each case but with similar gradients, with the **CNS3D CBS** case results revealing a good comparison with the experimental and **DNS** data. The remaining frames (*b*, *c*, *d*, *e* and *f*) compare the predicted Reynolds stresses components with the available data. It can be observed that all the cases follow the reference trends and are similar to each other, showing the predicted flow field physical characteristics. From the three sections analysed, Table 5.4, a proportional partition of energy trough the axial and radial components can be observed for all the cases, with a polarization towards the axial component. The energy partition for the radial terms, trough the sections, in the **CNS3D CBS** case reveals a tendency for the flow field to naturally swirl, in contrast, this is not observed for the **CNS3D HLLC** case as the same components peak values have the same order of magnitude. In accordance with the reference values and expected flow field behaviour, a quasi-isotropic turbulence with polarization towards the axial direction can be observed for both cases. Moreover, the difference in direction of the cross components shows the uncertainty nature of the flow field (direction of swirling), in particular $\langle u'v' \rangle$ component (negative value). Furthermore, the comparisons of shearing stresses reveals that both cases results are predicted with confidence.

Physical quantities	**CNS3D CBS**	**CNS3D HLLC**	**LDA**	**HWA**	**DNS**
Section $\frac{X-X_0}{D} = 15$					
$\langle u'u' \rangle$	0.083	0.105	0.086	0.064	0.053
$\langle v'v' \rangle$	0.075	0.065	0.047	0.035	0.032
$\langle w'w' \rangle$	0.062	0.064	0.048	0.035	0.032
$\langle u'v' \rangle$	0.018	0.016	0.023	0.019	0.018
$\langle u'w' \rangle$	0.020	0.024	0.023	0.019	0.018
Section $\frac{X-X_0}{D} = 20$					
$\langle u'u' \rangle$	0.088	0.071	0.086	0.064	0.045
$\langle v'v' \rangle$	0.064	0.056	0.047	0.034	0.030
$\langle w'w' \rangle$	0.051	0.051	0.048	0.034	0.030
$\langle u'v' \rangle$	-0.009	-0.009	0.023	0.019	0.018
$\langle u'w' \rangle$	0.024	0.029	0.023	0.019	0.018
Section $\frac{X-X_0}{D} = 25$					
$\langle u'u' \rangle$	0.077	0.077	0.086	0.064	0.048
$\langle v'v' \rangle$	0.074	0.067	0.047	0.035	0.035
$\langle w'w' \rangle$	0.060	0.061	0.048	0.034	0.030
$\langle u'v' \rangle$	0.013	0.022	0.023	0.019	0.018
$\langle u'w' \rangle$	0.028	0.022	0.023	0.019	0.018

Table 5.4: Riemann Solver sections results, peak values. **HWA**[116], **LDA**[115] and **DNS**[110].

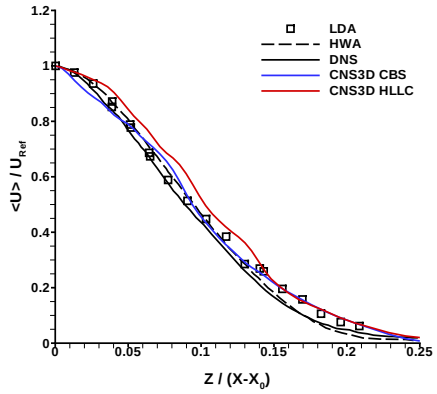

(a) Velocity distribution, axial component.

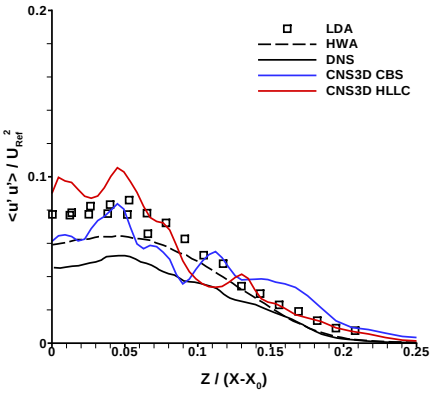

(b) $\langle u'u' \rangle$ component.

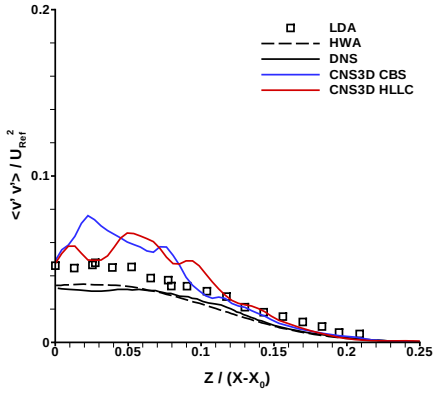

(c) $\langle v'v' \rangle$ component.

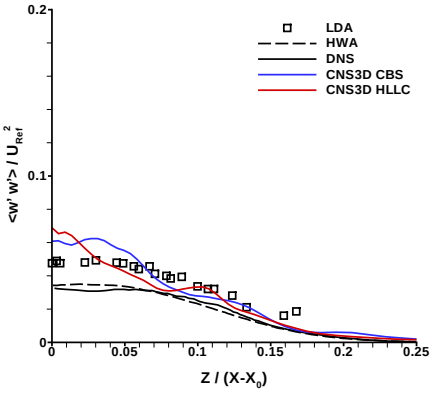

(d) $\langle w'w' \rangle$ component.

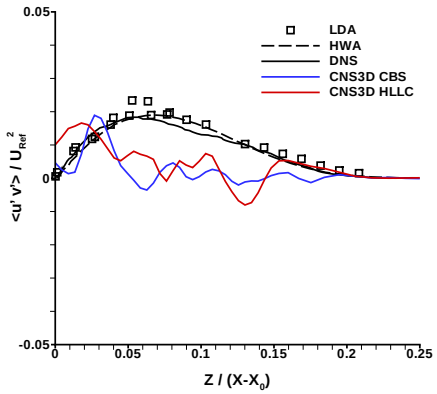

(e) $\langle u'v' \rangle$ component.

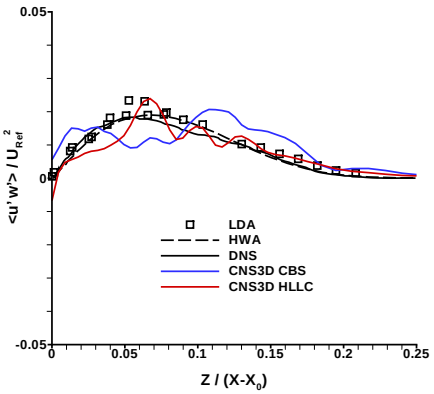

(f) $\langle u'w' \rangle$ component.

Figure 5.8: Section $\frac{X - X_0}{D} = 15$ results. **HWA**[116], **LDA**[115] and **DNS**[110].

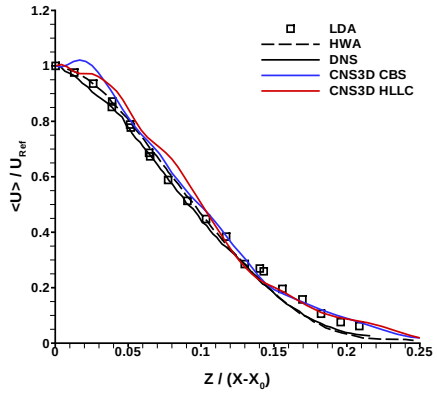

(a) Velocity distribution, axial component.

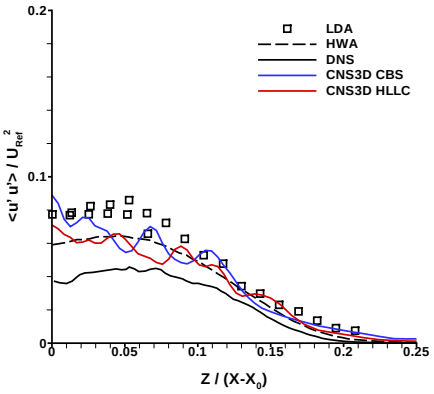

(b) $\langle u'u' \rangle$ component.

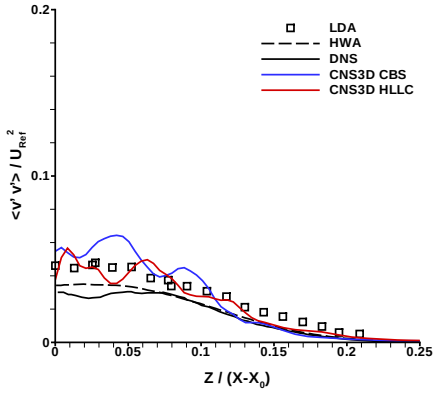

(c) $\langle v'v' \rangle$ component.

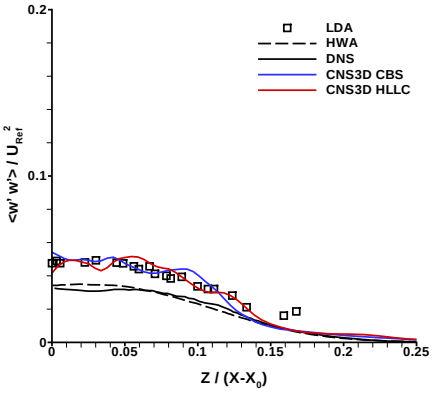

(d) $\langle w'w' \rangle$ component.

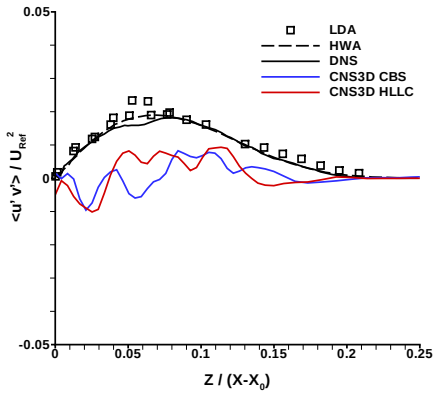

(e) $\langle u'v' \rangle$ component.

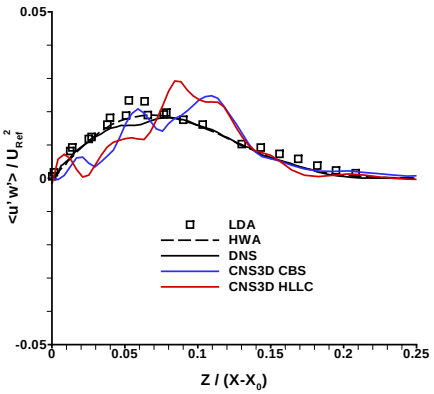

(f) $\langle u'w' \rangle$ component.

Figure 5.9: Section $\frac{X - X_0}{D} = 20$ results. **HWA**[116], **LDA**[115] and **DNS**[110].

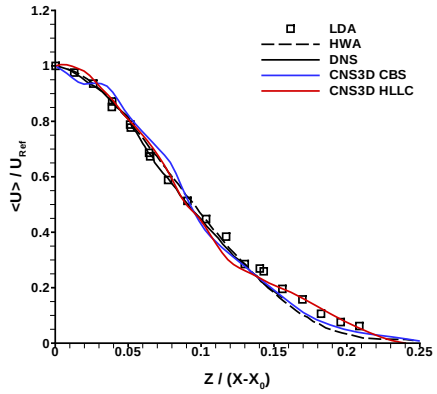

(a) Velocity distribution, axial component.

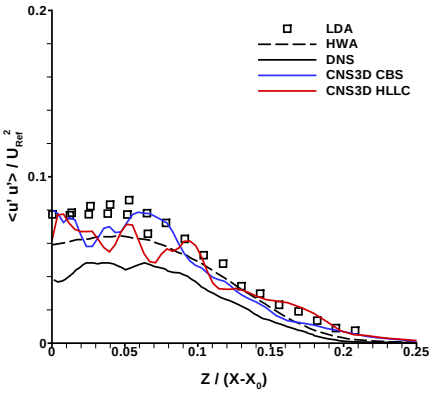

(b) $\langle u'u' \rangle$ component.

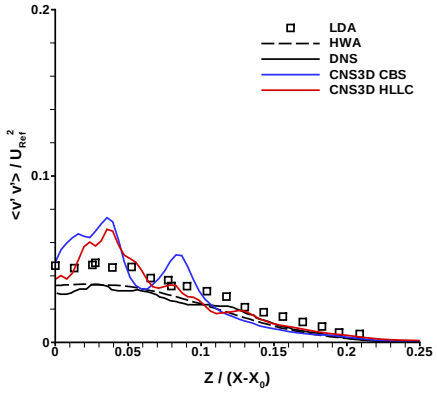

(c) $\langle v'v' \rangle$ component.

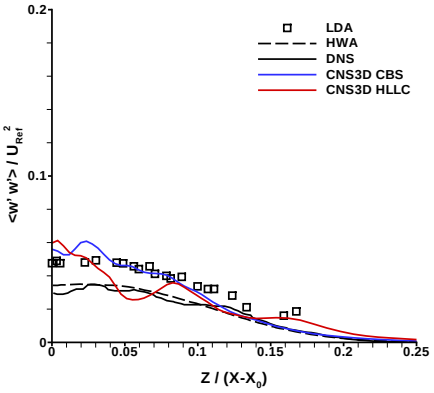

(d) $\langle w'w' \rangle$ component.

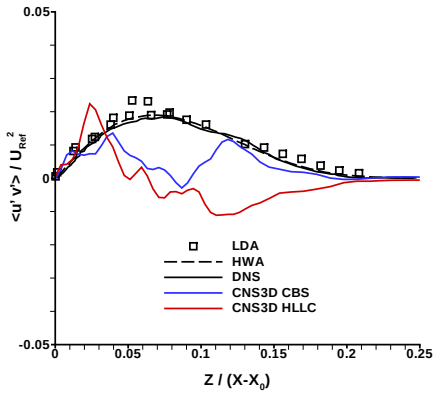

(e) $\langle u'v' \rangle$ component.

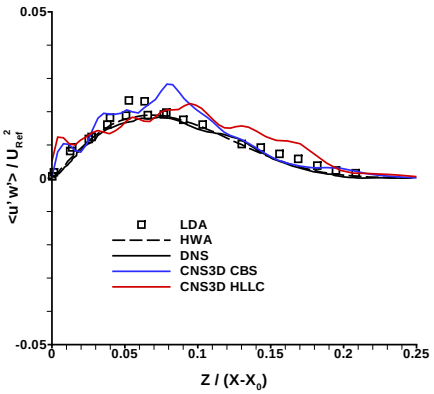

(f) $\langle u'w' \rangle$ component.

Figure 5.10: Section $\frac{X - X_0}{D} = 25$ results. **HWA**[116], **LDA**[115] and **DNS**[110].

The results of this analysis reveal a strong evidence that both Riemann solvers methodologies predict accurately the developed turbulent jet. The comparison between the predicted and experimental/numeric mean flow characteristics and Reynolds stresses, in this study, reveals agreement for both cases, with the **CNS3D CBS** results as the most accurate. Therefore, as far as physics is concerned, the **CNS3D CBS** case resolves the flow field properties (e.g., from the turbulence point of view, the energy containing motion is well balanced).

Low Mach Number Limiting

To study the effects that the **LMC** have over the flow field behaviour two methods have been selected, the **CBS** 5^{th}-order **MUSCL** augmented with **LMC** and the **CBS** 5^{th}-order **MUSCL**, respectively. The jet's central line and wake sections will be studied, as previously mentioned.

Central Line

Figure 5.11 show the effects of the **LMC** in resolving the variations in the axial velocity intensity trough the jet's central line. It can be observed, for the jet velocity predictions, in the laminar and transition regions a correspondence to the experimental and numerical values for the **CNS3D** 5^{th} **ORDER LMC** ($0 \leq \frac{X - X_0}{D} \lessapprox 8$) and an extended similarity exists for **CNS3D** 5^{th} **ORDER** ($0 \leq \frac{X - X_0}{D} \lessapprox 10$); the velocity gradient of the **CNS3D** 5^{th} **ORDER LMC** case gives a similar value as the experimental/numerical gradient values ($10 \lessapprox \frac{X - X_0}{D} \lessapprox 30$). The far-filed back pressure or blockage effects over the jet's size improves with **LMC** augmentation, enhancing the resolution in predicting locally the flow field for the vortical ring break down region, as it can be seen in Table 5.5. As consequence, the correct jet's induced entrainment effects are improved by the **LMC** augmentation. The **CNS3D** 5^{th} **ORDER** velocity magnitude value present an oscillation pattern at the end of the jet's core, this results from the adjusting of the predicted core by one unit of diameter, making the vortical ring break down region closer to the origin of the jet reference system (X_0).

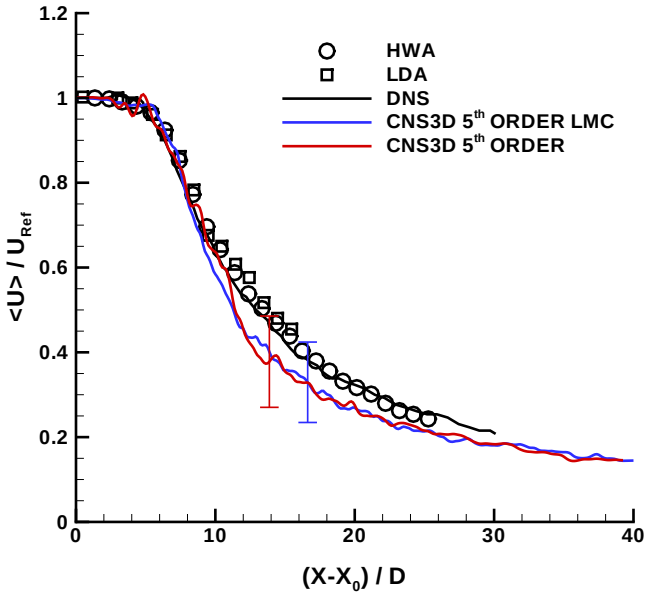

Figure 5.11: Central line velocity results. **HWA**[111], **LDA**[33] and **DNS**[110].

Figure 5.12, frame *a*, show the effective value of the turbulence intensity for the **CNS3D** 5^{th} **ORDER LMC** and **CNS3D** 5^{th} **ORDER** cases. It can be observed a difference in trends ($5 \lessapprox \frac{X - X_0}{D} \lessapprox 10$) and also in magnitude with different peak locations. The remaining frames (*b*, *c* and *d*) presents, from the inertial point of view, the jet's central line Reynolds stresses normal components results. Comparisons with experimental data reveals an over prediction for all the three component in both cases; however, the experimental trends of **CNS3D** 5^{th} **ORDER** case are improved by the **LMC** augmentation. The partition of energy between the normal stress components, axial and radial, is proportional in intensity, with a similar value in the radial component for the **CNS3D** 5^{th} **ORDER LMC**, revealing a quasi-isotropic turbulence behaviour with a polarization towards the axial component, as expected. Moreover, the energy partition results have been improved by the **LMC** augmentation.

Physical quantities	5^{th} **ORDER LMC**	5^{th} **ORDER**	**LDA**
X_0	0	1	0
Maximum error	0.154	0.217	*n.a.*
u'_{RMS}	0.110	0.126	*n.a.*
$\langle u'u' \rangle$	0.030	0.043	0.022
$\langle v'v' \rangle$	0.026	0.025	0.013
$\langle w'w' \rangle$	0.024	0.033	0.013

TABLE 5.5: **LMC** augmentation central line results, peak values. 5^{th} **ORDER LMC** is the **CNS3D** 5^{th} **ORDER LMC**, 5^{th} **ORDER** is the **CNS3D** 5^{th} **ORDER** and **LDA**[33].

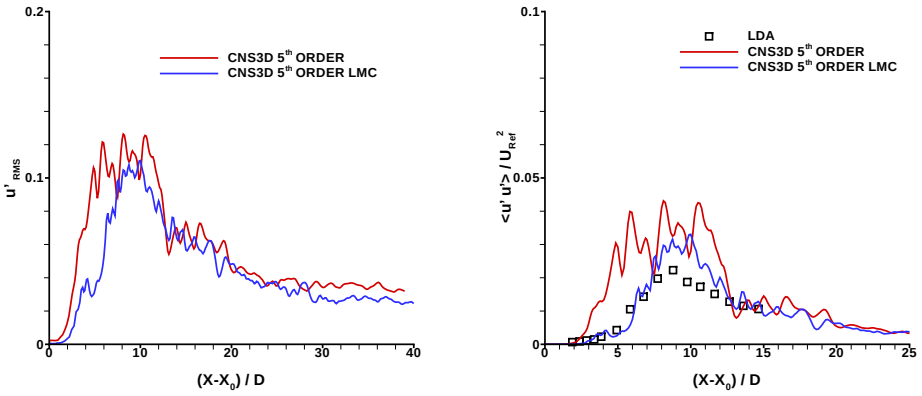

(a) Turbulence intensity effective value.

(b) $\langle u'u' \rangle$ component.

(c) $\langle v'v' \rangle$ component.

(d) $\langle w'w' \rangle$ component.

FIGURE 5.12: Central line turbulence intensity and normal stresses results. **LDA**[33].

Sections

Figure 5.13, Figure 5.14 and Figure 5.15, frames *a*, shows the cross sections average axial velocity values, where the intensity values are different between each case but

with locally similar gradients (**CNS3D** 5^{th} **ORDER**). The remaining frames (*b*, *c*, *d*, *e* and *f*) compare the predicted Reynolds stresses components with the available data. The reference trends can be observed for the **CNS3D** 5^{th} **ORDER LMC** case, showing the effects of the **LMC** augmentation. From the three sections analysed (Table 5.6), a proportional partition of energy trough the axial and radial components can be observed for both cases. In accordance with the reference values and expected flow field behaviour, a quasi-isotropic turbulence with polarization towards the axial direction can be observed for both cases, with the ratio improvement by the **LMC** augmentation. Moreover, the difference in direction of the cross components shows the uncertainty and the non-deterministic nature of the flow field, in particular $\langle u'v' \rangle$ component.

Physical quantities	5^{th} **ORDER LMC**	5^{th} **ORDER**	**LDA**	**HWA**	**DNS**
Section $\frac{X-X_0}{D} = 15$					
$\langle u'u' \rangle$	0.083	0.118	0.086	0.064	0.053
$\langle v'v' \rangle$	0.075	0.082	0.047	0.035	0.032
$\langle w'w' \rangle$	0.062	0.077	0.048	0.035	0.032
$\langle u'v' \rangle$	0.018	-0.025	0.023	0.019	0.018
$\langle u'w' \rangle$	0.020	0.025	0.023	0.019	0.018
Section $\frac{X-X_0}{D} = 20$					
$\langle u'u' \rangle$	0.088	0.091	0.086	0.064	0.045
$\langle v'v' \rangle$	0.064	0.079	0.047	0.034	0.030
$\langle w'w' \rangle$	0.051	0.069	0.048	0.034	0.030
$\langle u'v' \rangle$	-0.009	-0.009	0.023	0.019	0.018
$\langle u'w' \rangle$	0.024	0.035	0.023	0.019	0.018
Section $\frac{X-X_0}{D} = 25$					
$\langle u'u' \rangle$	0.077	0.118	0.086	0.064	0.048
$\langle v'v' \rangle$	0.074	0.056	0.047	0.035	0.035
$\langle w'w' \rangle$	0.060	0.056	0.048	0.034	0.030
$\langle u'v' \rangle$	0.013	0.021	0.023	0.019	0.018
$\langle u'w' \rangle$	0.028	0.037	0.023	0.019	0.018

Table 5.6: **LMC** augmentation sections results, peak values. 5^{th} **ORDER LMC** is the **CNS3D** 5^{th} **ORDER LMC**, 5^{th} **ORDER** is the **CNS3D** 5^{th} **ORDER**, **HWA**[116], **LDA**[115] and **DNS**[110].

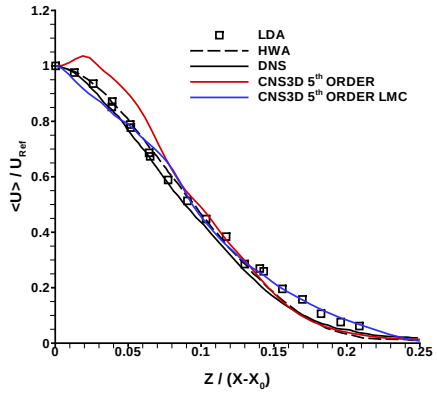

(a) Velocity distribution, axial component.

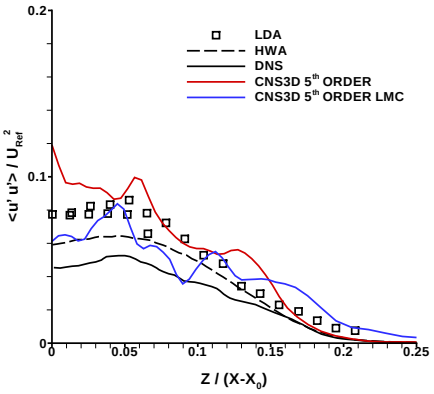

(b) $\langle u'u' \rangle$ component.

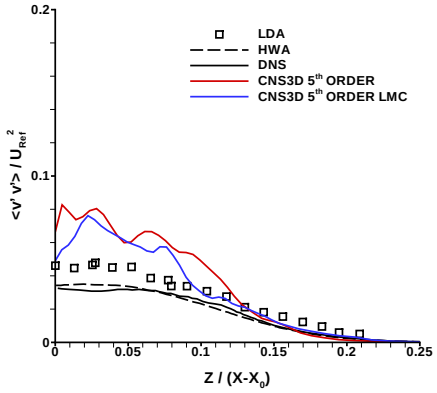

(c) $\langle v'v' \rangle$ component.

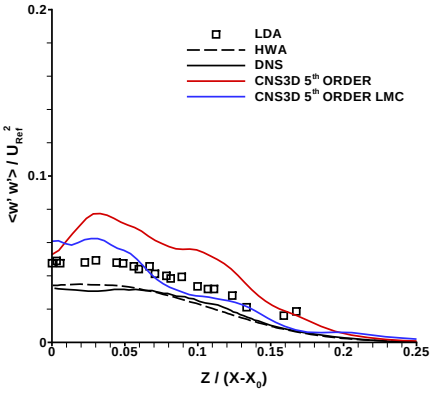

(d) $\langle w'w' \rangle$ component.

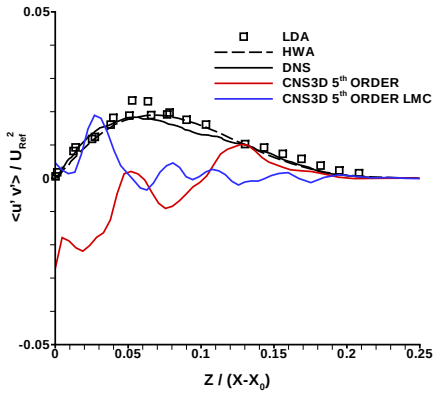

(e) $\langle u'v' \rangle$ component.

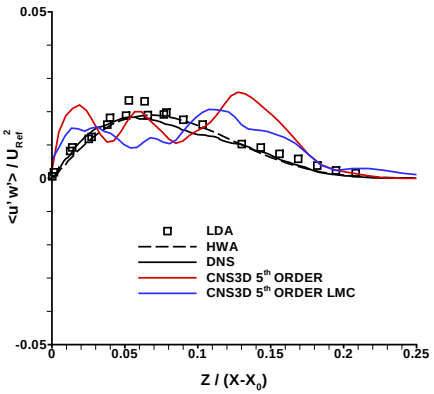

(f) $\langle u'w' \rangle$ component.

Figure 5.13: Section $\frac{X - X_0}{D} = 15$ results. **HWA**[116], **LDA**[115] and **DNS**[110].

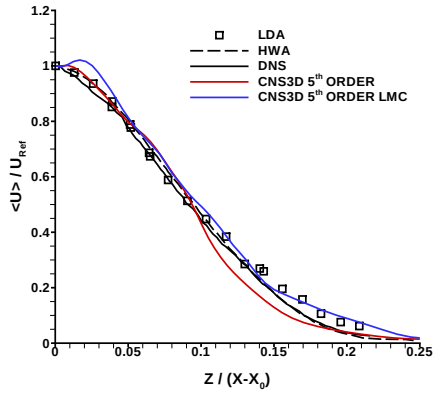

(a) Velocity distribution, axial component.

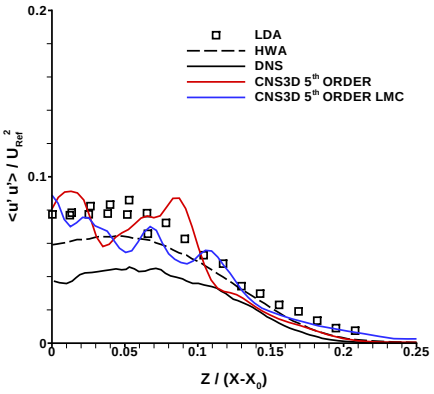

(b) $\langle u'u' \rangle$ component.

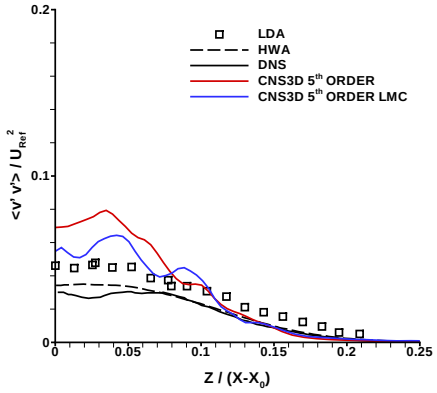

(c) $\langle v'v' \rangle$ component.

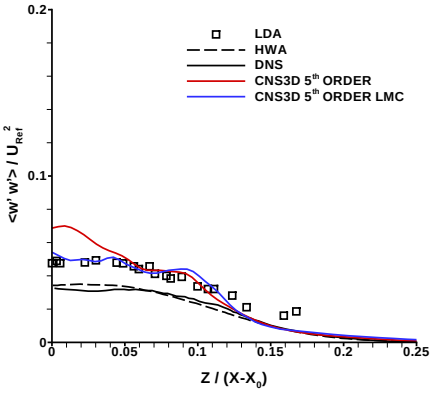

(d) $\langle w'w' \rangle$ component.

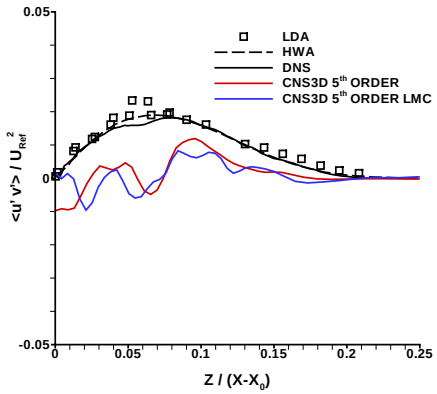

(e) $\langle u'v' \rangle$ component.

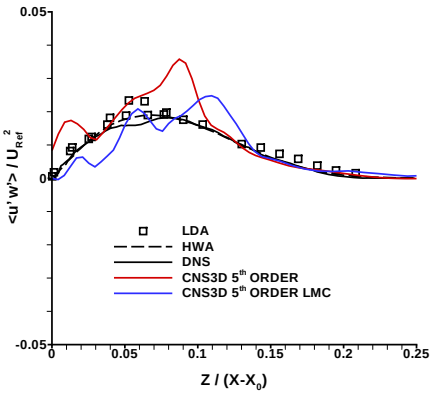

(f) $\langle u'w' \rangle$ component.

Figure 5.14: Section $\frac{X - X_0}{D} = 20$ results. **HWA**[116], **LDA**[115] and **DNS**[110].

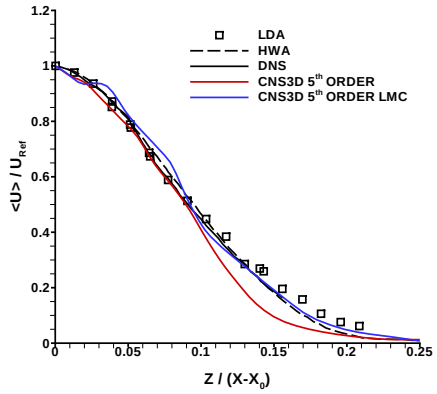

(a) Velocity distribution, axial component.

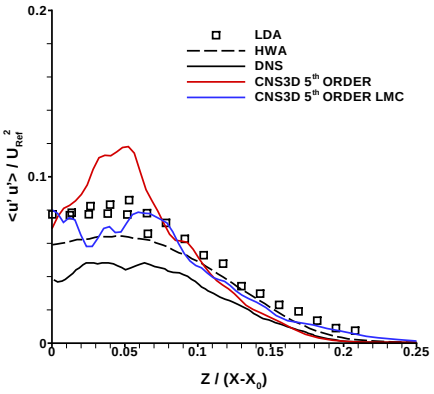

(b) $\langle u'u' \rangle$ component.

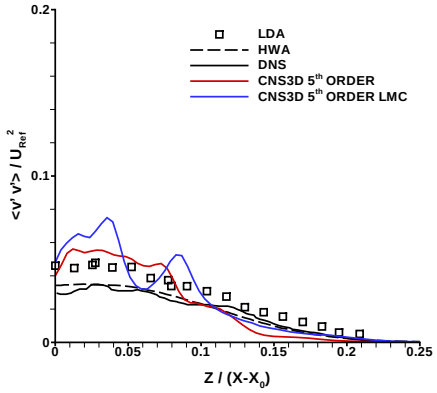

(c) $\langle v'v' \rangle$ component.

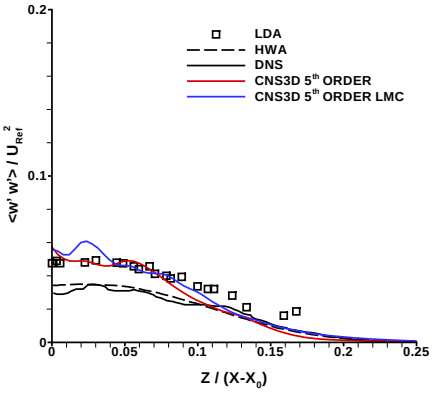

(d) $\langle w'w' \rangle$ component.

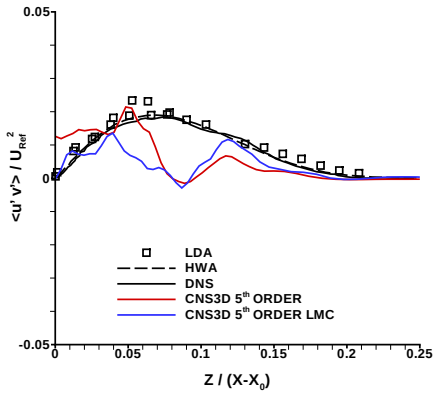

(e) $\langle u'v' \rangle$ component.

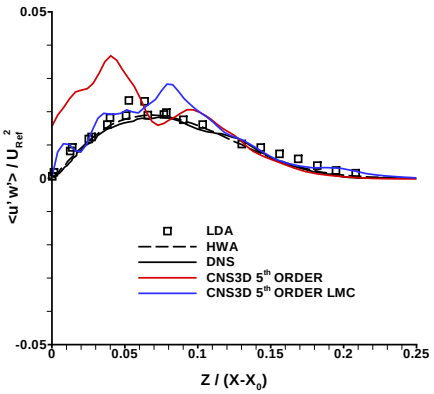

(f) $\langle u'w' \rangle$ component.

Figure 5.15: Section $\frac{X - X_0}{D} = 25$ results. **HWA**[116], **LDA**[115] and **DNS**[110].

The results of this analysis shows strong evidence of the **LMC** augmentation effects for the developed turbulent jet, as this augmentation just provide the "correct" amount of dissipation. Comparison between the predicted and experimental/numeric mean flow characteristics and Reynolds stresses in this study reveals a very good agreement for **CNS3D** 5^{th} **ORDER LMC** case. Therefore, as far as physics is concerned, the **CNS3D** 5^{th} **ORDER LMC** case predicts the flow field properties (e.g., from the turbulence point of view, the energy containing motion is well balanced and predicted).

MUSCL and WENO

To study of the effects that different reconstruction schemes have over the flow field two methods have been selected, the **CBS** 5^{th}-order **MUSCL** augmented with **LMC** and the **CBS** 5^{th}-order **WENO**, respectively. The jet's central line and wake sections have been studied, as previously mentioned.

Central Line

Figure 5.16 show the differences between the two selected schemes in resolving the variations in the axial velocity intensity trough the jet's central line. It can be observed for the laminar and transition regions of the jets that the velocity predictions are in agreement with the experimental and numerical references for both cases ($0 \leq \frac{X - X_0}{D} \lessapprox 8$). The far-filed back pressure or blockage effects over the jet's size is accurately predicted with **CNS3D MUSCL**, as consequence, the correct jet's induced entrainment effects can be better resolved by the use of the **MUSCL** scheme; the oscillatory pattern from the central axial velocity magnitude (**CNS3D WENO**) is the consequence of the reduction to the jet's reference system by one unit of diameter (Table 5.7). For the velocity gradient, the **CNS3D MUSCL** case gives a similar value as the experimental/numerical results ($10 \lessapprox \frac{X - X_0}{D} \lessapprox 30$). The flow field for the vortical rings break down region is captured with local accurately, as it can be seen in Table 5.7.

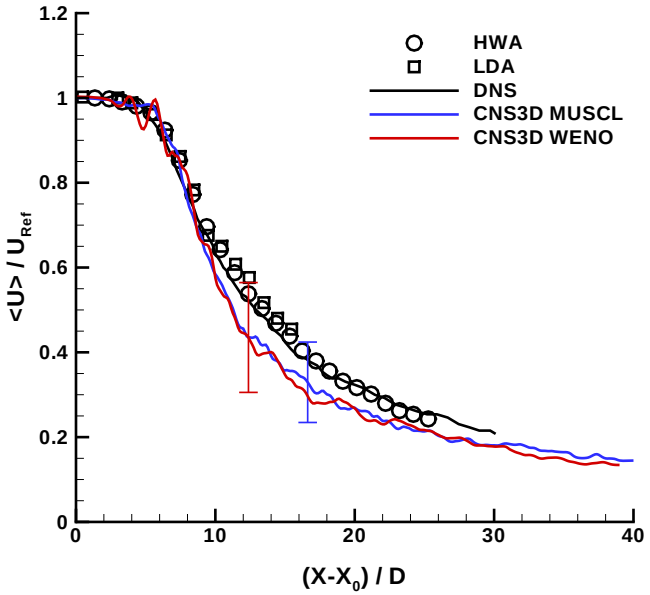

Figure 5.16: Central line velocity results. **HWA**[111], **LDA**[33] and **DNS**[110].

Figure 5.17, frame *a*, show the effective value of the turbulence intensity for the **CNS3D MUSCL** and **CNS3D WENO** cases. It can be observed a difference in trends ($6 \leq \frac{X - X_0}{D} \lessapprox 10$) and similar in magnitude with different peak locations. The remaining frames (*b*, *c* and *d*) presents, from the inertial point of view, the central line Reynolds stresses normal components results. Comparisons with experimental data reveal na over prediction for all the three component on both cases; however, the experimental trends are observed for **CNS3D MUSCL** case. The partition of energy between the normal stress components, axial and radial, is proportional in intensity, with a similar value in the radial components for the **CNS3D MUSCL**, revealing a quasi-isotropic turbulence behaviour with a polarization towards the axial component, as expected. Moreover, the **CNS3D WENO** results show equal partition of energy between the radial and $\langle v'v' \rangle$ components.

Physical quantities	**CNS3D MUSCL**	**CNS3D WENO**	**LDA**
X_0	0	1	0
Maximum error	0.154	0.238	*n.a.*
u'_{RMS}	0.110	0.106	*n.a.*
$\langle u'u' \rangle$	0.030	0.030	0.022
$\langle v'v' \rangle$	0.026	0.030	0.013
$\langle w'w' \rangle$	0.024	0.024	0.013

Table 5.7: Reconstruction schemes central line results, peak values. **LDA**[33].

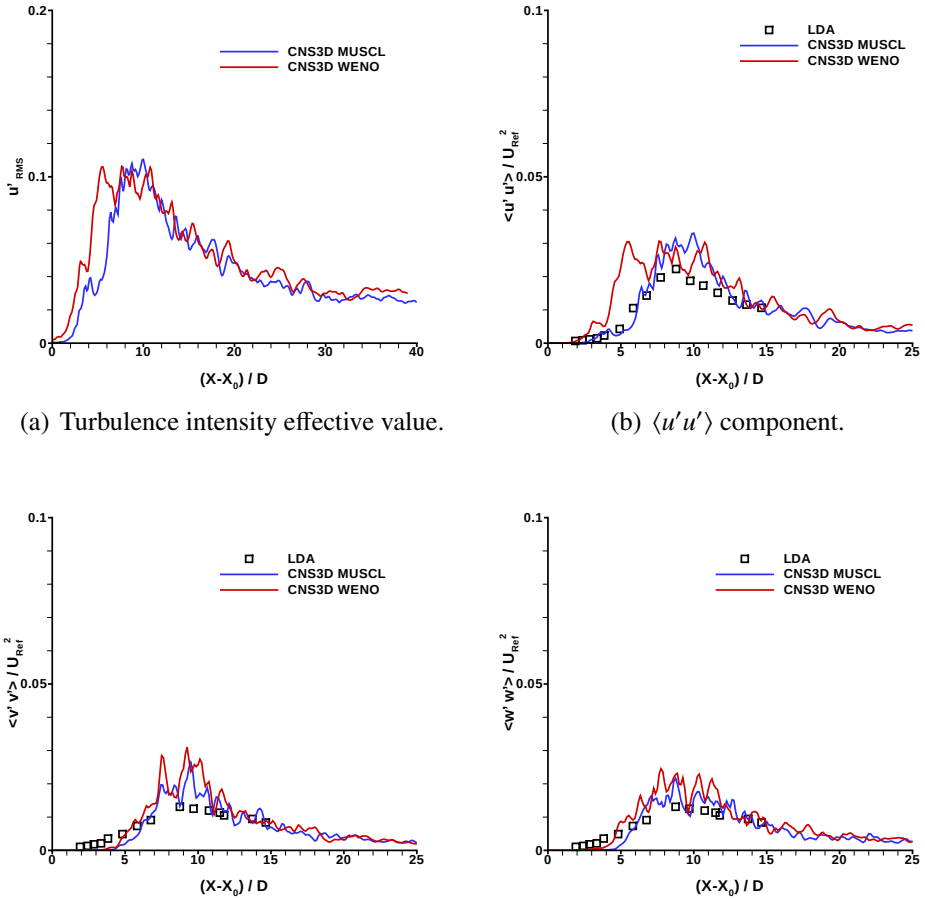

(a) Turbulence intensity effective value.

(b) $\langle u'u' \rangle$ component.

(c) $\langle v'v' \rangle$ component.

(d) $\langle w'w' \rangle$ component.

Figure 5.17: Central line turbulence intensity and normal stresses results. **LDA**[33].

Sections

Figure 5.18, Figure 5.19 and Figure 5.20, frames *a*, shows the cross sections average axial velocity values, where the intensities' and gradient's are correctly predicted, except the section $\frac{X-X_0}{D} = 15$ (**CNS3D WENO**) where the velocity intensity is over predicted. The remaining frames (*b*, *c*, *d*, *e* and *f*) compare the predicted Reynolds stresses components with the available data. The reference trends can be observed for both schemes with an overall over prediction for the **CNS3D WENO** case. From the three sections analysed, Table 5.8, a proportional partition of energy trough the axial and radial components can be observed for both the cases, with a polarization towards the axial component, as expected; the axial polarization is over predicted by the **CNS3D WENO** case. In accordance with the reference values and expected flow field behaviour, a quasi-isotropic

turbulence with polarization towards the axial direction is observed for both cases, with correct partition ratio in **CNS3D MUSCL** case. Moreover, the difference in direction of the cross components shows the uncertainty and the non-deterministic nature of the flow field, in particular $\langle u'v' \rangle$ component.

Physical quantities	**CNS3D MUSCL**	**CNS3D WENO**	**LDA**	**HWA**	**DNS**
Section $\frac{X-X_0}{D} = 15$					
$\langle u'u' \rangle$	0.083	0.129	0.086	0.064	0.053
$\langle v'v' \rangle$	0.075	0.082	0.047	0.035	0.032
$\langle w'w' \rangle$	0.062	0.068	0.048	0.035	0.032
$\langle u'v' \rangle$	0.018	-0.009	0.023	0.019	0.018
$\langle u'w' \rangle$	0.020	0.029	0.023	0.019	0.018
Section $\frac{X-X_0}{D} = 20$					
$\langle u'u' \rangle$	0.088	0.116	0.086	0.064	0.045
$\langle v'v' \rangle$	0.064	0.068	0.047	0.034	0.030
$\langle w'w' \rangle$	0.051	0.051	0.048	0.034	0.030
$\langle u'v' \rangle$	-0.009	-0.011	0.023	0.019	0.018
$\langle u'w' \rangle$	0.024	0.025	0.023	0.019	0.018
Section $\frac{X-X_0}{D} = 25$					
$\langle u'u' \rangle$	0.077	0.115	0.086	0.064	0.048
$\langle v'v' \rangle$	0.074	0.054	0.047	0.035	0.035
$\langle w'w' \rangle$	0.060	0.063	0.048	0.034	0.030
$\langle u'v' \rangle$	0.013	-0.014	0.023	0.019	0.018
$\langle u'w' \rangle$	0.028	0.043	0.023	0.019	0.018

Table 5.8: Reconstruction schemes sections results, peak values. **HWA**[116], **LDA**[115] and **DNS**[110].

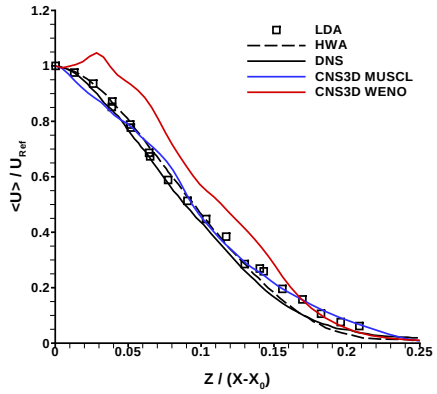

(a) Velocity distribution, axial component.

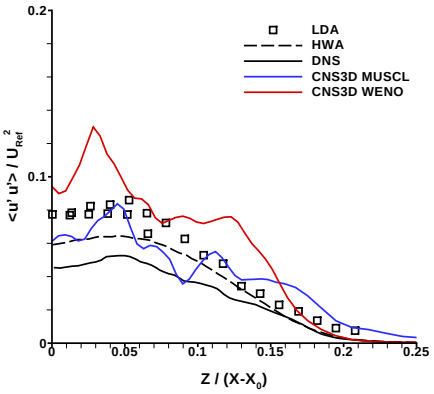

(b) $\langle u'u' \rangle$ component.

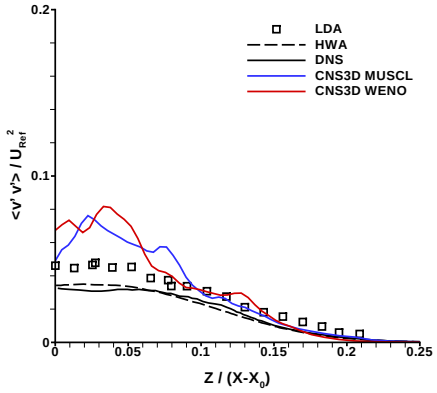

(c) $\langle v'v' \rangle$ component.

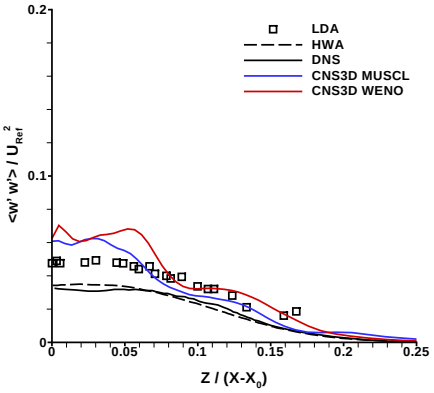

(d) $\langle w'w' \rangle$ component.

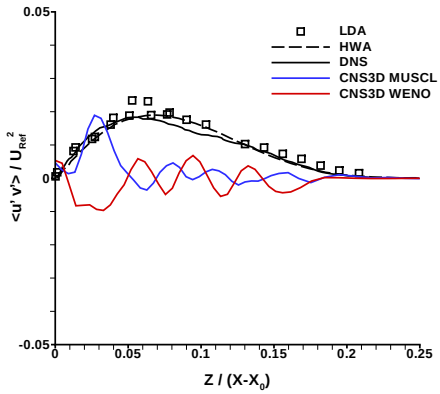

(e) $\langle u'v' \rangle$ component.

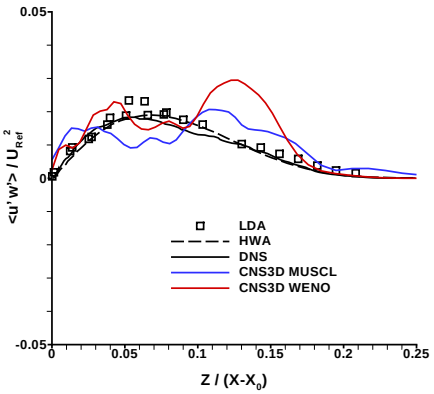

(f) $\langle u'w' \rangle$ component.

Figure 5.18: Section $\frac{X - X_0}{D} = 15$ results. **HWA**[116], **LDA**[115] and **DNS**[110].

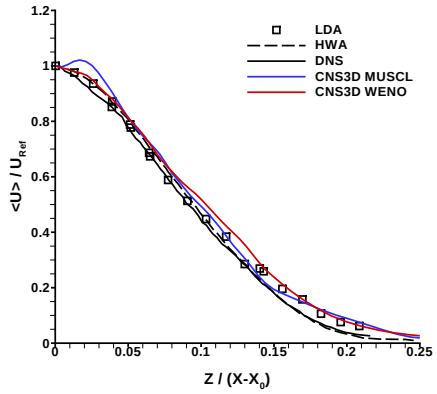

(a) Velocity distribution, axial component.

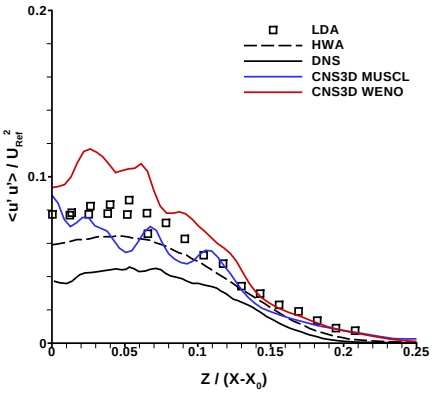

(b) $\langle u'u' \rangle$ component.

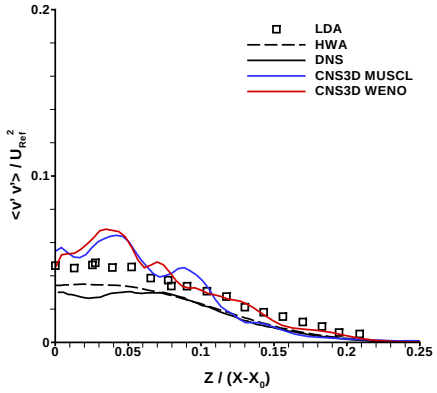

(c) $\langle v'v' \rangle$ component.

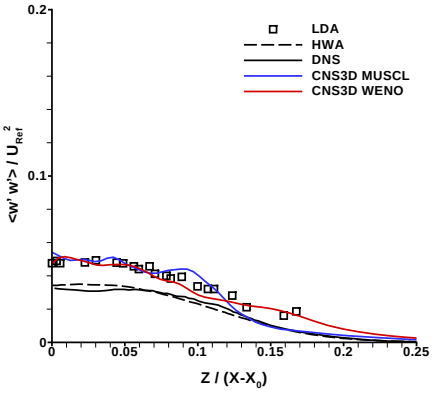

(d) $\langle w'w' \rangle$ component.

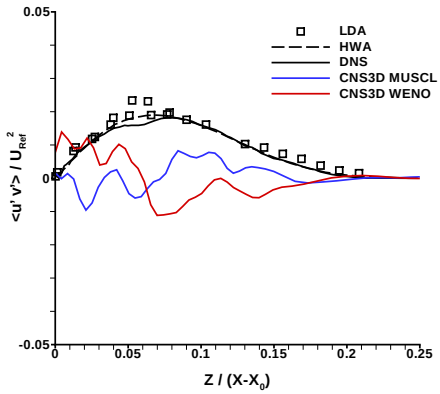

(e) $\langle u'v' \rangle$ component.

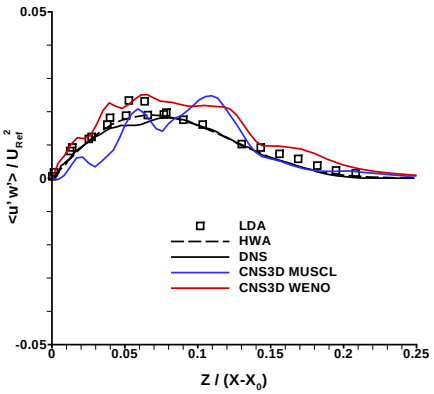

(f) $\langle u'w' \rangle$ component.

Figure 5.19: Section $\frac{X - X_0}{D} = 20$ results. **HWA**[116], **LDA**[115] and **DNS**[110].

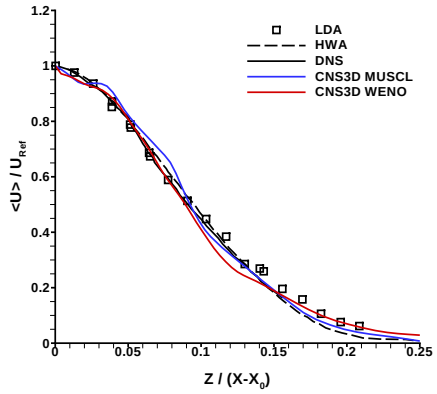

(a) Velocity distribution, axial component.

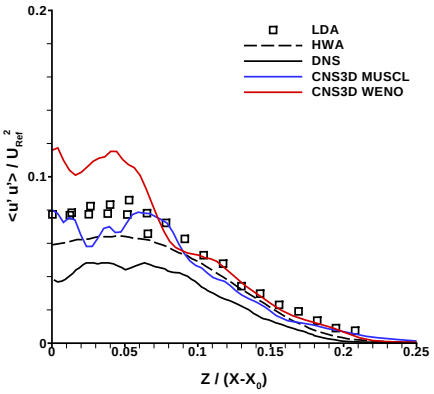

(b) $\langle u'u' \rangle$ component.

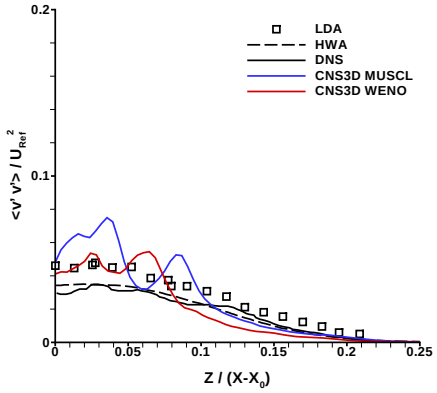

(c) $\langle v'v' \rangle$ component.

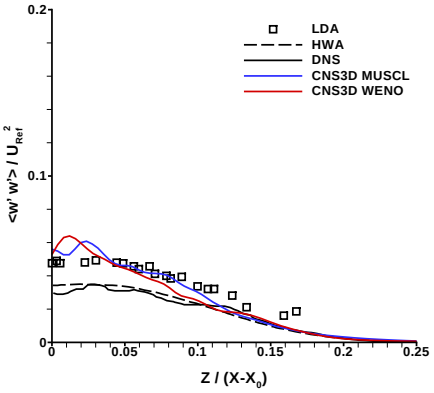

(d) $\langle w'w' \rangle$ component.

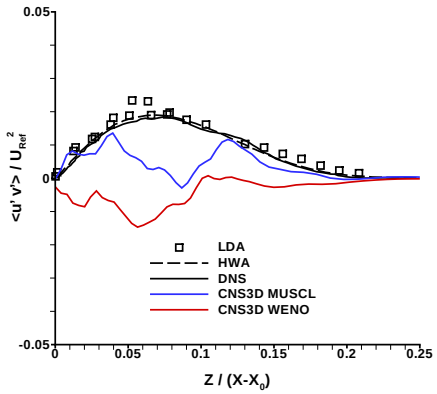

(e) $\langle u'v' \rangle$ component.

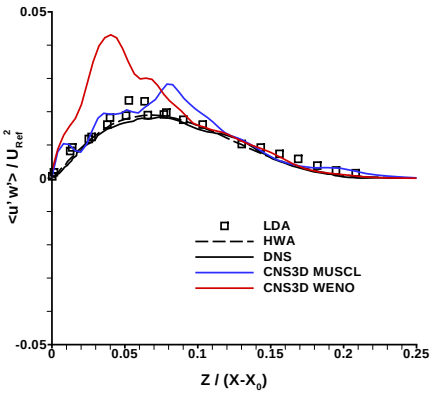

(f) $\langle u'w' \rangle$ component.

Figure 5.20: Section $\frac{X - X_0}{D} = 25$ results. **HWA**[116], **LDA**[115] and **DNS**[110].

The results of this analysis show strong evidence that the **MUSCL** scheme predicts more accurately the effects of a developed turbulent jet. The comparisons between the predicted and experimental/numeric mean flow characteristics and Reynolds stresses in this study agrees for **CNS3D MUSCL** case. Therefore, as far as physics is concerned, the **CNS3D MUSCL** case predicts the flow field properties (e.g., from the turbulence point of view, the energy containing motion is well balanced).

High-Order

To study the effects of different spatial high-order reconstruction schemes have over the flow field three numerical methods have been selected, the **CBS** 2^{nd}-order **MUSCL** augmented with **LMC**, the **CBS** 5^{th}-order **MUSCL** augmented with **LMC** and **CBS** 9^{th}-order **WENO**, respectively. The jet's central line and wake sections are studied, as previously mentioned.

Central Line

Figure 5.21 show the differences between three high-order reconstruction schemes in predicting the variations in the axial velocity intensity trough the jet's central line. It can be observed for the laminar and transition regions that the jet velocity predictions correspond, locally, to the experimental and numerical values for all cases ($0 \leq \frac{X - X_0}{D} \lessapprox 8$). The far-filed back pressure or blockage effects over the jet's size is accurately predicted with **CNS3D** 5^{th} **ORDER** and **CNS3D** 9^{th} **ORDER** schemes. The break down region of the vortical ring structure (transition region) is accurately captured, locally, as it can be seen in Table 5.9, consequently, the correct jet's induced entrainment effects are better resolved by the use of the 5^{th} and 9^{th} -order schemes. For the velocity gradient, the **CNS3D** 5^{th} **ORDER** case gives a similar value as the experimental/numerical results ($10 \lessapprox \frac{X - X_0}{D} \lessapprox 30$). The oscillatory pattern of the central line velocity amplitude (**CNS3D** 5^{th} **ORDER**) is the consequence of the non smooth structures of the flow field, the numerical nature of the reconstruction scheme [124, 125] added to the spatial order, creates locally a non smooth stencil.

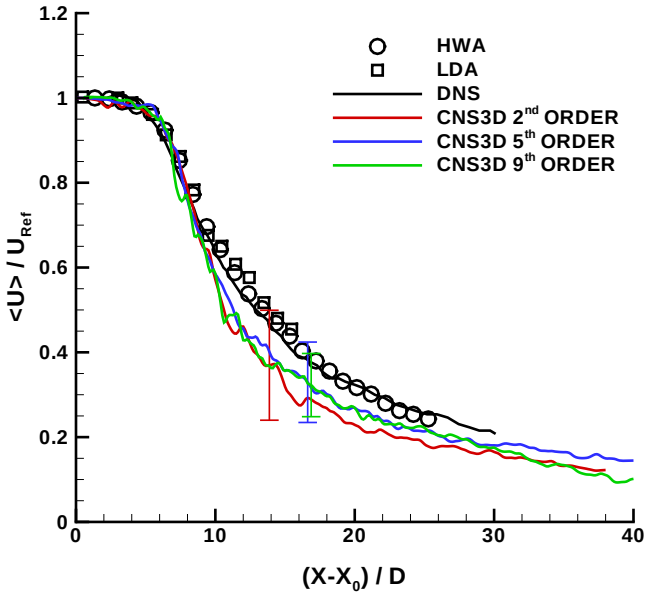

FIGURE 5.21: Central line velocity results. **HWA**[111], **LDA**[33] and **DNS**[110].

Figure 5.22, frame *a*, show the effective value of the turbulence magnitude for the **CNS3D** 2^{nd} **ORDER**, **CNS3D** 5^{th} **ORDER** and **CNS3D** 9^{th} **ORDER** cases. It can be observed a difference in trend for the 2^{nd}-order scheme ($6 \lessapprox \frac{X - X_0}{D} \lessapprox 10$), and different magnitudes with different down stream peak locations. The remaining frames (*b*, *c* and *d*) presents, from the inertial point of view, the central line Reynolds stresses normal components results. Comparisons with experimental data reveal an over prediction for all the three component in all cases; however, the experimental trends can be observed for the 5^{th}-order and 9^{th}-order cases. The partition of energy between the normal stress components, axial and radial, is proportional in intensity, with a higher value in the axial component for **CNS3D** 2^{nd} **ORDER** and **CNS3D** 9^{th} **ORDER** cases, revealing a quasi-isotropic turbulence behaviour with a polarization towards the axial component, as expected, for **CNS3D** 5^{th} **ORDER**.

Physical quantities	2^{nd} **ORDER**	5^{th} **ORDER**	9^{th} **ORDER**	**LDA**
X_0	2	0	0	0
Maximum error	0.297	0.154	0.234	*n.a.*
u'_{RMS}	0.134	0.110	0.123	*n.a.*
$\langle u'u' \rangle$	0.048	0.030	0.040	0.022
$\langle v'v' \rangle$	0.029	0.026	0.027	0.013
$\langle w'w' \rangle$	0.029	0.024	0.026	0.013

TABLE 5.9: Spatial resolution central line results, peak values. 2^{nd} **ORDER** is the **CNS3D** 2^{nd} **ORDER**, 5^{th} **ORDER** is the **CNS3D** 5^{th} **ORDER**, 9^{th} **ORDER** is the **CNS3D** 9^{th} **ORDER** and **LDA**[33].

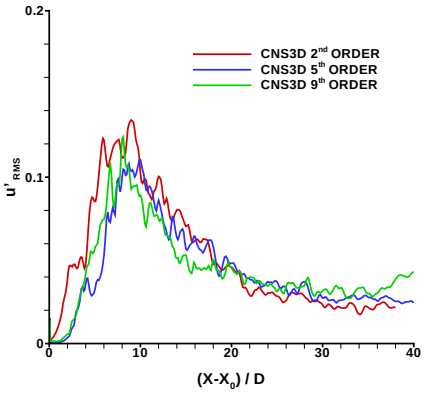

(a) Turbulence intensity effective value.

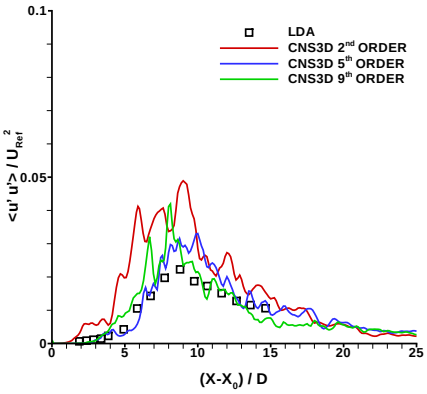

(b) $\langle u'u' \rangle$ component.

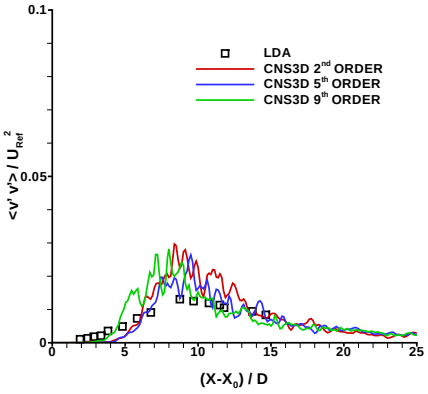

(c) $\langle v'v' \rangle$ component.

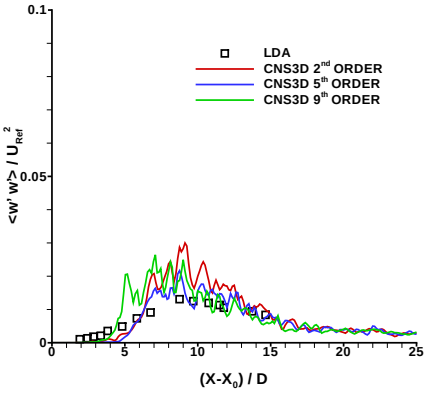

(d) $\langle w'w' \rangle$ component.

FIGURE 5.22: Central line turbulence intensity and normal stresses results. **LDA**[33].

Sections

Figure 5.23, Figure 5.24 and Figure 5.25, frames *a*, shows the cross sections average axial velocity values, where the velocity gradients are predicted correctly, locally; the velocity magnitude values are over predicted for **CNS3D** 2^{nd} **ORDER**. The remaining frames (*b*, *c*, *d*, *e* and *f*) compare the predicted Reynolds stresses components with the available data. The reference trends can be observed for all the selected schemes, an overall over prediction for **CNS3D** 2^{nd} **ORDER** case is noticed, as the employed numerical scheme in conjunction with the grid resolution in not enough dissipative. From the three sections analysed, Table 5.10, a proportional partition of energy trough the axial and radial components can be observed for the analysed cases, with a polarization towards the axial component, as expected. In accordance with the reference values and expected flow field behaviour, a quasi-isotropic turbulence with polarization towards the axial direction can be observed for all cases, with a correct partition ratio in **CNS3D** 5^{th} **ORDER** case. Moreover, the difference in direction of the cross components show the randomness nature of the flow field, in particular $\langle u'v' \rangle$ component.

Physical quantities	2^{nd} **ORDER**	5^{th} **ORDER**	9^{th} **ORDER**	**LDA**	**HWA**	**DNS**
Section $\frac{X-X_0}{D} = 15$						
$\langle u'u' \rangle$	0.159	0.083	0.071	0.086	0.064	0.053
$\langle v'v' \rangle$	0.101	0.075	0.065	0.047	0.035	0.032
$\langle w'w' \rangle$	0.095	0.062	0.054	0.048	0.035	0.032
$\langle u'v' \rangle$	-0.016	0.018	-0.012	0.023	0.019	0.018
$\langle u'w' \rangle$	0.051	0.020	0.017	0.023	0.019	0.018
Section $\frac{X-X_0}{D} = 20$						
$\langle u'u' \rangle$	0.109	0.088	0.099	0.086	0.064	0.045
$\langle v'v' \rangle$	0.072	0.064	0.067	0.047	0.034	0.030
$\langle w'w' \rangle$	0.076	0.051	0.083	0.048	0.034	0.030
$\langle u'v' \rangle$	-0.020	-0.009	-0.015	0.023	0.019	0.018
$\langle u'w' \rangle$	0.043	0.024	0.026	0.023	0.019	0.018
Section $\frac{X-X_0}{D} = 25$						
$\langle u'u' \rangle$	0.117	0.077	0.078	0.086	0.064	0.048
$\langle v'v' \rangle$	0.092	0.074	0.058	0.047	0.035	0.035
$\langle w'w' \rangle$	0.080	0.060	0.076	0.048	0.034	0.030
$\langle u'v' \rangle$	0.014	0.013	0.012	0.023	0.019	0.018
$\langle u'w' \rangle$	0.030	0.028	0.024	0.023	0.019	0.018

Table 5.10: Spatial resolution sections results, peak values. 2^{nd} **ORDER** is the **CNS3D** 2^{nd} **ORDER**, 5^{th} **ORDER** is the **CNS3D** 5^{th} **ORDER**, 9^{th} **ORDER** is the **CNS3D** 9^{th} **ORDER**, **HWA**[116], **LDA**[115] and **DNS**[110].

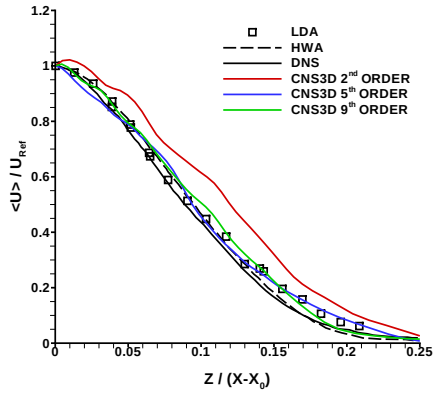

(a) Velocity distribution, axial component.

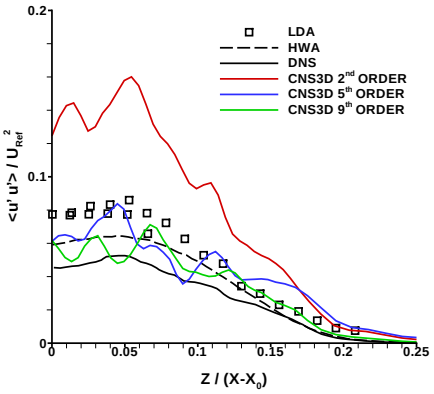

(b) $\langle u'u' \rangle$ component.

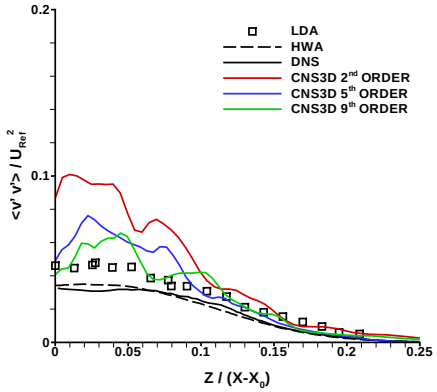

(c) $\langle v'v' \rangle$ component.

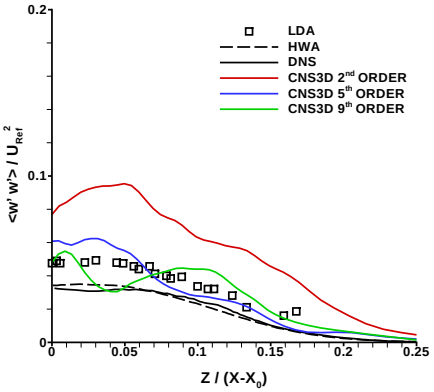

(d) $\langle w'w' \rangle$ component.

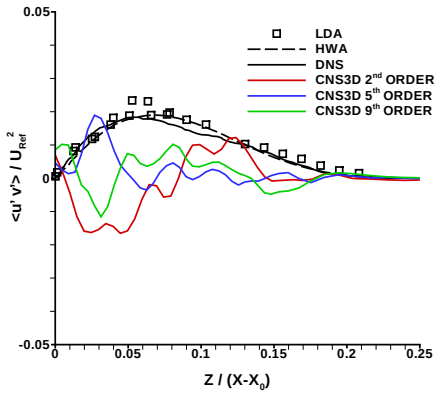

(e) $\langle u'v' \rangle$ component.

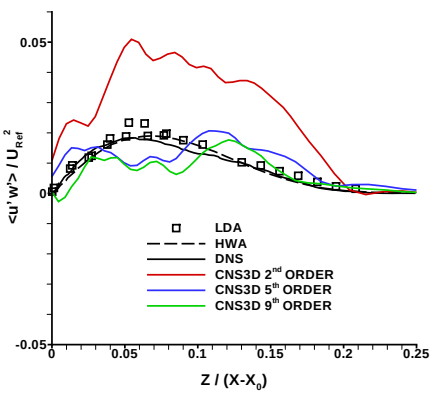

(f) $\langle u'w' \rangle$ component.

FIGURE 5.23: Section $\frac{X - X_0}{D} = 15$ results. **HWA**[116], **LDA**[115] and **DNS**[110].

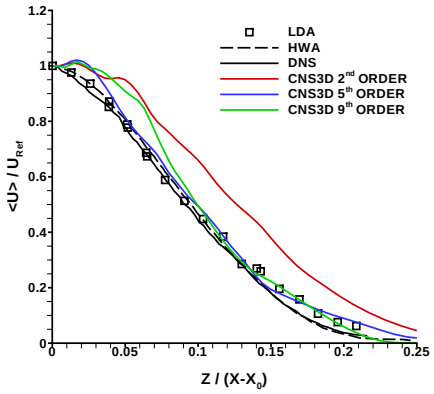

(a) Velocity distribution, axial component.

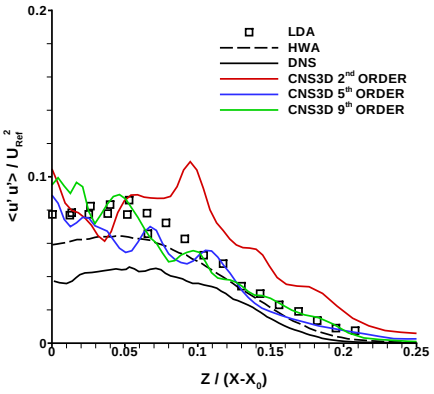

(b) $\langle u'u' \rangle$ component.

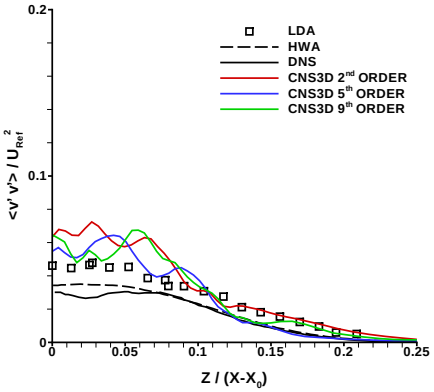

(c) $\langle v'v' \rangle$ component.

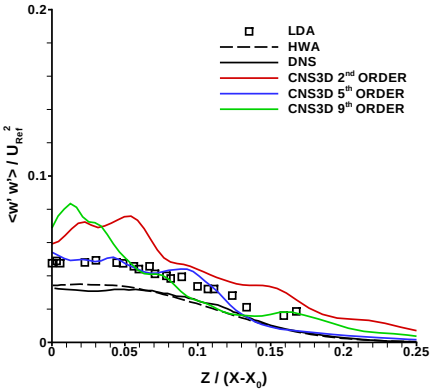

(d) $\langle w'w' \rangle$ component.

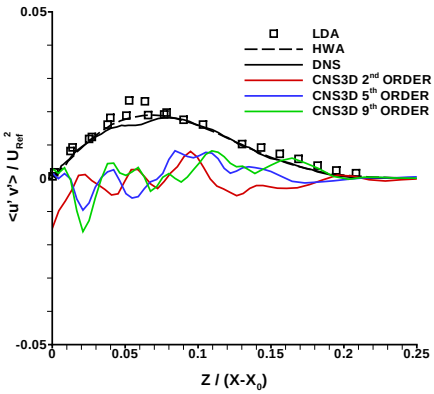

(e) $\langle u'v' \rangle$ component.

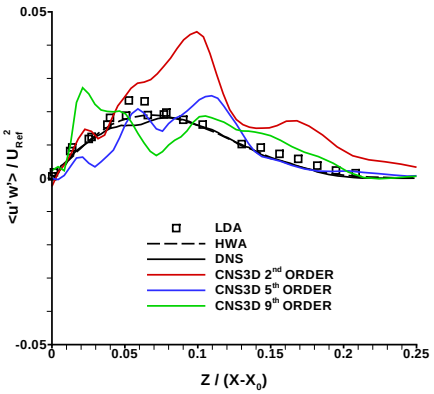

(f) $\langle u'w' \rangle$ component.

FIGURE 5.24: Section $\frac{X - X_0}{D} = 20$ results. **HWA**[116], **LDA**[115] and **DNS**[110].

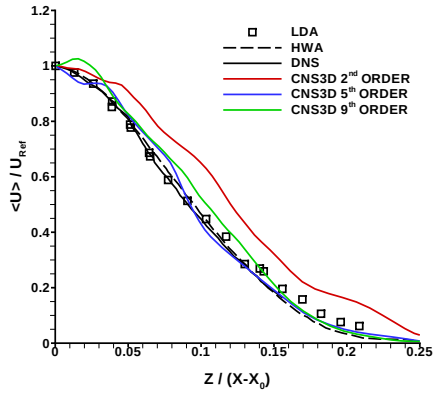

(a) Velocity distribution, axial component.

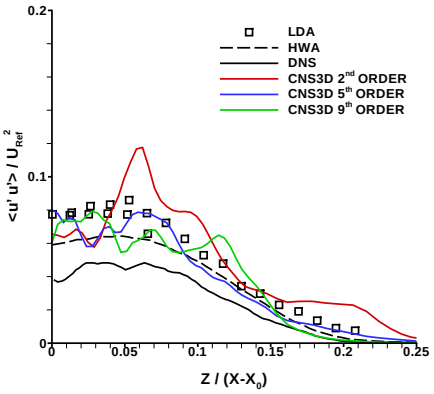

(b) $\langle u'u' \rangle$ component.

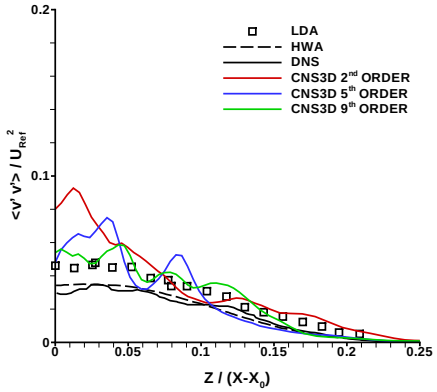

(c) $\langle v'v' \rangle$ component.

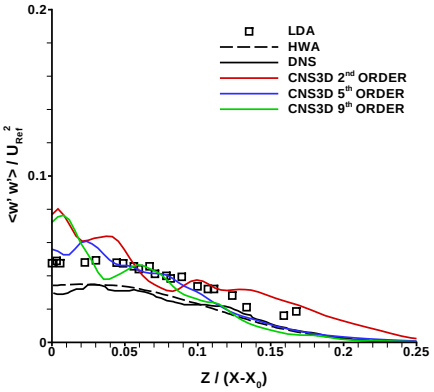

(d) $\langle w'w' \rangle$ component.

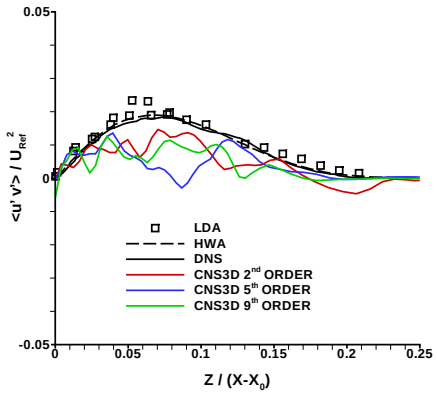

(e) $\langle u'v' \rangle$ component.

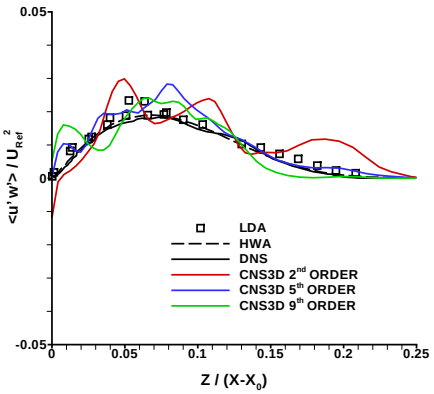

(f) $\langle u'w' \rangle$ component.

Figure 5.25: Section $\frac{X - X_0}{D} = 25$ results. **HWA**[116], **LDA**[115] and **DNS**[110].

The comparison between the predicted and experimental/numeric mean flow characteristics and Reynolds stresses in this study agrees for the 5^{th}-order method. Therefore, as far as physics is concerned, the **CNS3D** 5^{th} **ORDER** case predicts the flow field properties (e.g., from the turbulence point of view, the energy containing motion is well balanced).

Summary

The correlation between predicted and experimental/numeric mean flow characteristics and Reynolds stresses is in very good agreement for the **CBS** Riemann solver with the 5^{th}-order **MUSCL** scheme augmented with **LMC**. For instance, according to the simulations, the center line velocity comes out with some discrepancies from the reference values, but with a more accurate result. The partition of energy between the Reynolds stresses normal components are closer and proportional to the reference values, as expected; the high order spatial accuracy in conjunction with the mesh resolution give the " correct" amount of dissipation. Moreover, the Reynolds stresses values indicate a good correlation with the experimental data of [33].

5.2.3 Spectral analysis

Finalizing the physical study (velocity and energy analyses) of the previous subsection, p-study, the total kinetic energy frequency spectra ($E(\nu)$) will be presented for the jet's axial distance (central line), with the correspondent periodgrams (ν vs ϕ) and temporal total kinetic energy ($E(T)$) in Appendix G, for all the selected numerical variants. As described in Section 1.2, the spectrograms interpretation indicate the jet's flow field characteristics, this is physically appealing and can be of great help in inferring the flow field properties. From the results of [33, 113, 114] (jet cross section) it is possible to make a qualitative comparison for the jet's core region ($0 \leq \frac{X}{D} \lessapprox 5$), assuming for that reason a similar physical behaviour between radial and axial directions. The slopes, in the following figures, represent the evolution of the energy decay rate trough out the jet's down stream flow field. As upper slope limit, the local isotropy hypothesis (Kolmogorov [38, 39] $-\frac{5}{3}$ decay rate) is used as asymptotic reference, where the small eddies in the flow are statistical independent in preferred directions of the large eddies.

Figure 5.26, Figure 5.27 and Figure 5.28, shows the evolution of the spectral energy trough the jet's central line. It can be observed as the axial position is increased, the amplitude values of the production region also increase, reaching an approximate level for

the jet's transition region ($\frac{X}{D} \geq 10$). For the far-field region ($30 \leq \frac{X}{D} \leq 40$), the amplitude production region shrinks, in amplitude and size, and is almost non-existent for the farthest probe points, the jet's effects can be negligible, or in other words, the flow field energy can be consider purely inertial. From the dissipation point of view, it can be noticed the change in slope trough out the jet's central line. Starting from the jet's discharge and moving down stream, the low frequencies states are exited in the production region with no associated dissipation, a high intensity peak in frequency is observed followed by a drop in amplitude; the spectral energy values at frequencies higher then the peak values can be consider as background noise ($\frac{X}{D} = 0$), this can be confirmed by the associated randomness in phase (Appendix G). Furthermore, the remaining spectrograms points reveals a transfer of energy from the lower to the higher frequencies states, with the changing in dissipation rates towards the asymptotic value, as the higher frequencies become more exited. The observed trends can be explained by the population of the high frequencies states at the expenses of the low frequency states, meaning a surging in energy from the lower to the higher states. Moreover, as the production states and lower frequencies becomes unexcited, the dissipation rate changes away from the asymptotic reference level, populating them the higher frequency states until the energy is dissipated as heat, at the viscous level.

Table 5.11, reveals the spectral peak frequency to be in accordance with the predicted resonant frequency, for this class of flows [126]. The difference between the simulated results and experimental value can be explained by the different at down stream probe locations, but still inside of the jet's core (laminar region); however the simulated Strouhal numbers are inside the experimental numerical range, with the exception of **CBS WENO 9^{th}-order** case. Moreover, Figure 5.26 frames *d* and *e*, a second peak with similar magnitude can be observed with a frequency ratio between the peaks of $\frac{4}{5}$ (**CBS MUSCL 2^{nd}-order LMC**) and $\frac{1}{2}$ (**CBS WENO 5^{th}-order**), respectively.

Numerical schemes	ν_{Max}	**St**
CBS MUSCL 5^{th}-order LMC	85	0.256
HLLC MUSCL 5^{th}-order LMC	85	0.256
CBS MUSCL 5^{th}-order	80	0.241
CBS WENO 5^{th}-order	85	0.256
CBS MUSCL 2^{nd}-order LMC	75	0.226
CBS WENO 9^{th}-order	45	0.135

Table 5.11: Resonant frequencies at $\frac{X}{D} = 5$ and correspondent Strouhal numbers.

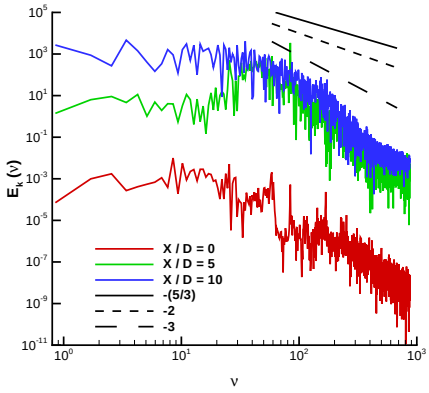

(a) **CBS MUSCL 5^{th}-order LMC**.

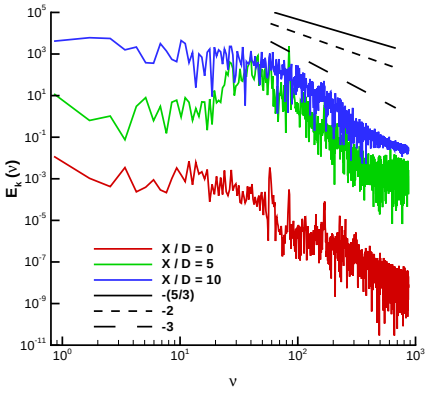

(b) **HLLC MUSCL 5^{th}-order LMC**.

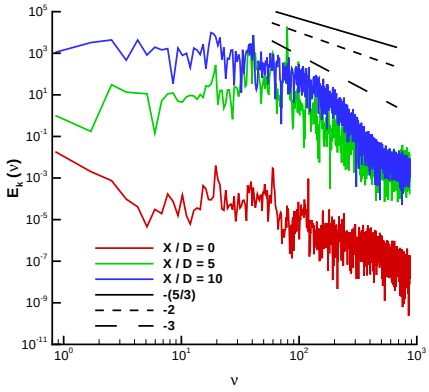

(c) **CBS MUSCL 5^{th}-order**.

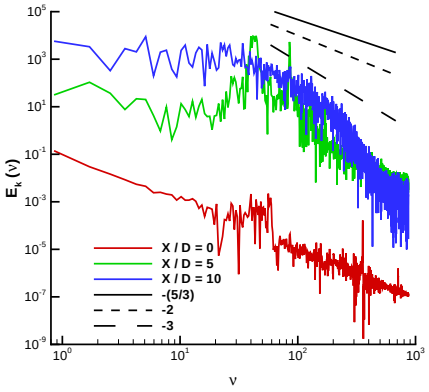

(d) **CBS WENO 5^{th}-order**.

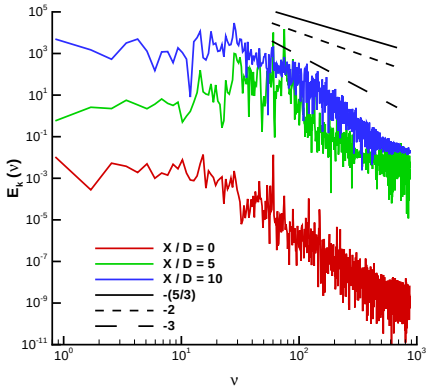

(e) **CBS MUSCL 2^{nd}-order LMC**.

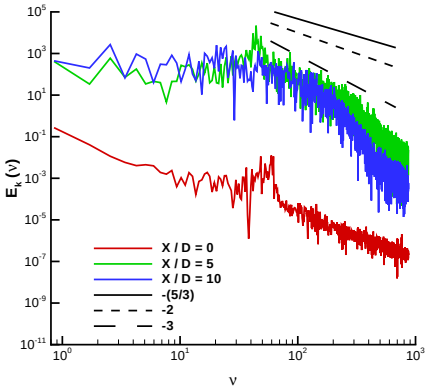

(f) **CBS WENO 9^{th}-order**.

Figure 5.26: Central line kinetic energy spectrograms, points $\frac{X}{D} = (0, 5, 10)$.

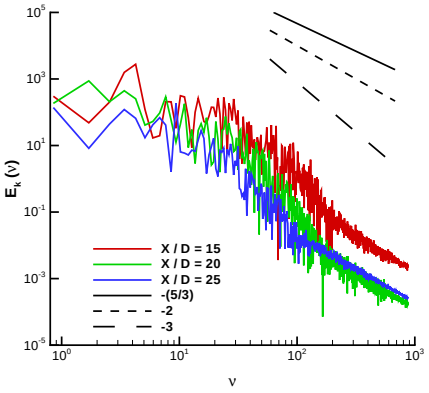

(a) **CBS MUSCL 5^{th}-order LMC**.

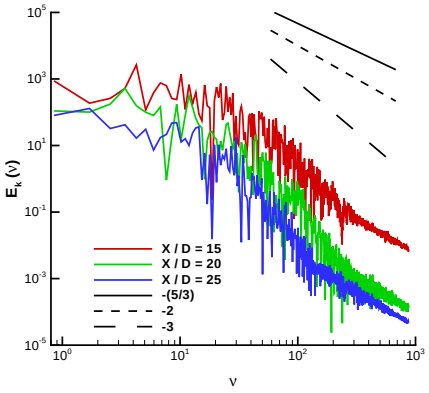

(b) **HLLC MUSCL 5^{th}-order LMC**.

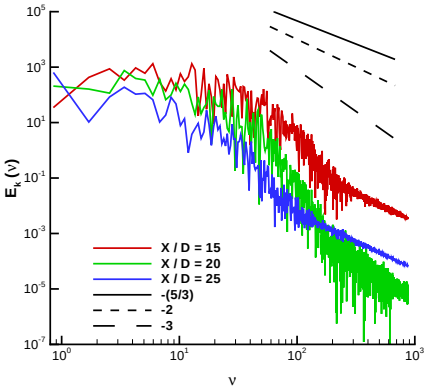

(c) **CBS MUSCL 5^{th}-order**.

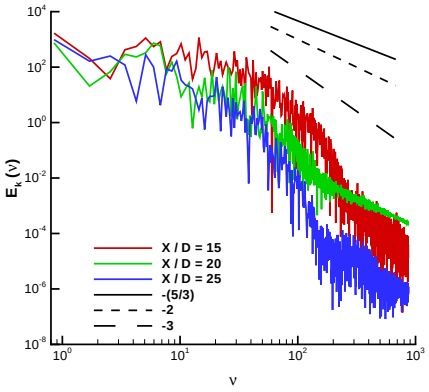

(d) **CBS WENO 5^{th}-order**.

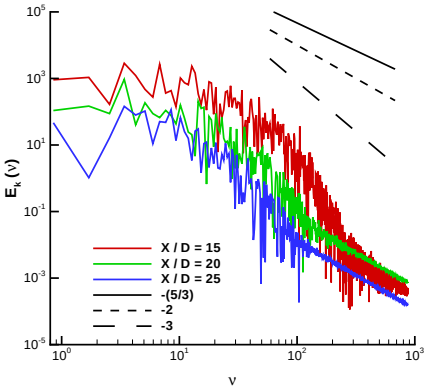

(e) **CBS MUSCL 2^{nd}-order LMC**.

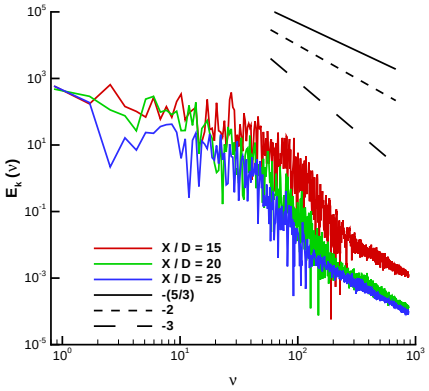

(f) **CBS WENO 9^{th}-order**.

Figure 5.27: Central line kinetic energy spectrograms, points $\frac{X}{D} = (15, 20, 25)$.

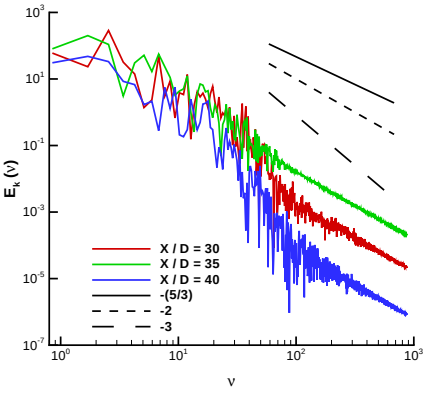

(a) **CBS MUSCL 5^{th}-order LMC**.

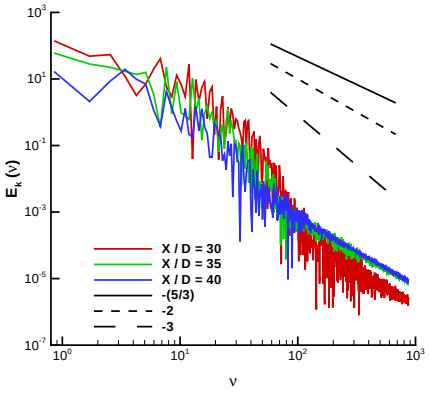

(b) **HLLC MUSCL 5^{th}-order LMC**.

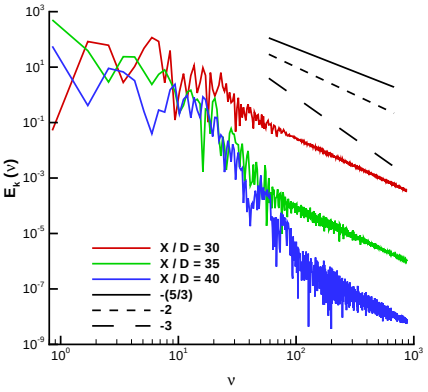

(c) **CBS MUSCL 5^{th}-order**.

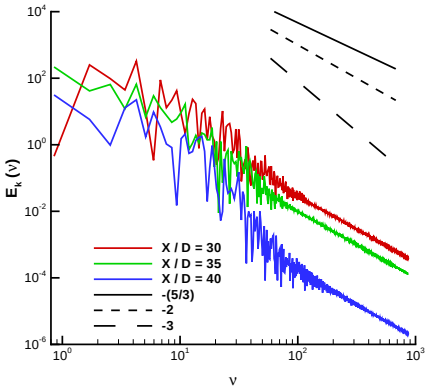

(d) **CBS WENO 5^{th}-order**.

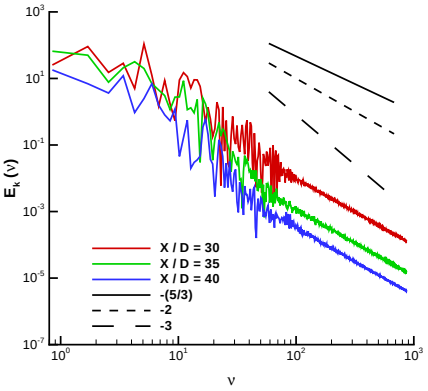

(e) **CBS MUSCL 2^{nd}-order LMC**.

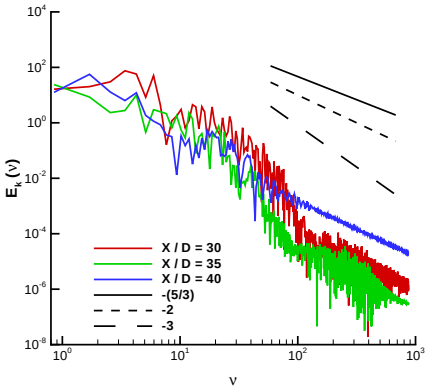

(f) **CBS WENO 9^{th}-order**.

Figure 5.28: Central line kinetic energy spectrograms, points $\frac{X}{D} = (30, 35, 40)$.

From this analysis, it is possible to conclude that all the selected methods are able to describe the evolution of the energy dissipation decay trough out the jet's central line. Moreover, the resonant frequency of the system is accurately predicted for all 5^{th} and 2^{nd} order methods. Furthermore, the total kinetic energy decay rate is in accordance to the theoretical and experimental results.

5.2.4 Buoyancy

Forced periodic jets and wakes by laterally perturbing sinusoidally an exhausting tube from which smoke is issued into free stream shows that the natural occurring random eddying motions could be locked in with the perturbing frequency [127–129]. From the examination of the geometrical three dimensional patterns a classification of the simplest occurring structures was developed. Those structures have a single or double sided, with the former as the result of either buoyancy effects or how the vorticity has been generated at the source. As an interesting observation, the previous classification is further investigated by the analysis of the source effects in terms of Fourier space. From the extensive literature about jet flows, a jet issuing into a free-stream induces an entrainment effect over the surroundings and the correspondent effect influences the jet mixing structures (free shear layer), this occurs as a cause-effect close cycle interaction between the jet flow and free stream. The perturbations at the source are them amplified trough the mixing region. Due to entrainment, the vortical rings downstream movement can be either in phase (vortical plane normal to jet's axis) or off-phase (vortical plane tilted to jet's axis) giving then a helically pattern.

Figure 5.29, the instantaneous snapshots of jets flow fields reveals the different pattern in vortical structures at the jet's core, as it can be seen by the "wavy" pattern of the mixing region. The rings break down will be amalgamated into flow structures with upstream velocity.

Figure 5.30, shows the iso-surfaces ($U = -0.5$) for two different buoyant jets, in frame *a* the back-flow structures confine the jet to a neutral state; while in frame *b*, as it can clearly be seen, the amalgamated region of upstream velocity exerting blockage effects over the wake, resulting in the bending of the jet flow. Furthermore, in the case of a neutral buoyant jet, the structures can be mirrored; in contrast, the structure responsible for the buoyant jet effect is unique.

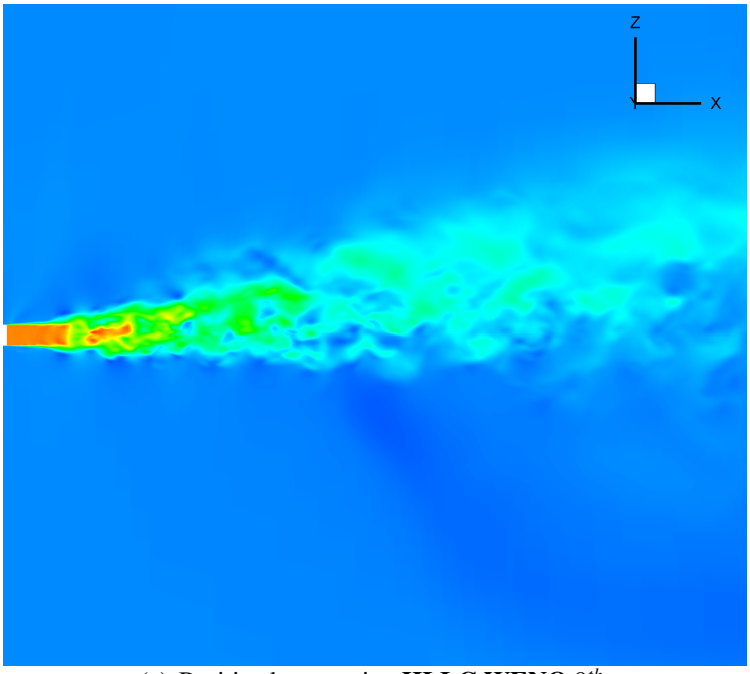

(a) Positive buoyant jet, **HLLC WENO** 9^{th}.

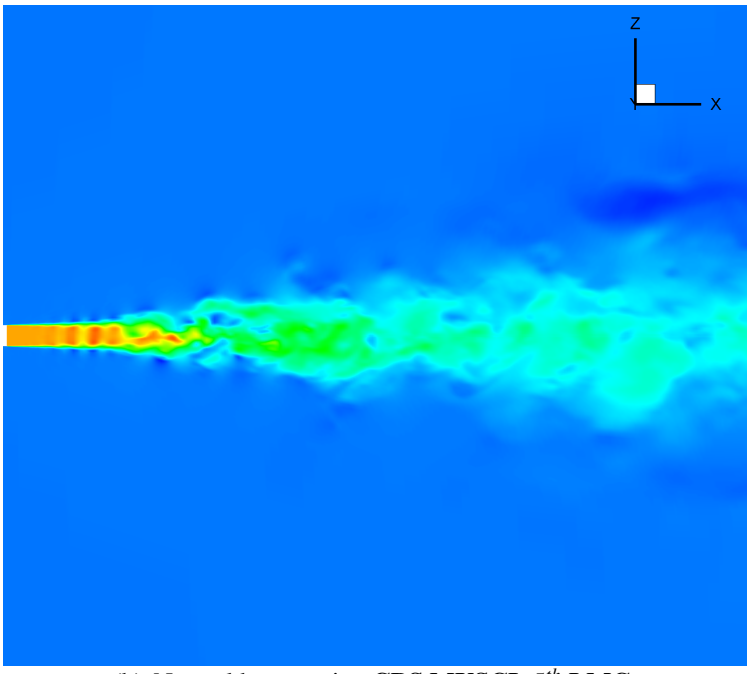

(b) Neutral buoyant jet, **CBS MUSCL** 5^{th} **LMC**.

Figure 5.29: Instantaneous snapshots of buoyant jets.

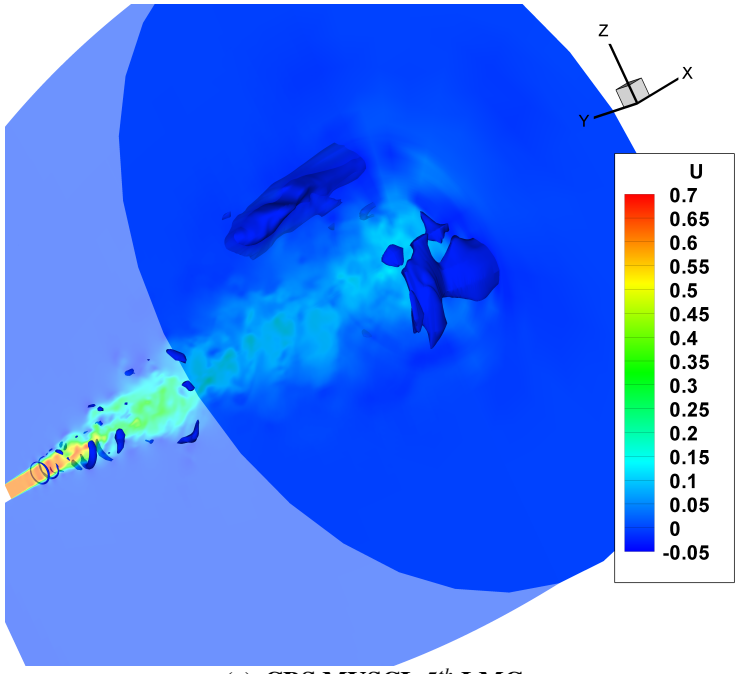

(a) **CBS MUSCL** 5^{th} **LMC**.

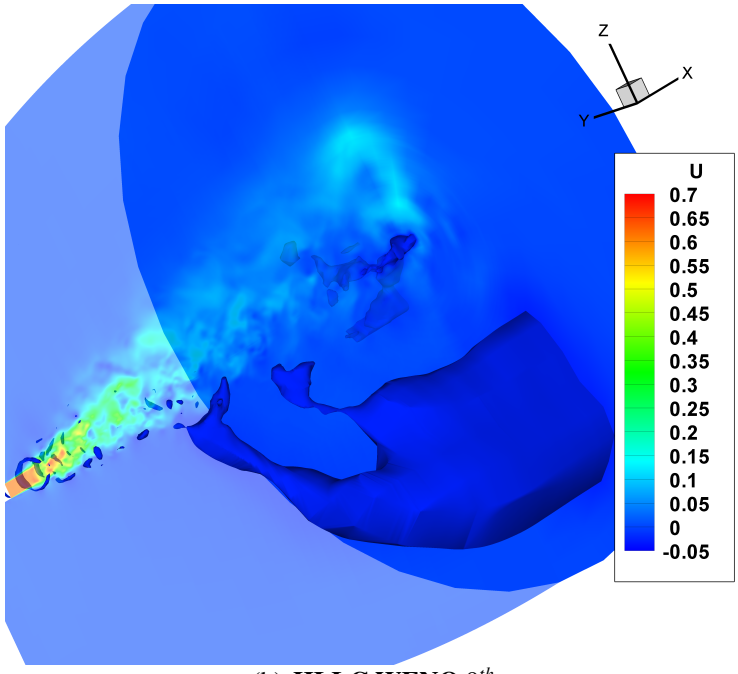

(b) **HLLC WENO** 9^{th}.

Figure 5.30: Buoyancy Iso-surfaces.

In order to explain the reason of different jet's behaviours, four points were chosen at the lip of the jet's exhaust, being labelled as following:

Points Labelling	Axial	Radial	Azimuthal
N	0	0.5	0
S	0	0.5	π
E	0	0.5	$\frac{\pi}{2}$
W	0	0.5	$-\frac{\pi}{2}$

Figure 5.31, shows the spectrograms of four different methods used in this study, frame *a* buoyant and the remaining frames neutral buoyant jet's. As it can be seen clearly in frame *a*, at the spectral lower frequency range ($\nu \leq 100$), the differences in amplitude and frequency patterns for all the four points, while on the remaining frames the same four probe points are correlated with each other, in frequency and amplitude, over the same frequency range.

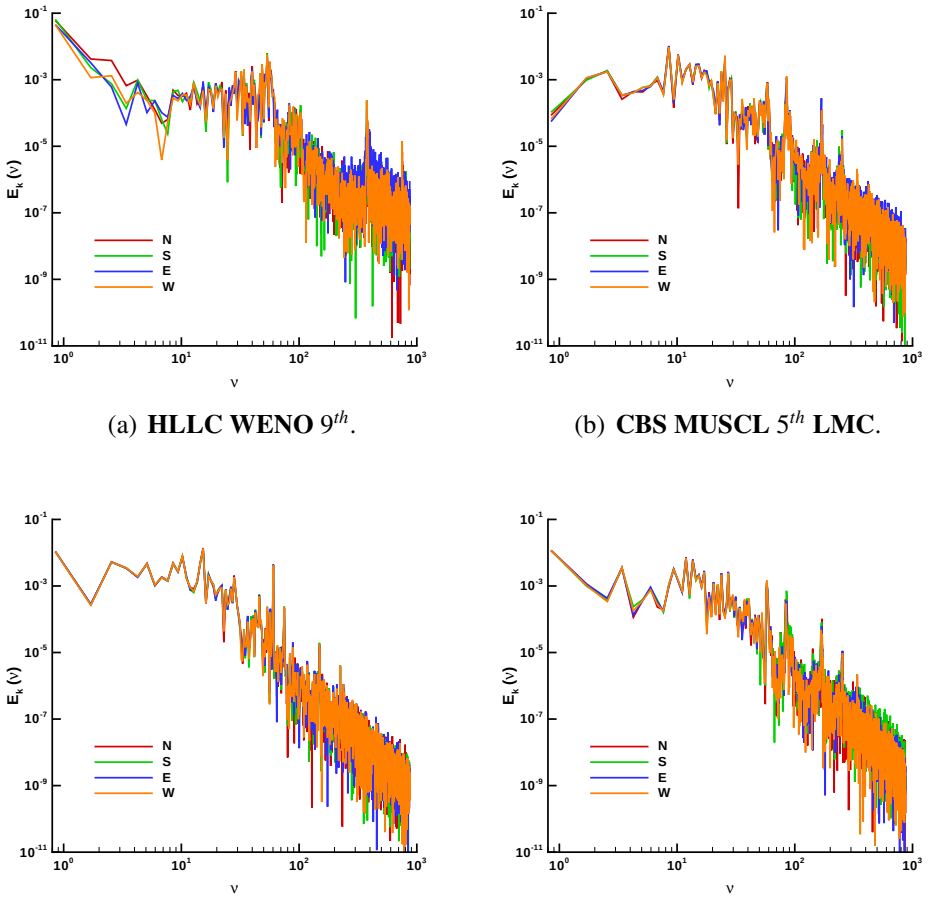

(a) **HLLC WENO** 9^{th}.

(b) **CBS MUSCL** 5^{th} **LMC**.

(c) **CBS MUSCL** 2^{nd} **LMC**.

(d) **HLLC MUSCL** 5^{th} **LMC**.

Figure 5.31: Spectrograms at exhausts lip.

It can be deducted, that the differences in amplitude and frequency, for the lower range of the spectrum between each probe point, will influence the down stream wake patterns, originating then a buoyant jet, as consequence. Furthermore, from the jet point of view, the experimental induced oscillations of the jet discharge and the jet induced entrainment (simulation) have equivalents effects, despite the fact of having different causes.

5.3 Discussion

In this chapter, the study of different methodologies in simulating a high subsonic jet issuing into a static free stream has been presented. It is suggested that the corrections and reviews done in the flow solver, during this project, have physical meaning and are independent of the numerics and discretization levels. These results, also, expand and enhance the mathematical conclusions form the previous chapter, Chapter 4, proving the robustness of the geometrical method. Moreover, from this analysis, the results show that effects of the grid refinement can be comparable to the effects of the Riemann solver and numerical schemes (spatial accuracy). Furthermore, the differences in results of the predicted jet's core length do not invalidate the discretization or numerical methods, as the system of equations that describe the flow field take into account the distance between inertial and non-inertial references systems. The following observations can be made:

- The results of each case have a physical meaningful result, with the accuracy being dependent on the conjugation of the mesh size and spatial order.
- The **CNS3D CBS** Riemann solver captures (slightly) better the physical properties than the **CNS3D HLLC**.
- The **LMC** augmentation effects enhance the **CNS3D** 5^{th}**-order** scheme by improving a uniform dissipation at the lower scales.
- The physical nature of the reconstruction schemes is apparently, with **CNS3D MUSCL** as the most accurate method.
- The **CNS3D** 5^{th}**-order** results with great confidence the physical properties then the **CNS3D** 2^{nd}**-order** and **CNS3D** 9^{th}**-order**.
- As Fourier analysis is concerned, the 2^{nd} and 5^{th} order methods capture the resonance frequency, a unique characteristic of any physical system.

- A possible cause for the effects of jet's buoyancy is directly connected to the effects at the jet exhaust's lip.

Concluding, Figure 5.32, show a series of instantaneous snapshots for the axial velocity (in the medium grid) demonstrating the unsteadiness and uncertainty of the flow field. From the previous observations and analysis, it can be concluded the best cost effective scheme to predict the physical characteristics of a Static Jet is the **CBS** 5^{th}**-order LMC** with a **MEDIUM** discretization level. As a final remark, in Appendix H the complete set of result is presented and can be used as a data base for future references.

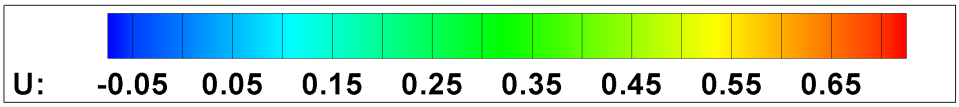

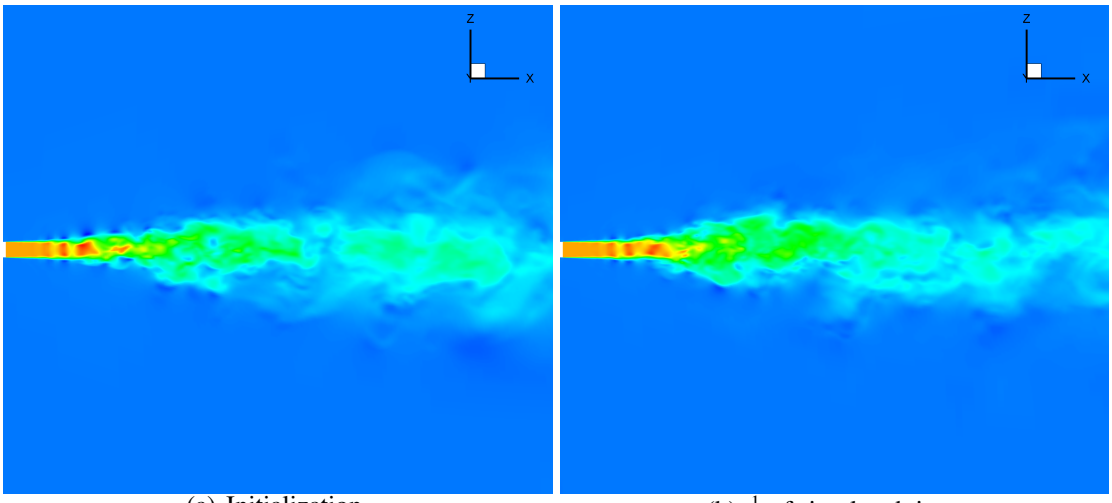

(a) Initialization.

(b) $\frac{1}{3}$ of simulated time.

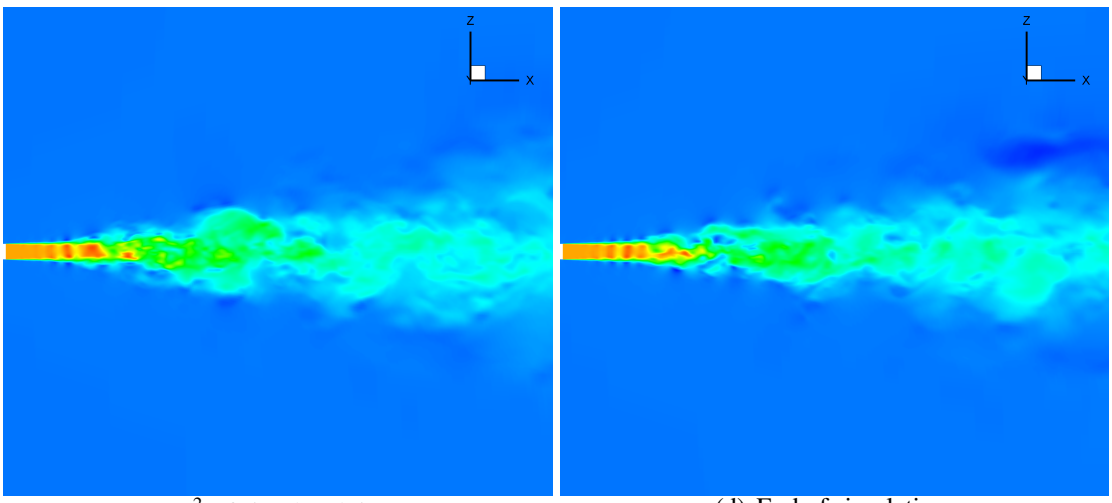

(c) $\frac{2}{3}$ of simulated time.

(d) End of simulation.

Figure 5.32: Instantaneous axial velocity profiles of the static jet.

6
Co-Flow Jet

6.1 Introduction

As it has been shown in Chapter 4 all the methodologies have reached a statistical steady state level, giving mathematical meaning to the obtained results. In this chapter, predictions are made for a jet issuing into a free-stream surrounding, with a small velocity. This case is studied from the physical point of view (velocity, energy and elasticity/plasticity) for the jet's central line, extending the validity of the previous analysis. Moreover the analysis from Chapter 5 is mimicked in this study. The behaviour of the flow in the near-field region is influenced not only by the initial turbulence profiles, usually not known adequately and for this reason not used, but also by the possible formation of orderly structures in the mixing layers at the edges of the potential jet's core (vortical rings) that break down as chaotic structures. The existence of these structures, a non-turbulence phenomenon and not accounted for, may affect the jet development for a significant distance downstream, as it will be seen. Furthermore, the energy partition between the normal components of the Reynolds stresses trough the jet's central line is an indicator of isotropic turbulence. Also, the energy decay rate is analysed for each

methodology. The linear grow of the wake's spreading size, trough the sections profiles, indicates self-similarity behaviour and physical steadiness. Accordingly, comparisons between the different methodologies with experimental data will identify the most efficient and accurate method to predict a high subsonic turbulent jet under a co-flow free stream.

6.2 Methodology and Results

Simulations have been performed for an isothermal, round jet into a co-flow free stream at a Reynolds number of 10000 based on the jet's outlet diameter and velocity ($Ma_{Jet} = 0.9$) at standard sea level, temperature and pressure (Table 4.1). The grids employed, as in the previous chapters, where based on the grids of [110, 119] and clustered according to [122, 123], a detailed description can be seen in Appendix C.

The velocities and stresses along the jet axis and radial sections become adimensional with reference to the axial flow velocity at the jet's geometrical center, ΔU_{Ref}, with $\Delta U = U_{Jet} - U_{\infty}$. The reduced data comparisons are performed from the jet inertial coordinate system (Appendix D). The boundary conditions were set up as inflow for the jet discharge and upstream of the jet exit ($Ma_{\infty} = 0.27 \cdot Ma_{Jet}$); no-slip at the wall of the engine's nozzle, transparent for the domain geometrical singularity and outflow (non-reflective boundary conditions) for the rest of the domain.

The time averaging starts after developing the flow for approximate 1500 time units, and covers 1500 time units, with $\frac{1}{5}$ of the time window spam allocated to the spectral analysis. The h-study is performed with the **HLLC** Riemann solver with the 5^{th}-order **MUSCL** scheme and augmented with **LMC**. For the p-study (*Medium* mesh), a selection of the methods used on the previous chapter (Chapter 4) is employed according to the comparisons to be performed. These comparisons reflect the differences between the **CBS** and **HLLC** Riemann solvers, effects of **LMC** augmentation, limiters and reconstruction schemes (**MUSCL** and **WENO**) and spatial resolution (**Order**). Moreover, on the h and p studies, the Runge-Kutta **TVD** third order time integration has been employed, with **CFL**= 0.5. The comparison results are presented against experimental data from Hot Wire Anemometry (**HWA**) [111] and LASER Doppler Anemometry (**LDA**) [33].

The average velocities and Reynolds stress results (Central Line) in this chapter are compared in the following subsections, h-study and p-study. The scale in the stresses figures is chosen to facilitate a better comparison between each component. An observation should be made for the case of the normal stresses components, by the physical nature of

the flow field and according to [21] it will be only possible to compare the central line values with experimental and numerical reference data from a static jet, even if they are not a good indicator. It is not suitable to use the reference data to analyse the sections results. As an indicator of physical convergence, self-similarity should be achieved trough the jet's wake planes, these results are presented in Appendix F. The normal inertial sections are located at:

- Sections $\frac{X - X_0}{D} = (15, 20, 25)$.

Furthermore, the temporal power spectral density of the Total Kinetic Energy ($E_k(\nu)$) is analysed. The frequency domain (ν) is related to the inverse of the adimensional computational time, with a maximum value proportional to the computational time steep; the scale of power spectrum density is arbitrary and the position of all the different curves have been faithfully reproduced. The probe points encompasses the jet's near-field, transition and far-field regions, over the central line. The location of the probe points are domain's referenced and have the following coordinates:

- $\frac{X}{D} = (0, 5, 10, 15, 20, 25, 30, 35, 40)$.

6.2.1 *h*-study

In this subsection, the ability of each mesh in capturing the physical properties of the flow field is analysed. Self-similarity results, Appendix F Figure F.26, show that the three grids refinements have converged to a physical steady state, reinforcing and confirming the mathematical conclusions for the statistical steady state.

Central Line

Figure 6.1, show the ability of each mesh in capturing the variations of the axial velocity trough the jet's central line. It can be observed for the laminar and transition regions the jet velocity predictions correspond to the experimental result ($0 \leq \frac{X - X_0}{D} \lessapprox 10$). The far-filed back pressure or blockage effects over the jet's size is explained by the ability of each mesh, in combination with the numerical method, in resolving locally the flow field for the break down region of the jet's vortical rings. As it can be seen in Table 6.1, the results for the jet's core are improved with the mesh refinements; also, the jet and free stream induced entrainment effects, by consequence, are correctly balanced out, giving

a velocity gradient similar to the reference one ($14 \lessapprox \frac{X - X_0}{D} \leq 30$) in the *Medium* and *Fine* meshes. The break down of the vortical rings is enhanced by the discretization level, *Fine* case, capturing the oscillatory pattern for the average velocity distribution.

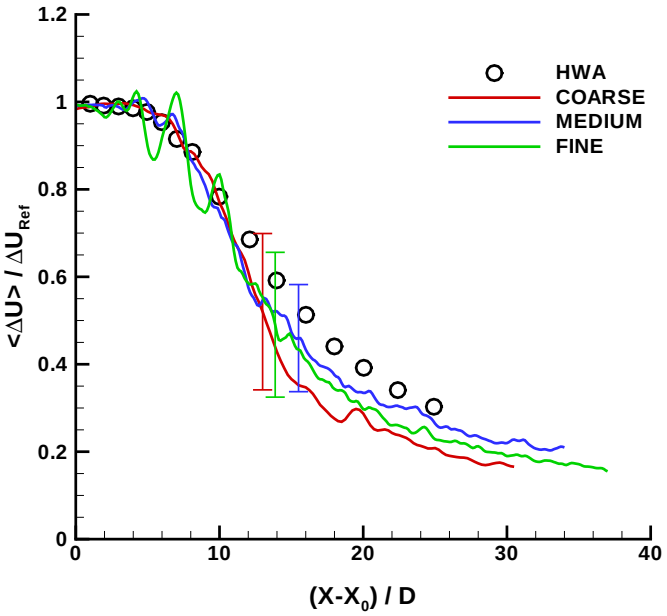

Figure 6.1: Central line velocity results. **HWA**[111].

Figure 6.2, frame *a*, show the effective value for the turbulence intensity for all meshes, with the same peak value location for the *Medium* and *Fine* cases. The remaining frames (*b*, *c* and *d*) shows the central line normal components of Reynolds stresses, from the inertial point of view. Comparisons with experimental data reveals an over prediction for all the three component on the *Coarse* and *Fine* cases, with all the results following the experimental trend. The peak values location, as expected, are located downstream of the reference ones. The partition of energy between the normal stress components, axial and radial, is markedly different in intensity, but proportional between each component (Table 6.1, *Medium* and *Fine* cases) revealing a quasi-isotropic turbulence behaviour with a polarization towards the axial component, as expected. The *Coarse* case, reveals an equal partition of energy between the radial components.

Physical quantities	**Coarse**	**Medium**	**Fine**	**LDA**
X_0	10	6	3	*n.a.*
Maximum error	0.391	0.108	0.245	*n.a.*
u'_{RMS}	0.082	0.075	0.090	*n.a.*
$\langle u'u' \rangle$	0.034	0.030	0.041	0.022
$\langle v'v' \rangle$	0.023	0.015	0.025	0.013
$\langle w'w' \rangle$	0.023	0.022	0.032	0.013

TABLE 6.1: Central line results, peak values. **LDA**[33].

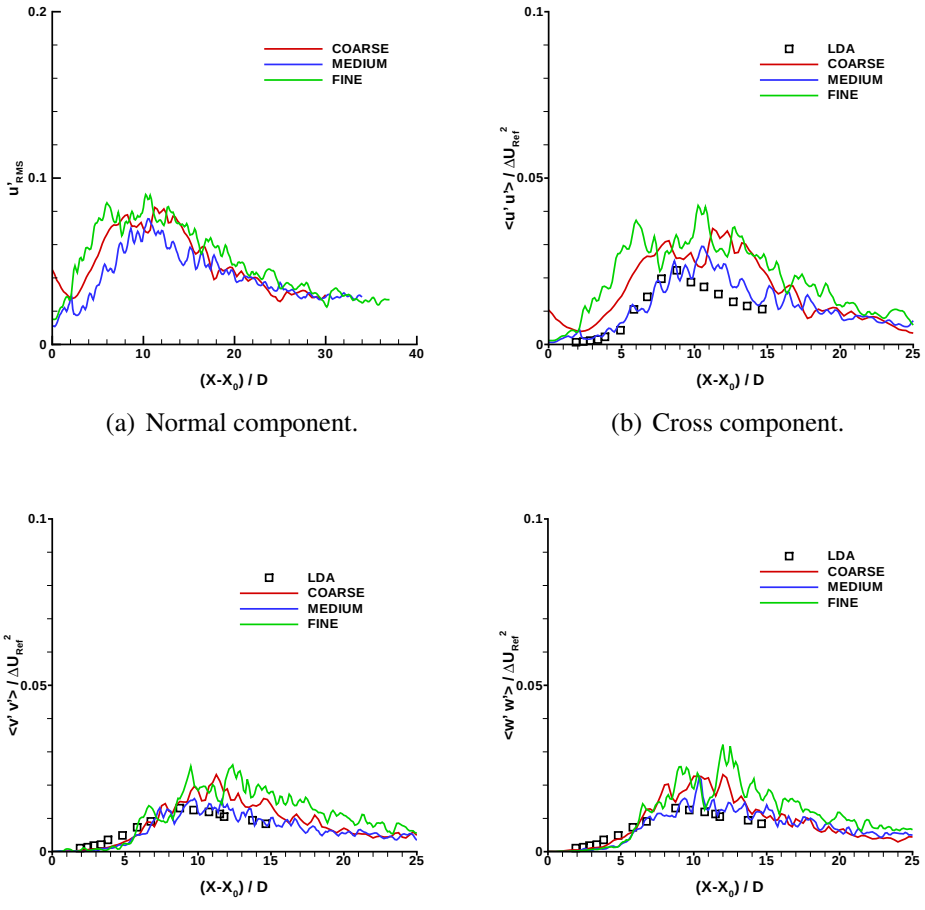

(a) Normal component.

(b) Cross component.

(c) Normal component.

(d) Cross component

FIGURE 6.2: Central line Reynolds stresses results. **LDA**[33].

Summary

The results of this subsection shows strong evidence that the grid and numerics used in this study are good enough for the developed turbulent jet (i.e., after the $3D$ breakdown and

full flow chaotization). The comparison between the predicted and experimental mean flow characteristics and Reynolds stresses in this study reveals a very good agreement for the *Medium* case. For instance, according to the simulations, the center line velocity magnitude comes out with some discrepancies (under prediction) from the reference value but with a similar result in the *Medium* case, the velocity gradient is observed as a lower error. Moreover, the stresses analyses reveals similarities between the *Medium* and *Fine* cases, with the results of the *Medium* case as the closest to the experimental reference data. Therefore, as far as physics is concerned, the *Medium* case captures with accuracy the flow field properties (e.g., from the turbulence point of view, the energy containing motion is captured). With this study, the *Medium* mesh has been selected to perform the *p*-study where the different employed methods are analyticity compared. Furthermore, the predictions of this study show that the azimuthal discretization do not affect the ability in capture the flow field's physical quantities.

6.2.2 *p*-study

From the previous subsection, *h*-study, the medium grid has been selected to perform the *p*-study. The same developed jet initial and boundary conditions have been applied for this study. The previous detailed analysis have been replicated over the flow field and an extended analysis of the power spectrum density for the central line reference probe points, these results will be presented in the following subsection. From all the methodologies used in Chapter 4, a selection will be used to represent the differences between each numerical method/scheme. The following numerical variants employed in this study are:

- The **CBS** Riemann solver with the 2^{nd}-order **MUSCL** scheme and **L**ow-**M**ach **L**imiting, henceforth labelled as '**CNS3D** 2^{nd} **ORDER**'.
- The **CBS** Riemann solver with the 5^{th}-order **MUSCL** scheme and **L**ow-**M**ach **L**imiting, henceforth labelled as '**CNS3D CBS**'.
- The **HLLC** Riemann solver with the 5^{th}-order **HLLC** scheme, henceforth labelled as '**CNS3D** 5^{th} **ORDER**'.
- The **HLLC** Riemann solver with the 5^{th}-order **WENO** scheme, henceforth labelled as '**CNS3D WENO**'.

- The **HLLC** Riemann solver with the 9^{th}-order **WENO** scheme, henceforth labelled as '**CNS3D** 9^{th} **ORDER**'.
- The **HLLC** Riemann solver with the 5^{th}-order **MUSCL** scheme and **L**ow-**M**ach **L**imiting, henceforth labelled as '**CNS3D CBS**, **CNS3D** 5^{th} **ORDER LMC**, **CNS3D MUSCL** and **CNS3D** 5^{th} **ORDER**', accordingly.

As previously mention, the selected methods have reached a self-similar state or physical steadiness. This can be observed in Appendix F(Figure F.30, Figure F.34, Figure F.38, Figure F.42 and Figure F.46), enhancing and extending the mathematical steady state conclusions of Chapter 4.

Riemann Solver

In this analysis, two methods have been selected to compare the differences between the library's Riemann solvers, the **HLLC** and **CBS** 5^{th}-order **MUSCL** augmented with **LMC**, respectively. The comparative study has been performed over the jet's central line, as previously mentioned.

Central Line

Figure 6.3, show the ability of each Riemann solver in capturing the variations in the axial intensity velocity trough the jet's central line. It can be observed for the laminar and transition regions, the jet velocity predictions have an accurate correspondence with the experimental result for the **CNS3D HLLC** case ($0 \leq \frac{X - X_0}{D} \lessapprox 10$). The far-filed back pressure or blockage effects over the jet's size can be explained by the ability of the Riemann solvers in predicting locally the flow field for jet's vortical rings break down region. Also by consequence, the jet's induced entrainment effects can be considered balanced out, giving a velocity gradient similar to the reference one, **CNS3D HLLC** ($15 \lessapprox \frac{X - X_0}{D} \leq 30$).

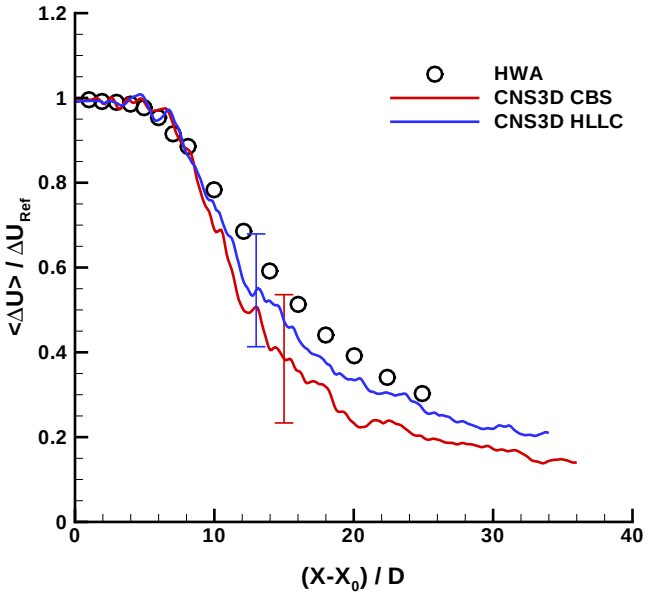

Figure 6.3: Riemann Solver, central line velocity. **HWA**[111].

As it can be seen in Table 6.2, the results for both Riemann solvers reveals a difference of two calibres between them, but with a decrease in error magnitude for the **CNS3D HLLC** case.

Physical quantities	**CNS3D CBS**	**CNS3D HLLC**	**LDA**
X_0	4	6	*n.a.*
Maximum error	0.404	0.108	*n.a.*
u'_{RMS}	0.092	0.075	*n.a.*
$\langle u'u' \rangle$	0.044	0.030	0.022
$\langle v'v' \rangle$	0.040	0.015	0.013
$\langle w'w' \rangle$	0.028	0.022	0.013

Table 6.2: Riemann Solver central line results, peak values. **LDA**[33].

Figure 6.4,frame *a*, show the effective value of the turbulence intensity for the selected cases, with different magnitudes and same peak values location. The remaining frames (*b*, *c* and *d*) presents, from the inertial point of view, the central line Reynolds stresses normal components results. Comparisons with experimental data reveals an over prediction for all the three component in both cases, with the exception in the $\langle v'v' \rangle$ component of **CNS3D HLLC** case. However, the experimental trends can be observed, with the down stream peak value locations being close to the reference ones, radial components. The

partition of energy between the normal stresses components, axial and radial, is proportional in intensity (**CNS3D HLLC**), revealing a quasi-isotropic turbulence behaviour with polarization towards the axial component, as expected. Moreover, the energy partition for **CNS3D CBS** case has the same order of magnitude for $\langle u'u' \rangle$ and $\langle v'v' \rangle$ components, showing a non-axial polarization.

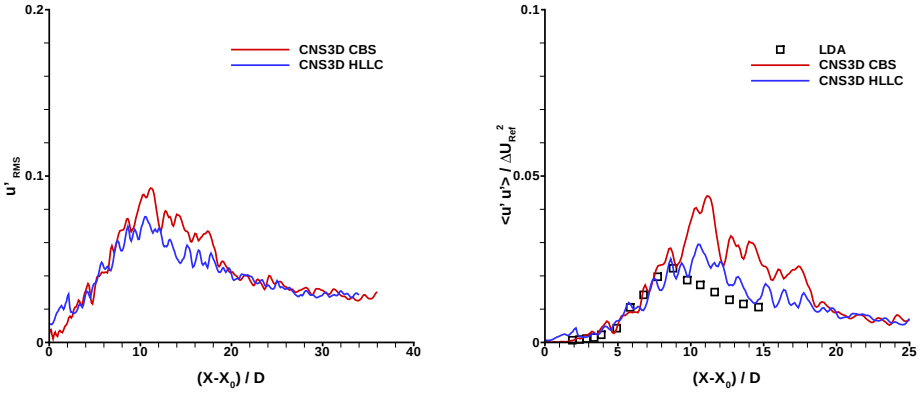

(a) Normal component. (b) Cross component.

(c) Normal component. (d) Cross component

Figure 6.4: Central line Reynolds stresses results. **LDA**[33].

The results of this analysis give strong evidence that the **HLLC** Riemann solver is good enough for the developed turbulent jet. The comparison between the predicted and experimental mean flow characteristics for the Reynolds stresses in this study reveals a very good agreement and accurate prediction for **CNS3D HLLC** case. Therefore, as far as physics is concerned, the **CNS3D HLLC** case captures the flow field properties (e.g., from the turbulence point of view, the energy containing motion is balanced).

Low Mach Number Corrections

To study the effects that the **LMC** have over the flow field two methods have been selected, the **CBS** 5^{th}-order **MUSCL** augmented with **LMC** and the **CBS** 5^{th}-order **MUSCL**, respectively. The jet's central line has been studied, as previously mentioned.

Central Line

Figure 6.5, show the effects of the **LMC** in resolving the variations in the axial intensity velocity trough the jet's central line. It can be observed, for the jet velocity predictions, in the laminar and transition regions a correspondence to the experimental value for the **CNS3D** 5^{th} **ORDER LMC** ($0 \leq \frac{X - X_0}{D} \lessapprox 10$) with a smaller similarity region for **CNS3D** 5^{th} **ORDER** ($0 \leq \frac{X - X_0}{D} \lessapprox 8$). The far-filed back pressure or blockage effects over the jet's size improves with **LMC** augmentation, enhancing the resolution in predicting locally the flow field for the $3D$ break down region of the jet's vortical rings.

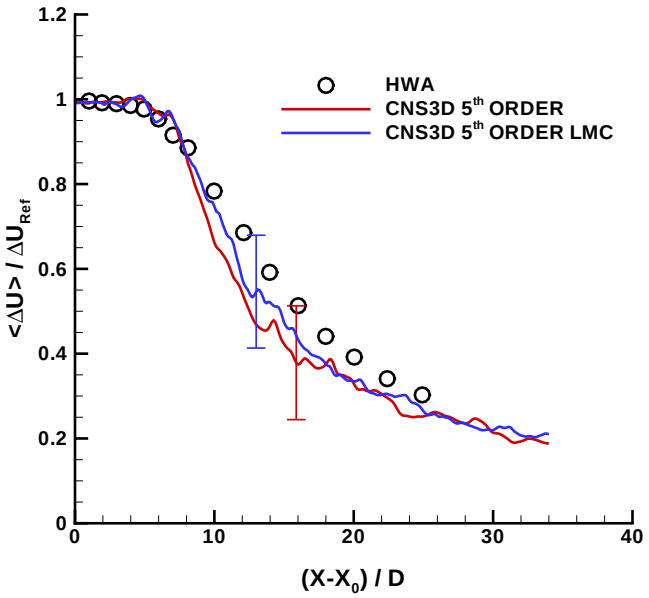

Figure 6.5: Central line velocity results. **HWA**[111].

As it can be seen in Table 6.3. For the velocity gradient, the **CNS3D** 5^{th} **ORDER LMC** case gives a similar value as the experimental one ($14 \lessapprox \frac{X - X_0}{D} \lessapprox 30$). As consequence, the correct jet's induced and free stream entrainment effects are slightly improved by the **LMC** augmentation.

Physical quantities	**CNS3D 5^{th} ORDER LMC**	**CNS3D 5^{th} ORDER**	**LDA**
X_0	6	6	*n.a.*
Maximum error	0.108	0.269	*n.a.*
u'_{RMS}	0.075	0.079	*n.a.*
$\langle u'u' \rangle$	0.030	0.033	0.022
$\langle v'v' \rangle$	0.016	0.035	0.013
$\langle w'w' \rangle$	0.022	0.036	0.013

TABLE 6.3: **LMC** augmentation central line results, peak values. **LDA**[33].

Figure 6.6, frame *a*, show the effective value of the turbulence intensity for the **CNS3D** 5^{th} **ORDER LMC** and **CNS3D** 5^{th} **ORDER** cases. It can be observed a similar trend and intensity, with close peak value locations. The remaining frames (*b*, *c* and *d*) presents, from the inertial point of view, the central line Reynolds stresses normal components results. Comparisons with experimental data reveals an over prediction, except for the $\langle v'v' \rangle$ component of **CNS3D** 5^{th} **ORDER LMC** case, with the same experimental trends. The partition of energy between the normal stress components, axial and radial, is proportional in intensity (**CNS3D** 5^{th} **ORDER LMC**) revealing a quasi-isotropic turbulence behaviour with a polarization towards the axial component, as expected. Moreover, the energy partition for **CNS3D** 5^{th} **ORDER** case is in the same order of magnitude and with the same peak values down stream locations, for axial and radial components, showing an isotropic turbulence behaviour; by exclusion, this result reveals the **LMC** augmentation enhances the resolution of the expected flow field physics, as the radial stress values for the **CNS3D** 5^{th} **ORDER** are clearly over predicted.

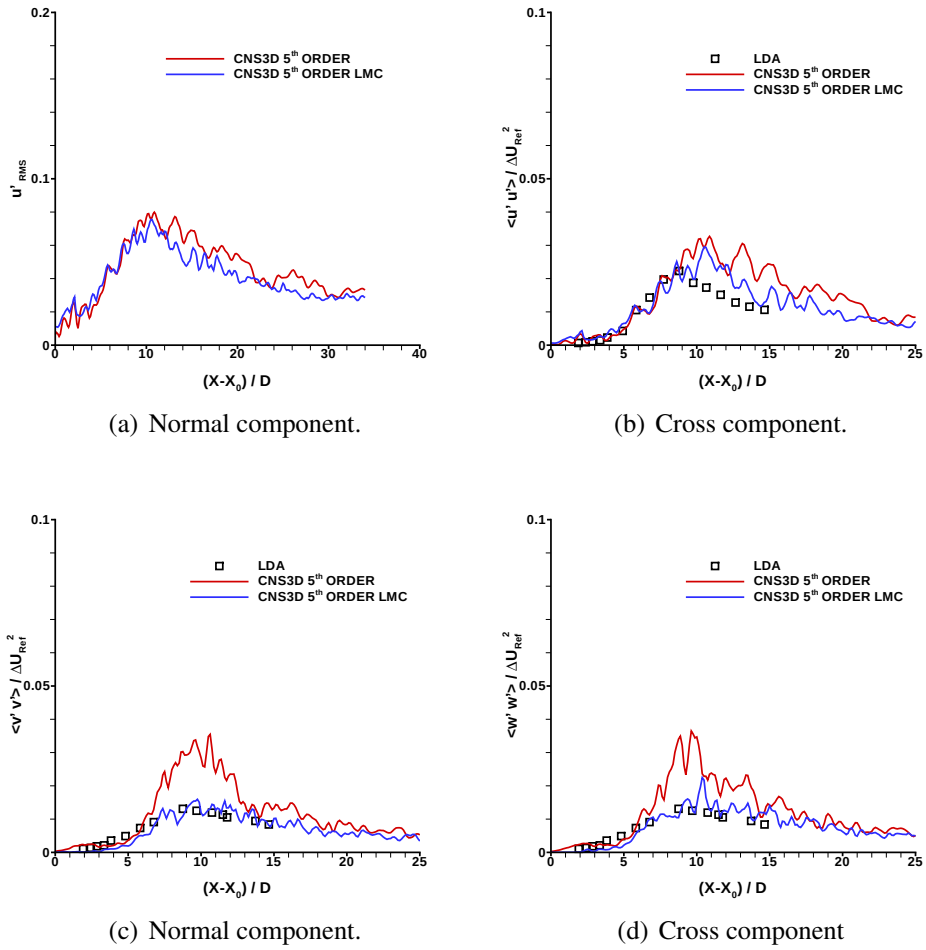

(a) Normal component.

(b) Cross component.

(c) Normal component.

(d) Cross component

FIGURE 6.6: Central line Reynolds stresses results. **LDA**[33].

The results of this analysis gives strong evidence of the **LMC** augmentation effects for the developed turbulent jet. The comparison between the predicted and experimental mean flow characteristics for the Reynolds stresses in this study shows well balanced partition of energy for **CNS3D** 5^{th} **ORDER LMC** case. Therefore, as far as physics is concerned, the **CNS3D** 5^{th} **ORDER LMC** case resolves with confidence the expected flow field properties (e.g., from the turbulence point of view, the energy containing motion is balanced).

MUSCL and WENO

To study of the effects that different reconstruction schemes have over the flow field two methods have been selected, the **HLLC** 5^{th}-order **MUSCL** augmented with **LMC** and the

CBS 5^{th}-order **WENO**, respectively. The comparative study has been performed over the jet's central line, as previously mentioned.

Central Line

Figure 6.7, show the differences between two reconstruction schemes in resolving the variations of the axial intensity velocity trough out the jet's central line. As it can be observed for the flow field laminar and transition regions, the predicted jet velocity distribution correspond to the experimental reference ($0 \leq \frac{X - X_0}{D} \lessapprox 10$), in both cases. The far-filed back pressure or blockage effects over the jet's size are enhanced with **CNS3D MUSCL** case, capturing locally the flow field of the transition region, as it can be seen on Table 6.4. For the velocity gradient the **CNS3D MUSCL** case has a similar value as the experimental reference ($14 \lessapprox \frac{X - X_0}{D} \lessapprox 30$); a similar region exists in the **CNS3D WENO** case, with lower magnitude. As consequence, the jet's induced entrainment in conjunction with the free stream effects can be better resolved by employing the **MUSCL** limiting scheme.

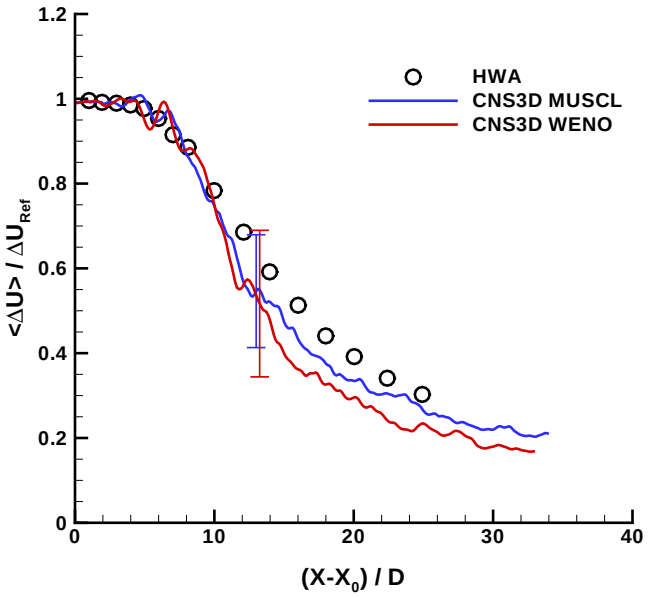

Figure 6.7: Central line velocity results. **HWA**[111].

Physical quantities	**CNS3D MUSCL**	**CNS3D WENO**	**LDA**
X_0	6	7	*n.a.*
Maximum error	0.108	0.299	*n.a.*
u'_{RMS}	0.075	0.089	*n.a.*
$\langle u'u' \rangle$	0.030	0.041	0.022
$\langle v'v' \rangle$	0.015	0.027	0.013
$\langle w'w' \rangle$	0.022	0.030	0.013

Table 6.4: Reconstruction schemes central line results, peak values. **LDA**[33].

Figure 6.8, frame *a*, show the effective value of the turbulence intensity for the selected methods. It can be observed a difference in trend ($6 \leq \frac{X - X_0}{D} \lessapprox 10$) and different magnitudes with the same peak value locations. The remaining frames (*b*, *c* and *d*) presents, from the inertial point of view, the central line Reynolds stresses normal components. Comparisons with experimental data reveals an over prediction for all the three component in the **CNS3D WENO** case. However, the experimental trends can be observed for both cases, with the exception of the axial component of **CNS3D WENO** case. The partition of energy between the normal stress components, axial and radial, is proportional in intensity. A proportional partition of energy in both cases reveals a quasi-isotropic turbulence behaviour with polarization towards the axial direction, as expected. Moreover, the **CNS3D MUSCL** results show are in agreement with the expected reference values.

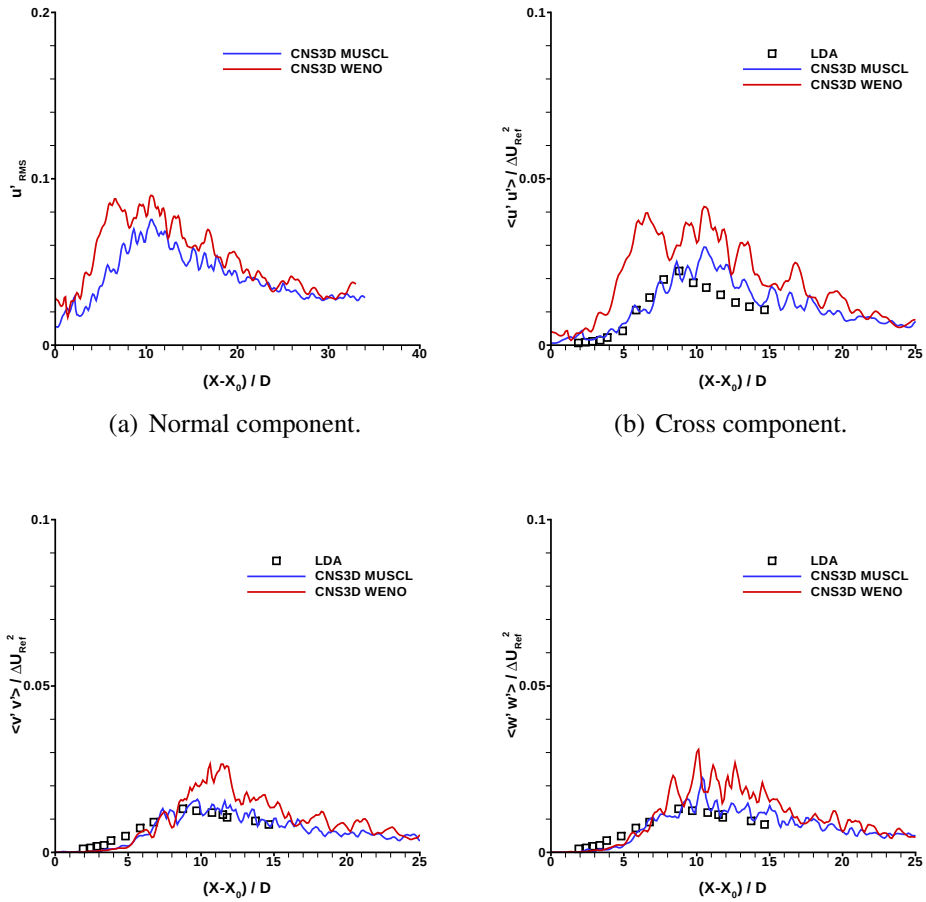

(a) Normal component.

(b) Cross component.

(c) Normal component.

(d) Cross component

Figure 6.8: Central line Reynolds stresses results. **LDA**[33].

The results of this analysis gives strong evidence of the **MUSCL** limiting scheme to predict more accurately the effects for the developed turbulent jet. Comparison between the predicted and experimental mean flow characteristics for the Reynolds stresses in this study agrees for **CNS3D MUSCL** case. Therefore, as far as physics is concerned, the **CNS3D MUSCL** case captures with confidence the flow field properties (e.g., from the turbulence point of view, the energy containing motion is balanced).

High-Order

To study of the effects that different spatial high-order reconstruction schemes have over the flow field three methods have been selected, the **CBS** 2^{nd}-order **MUSCL** augmented with **LMC**, the **HLLC** 5^{th}-order **MUSCL** augmented with **LMC** and **HLLC** 9^{th}-order

WENO, respectively. The comparative study has been performed over the jet's central line, as previously mentioned.

Central Line

Figure 6.9, show the differences between three high-order reconstruction schemes in resolving the variations of the axial velocity intensity trough the jet's central line. As it can be observed for the laminar and transition regions, the jet velocity predictions correspond to the experimental reference ($0 \leq \frac{X - X_0}{D} \lessapprox 10$), **CNS3D** 5^{th} **ORDER** and **CNS3D** 9^{th} **ORDER** cases. The far-filed back pressure or blockage effects over the jet's size has been improved with the numerical schemes' spatial order, capturing accurately the local flow field of the vortical rings $3D$ break down region, as it can be seen in Table 6.5. For the velocity gradient, the **CNS3D** 5^{th} **ORDER** and **CNS3D** 9^{th} **ORDER** cases gives similar values as the experimental reference ($14 \lessapprox \frac{X - X_0}{D} \lessapprox 30$). Consequently, the correct effects for the flow induced entrainment and free stream can be better predicted with the use of a 5^{th}-order scheme.

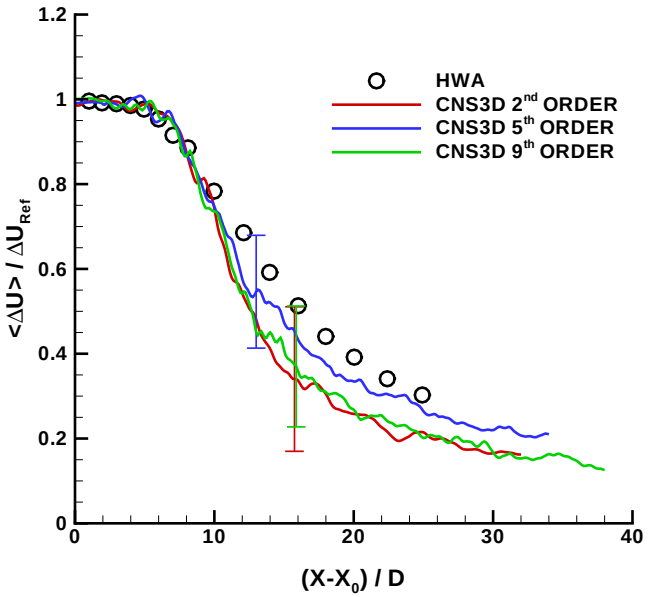

Figure 6.9: Central line velocity results. **HWA**[111].

Physical quantities	2^{nd} **ORDER**	5^{th} **ORDER**	9^{th} **ORDER**	**LDA**
X_0	8	6	2	*n.a.*
Maximum error	0.422	0.108	0.335	*n.a.*
u'_{RMS}	0.097	0.075	0.094	*n.a.*
$\langle u'u' \rangle$	0.040	0.030	0.046	0.022
$\langle v'v' \rangle$	0.038	0.015	0.033	0.013
$\langle w'w' \rangle$	0.028	0.022	0.034	0.013

TABLE 6.5: Spatial resolution central line results, peak values. 2^{nd} **ORDER** is the **CNS3D** 2^{nd} **ORDER**, 5^{th} **ORDER** is the **CNS3D** 5^{th} **ORDER**, 9^{th} **ORDER** is the **CNS3D** 9^{th} **ORDER** and **LDA**[33].

Figure 6.10, frame *a*, show the effective value of the turbulence intensity for the selected schemes. As it can be observed similarity in trends exists in the three cases. The 2^{nd}-order and 9^{th}-order cases have similar values with correspondence down stream peak value locations in the 2^{nd}-order and 5^{th}-order cases. The remaining frames (*b*, *c* and *d*) presents, from the inertial point of view, the central line Reynolds stresses normal components. Comparisons with experimental reference data reveals an over prediction for all the three component in the 2^{nd}-order and 9^{th}-order cases. However, the experimental trends can be observed for all cases. The partition of energy between the normal stress components, axial and radial, is proportional in intensity values with polarization in the axial direction, as expected. Moreover, for **CNS3D** 5^{th} **ORDER** case, the ratios of energy partition between radial and axial components is similar to the experimental ratio.

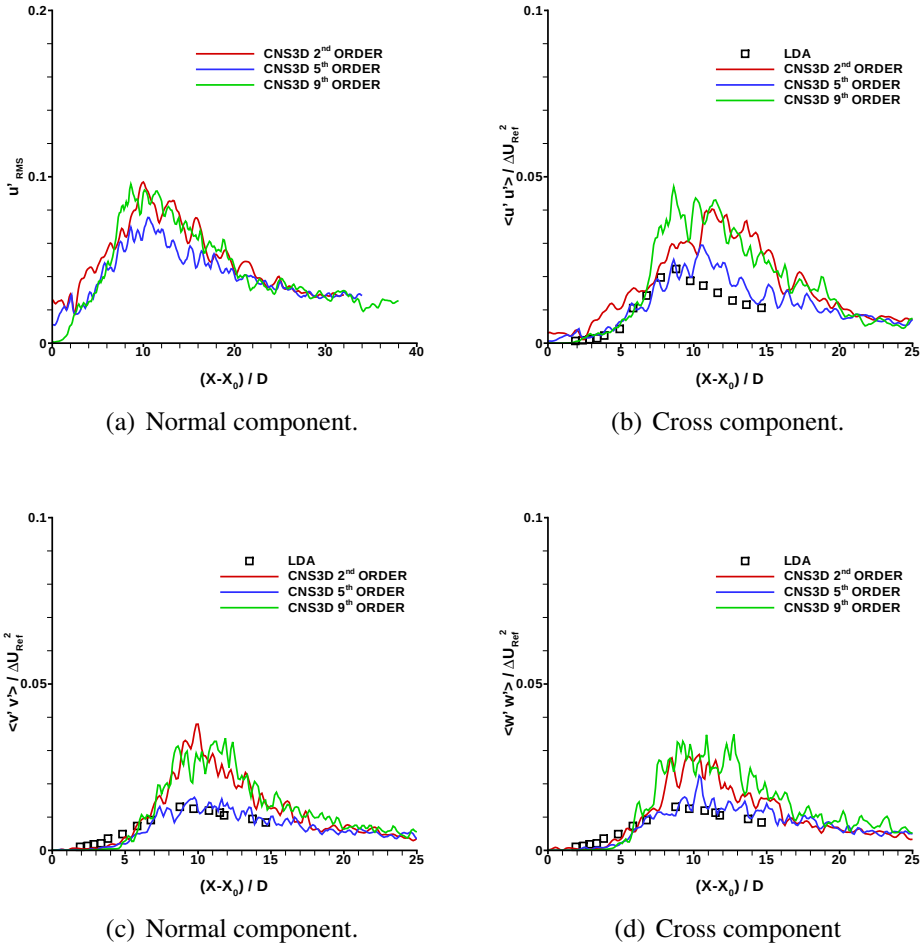

(a) Normal component.

(b) Cross component.

(c) Normal component.

(d) Cross component

FIGURE 6.10: Central line Reynolds stresses results. **LDA**[33].

The comparison between the predicted and experimental mean flow characteristics for the Reynolds stresses in this study reveals the 5^{th}-order method as the most accurate. Therefore, as far as physics is concerned the **CNS3D** 5^{th} **ORDER** case captures with confidence the flow field properties (e.g., from the turbulence point of view, the energy containing motion is well balanced).

Summary

The results of this subsection shows strong evidence that the numerics used in this study are good enough for the developed turbulent co-flow jet (i.e., after the $3D$ breakdown and full flow chaotization). The correlation between the predicted and experimental mean flow characteristics for the Reynolds stresses in this study agrees for the **HLLC** Riemann

solver with the 5^{th}-order **MUSCL** scheme augmented with **LMC**. For instance, according to the simulations, the center line velocity comes out with some discrepancies from the reference values, but with a more accurate result. The partition of energy between the Reynolds stresses, normal components, is closer and proportional the experimental data, as expected.

6.2.3 Spectral analysis

Finalizing the physical study (velocity and Reynolds stresses) of the previous subsection, p-study, the total kinetic energy frequency spectra ($E(\nu)$) will be presented for the jet's axial distance (Central Line), with the correspondent periodgrams (ν vs ϕ) and temporal total kinetic energy ($E(T)$) in Appendix G, for all the selected numerical variants. As described in Section 1.2, the spectrograms interpretation indicate the jet's flow field characteristics, this is physically appealing and can be of great help in inferring the flow field properties. From the results of [33, 113, 114] (jet cross section) it is possible to make a qualitative comparison for the jet's core region ($0 \leq \frac{X}{D} \lessapprox 5$), assuming for that reason a similar physical behaviour between radial and axial directions. The slopes, in the following figures, represent the evolution of the energy decay rate trough out the jet's down stream flow field. As upper slope limit, the local isotropy hypothesis (Kolmogorov [38, 39] $-\frac{5}{3}$ decay rate) is used as asymptotic reference, where the small eddies in the flow are statistical independent in preferred directions of the large eddies.

Figure 6.11, Figure 6.12 and Figure 6.13, shows the evolution of the spectral energy trough the jet's central line. It can be observed as the axial position is increased, the amplitude values of the production region also increase, reaching a approximate level for the jet's transition region ($\frac{X}{D} \geq 10$). For the far-field region ($30 \leq \frac{X}{D} \leq 40$), the amplitude production region shrinks, in size, and are almost non-existent for the farthest probe points, the jet's effects are no longer relevant, or in other words, the flow field energy can be consider purely inertial by the entrainment effects of the free stream. From the dissipation point of view, it can be noticed the change in slope trough out the jet's central line. Starting from the jet's discharge and moving down stream, the low frequencies states are exited on the production region with no associated dissipation, a high intensity peak in frequency is observed followed by a drop in amplitude; the spectral energy values at frequencies higher then the peak ones are consider as background noise ($\frac{X}{D} = 0$), this can be confirmed by the randomness in phase, figures for the correspondent point

in Appendix G, with a pattern that can be traced to the physical characteristics of each numerical method associated to the correspondent cell size. Furthermore, the remaining spectrograms points reveals a transfer of energy from lower to the higher frequencies states, with the changing in dissipation rates towards the asymptotic value, as the higher frequencies become more exited. The observed trends are explained by the population of the high frequencies states at the expenses of the low frequency states, meaning a surging in energy from the lower to the higher states. Moreover, as the production states and lower frequencies becomes unexcited, the dissipation rate changes away from the asymptotic reference level, populating them the higher frequency states until the energy is dissipated as heat, at viscous level.

Table 6.6, reveals the spectral peak frequency to be in accordance with the yielding experimental Strouhal number (**St** = 0.5 [33]) and in same order of magnitude with the predicted resonant frequency, for this class of flows. The difference between the simulated results and experimental one can be explained by the different down stream probe locations, but still inside of the jet's core (laminar region). However, the predicted Strouhal numbers are inside the experimental numerical range, the **HLLC WENO** 9^{th}**-order** case give an exact value.

Numerical schemes	ν_{Max}	**St**
HLLC MUSCL 5^{th}**-order LMC**	108	0.44
CBS MUSCL 5^{th}**-order LMC**	110	0.45
HLLC MUSCL 5^{th}**-order**	97	0.39
HLLC WENO 5^{th}**-order**	98	0.40
CBS MUSCL 2^{nd}**-order LMC**	98	0.40
HLLC WENO 9^{th}**-order**	118	0.50

Table 6.6: Resonant frequencies at $\frac{X}{D} = 5$ and correspondent Strouhal numbers.

From this analysis, it is possible to conclude that all the selected methods are able to describe the evolution of the energy dissipation decay trough out the jet's central line. Moreover, the resonant frequency of the system is accurately predicted for all the methods. Furthermore, the total kinetic energy decay rate is in accordance to the theoretical and experimental results.

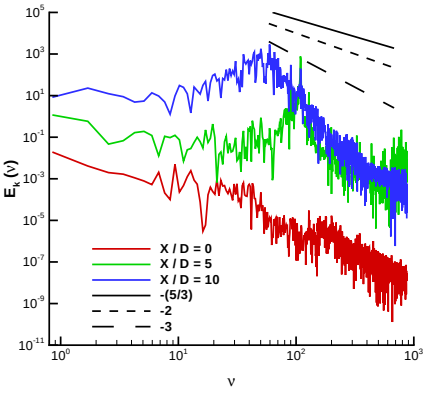

(a) **HLLC MUSCL 5^{th}-order LMC**.

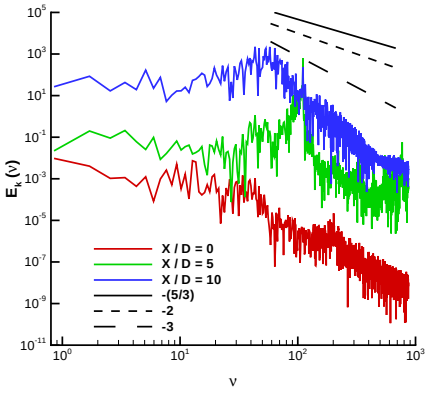

(b) **CBS MUSCL 5^{th}-order LMC**.

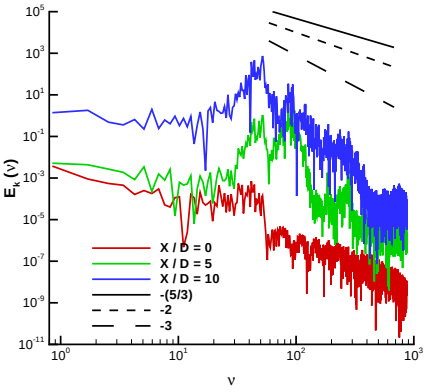

(c) **HLLC MUSCL 5^{th}-order**.

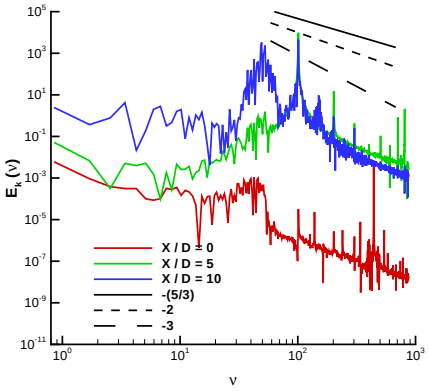

(d) **HLLC WENO 5^{th}-order**.

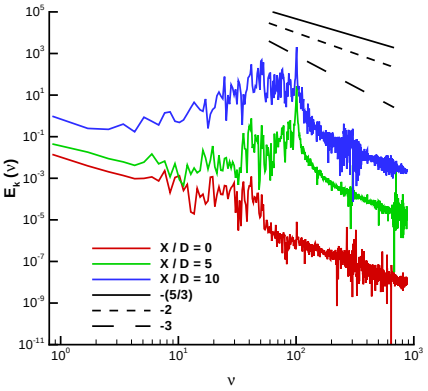

(e) **CBS MUSCL 2^{nd}-order LMC**.

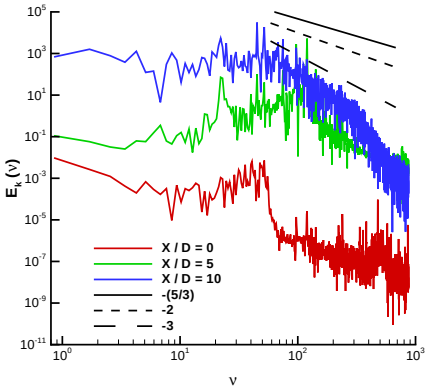

(f) **HLLC WENO 9^{th}-order**.

FIGURE 6.11: Central line kinetic energy spectrograms, points $\frac{X}{D} = (0, 5, 10)$.

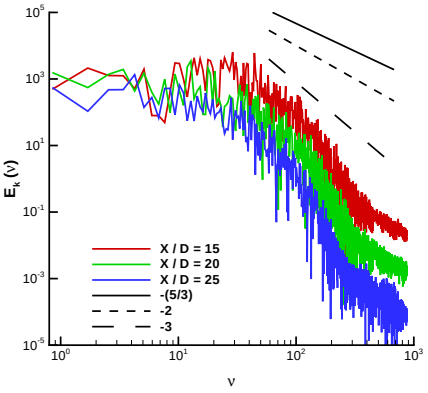

(a) **HLLC MUSCL 5^{th}-order LMC**.

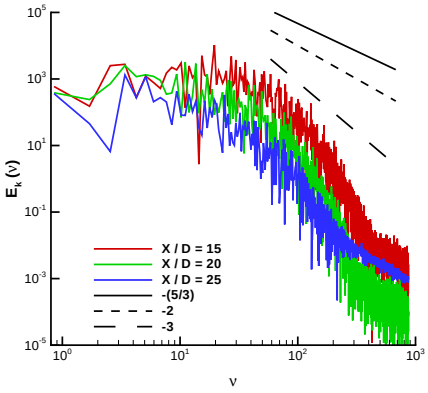

(b) **CBS MUSCL 5^{th}-order LMC**.

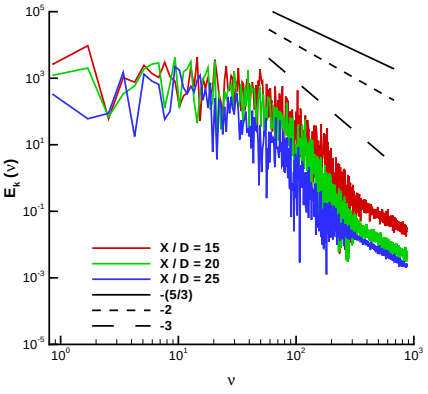

(c) **HLLC MUSCL 5^{th}-order**.

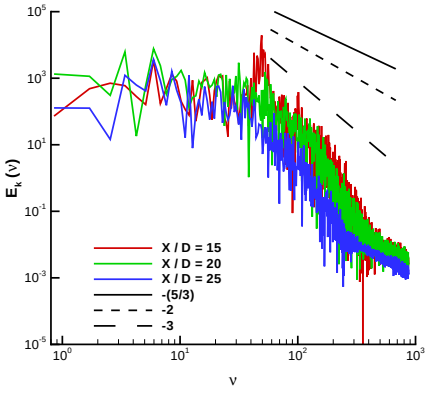

(d) **HLLC WENO 5^{th}-order**.

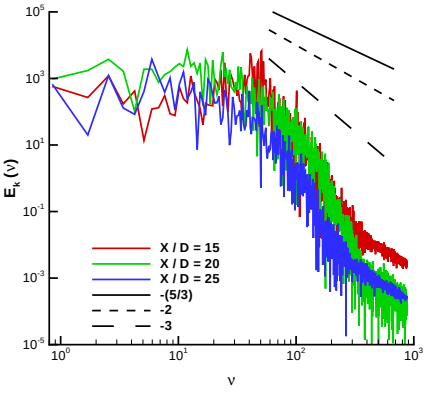

(e) **CBS MUSCL 2^{nd}-order LMC**.

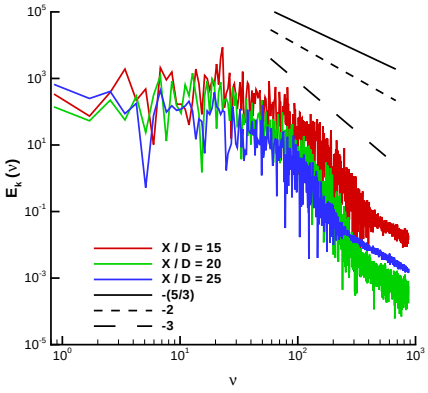

(f) **HLLC WENO 9^{th}-order**.

Figure 6.12: Central line kinetic energy spectrograms, points $\frac{X}{D} = (15, 20, 25)$.

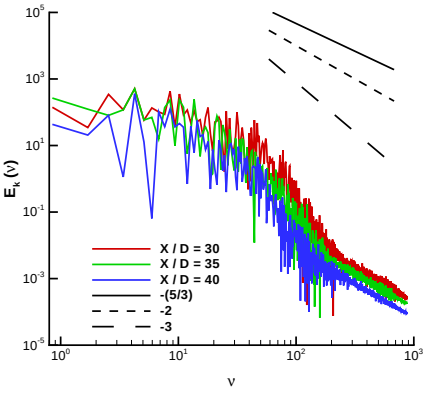

(a) **HLLC MUSCL 5^{th}-order LMC**.

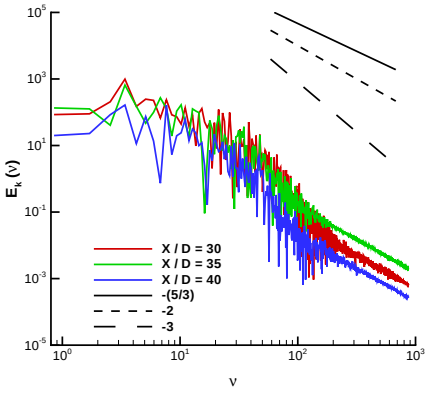

(b) **CBS MUSCL 5^{th}-order LMC**.

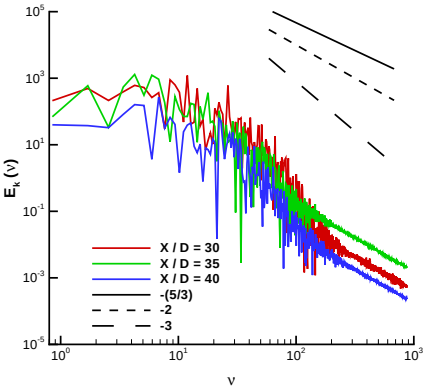

(c) **HLLC MUSCL 5^{th}-order**.

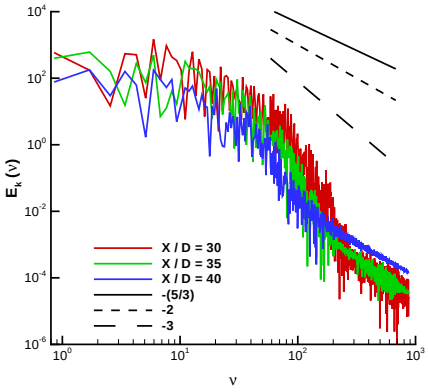

(d) **HLLC WENO 5^{th}-order**.

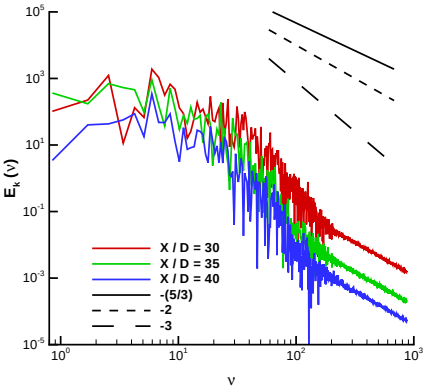

(e) **CBS MUSCL 2^{nd}-order LMC**.

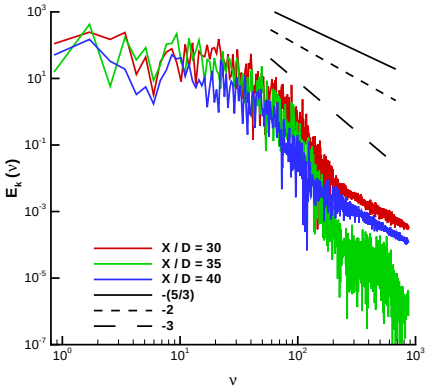

(f) **HLLC WENO 9^{th}-order**.

Figure 6.13: Central line kinetic energy spectrograms, points $\frac{X}{D} = (30, 35, 40)$.

6.3 Discussion

In this chapter, the study of different methodologies in simulating a high subsonic jet issuing into a free stream with a small velocity has been presented. It is suggested the corrections and reviews done on the flow solver, during this study, have physical meaning and are independent of the numerics and discretization levels. These results, also, expand and enhance the mathematical conclusions form the previous chapter, Chapter 4, proving the robustness of the geometrical method. Moreover, from this analysis, the results show that effects of the grid refinement can be comparable to the effects of the Riemann solver and numerical schemes (spatial accuracy). Furthermore, the differences in results of the predicted jet's core length do not invalidate the discretization or numerical methods, as the system of equations that describe the flow field take into account the distance between inertial and non-inertial references systems. The following observations can be made:

- The results of each case have a physical meaningful result, with the accuracy being dependent on the conjugation of the mesh size and spatial order.
- The **CNS3D HLLC** Riemann solver captures better the physical properties than the **CNS3D CBS**.
- The **LMC** augmentation effects enhance the **CNS3D** 5^{th}**-order** scheme by improving a uniform dissipation at the lower scales.
- The physical nature of the reconstruction schemes is apparently, with **CNS3D MUSCL** as the most accurate method.
- The **CNS3D** 5^{th}**-order** results captures with great confidence the physical properties then the **CNS3D** 2^{nd}**-order** and **CNS3D** 9^{th}**-order**.
- As Fourier analysis is concerned, all the methods capture the resonance frequency, a unique characteristic of any physical system.

Concluding, Figure 6.14, show a series of instantaneous snapshots for the axial velocity (in the medium grid) demonstrating the unsteadiness and uncertainty of the flow field. From the previous observations and analysis, it can be concluded the best cost effective scheme to predict the physical characteristics of a Co-flow jet is the **HLLC** 5^{th}**-order LMC** with a **MEDIUM** discretization level. As a final remark, in Appendix H the complete set of result is presented and can be used as a data base for future references.

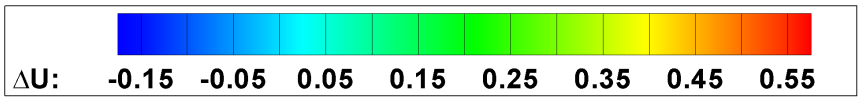

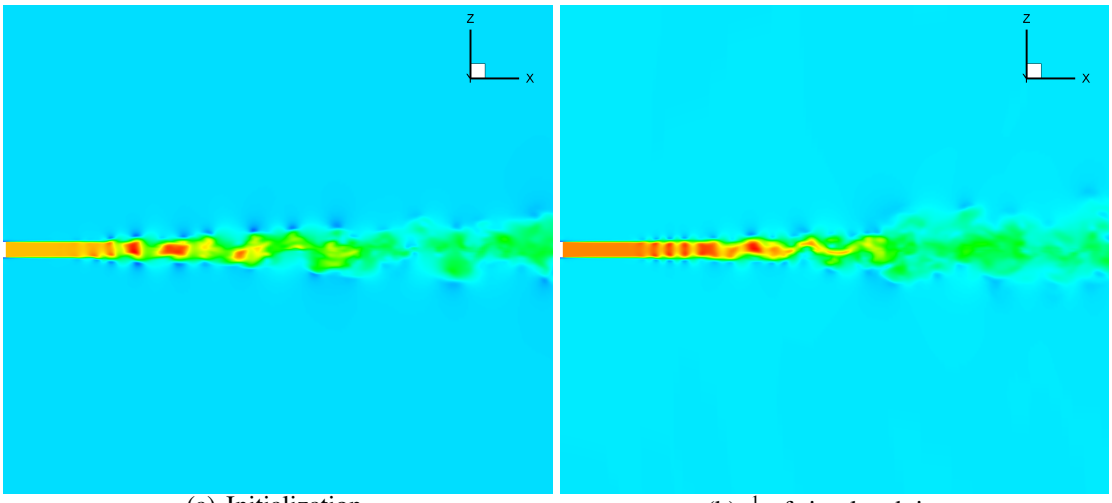

(a) Initialization.

(b) $\frac{1}{3}$ of simulated time.

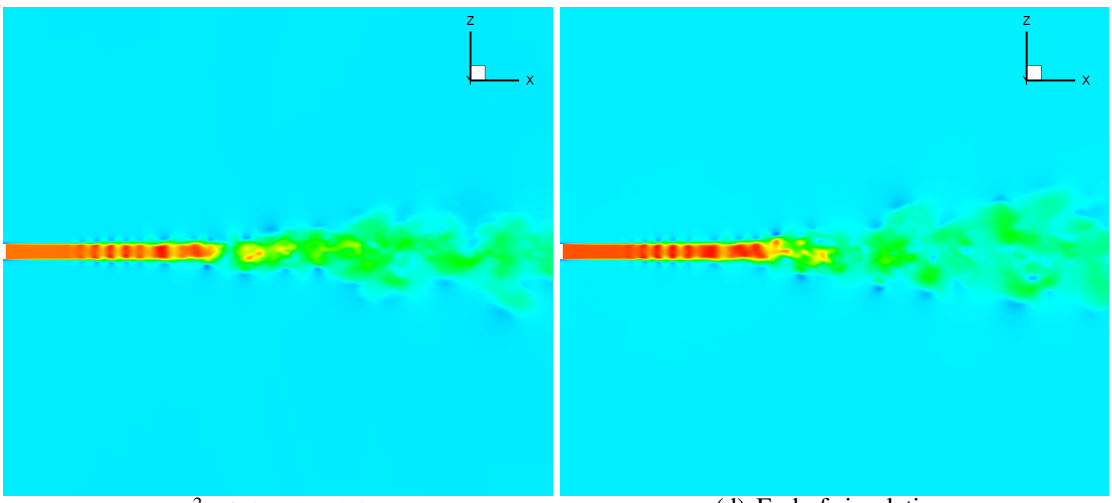

(c) $\frac{2}{3}$ of simulated time.

(d) End of simulation.

Figure 6.14: Instantaneous axial velocity profiles, co-flow jet.

Conclusions

7 Conclusions

The work completed in this thesis covered a wide range of numerical methods into simulating the behaviour of free shear layer flows (turbulent jet flows), using high-resolution methods in the context of Implicit Large Eddy Simulations (**ILES**). Improvements and reviews of the flow solver methods were performed without changing the context of **ILES**. The resulting findings and conclusions made will be presented in the following section, followed by recommendations for future work that may help in obtaining a deeper understanding of the solutions and results provided by using high-order and high-resolution methods and their inherent turbulence predicting capabilities with the hope of further improving them.

7.1 Conclusion of Work

Simulations based on the compressible **NSE** equations using high-order and high-resolution methods were carried out. No **SGS** turbulence model has been used as the aim of the investigation was to examine the **ILES** ability to successfully predict the behaviour of free shear flows under different flow regimes.

It has been demonstrated that by changing from the algebraic to the geometrical method, singularity correction (Jacobian of the Transformation) augmented with transparent boundary condition, the flow solver simulations can accurately predict with high confidence the flow field behaviour, without lost of accuracy, at different flow regimes and in the presence of sharp discontinuities (**CDN** test case). Furthermore, the review of the reconstruction schemes (**WENO**) has been performed with success and confirmed with Shock tube test cases (standard and $3D$). The study, later test case applied to the different methods, assures physical meaning to the flow field's central line results under the singularity correction influence. These changes (Chapter 3) enhances the flow solver robustness and increase the range of applicability to science and engineering problems of interest.

From the main part of this research, the fully developed turbulent jet flow (Ma_{Jet} = 0.9) issuing into a stagnant free stream ($Ma_\infty = 0$) and with a small free-stream velocity ($Ma_\infty = 0.27 \cdot Ma_{Jet}$), for which no current compressible **ILES** investigation has been conducted, under the current discretization of volume of interest (axisymmetric mesh). This study was concerned with the numerical ability in predicting a variety of complex flow phenomenon such as free shear layers development, interaction and break down. From the physical characterization (Velocity profiles, Reynolds stresses and Strouhal number), reduction to the jet's inertial reference system (jet core size) and buoyancy, the following conclusions can be made:

- Introduction of the error bar computation concept, for unsteady and time explicit simulations, with success. The need of proper amalgamation of results to construct an interval of trust to be superimposed on the possible average result. The average result augmented by the error bar generates a possible envelope with physical meaning. (Chapter 4)

- From the Static and Co-flow Jets, h-studies (Chapter 5 and Chapter 6), the $Medium$ discretization level yields the most accurate and less expensive predictions in comparison with the $Fine$ discretization level, that do not improve significantly (Static Case) and degrade considerably (Co-flow Case) the results.

- From the p-studies, Static and Co-flow Jets (Chapter 5 and Chapter 6), the reduced data analysis reveals:

  - Similarity of results between Riemann solvers (Static Case) and a more accurate prediction for the **HLLC** Riemann solver (Co-Flow Case).
  - The **LMC** augmentation in conjunction with the **MUSCL** 5^{th}**-order** scheme clearly shows a physical behaviour in both test cases.
  - For the same order of spatial accuracy and resolution, some differences in results for the Static Jet case can be observed between the **MUSCL** limiter and the **WENO** reconstruction schemes, while the Co-flow case clearly shows the **MUSCL** limiter predictions as the most accurate.
  - Concerning the high-order reconstruction schemes, it can be concluded that the results of the 2^{nd}**-order** order scheme are comparable to the *Coarse* mesh results, also, the 9^{th}**-order** scheme in the *Medium* mesh is comparable to the *Fine* mesh results, for both jet cases.

- Comparisons with experimental and empirical Strouhal number (jets near-fields) reveal the resonant frequency for this kind of systems is in accordance with the empirical results (Static Jet) and experimental results (Co-flow Jet). Furthermore, the evolution of the spectral total kinetic energy trough out the jet's central line fulfil the current understanding of energy decay rate, for the employed numerical methods.

- From the spectral analysis of the jets exhaust lip (Static Jet), it has been possible to deduct and conclude a possible reason for the buoyancy characteristic of jets wakes, as this kind of behaviour is a cause-effect interaction between the jet wake and free stream induced entrainment.

- Finalizing this study, it is possible to conclude the most efficient scheme to be employed to simulate a high subsonic turbulent jet is the **CBS MUSCL** 5^{th}**-order LMC** numerical scheme (Static Jet) and the **HLLC MUSCL** 5^{th}**-order LMC** numerical scheme (Co-flow Jet), in conjunction with a *Medium* discretization level.

As a final remark, converged and numerically stable solutions which predicts with some degree of trust the flow field characteristics and have achieved mathematical steadiness, by using higher-order statistics (Skewness and Kurtosis), do not always represents the natural behaviour of the flow, accurately. However, those predictions yield quasi-physical behaviour for the average velocities and Reynolds stresses, even when the predicted results have achieved similarity between wake profiles. Which highlights that the

main challenge of **ILES** is to provide not low, but rather adequate dissipation.

7.2 Future Work

In retrospect, the research detailed in this thesis has opened up several areas for future work. Several lessons have been learnt and more work needs to be done, primarily in order to control the computational cost of turbulent jet flows simulations, featuring free shear layers. The use of higher order methods allows for a significant reduction of grid cells trough out the domain. Therefore, the main focus in the future should be the development of a reliable strategy that covers both jet and wake flow conditions. Regarding the development of free shear layers, more fundamental studies are necessary to determine the exact requirements of different numerical methods for producing realistic results. It has been shown that the jet vortical ring production/break up regions and subsequent turbulent mixing (back pressure/blockage effect) strongly depends on the order of the scheme employed in conjunction with the grid resolution available. Here, comparisons with **DNS** and experimental data for relatively simple geometries are desirable, in particular for the Co-flow Jet case. In the context of free shear layer flows, an investigation of swirling, oscillating or a jet flow issuing into a cross free stream flow, with a small angle of incidence, could offer valuable insight and may be proposed. Another strategy that can be adopted, is the issuing of a jet with an inner boundary layer profile into a free stream. The previous recommendations, also allow, possible extension towards the verification and validation of the central lines' singularity corrections, implemented during this research.

Finally, extending the comparative study (Static and Co-flow Jets), by using the **LMC** augmentation in conjunction with the **WENO** 5^{th}**-order** scheme, to observe the effects and enhancements over the flow field resolution. Moreover, it is advise to compare the **WENO** 9^{th}**-order** scheme to it's counter part (**MUSCL** 9^{th}**-order** scheme) using both Riemann solvers (**CBS** and **HLLC**).

This research can lead, ultimately, to the development of an adequate turbulence-resolving "model" which ensures that numerical dissipation is correctly provided and in which is capable of accurately captures the physical flow field behaviour.

Appendices and References

References

[1] G. Falkovich and K. R. Sreenivasan. *Lessons from hydrodynamic turbulence*. Physics Today **59**(4), 43 (2006).

[2] S. B. Pope. *Turbulent flows* (Cambridge University Press, 2000).

[3] M. K. Stoellinger, C. P. Zemtsop, S. Heinz, and D. Stanescu. *A rans-les study of swirling and non-swirling jets*. AIAA (0925) (2007).

[4] R. Gleissl, R. M. Deslandes, and A. Baeten. *Assessment of missile plume impact characteristics*. AIAA (0675) (2007).

[5] S. Kawai and K. Fujii. *Computational analysis of the characteristics of subsonic, transonic and supersonic base flows*. AIAA (5156) (2005).

[6] K. D. Kennedy, B. J. Walker, M. C. DeMagistris, and J. L. Papp. *Tactical missile exhaust plume at angle of attack*. AIAA (3925) (2004).

[7] U. C. Glodberg, J. J. Gorski, and S. R. Chakravarthy. *Transonic turbulent flow computations for axisymmetric afterbodies*. AIAA (1465) (1985).

[8] B. Grossman and R. E. Melnik. *The numerical computation of the transonic flow over afterbodies including the effect of jet-plume and viscous interactions*. AIAA (0062) (1975).

[9] R. H. Adams. *Wind tunnel testing techniques for gas-particle flows in rocket exhaust plumes*. AIAA (0767) (1966).

[10] G. Avital, J. Pompan, J.Macales, S. Yaniv, and S. Gali. *Experimental and cfd study of rocket plume effects on missile longitudinal aerodynamic stability*. AIAA (5196) (2004).

[11] B. B. Roberts, R. O. Wallace, M. K. Craig, and D. Kanipe. *Rocket exhaust plume induced flowfield interaction experiences with the space shuttle*. AIAA (1549) (1983).

[12] C. R. James. *Aerodynamics of rocket plume interactions at supersonic speeds*. AIAA (1905) (1981).

[13] I.-S. Chang. *Unsteady-state underexpanded jet flows*. AIAA (3885) (2002).

[14] N. Sinha, D. Kenzakowski, J. Papp, and B. York. *Particulate dispersion in rocket exhaust plumes*. AIAA (4289) (2002).

[15] T. J. Birch, I. E. Wrisdale, and S. A. Prince. *Cfd predictions of missile flowfields*. AIAA (4211) (2000).

[16] S. M. Dash and D. C. Kenzakowski. *Turbulent aspects of plume aerodynamic interactions*. AIAA (2373) (1995).

[17] S. M. Dash. *Observations on practical turbulence modeling for high-speed jet/-plume flowfields*. AIAA (1789) (1991).

[18] B. S. Massey. *Mechnics of Fluids* (Chapman and Hall, 1989), 6th ed.

[19] C. R. Bobba, E.Venkatapathy, A. Krothapalli, J. H. DeHart, and D. P. Wishart. *Structure of supersonic plumes: Computations and measurements*. AIAA (0718) (1995).

[20] F. Grinstein, M. Glauser, and W. K. George. *Fluid Vortices*, chap. 3, pp. 65–94 (Kluwer Academic Publishing, 1995).

[21] S. F. Birch. *A review of axisymmetric jet flow data for noise applications*. AIAA (2602) (2006).

[22] R. A. White, J. Argrell, and S. E. Nyberg. *The wind tunnel simulation of propulsion jets and their modeling by congruent plumes including limits of applicability*. AIAA (0232) (1984).

[23] C. K. W. Tam, K. Viswanathan, K. K. Ahuja, and J. Panda. *The source of jet noise: Experimental evidence*. AIAA (3641) (2007).

[24] F. F. Grinstein, F. Hussain, and E. Oran. *Vortex-ring dynamics in a transitional subsonic free jet. a numerical study*. Europ. J. Mech. B, Fluids **9**(6), 499 (1990).

[25] A. J. Yule. *Large-scale structure in the mixing layer of a round jet*. J. Fluid Mech. **89**(3), 413 (1978).

[26] A. K. M. F. Hussain. *Coherent structures and turbulence*. J. Fluid Mech. **173**, 303 (1986).

[27] R. Gleissl and R. M. Deslandes. *Simulation of missile plumes for aircraft store compatibility assessments*. AIAA (0054) (2005).

[28] R. D. Blevins. *Applied Fluid Dynamics Handbook* (van Nostrand Reinhold Co., New York, 1984).

[29] W. G. Hill, R. C. Jenkins, and B. L. Gilbert. *Effects of initial boundary layer conditions on jet mixing*. Report re-508, Grumman Research Department (1975).

[30] K. B. M. Q. Zaman. *Effect of initial conditions on subsonic jet noise*. AIAA J. **23**(9), 1370 (1985).

[31] R. G. Batt, T. Kubota, and J. Laufer. *Experimental investigation of the effect of shear-flow turbulence on a chemical reaction*. AIAA (0721) (1970).

[32] R. G. Batt. *Some measurements on the effect of tripping the two-dimensional shear layer*. AIAA J. **13**(2), 245 (1975).

[33] J. C. Lau, P. J. Morris, and M. J. Fisher. *Measurements in subsonic and supersonic free jets using laser velocimeter*. J. Fluid Mech. **93**, 1 (1979).

[34] V. H. Arakeri, A. Krothapalli, V. Siddavaram, A. M.B., and L. L. *On the use of microjets to suppress turbulence in a mach 0.9 axisymmetric jet*. J. Fluid Mech. **490**, 75 (2003).

[35] J. C. Simonich, S. Narayanan, and T. J. B. M. Nishimura. *Aeroacoustic characterization, noise reduction, and dimensional scaling effects of high subsonic jets*. AIAA J. **39**(11), 2062 (2001).

[36] J. Bridges and M. P. Wernet. *Measurements of the aeroacoustic sound sources in hot jets*. AIAA (2003).

[37] L. D. Landau and E. M. Lifshitz. *Fluid Mechnics* (Pergamon Press, 1987), 2nd ed.

[38] A. Kolmogorov. *The local structure of turbulence in incompressible viscous fluid for very large reynolds' numbers*. Dokl. Akad. Nauk SSSR **30**, 301 (1941).

[39] A. Kolmogorov. *Dissipationof energy in the locally isotropic turbulence*. Dokl. Akad. Nauk SSSR **32**(1) (1941).

[40] L. D. Huebner, D. W. Witte, and E. H. Andrews. *Exhaust simulation testing of a hypersonic airbreathing model at transonic speeds*. AIAA (7001) (2003).

[41] K. S. Abdol-Hamid, S. P. Pao, C. A. Hunter, K. A. Deere, S. J. Massey, and A. Elmiligui. *Pab3d: Its history in the use of turbulence models in the simulation of jet and nozzle flows*. AIAA (0489) (2006).

[42] S. M. Dash, N. Sinha, D. C. Kenzakowski, and R. A. Lee. *Recent advances in jet/plume flowfield simulations*. AIAA (0260) (1995).

[43] J. P. Slotnick, P. G. B. M. Kandula, and F. W. Martin. *Numerical simulation of the space shuttle lunch vehicle flowfield with real gas solid rocket motoer plume effects*. AIAA (0521) (1993).

[44] U. C. Glodberg, J. J. Gorski, and S. R. Chakravarthy. *Flow field computations around nozzle/afterbody configurations at transonic mach numbers*. AIAA (4081) (1985).

[45] D. L. Bowers and J. A. Laughrey. *A summary of an agard assessement of testing techniques for aircraft afterbody flows*. AIAA (1639) (1985).

[46] R. G. Wilmoth and L. E. Putnam. *Subsonic/transonic prediction capabilities for nozzle/afterbody configurations*. AIAA (0192) (1984).

[47] D. Drikakis and J. Rider. *High Resolution Methods for Incompressible and Low-Speed Flows* (Springer-Verlag, Heidelberg, 2004).

[48] J. D. Anderson. *Computational Fluid Dynamics: The Basics with Application* (McGraw-Hill, 1995).

[49] D. C. Wilcox. *Turbulence Modeling For CFD* (DCW Industries, Inc., 1994), 2nd ed.

[50] F. Grinstein, L. Margolin, and W. Rider. *Implicit Large Eddy Simulation: Computing Turbulent Fluid Dynamics* (Cambridge University Press, 2007).

[51] D. Drikakis. *Advances in turbulent flow computations using high-resolution methods*. Progress in Aerospace Sciences **39**, 405 (2003).

[52] D. Drikakis. *Godunov Methods: Theory and Applications*, chap. Uniformaly high-order methods for unsteady incompressible flows, pp. 263–283 (Kluwer Academic Publishers, 2001).

[53] D. Drikakis and S. Tsangaris. *An implicit characteristic-flux-averaging method for the Euler equations for real gases*. Int. J. Numer. Meth. Fluids **12**, 711 (1991).

[54] D. Drikakis and S. Tsangaris. *On the solution of the compressible navier-stokes equations using improved flux vector splitting methods*. Applied Mathematical Modelling **17**(6), 282 (1993).

[55] J. Zoltak and D. Drikakis. *Hybrid upwind methods for the simulation of unsteady shockwave diffraction over a cylinder*. Comput. Methods Appl. Mech. Engrg. **162**(1-4), 165 (1998).

[56] A. Bagabir and D. Drikakis. *Mach number effects on shock-bubble interaction*. Shock Waves Journal **11**, 209 (2001).

[57] A. Bagabir and D. Drikakis. *Numerical experiments using high-resolution schemes for unsteady, inviscid, compressible flows*. Comput. Methods Appl. Mech. Engrg. **193**, 4675 (2004).

[58] D. Drikakis, M. Hahn, A. Mosedale, and B. Thornber. *Large eddy simulation using high-resolution and high-order methods*. Phil. Trans. R. Soc. A **367**, 2985 (2009).

[59] A. Mosedale and D. Drikakis. *Assessment of very high-order of accuracy in les models*. J. Fluids Eng. **129**, 1497 (2007).

[60] B. Thornber, D. Youngs, D. Drikakis, and R. Williams. *The influence of initial conditions on turbulent mixing due to richtmyer-meshkov instability*. J. Fluid Mech. **129**, 1504 (2010).

[61] S. Tissera, V. Titarev, and D. Drikakis. *Chemically reacting flows around a double-cone, including ablation effects*. AIAA (1285) (2010).

[62] M. Hahn and D. Drikakis. *Implicit large-eddy simulation of swept wing flow using high-resolution methods*. AIAA J. **47**, 618 (2009).

[63] S. K. Godunov. *A finite difference method for numerical computation of discontinuous solutions of the equations of fluid dynamics*. Matematicheski Sbornik **47**, 271 (1959).

[64] E. F. Toro. *Riemann Solvers and Numerical Methods for Fluid Dynamics - A Practical Introduction* (Springer-Verlag, Heidelberg, 1997).

[65] A. Eberle. *Characteristic flux averaging approach to the solution of euler's equations*. VKI Lecture Series (1987).

[66] B. van Leer. *Towards the ultimate conservative difference scheme: 3. upstream-centered finite-difference schemes for ideal compressible flow*. J. Comp. Phys. **23**(3), 263 (1977).

[67] K. H. Kim and C. Kim. *Accurate, efficient and monotonic numerical methods for multi-dimensional compressible flows part 1: Spatial discretization*. J. Comp. Phys. **208**(2), 527 (2005).

[68] K. H. Kim and C. Kim. *Accurate, efficient and monotonic numerical methods for multi-dimensional compressible flows part 2: multi-dimensional limiting process*. J. Comp. Phys. **208**(2), 570 (2005).

[69] B. Thornber, A. Mosedale, D. Drikakis, D. Youngs, and R. J. R. Williams. *An improved reconstruction method for compressible flows with low mach number features*. J. Comp. Phys. **227**(10), 4873 (2008).

[70] G. Jiang and C. Shu. *Efficient implementation of weighted eno scheme*. J. Comp. Phys. **126**, 202 (1996).

[71] D. Drikakis and F. Inok. *Computational uncertainty in turbulent flow simulations: Towards a numerical error bar* (2010).

[72] B. J. R. Thornber. *Implicit Large Eddy Simulation for Unsteady Multi-Component Compressible Turbulent Flows*. Ph.D. thesis, Cranfield University (2007).

[73] M. Hahn. *Implicit Large-Eddy Simulation of Low-Speed Separated Flows Using High-ResolutionMethods*. Ph.D. thesis, Cranfield University (2008).

[74] R. LeVeque. *Finite volume methods for hyperbolic problems* (2002).

[75] A. Harten. *High resolution schemes for hyperbolic conservation laws*. J. Comp. Phys. **135**(2), 260 (1997).

[76] H. Yang. *Convergence of godunov type schemes*. Appl. Math. Lett. **9**(5), 63 (1996).

[77] A. Jameson. *Time dependent calculations using multigrid, with applications to unsteady flows past airfoils and wings.* AIAA (1596) (1991).

[78] C. W. Shu. *Total-variation-diminishing time discretizations*. SIAM J. Sci. Stat. Comp. **9**, 1073 (1998).

[79] S. Gottlieb and C.-W. Shu. *Total variation diminishing runge-kutta schemes*. Mathematics of Computation **67**(221), 73 (1998).

[80] D. Balsara and C. Shu. *Monotonicity preserving weighted essentially non-oscillatory schemes with increasingly high order of accuracy*. J. Comp. Phys. **160**(2), 405 (2000).

[81] B. van Leer. *Towards the ultimate conservative difference scheme: 1. the quest of monotonicity*. Lecture Notes in Physics **18**, 163 (1973).

[82] B. van Leer. *Towards the ultimate conservative difference scheme: 2. monotonicity and conservation combined in a second-order scheme*. J. Comp. Phys. **14**(4), 361 (1974).

[83] B. van Leer. *Towards the ultimate conservative difference scheme: 4. a new approach to numerical convection*. J. Comp. Phys. **23**(3), 276 (1977).

[84] B. van Leer. *Towards the ultimate conservation difference scheme: 5. a second-order sequel to godunov's method*. J. Comp. Phys. **32**(1), 101 (1979).

[85] B. van Leer, L. Wen-Tzong, P. L. Roe, P. K. G., and T. Chang-Hsien. *Design of optimally smoothing multistage schemes for the euler equations*. AIAA (1933) (1989).

[86] A. Harten, B. Engquist, S. Osher, and S. Chakravarthy. *Uniformly high order accurate non-oscillatory schemes iii*. J. Comp. Phys. **71**, 231 (1987).

[87] C. W. Shu and S. Osher. *Efficient implementation of essentially non-oscillatory shock-capturing schemes*. J. Comp. Phys. **77**, 439 (1988).

[88] X. D. Liu, S. Osher, and T. Chan. *Weighted essentially non-oscillatory schemes*. J. Comp. Phys. **115**, 200 (1994).

[89] C. W. Shu and S. Osher. *Efficient implementation of essentially non-oscillatory shock-capturing schemes ii*. J. Comp. Phys. **83**, 32 (1989).

[90] B. Thornber, D. Drikakis, R. J. R. Williams, and D. Youngs. *On entropy generation and dissipation of kinetic energy in high-resolution shock-capturing schemes*. J. Comp. Phys. **227**(10), 4853 (2008).

[91] E. F. Toro, M. Spruce, and W. Speares. *Restoration of the contact surface in the hll-riemann solver*. Shock Waves Journal **4**(1), 25 (1994).

[92] A. Harten and J. Hyman. *Self adjusting grid methods for one-dimensional hyperbolic conservation laws*. J. Comp. Phys. **50**(2), 235 (1983).

[93] E. Shapiro. *Step-by-step eberle's scheme derivation*. Tech. rep., Cranfield University (2006).

[94] D. Drikakis, P. A. Govatsos, and D. E. Papatonis. *A characteristic-based method for incompressible flows*. Int. J. Numer. Meth. Fluids **19**, 667 (1994).

[95] E. F. Toro. *A linearized riemann solver for the time-dependent euler equations of gas dynamics*. Proceedings: Mathematical and Physical Sciences **434**(1892), 683 (1991).

[96] I. W. Kokkinakis. *Investigation of High-Resolution Methods in Large Eddy Simulation of Subsonic and Supersonic Wall Turbulent Flows*. Ph.D. thesis, Cranfield University (2009).

[97] J. W. Cooley and J. W. Tukey. *An algorithm for the machine calculation of complex fourier series*. Math. Comput. **19**, 297 (1965).

[98] J. W. Brown and R. Churchill. *Fourier Series and Boundary Value Problems* (McGraw-Hill, 1993).

[99] M. S. Liou. *A generalized procedure for constructing an upwind-based tvd scheme*. AIAA (0355) (1987).

[100] G. A. Sod. *A survey of several finite difference methods for systems of nonlinear hyperbolic conservation laws*. J. Comp. Phys. **27**, 1 (1978).

[101] M. L. Boas. *Mathematical Methods in the Physical Sciences, 2nd Edition* (John Wiley and Sons, 1983).

[102] R. Eisberg and R. Resnick. *Quantum Physics of Atoms, Molecules, Solids, Nuclei and Particles* (John Wiley and Sons, 1985), 2nd ed.

[103] J. Foo and G. Karniadakis. *Multi-element probabilistic collocation method in high dimensions*. J. Comp. Phys. **229**(5), 1536 (2010).

[104] P. J. Roache. *Quantification of uncertainty in computational fluid dynamics*. Ann. Rev. Fluid Mechanics **29**, 123 (1998).

[105] S. Ghosal. *In Turbulent Flow Computation*, chap. Analysis and control of errors in the numerical simulation of turbulence, pp. 101–140 (Kluwer Academic Publishers, 2002).

[106] A. I. of Aeronautics and Astronautics. *Guide for the verification and validation of computational fluid dynamics simulations*. AIAA (G-077) (1988).

[107] G. Karniadakis. *Toward a numerical error bar in cfd*. J. Fluids Eng. **117**(1), 7 (1995).

[108] C. Freitas. *Editorial policy statement on the control of numerical accuracy*. J. Fluids Eng. **115**, 339 (1993).

[109] J. Meyers, B. Geurts, and M. Baelmans. *Database analysis of errors in large-eddy simulation*. Phys. Fluids **15**(9), 2740 (2003).

[110] M. Shur, P. Spalart, M. Strelets, and A. Travin. *Towards the prediction of noise from jet engines*. Int. J. Heat Fluid Flow **24**, 551 (2003).

[111] A. P. Morse. *Axisymmetric turbulent shear flows with and with out swirling*. Ph.D. thesis, University of London (1980).

[112] P. Bradshaw, D. Ferris, and R. Johnson. *Turbulence in the noise-production region of a circular jet*. J. Fluid Mech. **19**, 591 (1964).

[113] I. Wygnanski and H. Fiedler. *The two-dimensional mixing region*. J. Fluid Mech. **41**, 327 (1970).

[114] I. Wygnanski and H. Fiedler. *Some measurements in the self-preserving jet*. J. Fluid Mech. **38**(3), 577 (1969).

[115] H. J. Hussein, S. P. Capp, and W. K. George. *Velocity measurements in a high-reynolds number, momentum-conserving, axisymmetric, turbulent jet*. J. Fluid Mech. **258**, 31 (1994).

[116] N. R. Panchapakesan and J. L. Lumey. *Turbulence measurements in axisymmetric jets of air and helium. part 1. air jet*. J. Fluid Mech. **246**, 197 (1993).

[117] H. K. Tanna. *An experimental study of jet noise. part 1: Turbulent mixing noise*. J. Sound Vib. **50**(3), 405 (1977).

[118] D. C. W. Dennisand and M. P. Sutton. *Assessing rocket plume damage to launch vehicles*. AIAA (4163) (2005).

[119] P. G. Tucker. *Novel miles computations for jet flows and noise*. Int. J. Heat Fluid Flow **25**, 625 (2004).

[120] F. Grinstein. *Vortex dynamics and entrainment in rectangular free jets*. Int. J. Numer. Meth. Fluids **47**, 69 (2001).

[121] D. Zwillinger. *Standard Mathematical Tables and Formulae* (Chapman and Hall, 1995).

[122] R. W. Luce and P. O. Jarvinen. *An approximate method for predicting plume sizes for nozzle flow into stil air*. AIAA J. **6**(1), 182 (1968).

[123] K. L. Nash, K. W. Whitaker, and L. M. Freeman. *Predicting exhaust plumes boundaries with supersonic external flows*. Journal of Spacecraft and Rockets **31**(5), 773 (1994).

[124] J. Qiu and C.-W. Shu. *On the construction, comparison, and local characteristic decomposition for high-order central weno schemes*. J. Comp. Phys. **183**(1), 187 (2002).

[125] V. A. Titarev and E. F. Toro. *Finite-volume weno schemes for three-dimensional conservation laws*. J. Comp. Phys. **201**(1), 238 (2004).

[126] M. M. Zdravkovic. *Flow around Circular Cylinders* (Oxford Science Publications, 1997).

[127] A. E. Perry and T. T. Lim. *Coherent structures in coflowing jets and wakes*. J. Fluid Mech. **88**(3), 451 (1978).

[128] A. E. Perry, T. T. Lim, and M. S. Chong. *The instantaneous velocity fields of coherent structures in coflowing jets and wakes*. J. Fluid Mech. **101**(2), 243 (1980).

[129] A. E. Perry and D. K. M. Tan. *Simple three-dimensional vortex motions in coherent jets and wakes*. J. Fluid Mech. **141**, 197 (1984).

[130] I. H. Shames. *Mechanics of Fluids, Volume I & II* (Edgard Blucher, 1991).

[131] F. Mandl. *Statistical Physics* (John Wiley and Sons, 1988), 2nd ed.

[132] F. Reif. *Fundamental of Statistical and Thermal Physics* (McGraw-Hill, 1985).

[133] A. R. Vick, E. H. Andrews, J. S. Dennard, and C. B. Craidon. *Comparisons of experimental free-jet boundaries with theoretical results obtained with the method of characteristics*. Tn-d-2327, NASA (1964).

A

Mathematical and Physical Relationships

In this appendix, the theoretical background on how to treat the relevant physical formulae and to calculate numerically the flow field behaviour and characteristics, is briefly presented. A more detailed explanation can be found out in different text books, e.g. Shames [130].

A.1 Navier-Stokes Equations System

The continuum description of fluids is based on the concept of the conservation laws. In any physical system, the mass, momentum and energy must be conserved. The physics of a flow is described by the Navier-Stokes equations. This set of equations comprise the following physical laws and principles:

- Conservation of matter (continuity equation);
- Momentum principle of Newton (momentum equation);
- Conservation of Energy (First law of Thermodynamics);

- Entropy Law (Second law of Thermodynamics).

Apart of this general laws and principles, numerous subsidiary laws exist, that are applied to specific systems, e.g. the Equation of State (**EOS**) for the perfect gas formulation, Newton's Law for viscosity (only applicable to certain viscus fluids), Fourier Law for heat conduction and Hooke Law for elastic solids, among others. [130]

The following figure represents the analytical concept of a Control Volume and Control Surface immerse into a fluid. Using the previous physical principles and laws into the concept, it is possible to derive the Navier-Stokes equations in a general form.

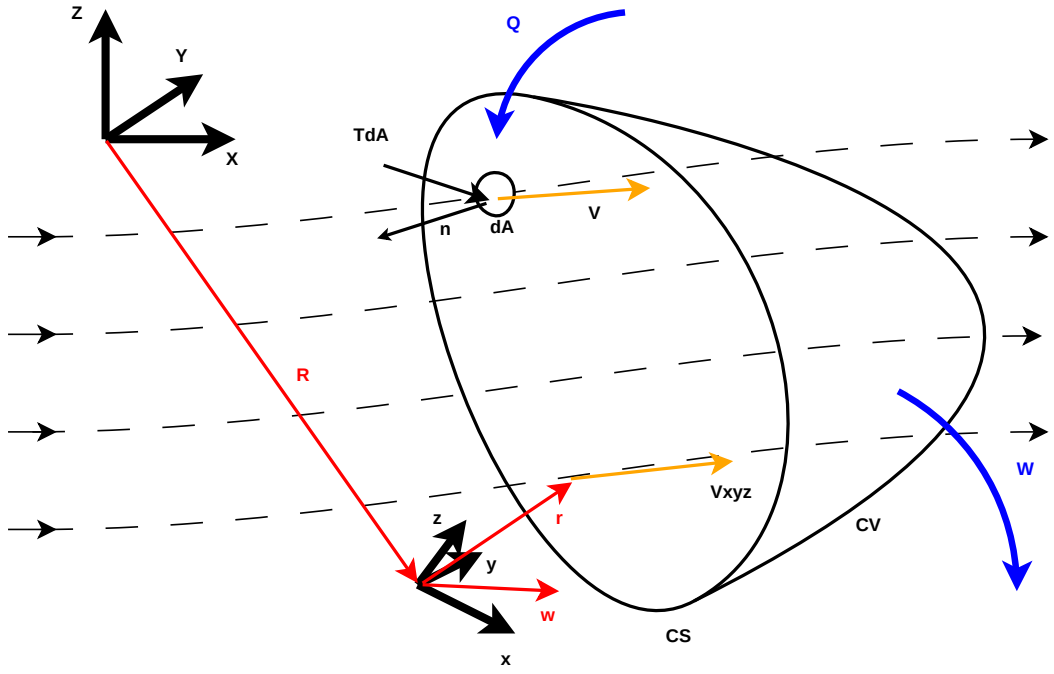

Figure A.1: Flow field generic representation under Control Volume and Control Surface, for inertial and non-inertial coordinate systems.

It should be remember that a system always has the same quantity of matter. In this sense, a correct system definition assure mass conservation; by consequence, the following relation can be established for any time instant:

$$\oiint_{CS}(\rho \mathbf{V} \cdot d\mathbf{A}) + \frac{\partial}{\partial t}\iiint_{CV}(\rho dV) = 0. \tag{A.1}$$

By considering the inertial reference system (XYZ) and one reference (xyz) moving inertially with the fluid, Figure A.1, the momentum equation can be written in two different forms. Assuming the non-inertial system only translates in relation to the inertial reference system, the momentum equation can be written as:

$$\mathbf{F}_S + \iiint_{CV} \mathbf{B}\rho dV - \iiint_{CV} \left(\ddot{\mathbf{R}} + 2\omega \times \mathbf{V}_{xyz} + \dot{\omega} \times \mathbf{r} + \omega \times (\omega \times \mathbf{r})\right)\rho dV = \tag{A.2}$$
$$\oiint_{CS} \mathbf{V}_{xyz}(\rho \mathbf{V}_{xyz} \cdot d\mathbf{A}) + \frac{\partial}{\partial t_{xyz}} \iiint_{CV} \mathbf{V}_{xyz}(\rho dV).$$

in case of rotation in the non-inertial reference system, the previous equation can them be written as:

$$\mathbf{M}_S + \iiint_{CV} (\mathbf{r} \times \mathbf{B})\rho dV - \iiint_{CV} \left(\mathbf{r} \times \left(\ddot{\mathbf{R}} + 2\omega \times \mathbf{V}_{xyz} + \dot{\omega} \times \mathbf{r} + \omega \times (\omega \times \mathbf{r})\right)\right)\rho dV = \tag{A.3}$$
$$\oiint_{CS} (\mathbf{r} \times \mathbf{V}_{xyz})(\rho \mathbf{V}_{xyz} \cdot d\mathbf{A}) + \frac{\partial}{\partial t_{xyz}} \iiint_{CV} (\mathbf{r} \times \mathbf{V}_{xyz})(\rho dV).$$

The variables on the previous equations can be explained in Figure A.1; $\mathbf{F}_S$ and $\mathbf{M}_S$ are the resulting contact force and momentum over the system, accordingly, and $\mathbf{B}$ is the distribution of field forces per unit of mass. The term $2\omega \times \mathbf{V}_{xyz}$ is the famous Coriolis force, $\dot{\omega} \times \mathbf{r}$ angular force and $\omega \times (\omega \times \mathbf{r})$ the centrifugal or centripetal force. The previous equations derivation is based in the mechanical principles of acceleration of particles.

In its general form, the first law of Thermodynamics applied to a fluid establishes, that the ratio of energy transfer to the Control Volume in the form of heat and work is equal to the efflux of stored energy into the Control Volume plus the ratio of increasing energy. The energy equation can them be written as:

$$\frac{dQ}{dt} - \frac{dW_S}{dt} + \oiint_{CS} \mathbf{T} \cdot \mathbf{V} d\mathbf{A} = \oiint_{CS} \mathcal{E}\,(\rho \mathbf{V} \cdot d\mathbf{A}) + \frac{\partial}{\partial t} \iiint_{CV} \mathcal{E}(\rho dV) \tag{A.4}$$

where $\mathcal{E} = \dfrac{\mathbf{V}^2}{2} + e + gh$, e is the internal energy and gh the potential energy. The terms $\dfrac{dW_S}{dt}$ axis work and $\oiint_{CS} \mathbf{T} \cdot \mathbf{V} d\mathbf{A}$ fluid work, with $\mathbf{T}$ as the intensity of force per unit of area

and **V** the fluid velocity that crosses the area element.

A.1.1 Integral and Differential forms

With the general form of Navier-Stokes equations defined, it is possible to assume the flow field as inertial and the previous equations (Equation (A.1) - Equation (A.4)) can be rewritten in integral and differential counterpart, accordingly, as follow:

- Continuity equations:

$$\frac{\partial}{\partial t}\iiint_{CV}\rho dV + \iint_{CS}\rho\mathbf{u}\cdot d\mathbf{A} = 0, \tag{A.5}$$

$$\frac{\partial\rho}{\partial t} + \nabla(\rho\mathbf{u}) = 0. \tag{A.6}$$

- Momentum equations:

$$\frac{\partial}{\partial t}\iiint_{CV}\rho\mathbf{u}dV + \iint_{CS}\rho\mathbf{u}\,(\mathbf{u}\cdot d\mathbf{A}) = \iint_{CS}\bar{\bar{\tau}}\cdot d\mathbf{A} + \iiint_{CV}\rho\mathbf{B}dV, \tag{A.7}$$

$$\frac{\partial\rho\mathbf{u}}{\partial t} + \nabla(\rho\mathbf{u}\otimes\mathbf{u}) = -\nabla\bar{\bar{\tau}}, \tag{A.8}$$

- Energy equations:

$$\begin{aligned}\frac{\partial}{\partial t}\iiint_{CV}\rho E_t dV + \iint_{CS}\rho E_t\mathbf{u}\cdot d\mathbf{A} \;=\; & \iiint_{CV}q\rho dV + \iint_{CS}k\nabla T d\mathbf{A} + \\ & \iiint_{CV}\rho\mathbf{B}\cdot\mathbf{u}dV - \iint_{CS}p\mathbf{u}\cdot d\mathbf{A} + \iint_{CS}\left(\bar{\bar{\tau}}\cdot\mathbf{u}\right)\cdot d\mathbf{A}.\end{aligned} \tag{A.9}$$

$$\frac{\partial\rho E_t}{\partial t} + \nabla(\rho\mathbf{u}E_t) = -\nabla(\bar{\bar{\tau}}\mathbf{u}) - \nabla q, \tag{A.10}$$

$$E_t = e + E_k = e + \frac{\mathbf{u}^2}{2} = e + \frac{u^2+v^2+w^2}{2}. \tag{A.11}$$

The definition of total energy has been changed, as the effect of the potential energy is assumed to be negligible. Where **u**, e, and q stands for the velocity magnitude, internal

energy, and heat flux, respectively.

From Equation (A.7) - Equation (A.9), it can be observed the introduction of a tensor ($\overline{\overline{\tau}}$). The tensor $\overline{\overline{\tau}}$, is the stress tensor in a Newtonian fluid and it general form is given by:

$$\overline{\overline{\tau}} = -\delta_{ij}p + \nu\left(\frac{\partial u_i}{\partial x_j} + \frac{\partial u_j}{\partial x_i} - \frac{2}{3}\delta_{ij}\frac{\partial u_k}{\partial x_k}\right) \tag{A.12}$$

where p is the pressure, $\frac{\partial u_i}{\partial x_j} + \frac{\partial u_j}{\partial x_i}$ the shear stress, $\frac{\partial u_k}{\partial x_k}$ the normal stress and ν is the dynamic viscosity coefficient.

Shear and Normal Stresses

The friction between layers of fluid is described by the stress tensor $\overline{\overline{\tau}}$. The following figure, illustrates the concept of stress behaviour over a control Volume.

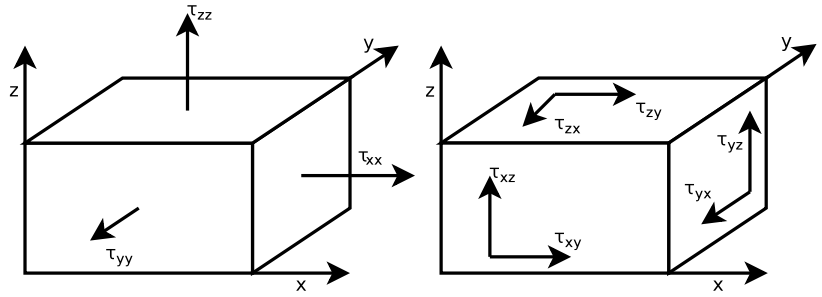

(a) Normal Stresses (b) Shear Stresses

Figure A.2: Stresses concept over a Control Volume.

From Figure A.2 it is possible to give a generalise mathematical expression for the stress tensor $\overline{\overline{\tau}}$:

$$\overline{\overline{\tau}} = \begin{bmatrix} \tau_{xx} & \tau_{xy} & \tau_{xz} \\ \tau_{yx} & \tau_{yy} & \tau_{yz} \\ \tau_{zx} & \tau_{zy} & \tau_{zz} \end{bmatrix}. \tag{A.13}$$

A.1.2 Conservative Matrix form

With the Navier-Stokes equation system written in a "simplified" manner, the conservative matrix form is presented here in Cartesian coordinates. This form is of great utility in terms of numerics.

$$\frac{\partial \mathbf{U}}{\partial t} + \frac{\partial \mathbf{E}}{\partial x} + \frac{\partial \mathbf{F}}{\partial y} + \frac{\partial \mathbf{G}}{\partial z} = 0 \tag{A.14}$$

$$\begin{aligned}
\mathbf{U} &= \begin{bmatrix} \rho \\ \rho u \\ \rho v \\ \rho w \\ \rho e \end{bmatrix} \\
\mathbf{E} &= \begin{bmatrix} \rho u \\ \rho u^2 + p - \tau_{xx} \\ \rho uv - \tau_{xy} \\ \rho uw - \tau_{xz} \\ u(\rho e + p) - u\tau_{xx} - v\tau_{xy} - w\tau_{xz} + qx \end{bmatrix} \\
\mathbf{F} &= \begin{bmatrix} \rho v \\ \rho uv - \tau_{yx} \\ \rho v^2 + p - \tau_{yy} \\ \rho vw - \tau_{yz} \\ v(\rho e + p) - u\tau_{yx} - v\tau_{yy} - w\tau_{yz} + qy \end{bmatrix} \\
\mathbf{G} &= \begin{bmatrix} \rho w \\ \rho uw - \tau_{zx} \\ \rho vw - \tau_{zy} \\ \rho w^2 + p - \tau_{zz} \\ w(\rho e + p) - u\tau_{zx} - v\tau_{zy} - w\tau_{zz} + qz \end{bmatrix}
\end{aligned} \tag{A.15}$$

A.1.3 Transformation from Cartesian to Generalized Coordinates

Going a step further, the system of equations (Equation (A.14)) can be transformed into a generalized curvilinear coordinates system. The transformation is then given by

$$\begin{aligned}
\xi &= \xi(x, y, z, t); \\
\eta &= \eta(x, y, z, t); \\
\zeta &= \zeta(x, y, z, t); \\
\tau_{time} &= t,
\end{aligned} \tag{A.16}$$

yielding the following form:

$$\frac{\partial \overline{\mathbf{U}}}{\partial \tau_{time}} + \frac{\partial \overline{\mathbf{E}}}{\partial \xi} + \frac{\partial \overline{\mathbf{F}}}{\partial \eta} + \frac{\partial \overline{\mathbf{G}}}{\partial \zeta} = 0 \tag{A.17}$$

with,

$$\begin{aligned} \overline{\mathbf{U}} &= JU \\ \overline{\mathbf{E}} &= J(E\xi_x + F\xi_y + G\xi_z) \\ \overline{\mathbf{F}} &= J(E\eta_x + F\eta_y + G\eta_z) \\ \overline{\mathbf{G}} &= J(E\zeta_x + F\zeta_y + G\zeta_z) \end{aligned} \tag{A.18}$$

where J is the Jacobian determinant of the transformation from Cartesian (x, y, z) to curvilinear (ξ, η, ζ) coordinates,

$$J = \left| \frac{\partial(x, y, z)}{\partial(\xi, \eta, \zeta)} \right| \tag{A.19}$$

Now, the Equation (A.6) - Equation (A.10) have been reduced to a single equation that can be simply codified into a flow solver.

A.1.4 Nondimensionalization of the Governing Equations

Having the reference variables L, u, and ρ as length, velocity and density, respectively. The relevant dimensionless variables in the Navier-Stokes equations, can be define as:

$$\begin{aligned} u_i^* &= \tfrac{u_i}{U} \\ x_i^* &= \tfrac{x_i}{L} \\ t^* &= \tfrac{tU}{L} \\ p^* &= \tfrac{p}{\rho U^2} \\ e^* &= \tfrac{e}{U^2} \end{aligned} \tag{A.20}$$

with the index i representing the three components of velocity and space, respectively.

By replacing the variables of the Navier-Stokes equations with the dimensionless counterparts, the result in the continuity equation is a invariance; on the momentum equation, the *RHS* contains one parameter, which is known as the Reynolds number. The momentum equation, can be now rewritten as

$$\frac{\partial u_i^*}{\partial t^*} + \frac{\partial u_i^* u_j^*}{\partial x_j^*} = -\frac{\partial p^*}{\partial x_i^*} + \frac{1}{Re} \frac{\partial^2 u_j^*}{\partial x_j^* \partial x_j^*} \tag{A.21}$$

for simplicity, the superscript $*$ on the dimensionless variables can be omitted.

For the majority of fluid phenomena studied in sciences and engineering, the following variables are considered important:

- pressure (p),
- temperature (T),
- length (L),
- viscosity (μ),
- superficial tension (σ),
- speed of sound (c),
- density (ρ),
- velocity ($\mathbf{V}$).

From the previous list, a set of dimensionless groups can be formed and its physical meaning understood:

- Reynolds number, $Re = \frac{\rho \mathbf{V} \mathbf{L}}{\nu}$, represents the ratio of inertial to viscous forces and can also be understood as a scaling parameter;
- Mach number, $Ma = \frac{\mathbf{V}^2}{c}$, represents the ratio of flow speed to pressure waves, it measures compressibility;
- Strouhal Number, $St = \frac{\nu L}{\mathbf{V}}$, represents the ratio of flow time to induced time;
- Prandtl number, $Pr = \frac{c_p \mu}{k}$, represents the ratio of momentum diffusivity (kinematic viscosity) to thermal diffusivity.

As it can be seen, previously, the dimensionless numbers can also be related between them. One important relation that can be established is between the Reynolds and Strouhal numbers. From this relation one can estimate the resonance frequency of a particular system.

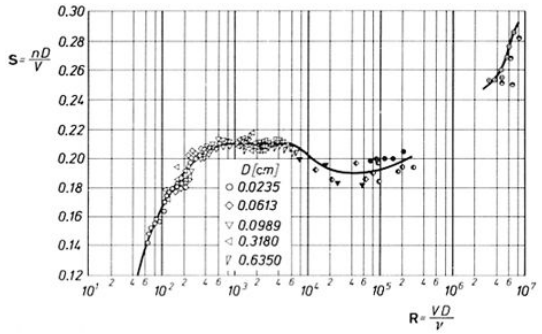

Figure A.3: Experimental results of the relation between Strouhal number and Reynolds number.[126]

Based on Figure A.3 [126] an experimental formula can be established,

$$St = 0.198\left(1 - \frac{19.7}{Re}\right), \tag{A.22}$$

this formula will holds true for the range $250 < Re < 2 \times 10^5$.

A.2 Closure of the Navier-Stokes Equations system

There exist five equations to be solved, but the number of unknowns are more then five (density, the three components of velocity, pressure, energy, stresses and heat fluxes). To close the above system, modelling assumptions are used, e.g. for a perfect gas assumption, the equation of state $p = \rho\overline{R}T$ is employed to close the set of equations.

A.2.1 Equation of State

This equation of state holds true for the majority systems in classical physics. Despite of its experimental origins, using the Grand Canonical distribution from Statistical Physics, it is possible to be analytically derived [131, 132].

$$p = \rho\overline{R}T, \tag{A.23}$$

where $\overline{R}$ is the specific gas constant. An extra unknown is then introduced that of temperature T; thus to complete the closure of the set of equations, a extra relation is required. By using the thermodynamic relation between state variables (Caloric Equation of State) it is possible to fulfil the close of the equations system.

The specific heats at constant pressure and volume (c_p and c_v) can be related by $c_p - c_v = R$, where R is a constant, specific to each fluid. The ratio between specific heats ($\gamma = \frac{c_p}{c_v}$), form thermodynamics, characterize the fluid, in the case of air $\gamma = 1.4$, at standard atmospheric conditions. Other definition can be employed as, $c_p = \frac{\gamma R}{\gamma - 1}$ and $c_v = \frac{R}{\gamma - 1}$.

The total density-energy is then given by multiplying Equation (A.11) by ρ, this allow to calculate the internal energy as:

$$e = c_v T = \frac{RT}{\gamma - 1} = \frac{\rho RT}{\rho(\gamma - 1)} = \frac{p}{\rho(\gamma - 1)}, \tag{A.24}$$

where e is the internal energy and T is the absolute temperature.

A.2.2 Heat flux

The heat flux q, also known as Fourier Law, is the intrinsic property of matter which relates its ability to conduct heat. Heat flux by conduction involves transfer of energy within a material without any motion of the material as a whole. Conduction takes place when a temperature gradient exists in a fluid, or solid, medium. Thus, Fourier Law can be written in integral and differential forms, as:

$$\frac{\partial Q}{\partial t} = -k \oiint_{CS} \nabla T \, d\mathbf{A} \tag{A.25}$$

$$q = -k \nabla T, \tag{A.26}$$

where k is the thermal conductivity and ∇T is the temperature gradient. The thermal conductivity is often treated as a constant, however, this is not always true. In anisotropic materials, the thermal conductivity typically is a function of direction. Assuming k is composed by laminar and a turbulent components, the mechanisms of turbulent transport can be correctly accounted. In the case of **ILES** where no turbulence model is used explicitly, the turbulent thermal conductivity is neglected and therefore equals zero. In order to account for the laminar and turbulent components of the thermal conductivity, the Prandtl number is also expressed in the form of the two same components. Furthermore, since the ratio c_p/Pr is approximately constant for most gases, the thermal conductivity k may also be calculated by:

$$k = \frac{\mu c_p}{Pr_l} + \frac{\mu c_p}{Pr_t}. \tag{A.27}$$

For air, the value of the laminar Prandtl number $Pr_l = 0.72$ while its turbulent counterpart $Pr_t = 0.9$.

A.2.3 Sutherland's Law

The relation between temperature and viscosity can be understood by the Sutherland's law. This law is used to derive the dynamic viscosity of an ideal gas as a function of the local temperature. It is valid for a range of absolute temperatures ($0 < T < 555$).

$$\frac{\mu}{\mu_0} = \left(\frac{T}{T_0}\right)^{3/2} \frac{T_0 + S_u}{T + S_u} \tag{A.28}$$

where T, T_0 and S_u are system, reference ($T_0 = 273.15(K)$) and Sutherland's temperature ($S_u = 110.0(K)$), accordingly, and μ_0 is a reference viscosity at a reference temperature T_0.

B

Shock Tube Results

In this appendix the remaining results from the Shock Tube test case analyses are presented. From these analyses, it can be observed the improvement in results with grid resolution for all the employed methodologies. Moreover, the over/under shoot in results at $X = 0.5$ can be associated to the Riemann solvers characteristics.

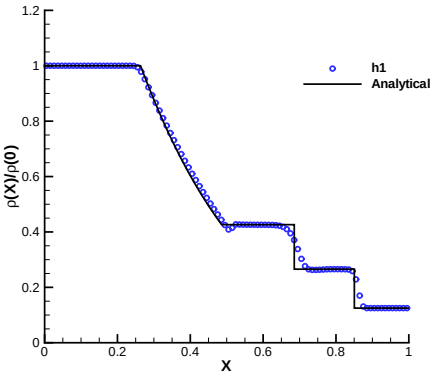

(a) Density, $h1$.

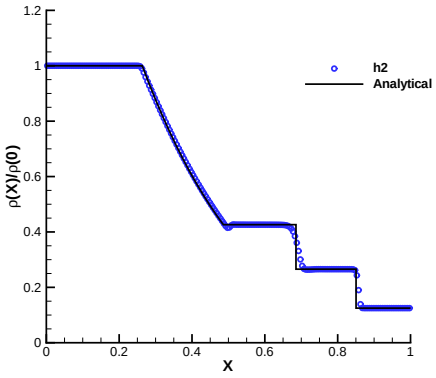

(b) Density, $h2$.

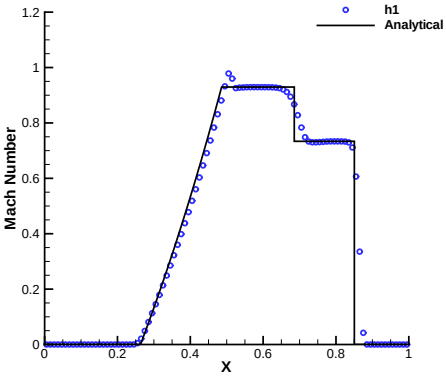

(c) Mach Number, $h1$.

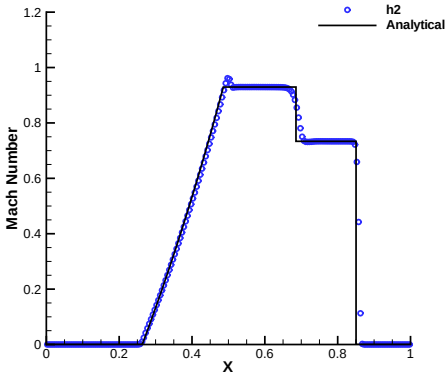

(d) Mach Number, $h2$.

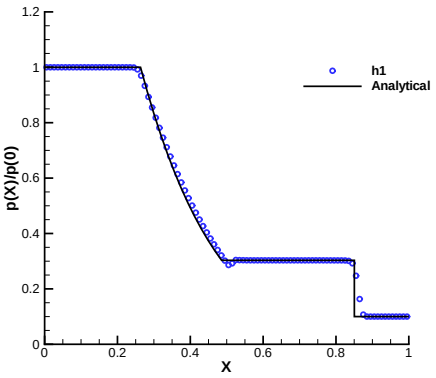

(e) Pressure, $h1$.

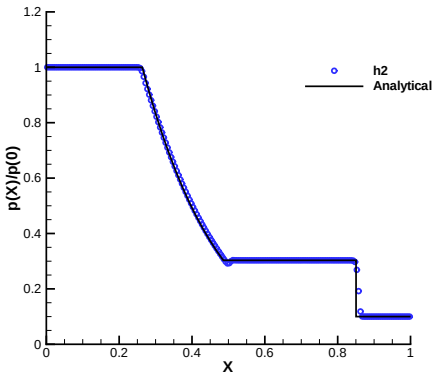

(f) Pressure, $h2$.

FIGURE B.1: *CBS* **MUSCL** 2^{nd} **LMC**, $h1$ $h2$.

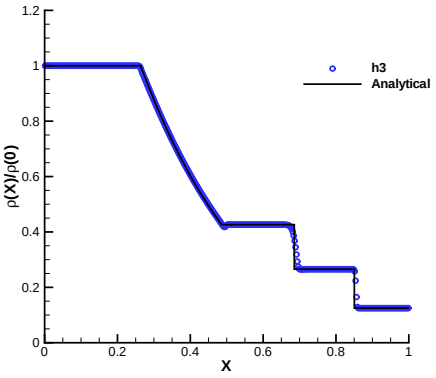

(a) Density, *h*3.

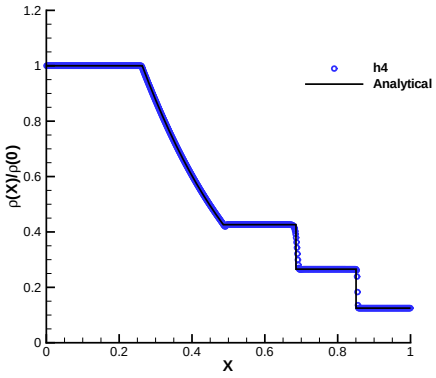

(b) Density, *h*4.

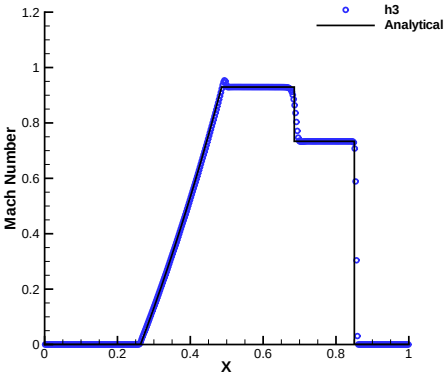

(c) Mach Number, *h*3.

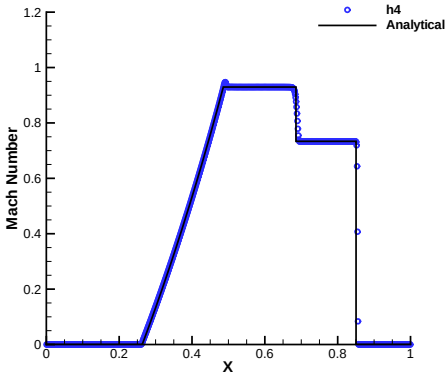

(d) Mach Number, *h*4.

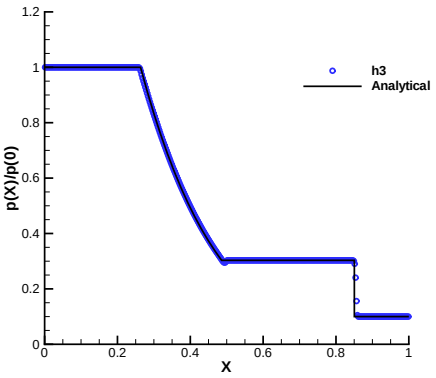

(e) Pressure, *h*3.

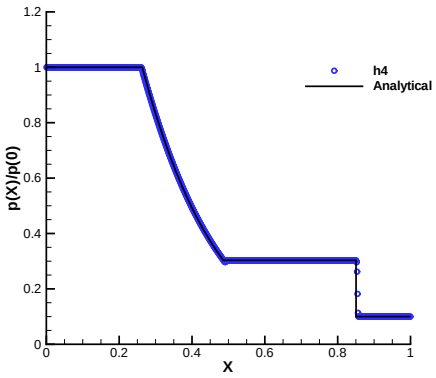

(f) Pressure, *h*4.

FIGURE B.2: *CBS* **MUSCL** 2^{nd} **LMC**, *h*3 *h*4.

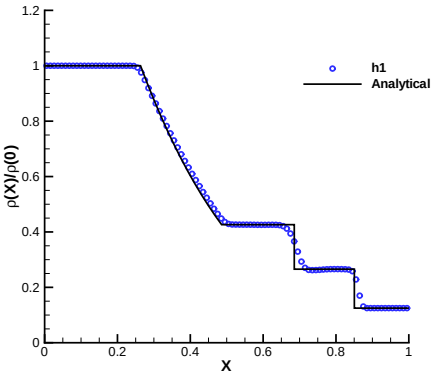

(a) Density, $h1$.

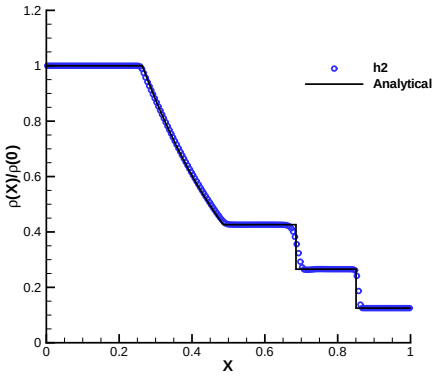

(b) Density, $h2$.

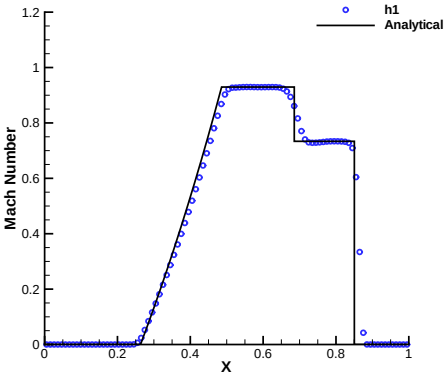

(c) Mach Number, $h1$.

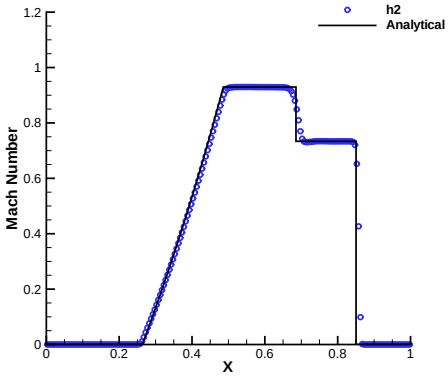

(d) Mach Number, $h2$.

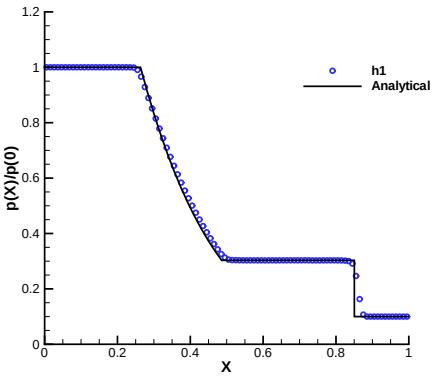

(e) Pressure, $h1$.

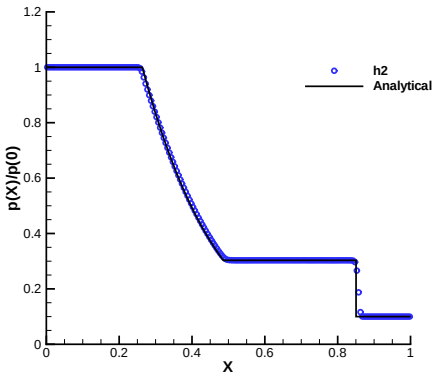

(f) Pressure, $h2$.

FIGURE B.3: *HLLC* **MUSCL** 2^{nd} **LMC**, $h1$ $h2$.

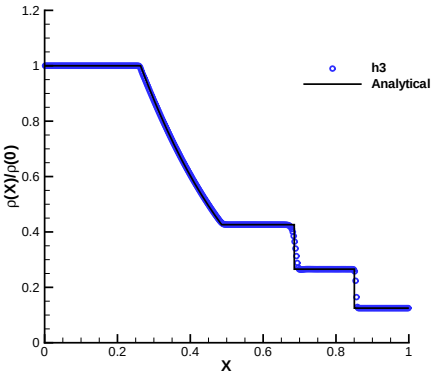

(a) Density, *h*3.

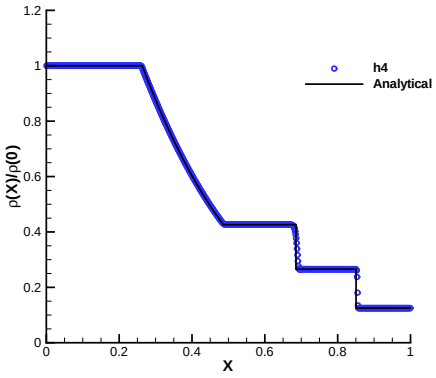

(b) Density, *h*4.

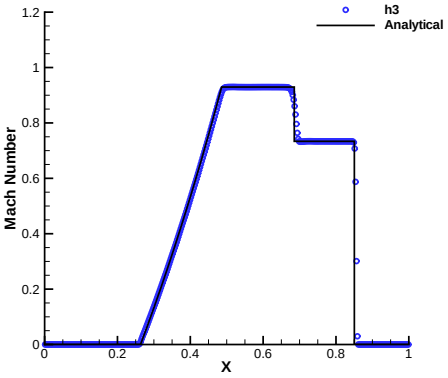

(c) Mach Number, *h*3.

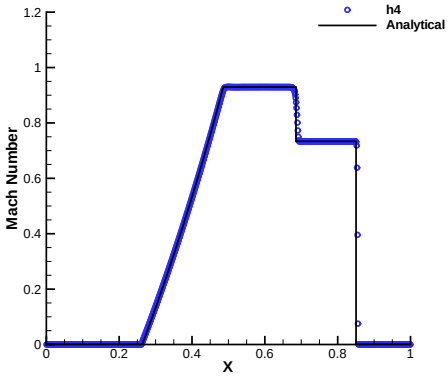

(d) Mach Number, *h*4.

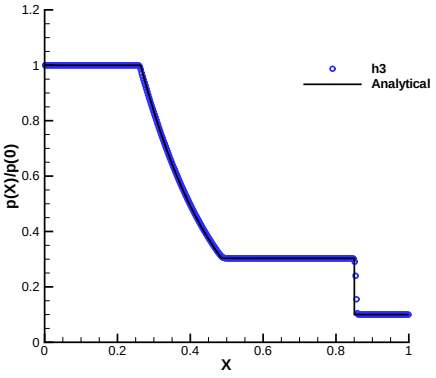

(e) Pressure, *h*3.

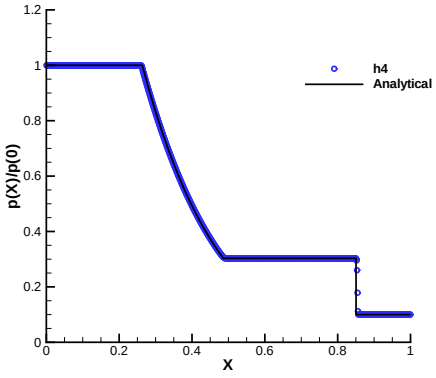

(f) Pressure, *h*4.

FIGURE B.4: *HLLC* **MUSCL** 2^{nd} **LMC**, *h*3 *h*4.

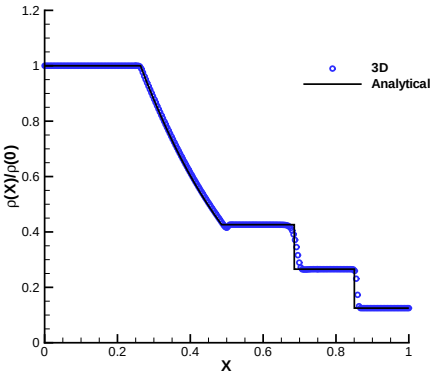

(a) Density, CBS.

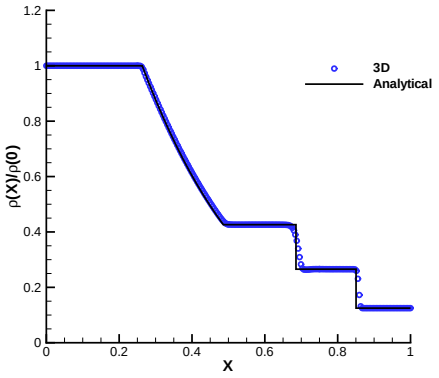

(b) Density, HLLC.

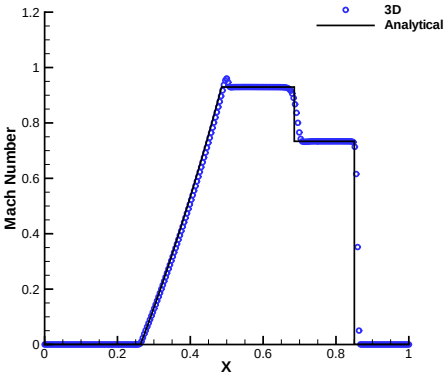

(c) Mach Number, CBS.

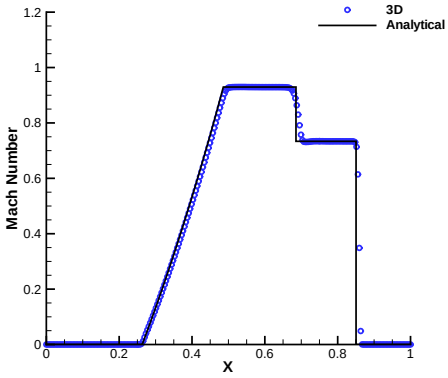

(d) Mach Number, HLLC.

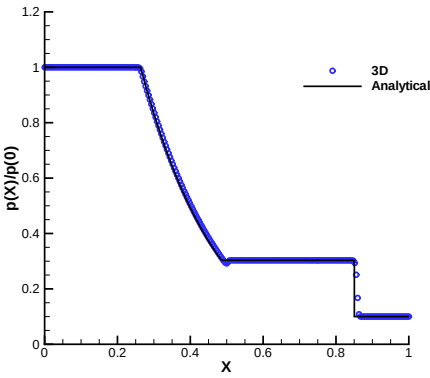

(e) Pressure, CBS.

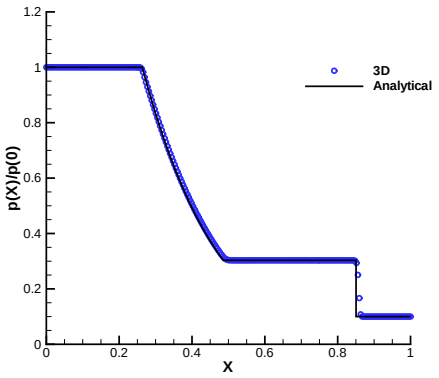

(f) Pressure, HLLC.

FIGURE B.5: **MUSCL** 2^{nd} **LMC**, $3D$.

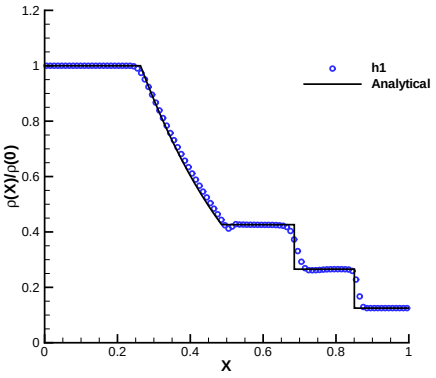

(a) Density, $h1$.

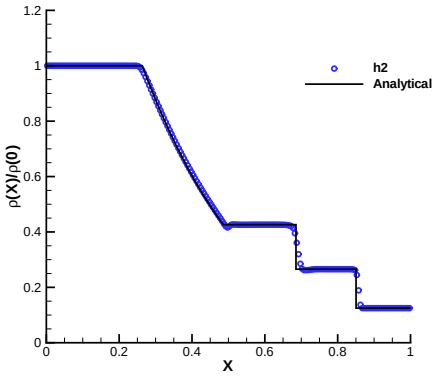

(b) Density, $h2$.

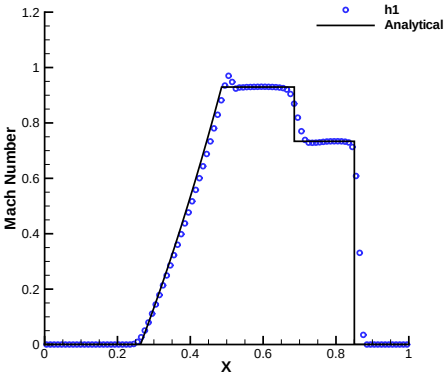

(c) Mach Number, $h1$.

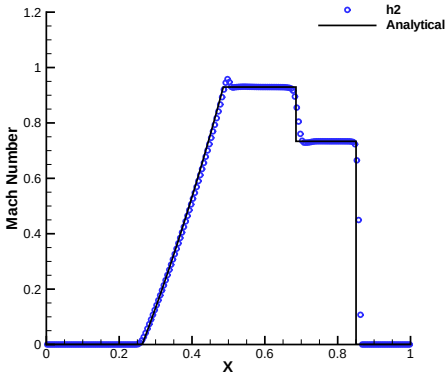

(d) Mach Number, $h2$.

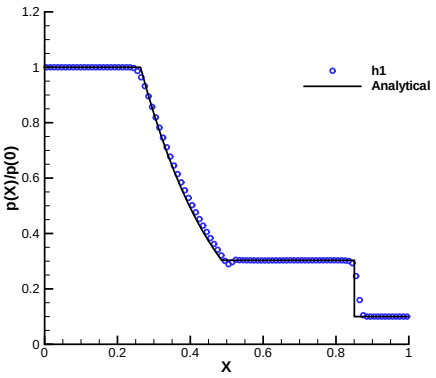

(e) Pressure, $h1$.

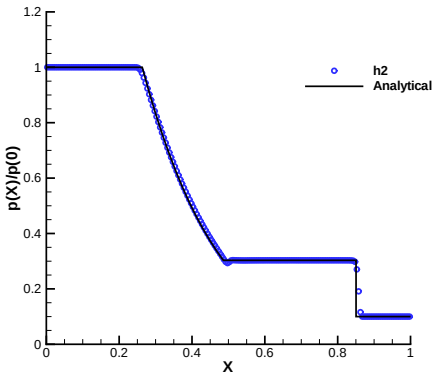

(f) Pressure, $h2$.

FIGURE B.6: *CBS* **MUSCL** 5^{th}, $h1$ $h2$.

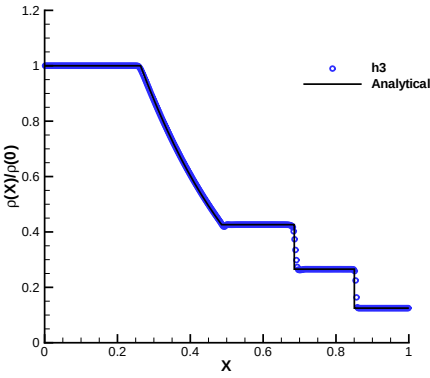

(a) Density, $h3$.

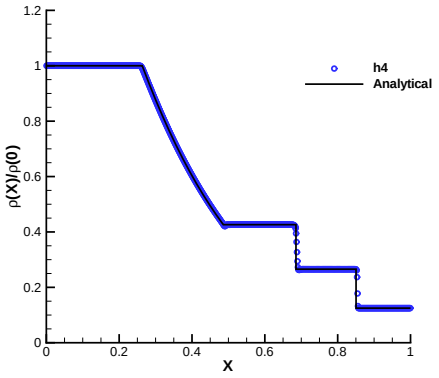

(b) Density, $h4$.

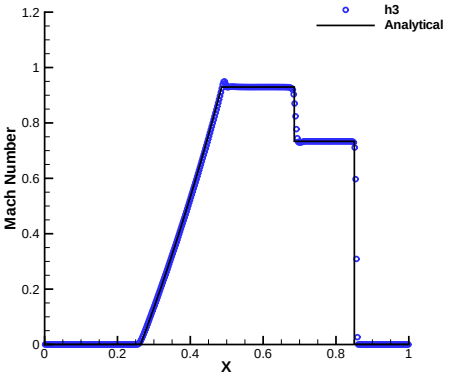

(c) Mach Number, $h3$.

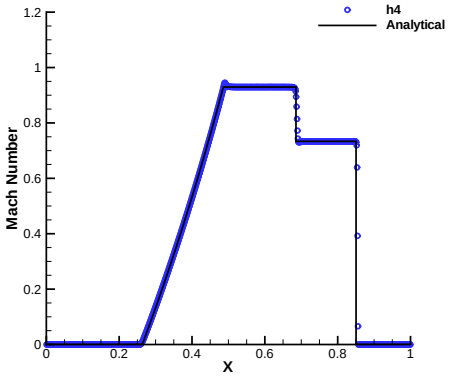

(d) Mach Number, $h4$.

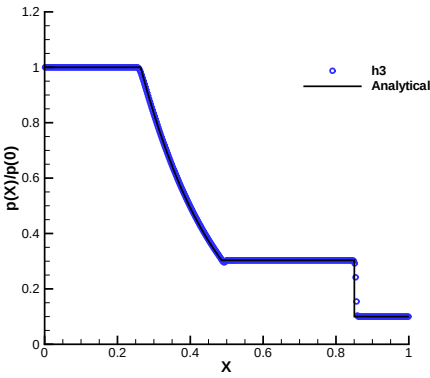

(e) Pressure, $h3$.

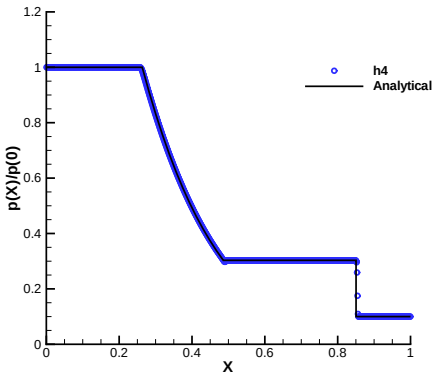

(f) Pressure, $h4$.

FIGURE B.7: *CBS* **MUSCL** 5^{th}, $h3$ $h4$.

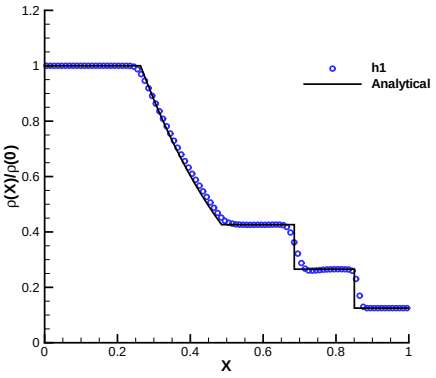

(a) Density, $h1$.

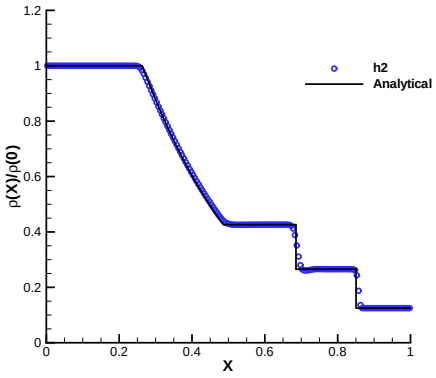

(b) Density, $h2$.

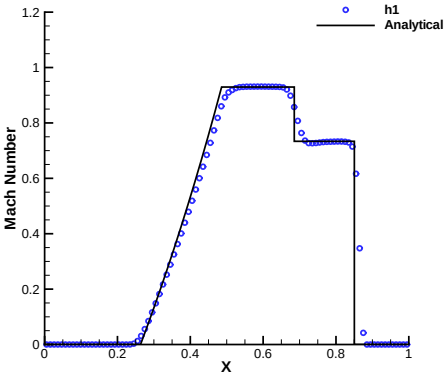

(c) Mach Number, $h1$.

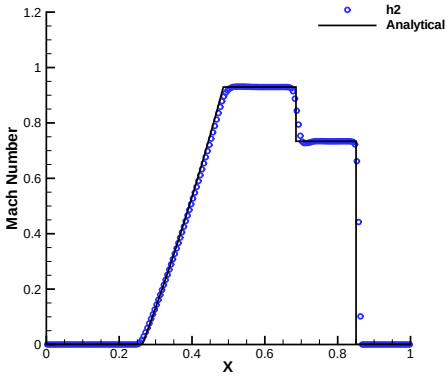

(d) Mach Number, $h2$.

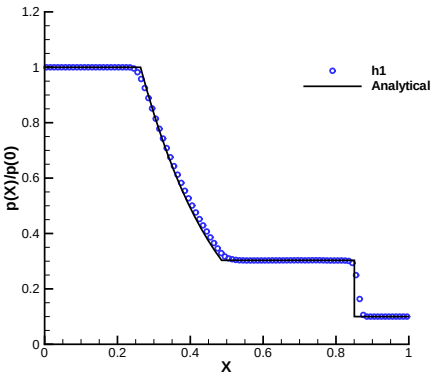

(e) Pressure, $h1$.

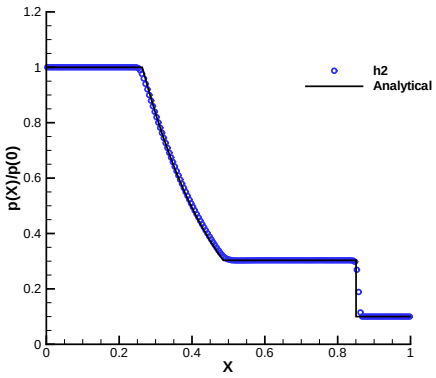

(f) Pressure, $h2$.

FIGURE B.8: *HLLC* **MUSCL** 5^{th}, $h1$ $h2$.

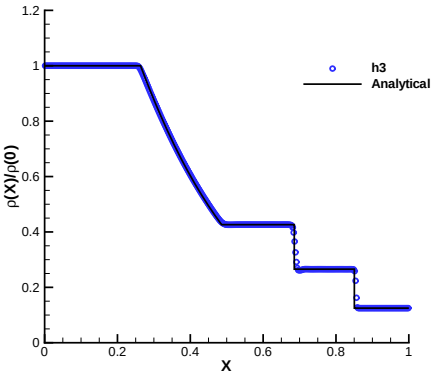

(a) Density, *h*3.

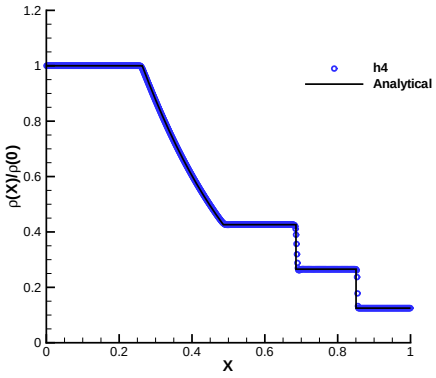

(b) Density, *h*4.

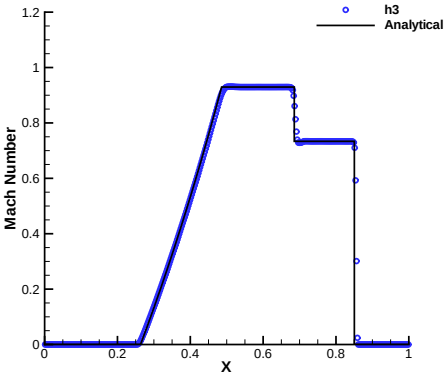

(c) Mach Number, *h*3.

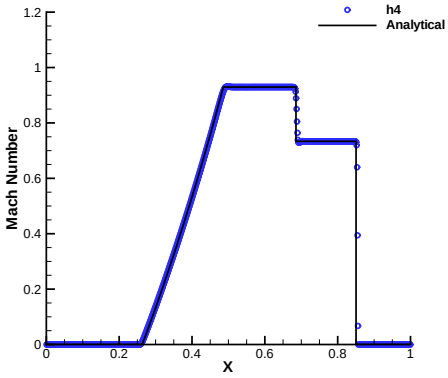

(d) Mach Number, *h*4.

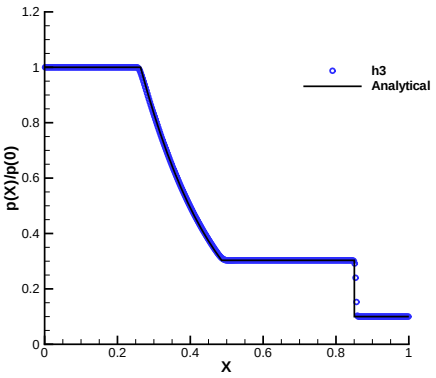

(e) Pressure, *h*3.

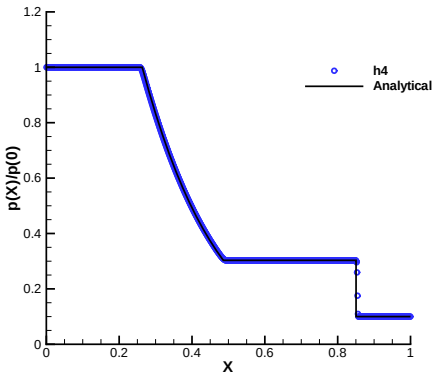

(f) Pressure, *h*4.

FIGURE B.9: *HLLC* **MUSCL** 5^{th}, *h*3 *h*4.

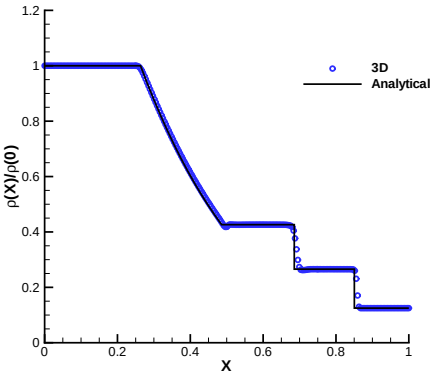

(a) Density, CBS.

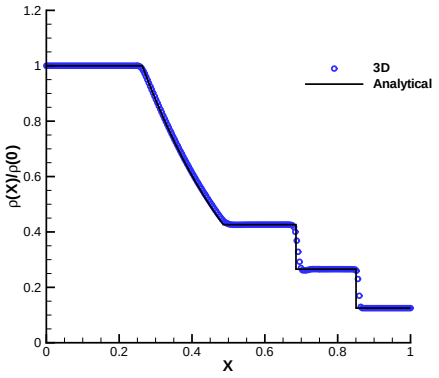

(b) Density, HLLC.

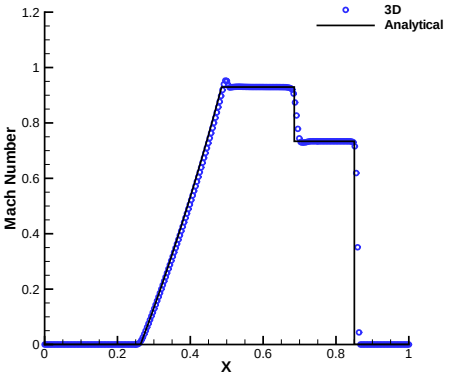

(c) Mach Number, CBS.

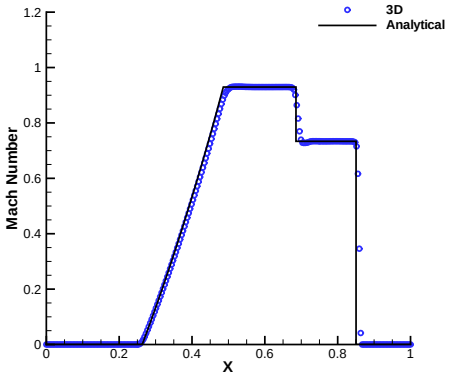

(d) Mach Number, HLLC.

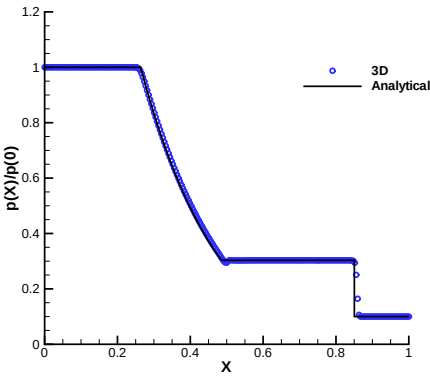

(e) Pressure, CBS.

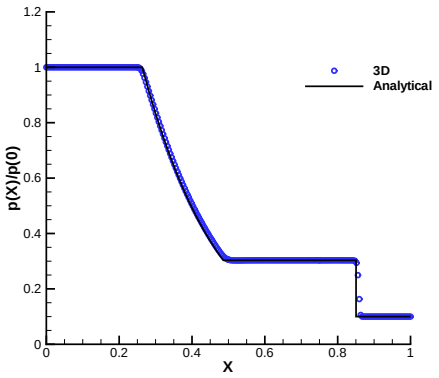

(f) Pressure, HLLC.

FIGURE B.10: **MUSCL** 5^{th}, $3D$.

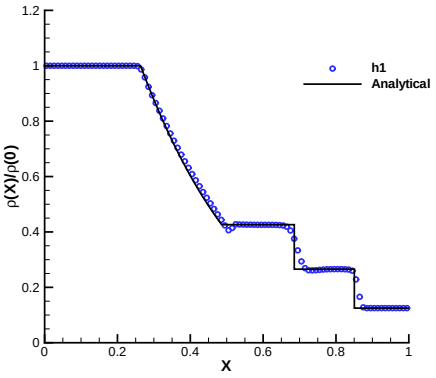

(a) Density, $h1$.

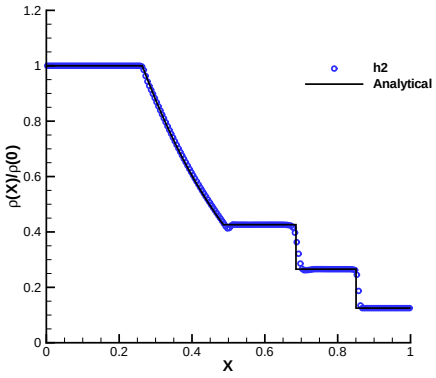

(b) Density, $h2$.

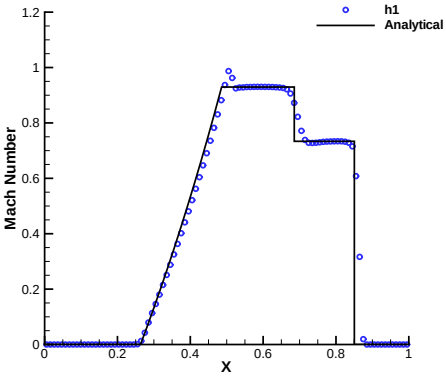

(c) Mach Number, $h1$.

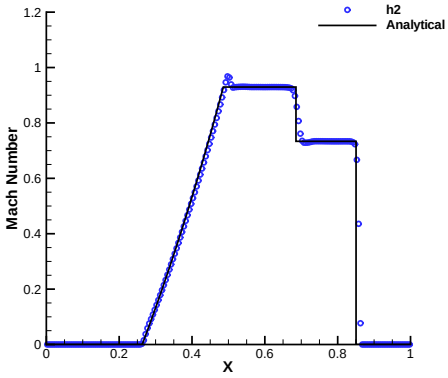

(d) Mach Number, $h2$.

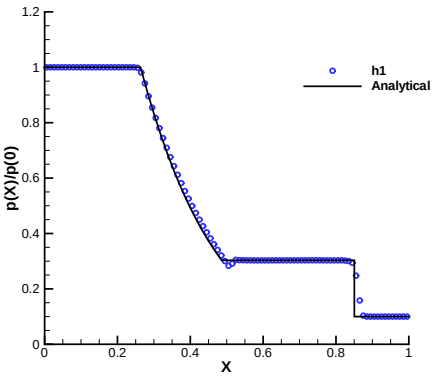

(e) Pressure, $h1$.

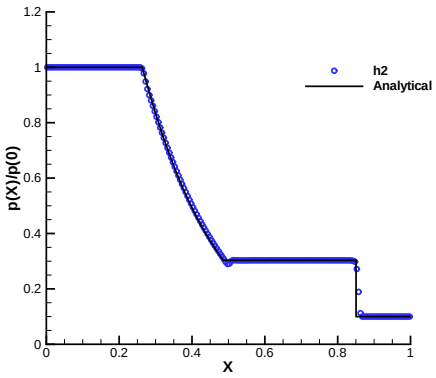

(f) Pressure, $h2$.

FIGURE B.11: *CBS* **MUSCL** 5^{th} **LMC**, $h1$ $h2$.

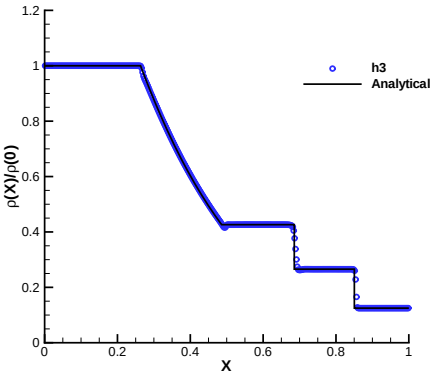

(a) Density, *h*3.

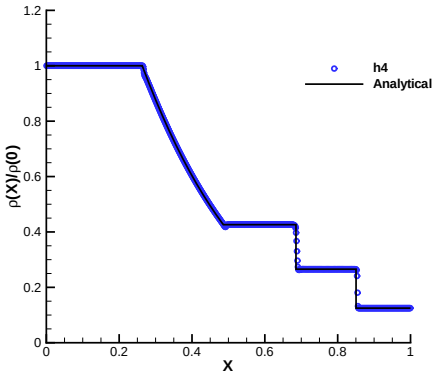

(b) Density, *h*4.

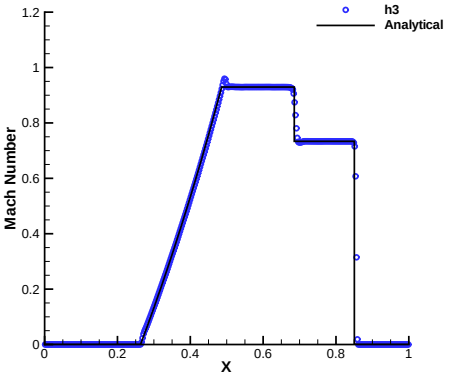

(c) Mach Number, *h*3.

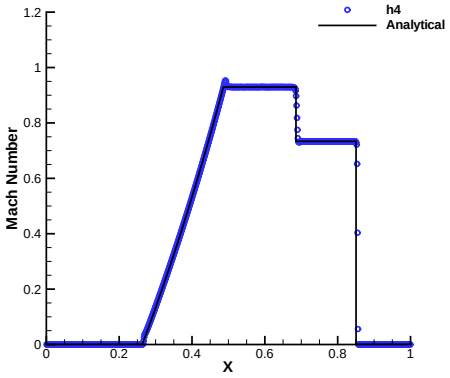

(d) Mach Number, *h*4.

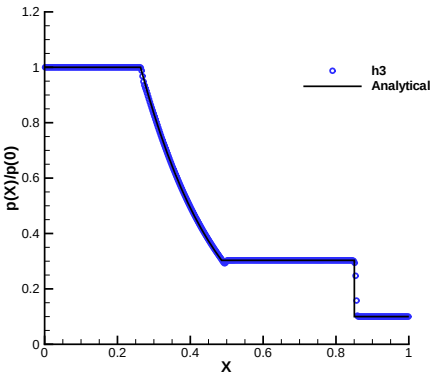

(e) Pressure, *h*3.

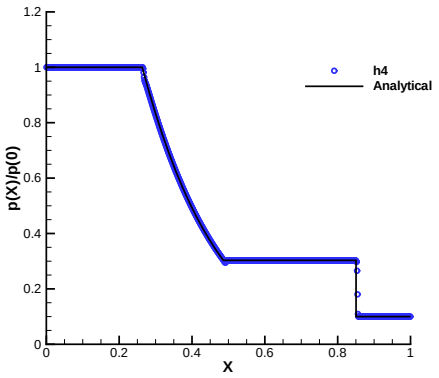

(f) Pressure, *h*4.

FIGURE B.12: *CBS* **MUSCL** 5^{th} **LMC**, *h*3 *h*4.

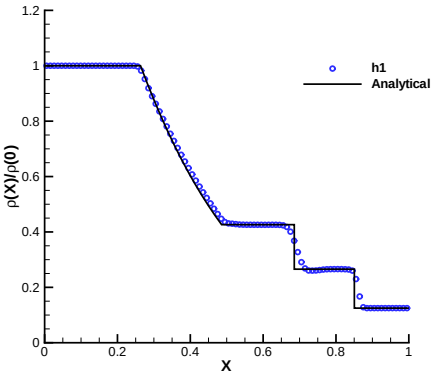

(a) Density, $h1$.

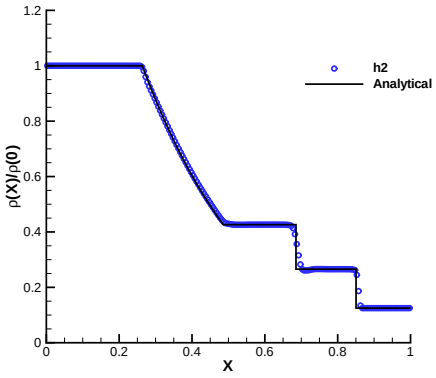

(b) Density, $h2$.

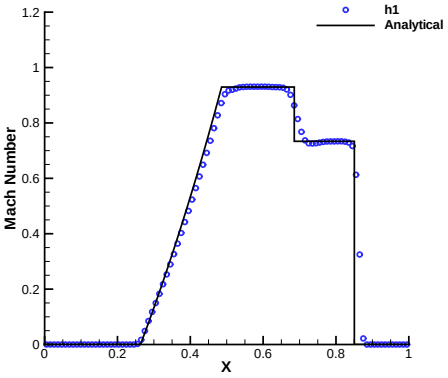

(c) Mach Number, $h1$.

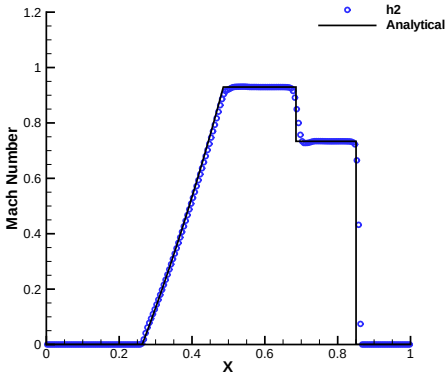

(d) Mach Number, $h2$.

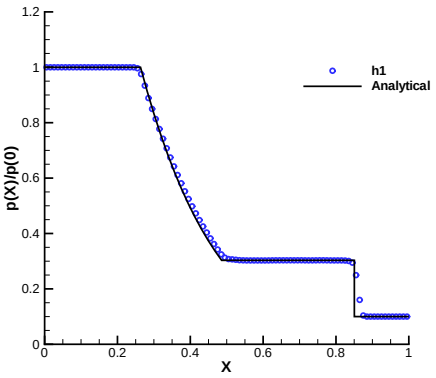

(e) Pressure, $h1$.

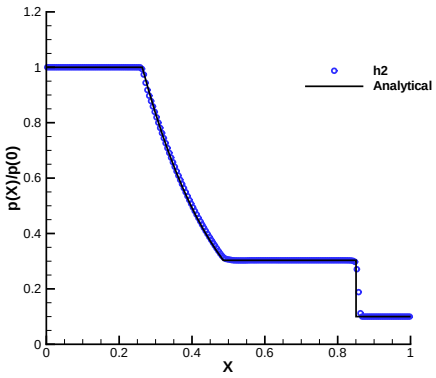

(f) Pressure, $h2$.

FIGURE B.13: *HLLC* **MUSCL** 5^{th} **LMC**, $h1$ $h2$.

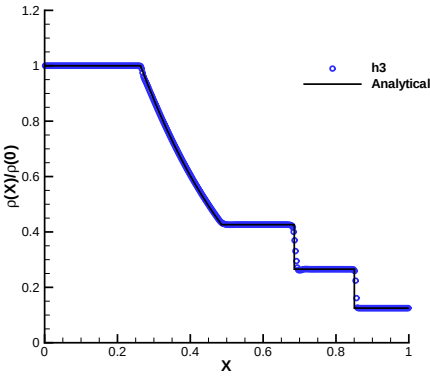

(a) Density, *h*3.

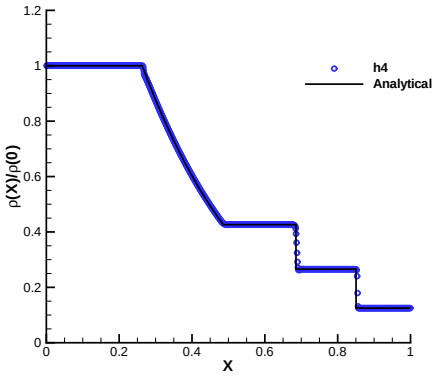

(b) Density, *h*4.

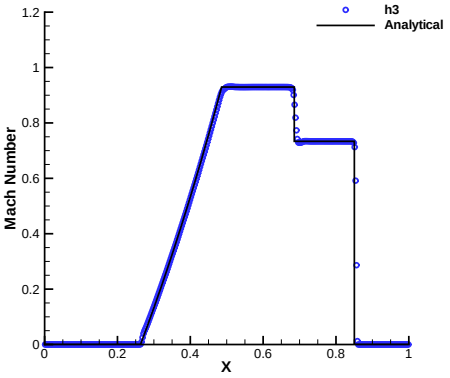

(c) Mach Number, *h*3.

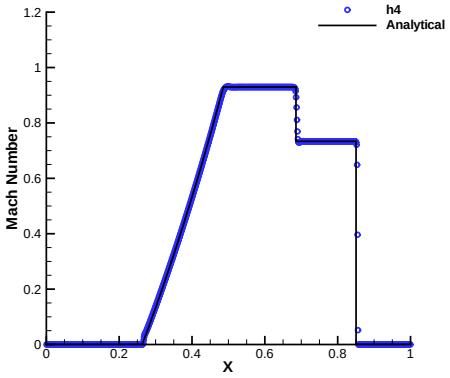

(d) Mach Number, *h*4.

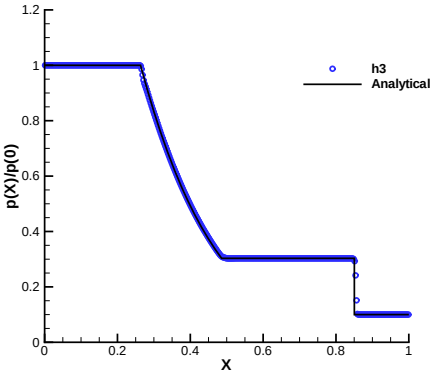

(e) Pressure, *h*3.

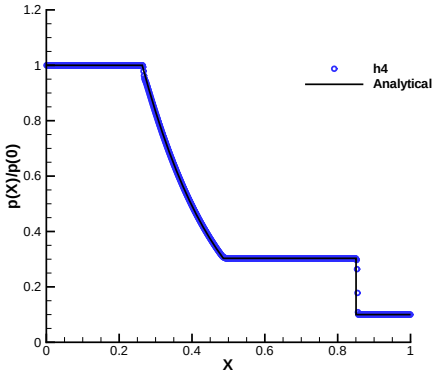

(f) Pressure, *h*4.

FIGURE B.14: *HLLC* **MUSCL** 5^{th} **LMC**, *h*3 *h*4.

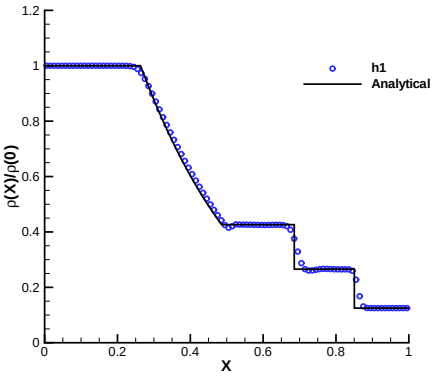

(a) Density, $h1$.

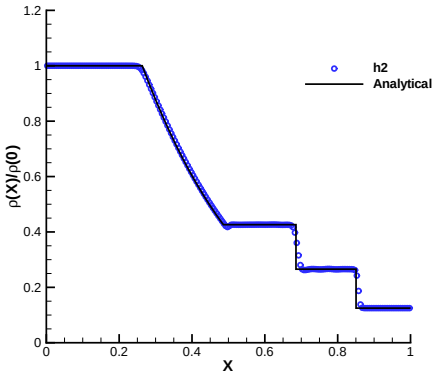

(b) Density, $h2$.

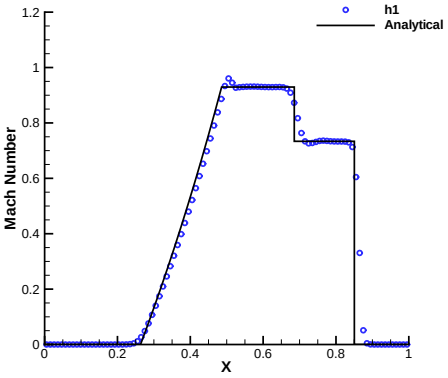

(c) Mach Number, $h1$.

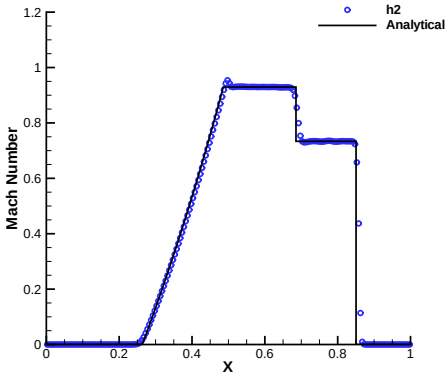

(d) Mach Number, $h2$.

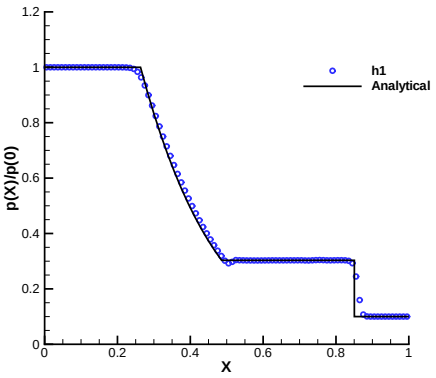

(e) Pressure, $h1$.

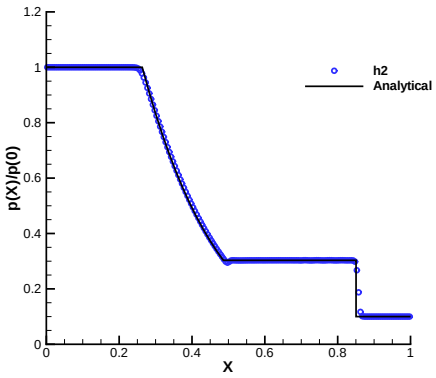

(f) Pressure, $h2$.

FIGURE B.15: *CBS* **WENO** 5^{th}, $h1$ $h2$.

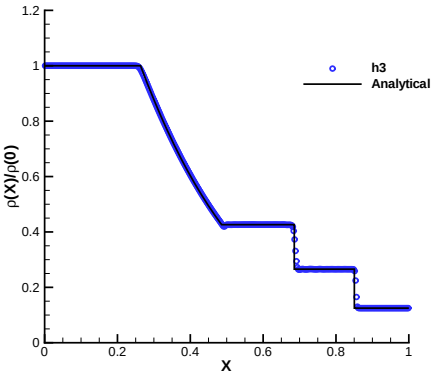

(a) Density, $h3$.

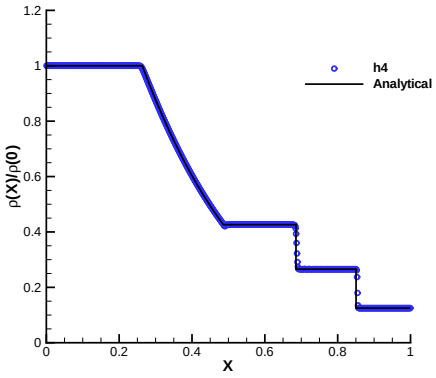

(b) Density, $h4$.

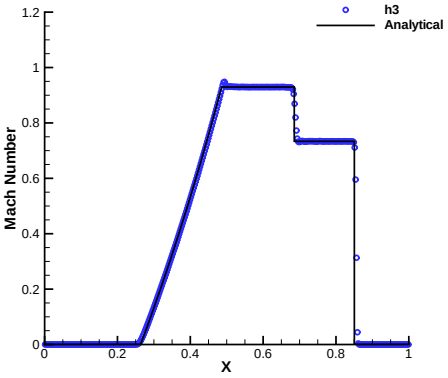

(c) Mach Number, $h3$.

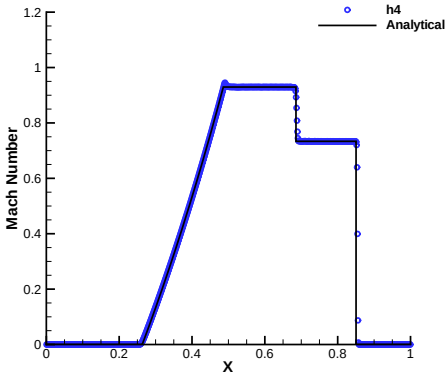

(d) Mach Number, $h4$.

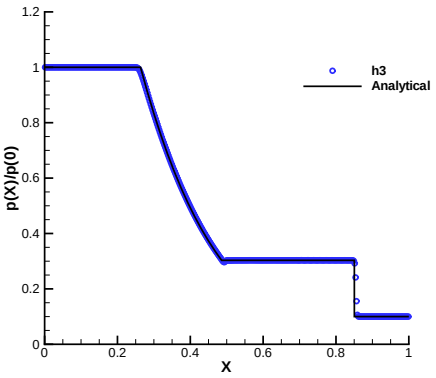

(e) Pressure, $h3$.

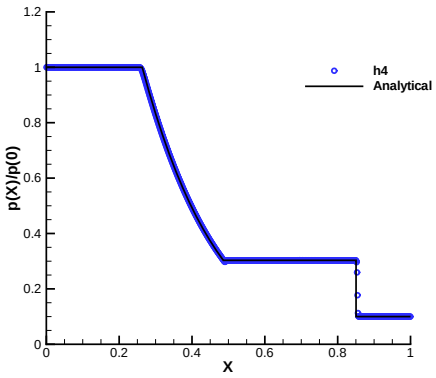

(f) Pressure, $h4$.

FIGURE B.16: *CBS* **WENO** 5^{th}, $h3$ $h4$.

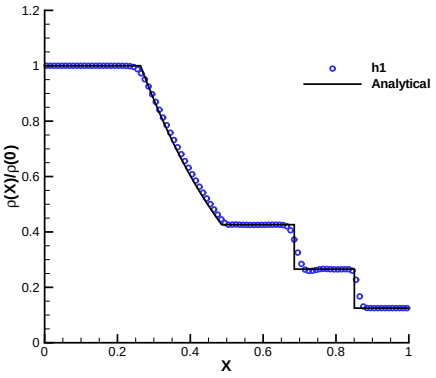

(a) Density, $h1$.

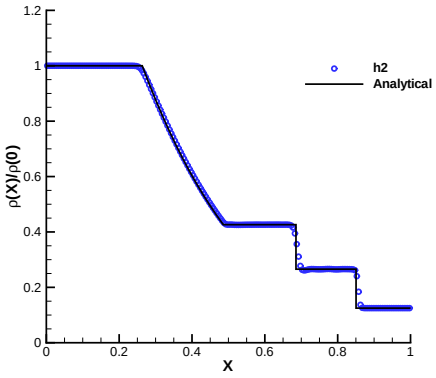

(b) Density, $h2$.

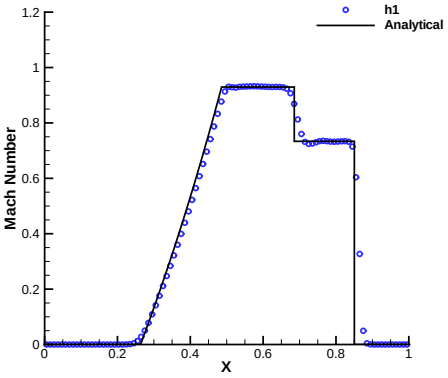

(c) Mach Number, $h1$.

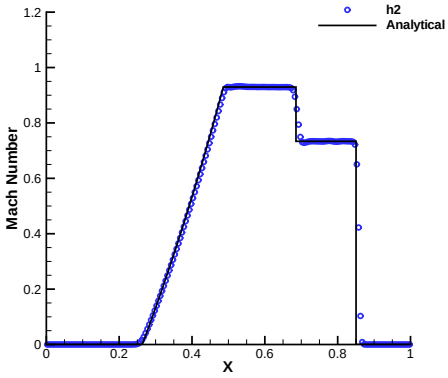

(d) Mach Number, $h2$.

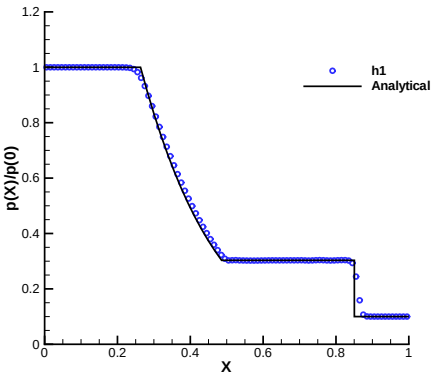

(e) Pressure, $h1$.

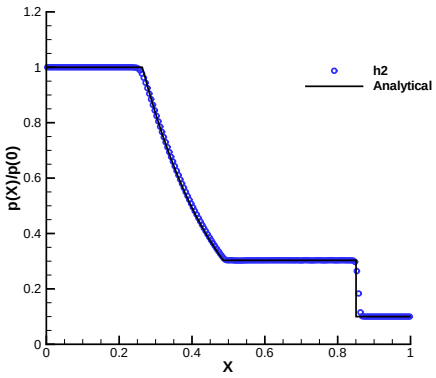

(f) Pressure, $h2$.

FIGURE B.17: *HLLC* **WENO** 5^{th}, $h1$ $h2$.

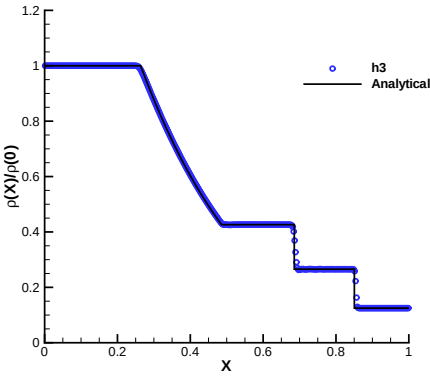

(a) Density, $h3$.

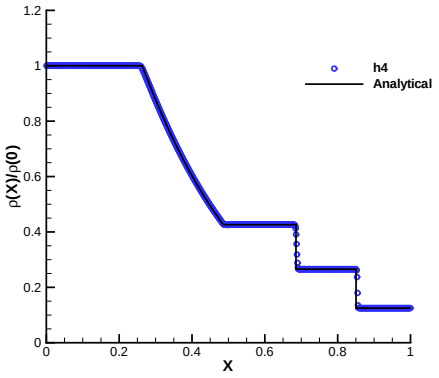

(b) Density, $h4$.

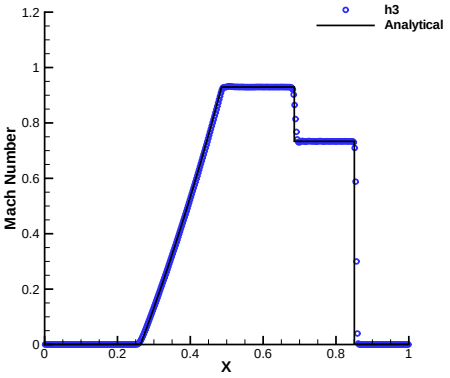

(c) Mach Number, $h3$.

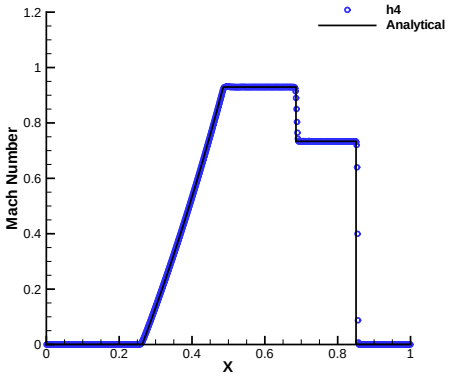

(d) Mach Number, $h4$.

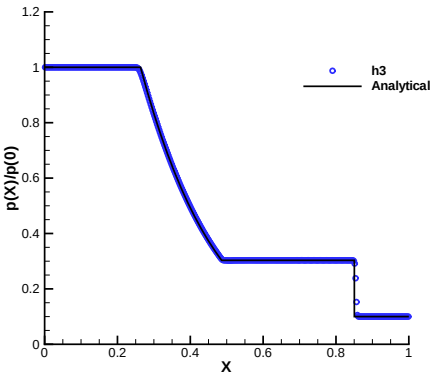

(e) Pressure, $h3$.

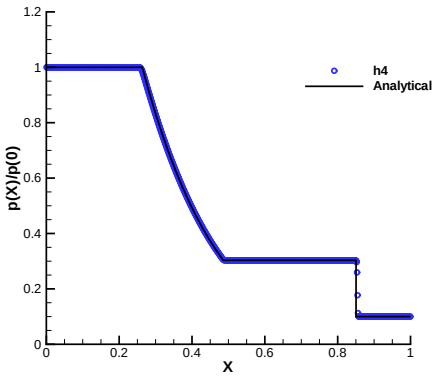

(f) Pressure, $h4$.

FIGURE B.18: *HLLC* **WENO** 5^{th}, $h3$ $h4$.

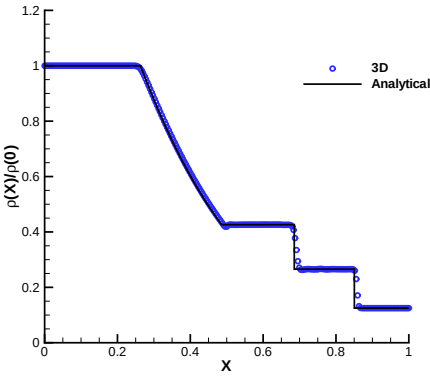

(a) Density, CBS.

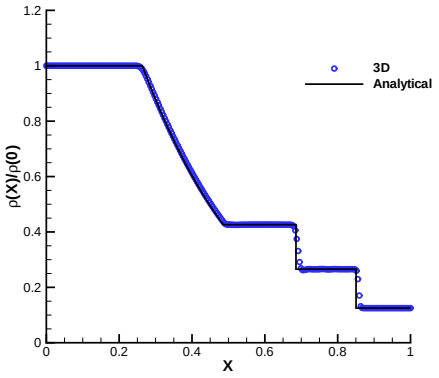

(b) Density, HLLC.

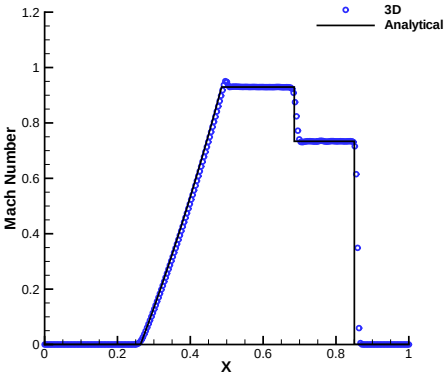

(c) Mach Number, CBS.

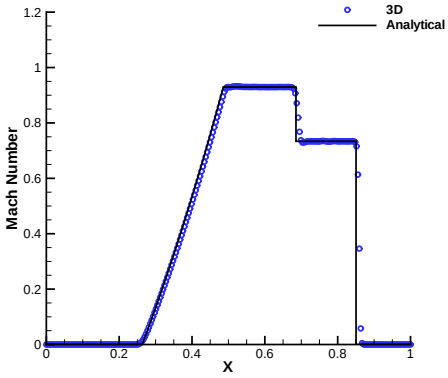

(d) Mach Number, HLLC.

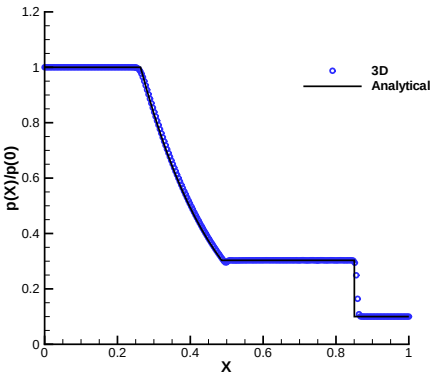

(e) Pressure, CBS.

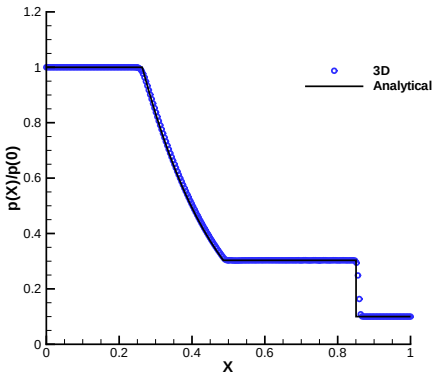

(f) Pressure, HLLC.

FIGURE B.19: **WENO** 5^{th}, $3D$.

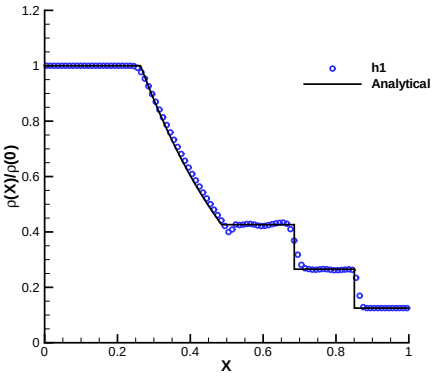

(a) Density, $h1$.

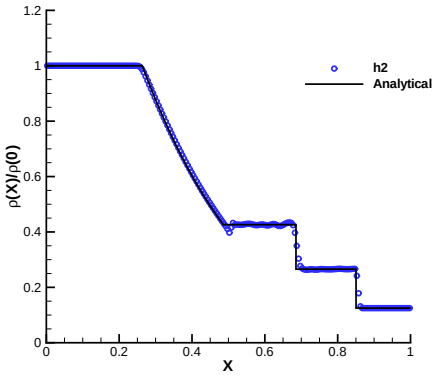

(b) Density, $h2$.

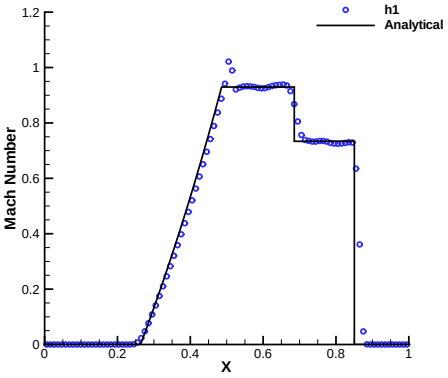

(c) Mach Number, $h1$.

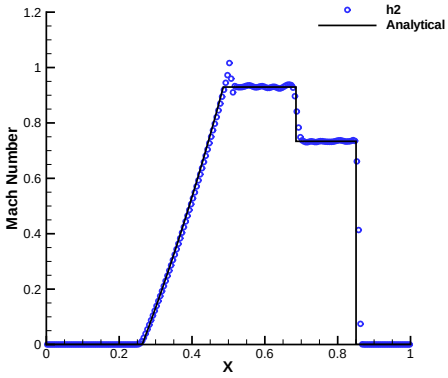

(d) Mach Number, $h2$.

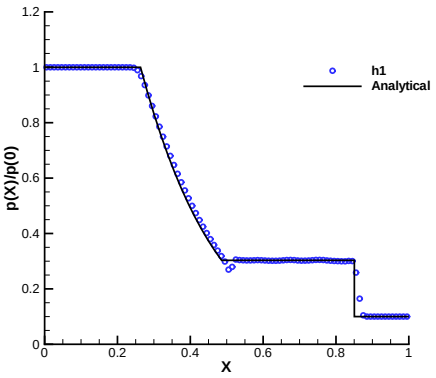

(e) Pressure, $h1$.

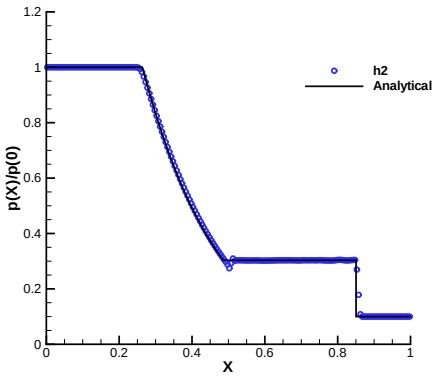

(f) Pressure, $h2$.

FIGURE B.20: *CBS* **WENO** 9^{th}, $h1$ $h2$.

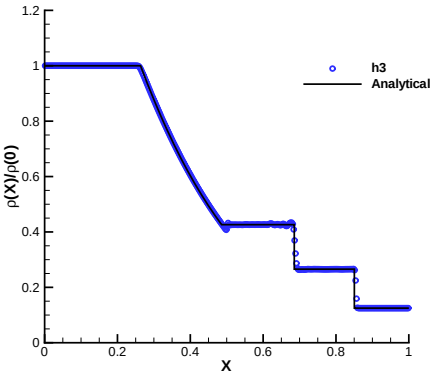

(a) Density, $h3$.

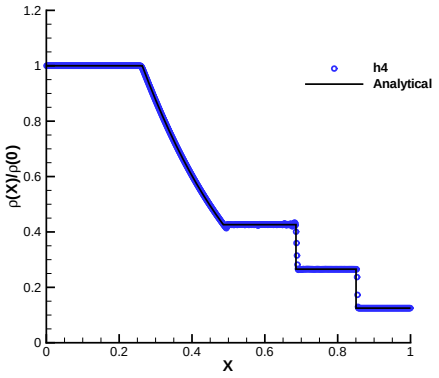

(b) Density, $h4$.

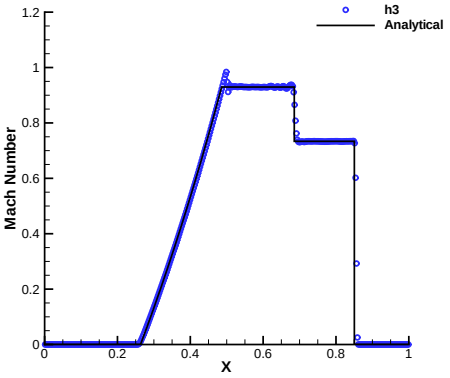

(c) Mach Number, $h3$.

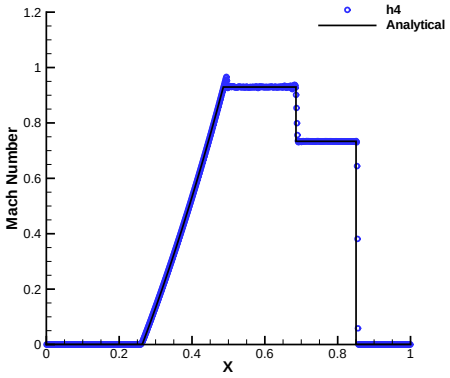

(d) Mach Number, $h4$.

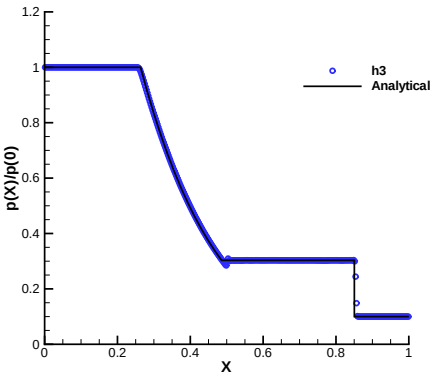

(e) Pressure, $h3$.

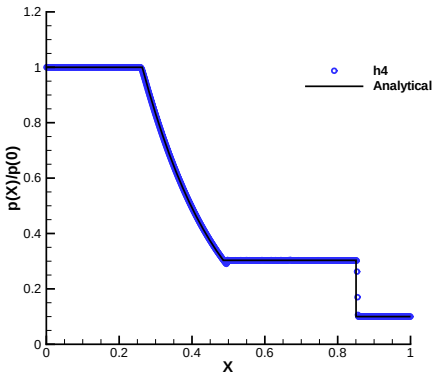

(f) Pressure, $h4$.

FIGURE B.21: *CBS* **WENO** 9^{th}, $h3$ $h4$.

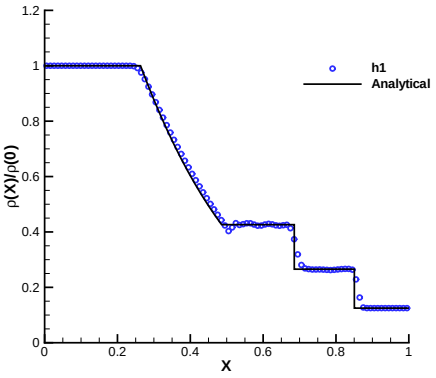

(a) Density, $h1$.

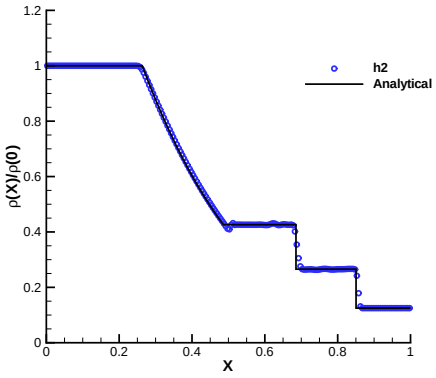

(b) Density, $h2$.

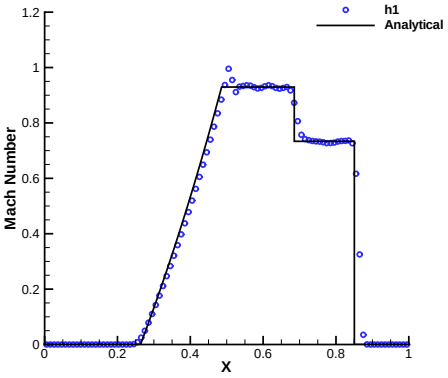

(c) Mach Number, $h1$.

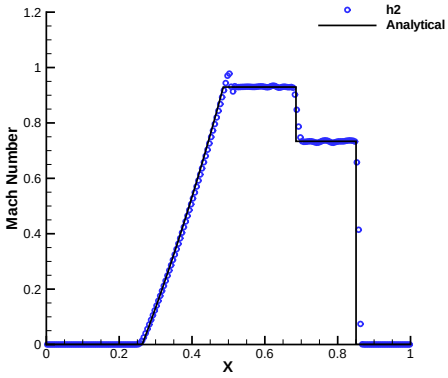

(d) Mach Number, $h2$.

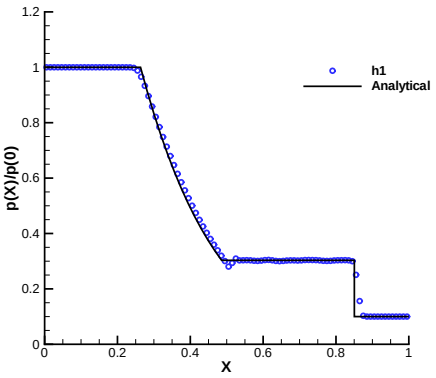

(e) Pressure, $h1$.

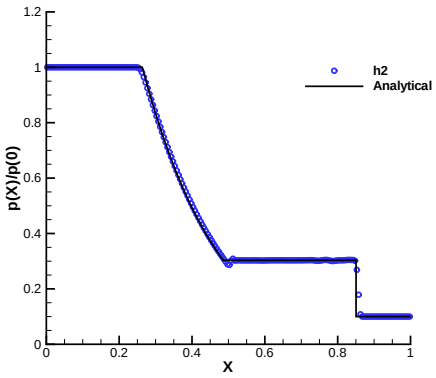

(f) Pressure, $h2$.

FIGURE B.22: *HLLC* **WENO** 9^{th}, $h1$ $h2$.

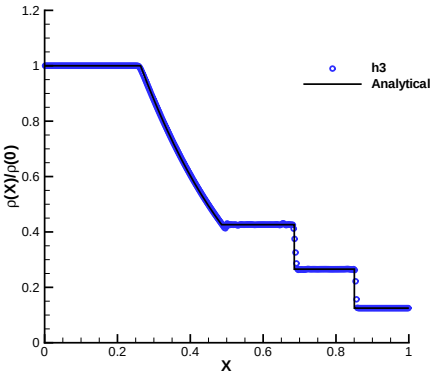

(a) Density, $h3$.

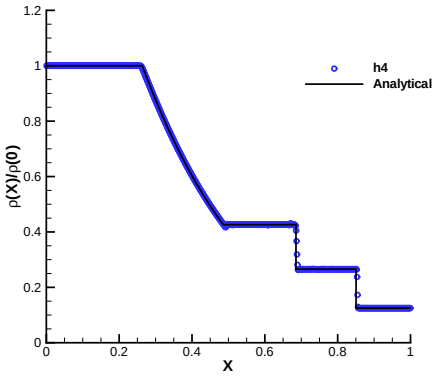

(b) Density, $h4$.

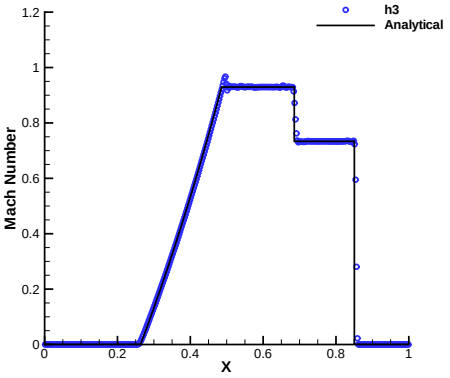

(c) Mach Number, $h3$.

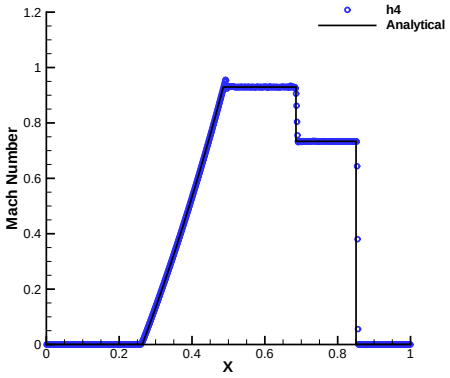

(d) Mach Number, $h4$.

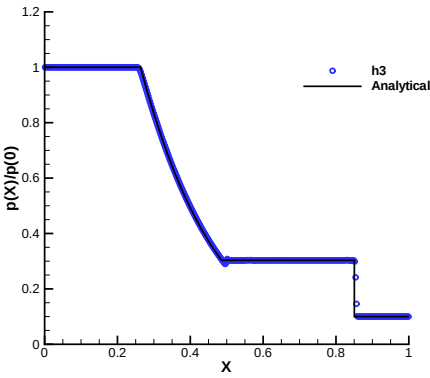

(e) Pressure, $h3$.

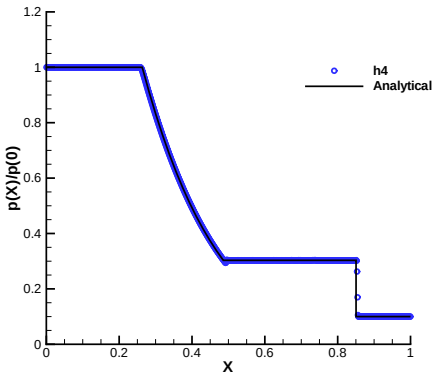

(f) Pressure, $h4$.

FIGURE B.23: *HLLC* **WENO** 9^{th}, $h3$ $h4$.

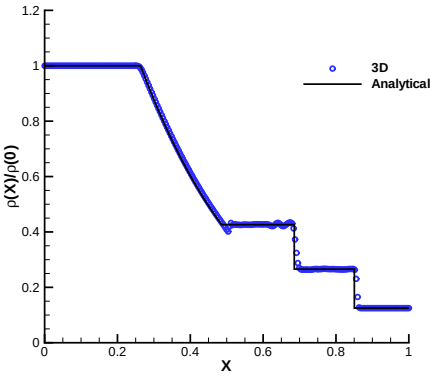

(a) Density, CBS.

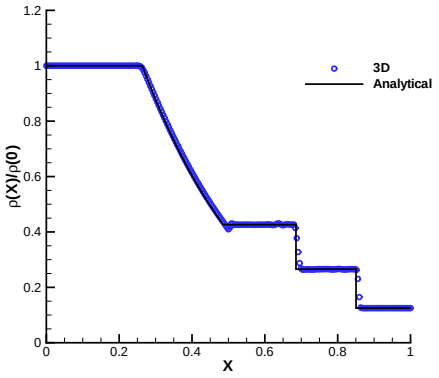

(b) Density, HLLC.

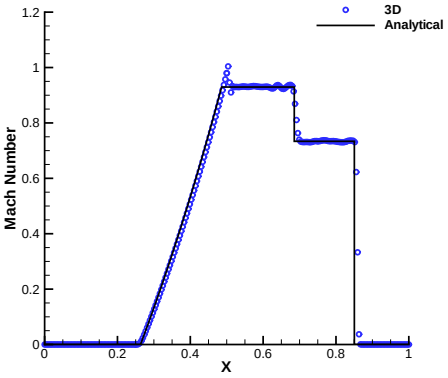

(c) Mach Number, CBS.

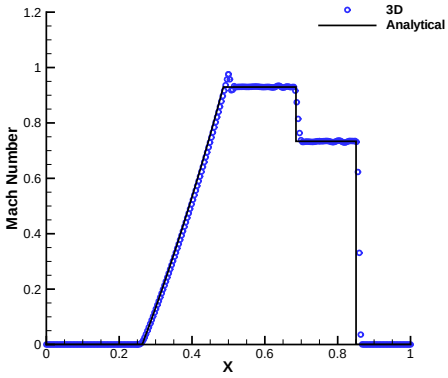

(d) Mach Number, HLLC.

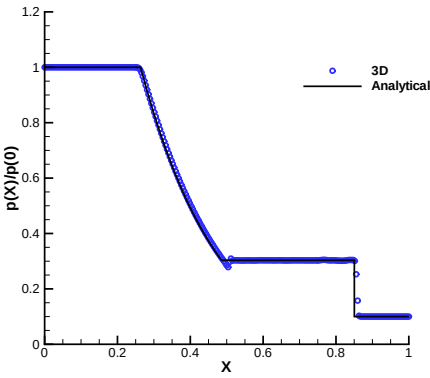

(e) Pressure, CBS.

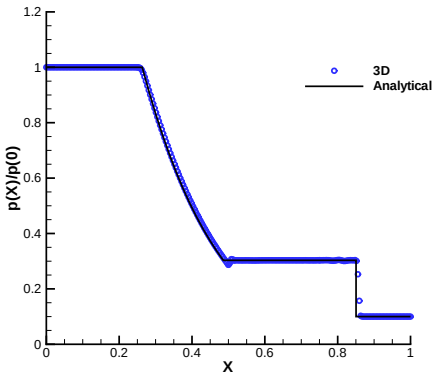

(f) Pressure, HLLC.

FIGURE B.24: *CBS* **WENO** 9^{th}, $3D$.

C

Clustering and Discretization

C.1 Domain Discretization and Clustering

In general, boundaries of free shear layers from jet flows are similar in shape, differing only in absolute size and slenderness ratio, τ. For the prediction of jet shape and the correspondent grid clustering the Method of Characteristics have been applied [122, 123]. This analysis predicts an ever expanding plume, which tends asymptotically to a maximum diameter. The contact surface, or free shear layer, is then represented in parametric form by a function which closely simulates the plume shape, but allows variability in size and slenderness ratio.

$$\frac{y}{y_m} = \frac{2n}{2n-1}\left(\left(\frac{x}{x_m}\right)^{0.5} - \frac{1}{2n}\left(\frac{x}{x_m}\right)^{n}\right). \tag{C.1}$$

A value of $n = 2.5$ has been chosen as most closely fitting the experimental results of [133]. The change of n affects only the external lateral force, which is proportional to the area under the plume's shape curve. By force and momentum balances it is possible to write a system of equations which allow us to calculate the plume's shape.

$$\frac{p_c}{p_\infty} = \left(\frac{x_m}{r^*}\right)^2 \frac{\tau}{2f_1}$$
$$\frac{y_m}{r^*} = \frac{x_m}{r^*}\tau, \tag{C.2}$$

where

$$f_1 = 2\lambda C_{Fmax}\left(\frac{c}{\pi}\right)^2 \int_0^{\theta_{max}} f(\theta)\sin^2\theta d\theta, \tag{C.3}$$

with,

$$f(\theta) = e^{-\lambda^2(1-\cos\theta)^2} \tag{C.4}$$

and

$$\lambda = \left(\pi^{1/2}\left(1 - \frac{C_{Fex}}{CC_{Fmax}}\right)\right)^{-1}. \tag{C.5}$$

The wake's maximum diameter location is only a function of the pressure ratio p_c/p_∞, and the slenderness ratio is only a function of exit Mach number. This approximate method underestimates but is able to predict the maximum wake diameter quite accurately, for pressure ratios values from 10 to 10^7.

C.1.1 Summary

Using this methodology, the discretization of the geometrical domain is performed on three levels:

- *Coarse* mesh with 500000 cells, with 16 blocks;
- *Medium* mesh with 1000000 cells, with 32 blocks;
- *Fine* mesh with 2000000 cells, with 64 blocks.

The following figures present the end result of the clustered domains that have been used in this study.

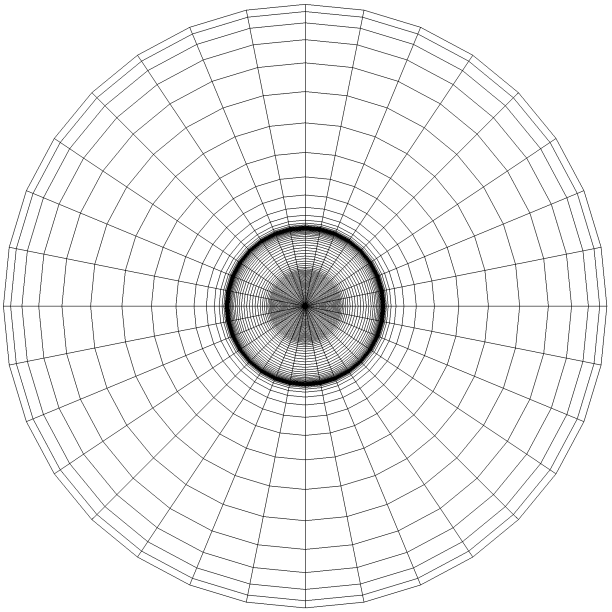

(a) Section $\odot YZ$.

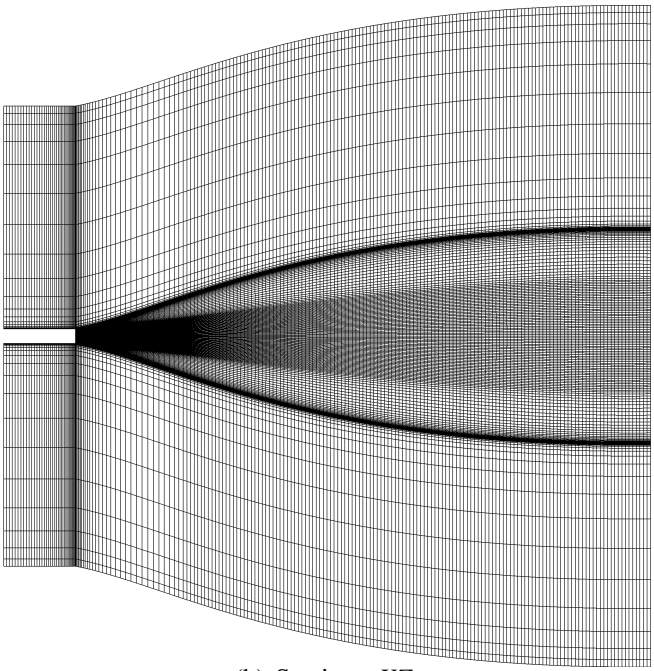

(b) Section $\odot XZ$.

Figure C.1: Jets domain, Coarse mesh.

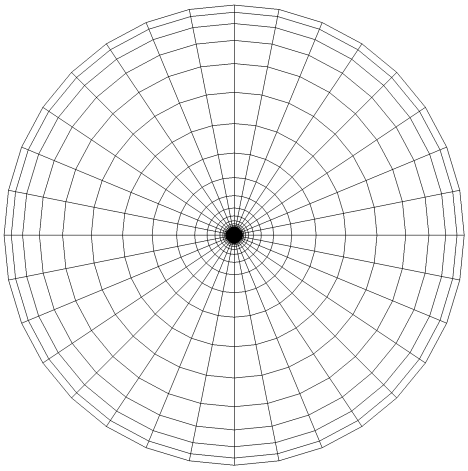

(a) Section $\odot YZ$.

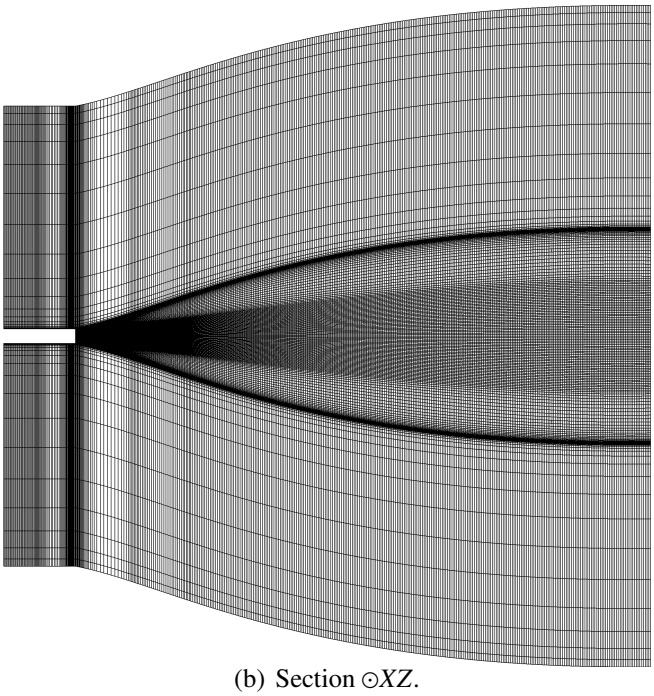

(b) Section $\odot XZ$.

Figure C.2: Jets domain, Medium mesh.

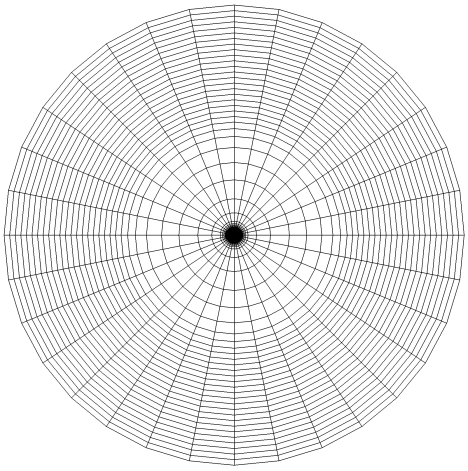

(a) Section $\odot YZ$.

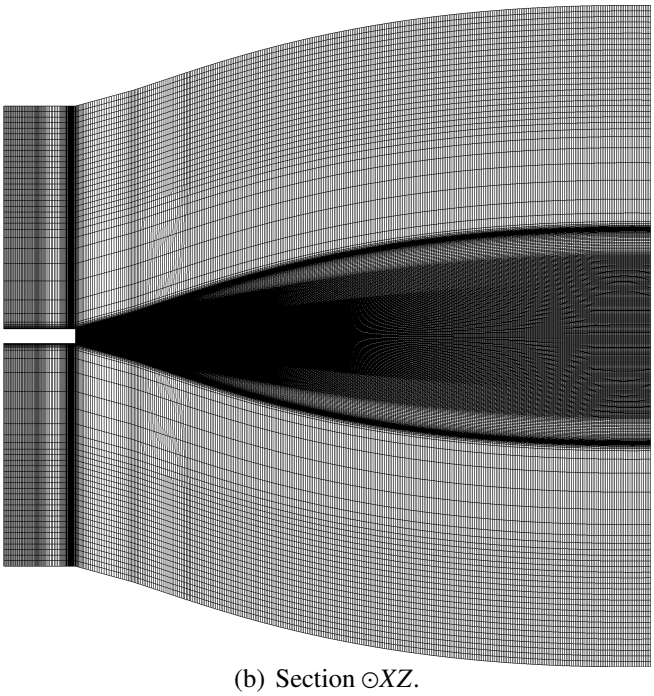

(b) Section $\odot XZ$.

Figure C.3: Jets domain, Fine mesh.

D

Reference Coordinate System

In this appendix, an analytical method for determining the jets core length size is presented. From the work of [33], a general equation for the mean velocity distribution has been determined and employed. The velocity distribution, over the jet's central line, can be approximately computed using the following formula, for an isothermal and isobaric jet:

$$\frac{U}{U_{Jet}} = 1 - e^{\left(\frac{1.35}{\left(1 - \frac{X}{X_c}\right)}\right)}, \tag{D.1}$$

for the range of $0.3 \leq Ma \leq 1.4$, with the jet's core length (X_c) computed as:

$$X_c = 4.2 + 1.1 Ma_{Jet}^2. \tag{D.2}$$

The following table shows the empirical jet sizes core length for the Static and Co-flow jet cases.

Core length size	**Static Jet**	**Co-flow Jet**
X_c	5.10	4.67

Table D.1: Central line predicted results, jets core length size.

In order to calculate the value of X_0 for each case, the decay rate slope has been fitted with the experimental velocity decay rate. The same slope is then shifted along the abscissa axis until the correspondent slope becomes tangential to the predicted velocity decay rate distribution. The X_0 value will be determined by the intersection of the correspondent slope with the abscissa axis. The following formulation has been employed to compute the jet's inertial reference system location:

$$X_c = X_{Predictions} - X_0. \tag{D.3}$$

The figures of the following sections, illustrate are the grafical computation of the jet's virtual origin value X_0.

D.1 Static Jet

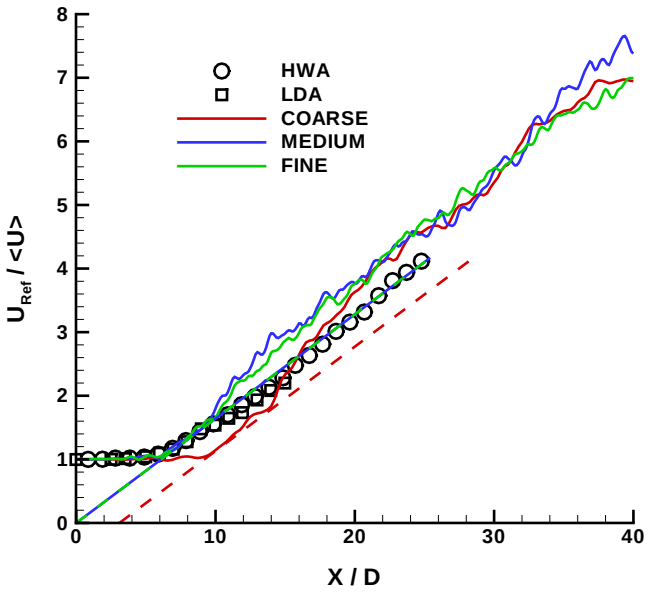

Figure D.1: Static Jet Central Line decay rate, *h*-study. **HWA**[111] and **LDA**[33].

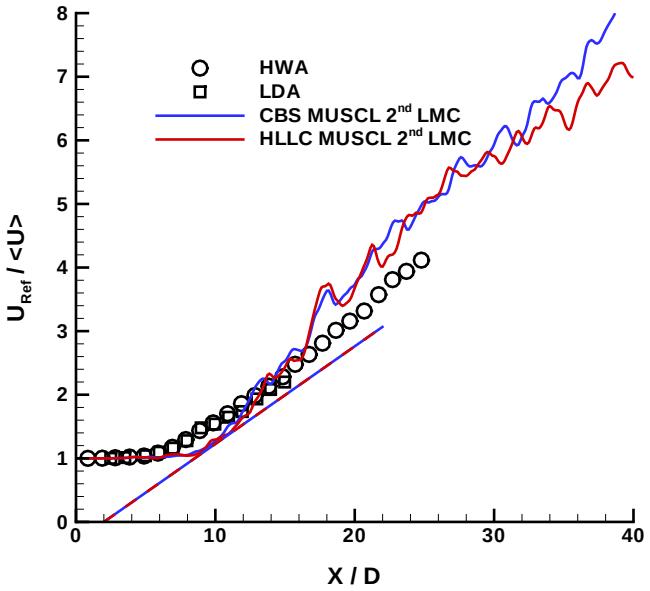

FIGURE D.2: Static Jet Central Line decay rate, **MUSCL** 2^{nd} **LMC**, p-study. **HWA**[111] and **LDA**[33].

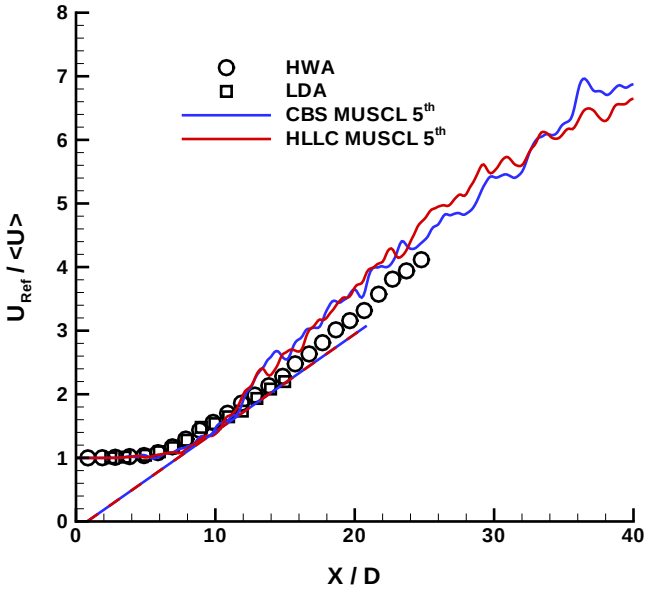

FIGURE D.3: Static Jet Central Line decay rate, **MUSCL** 5^{th}, p-study. **HWA**[111] and **LDA**[33].

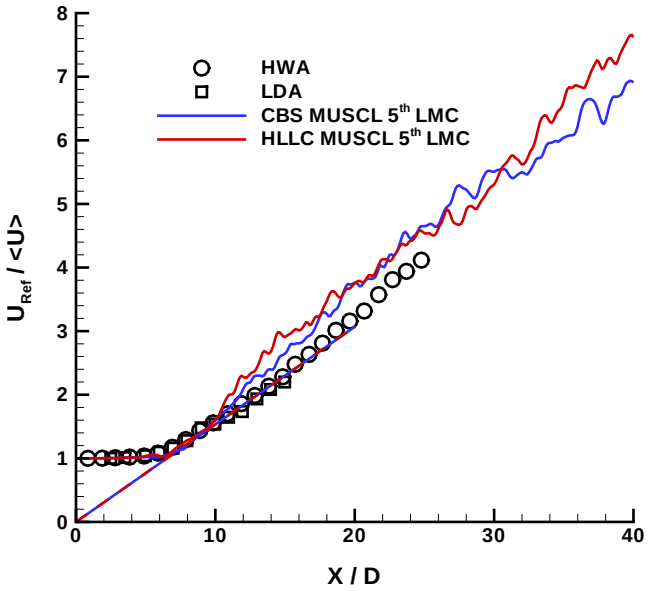

Figure D.4: Static Jet Central Line decay rate, **MUSCL** 5^{th} **LMC**, p-study. **HWA**[111] and **LDA**[33].

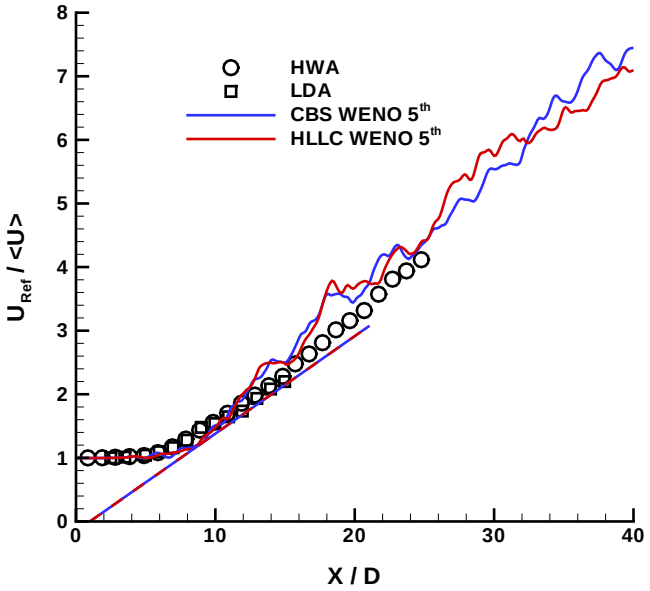

Figure D.5: Static Jet Central Line decay rate, **WENO** 5^{th}, p-study. **HWA**[111] and **LDA**[33].

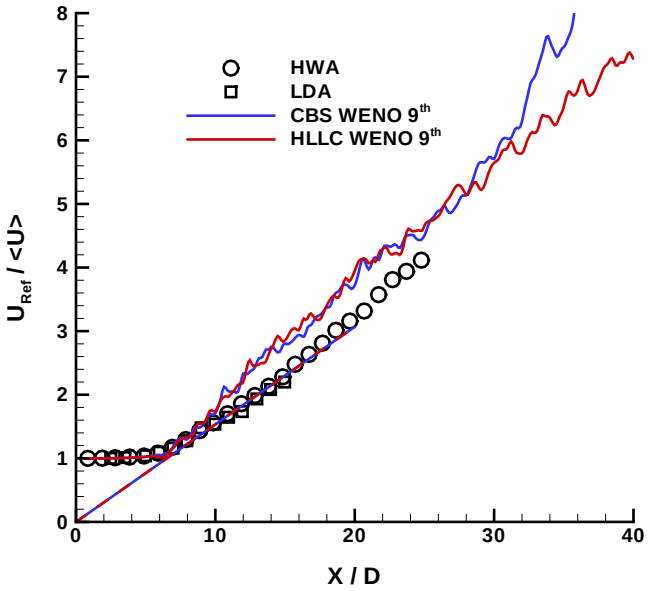

Figure D.6: Static Jet Central Line decay rate, **WENO** 9^{th}, p-study. **HWA**[111] and **LDA**[33].

D.2 Co-flow Jet

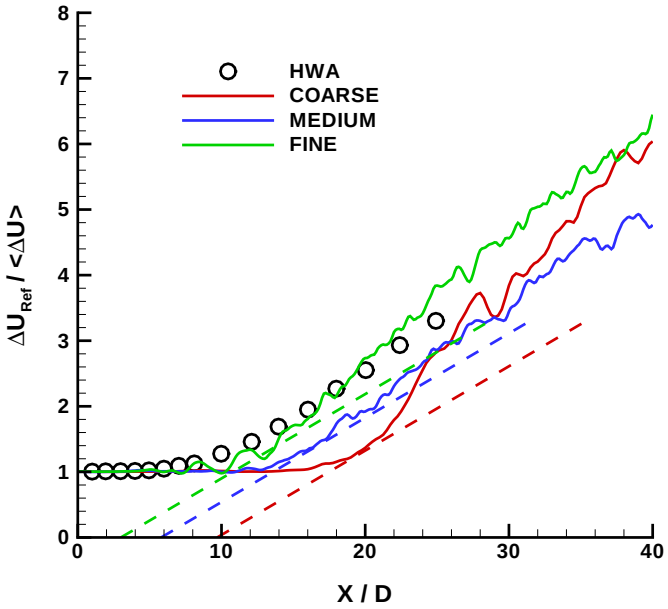

Figure D.7: Co-flow Jet Central Line decay rate, *h*-study. **HWA**[111].

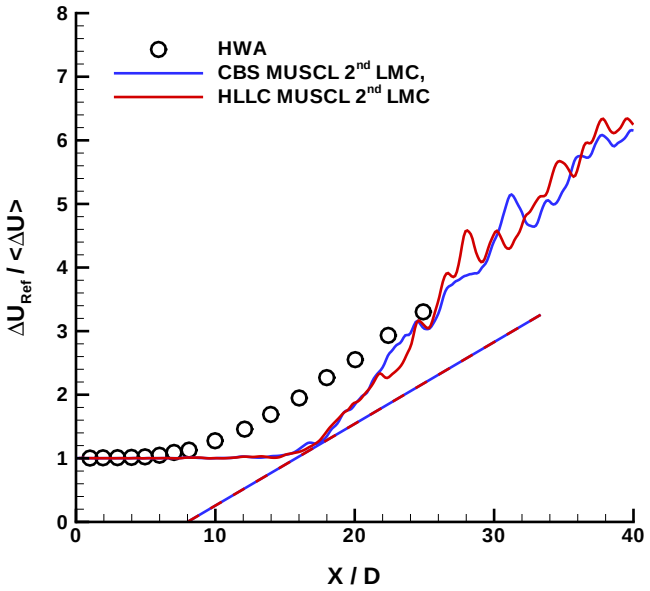

Figure D.8: Co-Flow Jet Central Line decay rate, **MUSCL** 2^{nd} **LMC**, p-study. **HWA**[111].

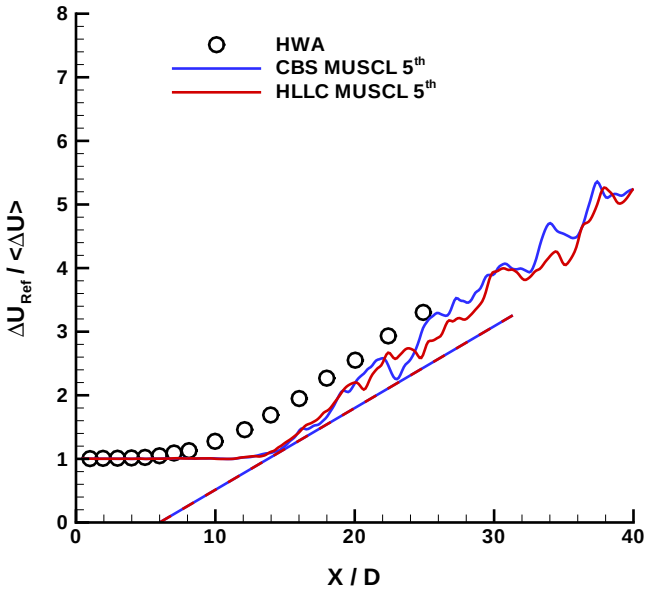

Figure D.9: Co-Flow Jet Central Line decay rate, **MUSCL** 5^{th}, p-study. **HWA**[111].

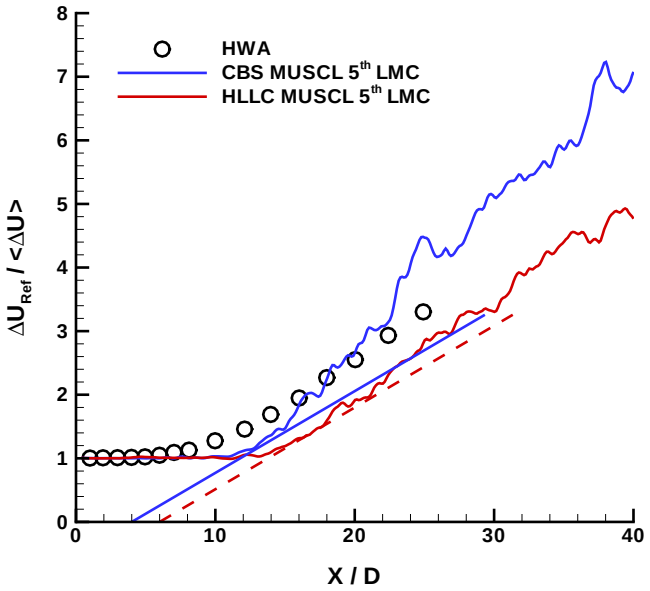

Figure D.10: Co-Flow Jet Central Line decay rate, **MUSCL** 5^{th} **LMC**, p-study. **HWA**[111].

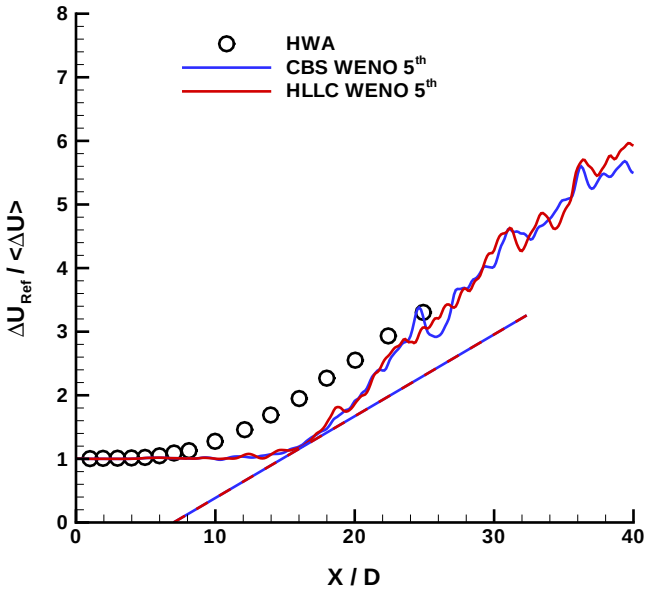

Figure D.11: Co-Flow Jet Central Line decay rate, **WENO** 5^{th}, p-study. **HWA**[111].

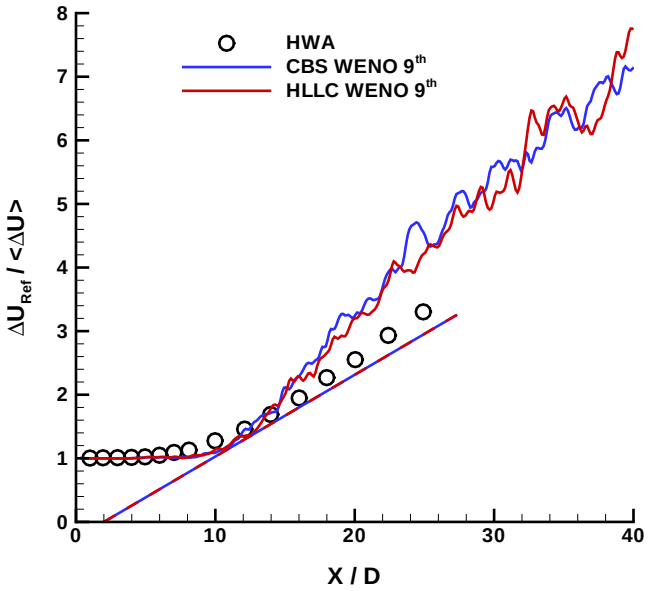

Figure D.12: Co-Flow Jet Central Line decay rate, **WENO** 9^{th}, p-study. **HWA**[111].

E

Error Bar

In this appendix, the *p*-study results from both jet cases are presented by Riemann solver. The velocity distributions results are from the jet inertial reference system.

E.1 Static Jet

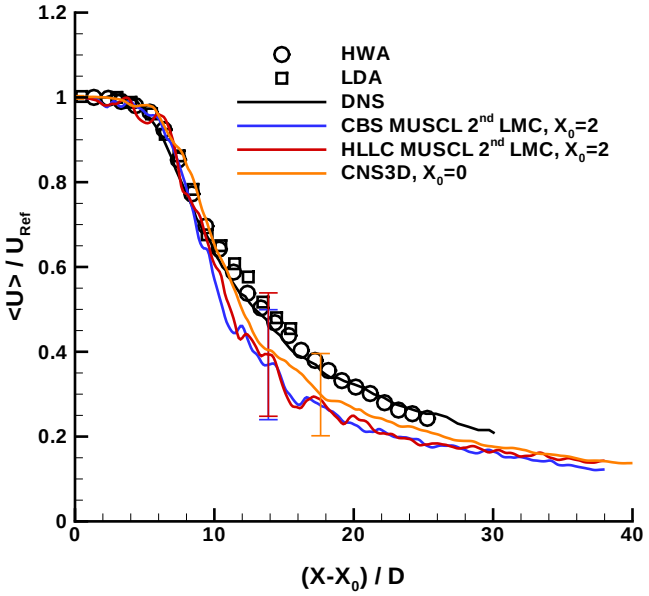

FIGURE E.1: Static Jet Central Line velocity distribution, **MUSCL** 2^{nd} **LMC**, p-study.

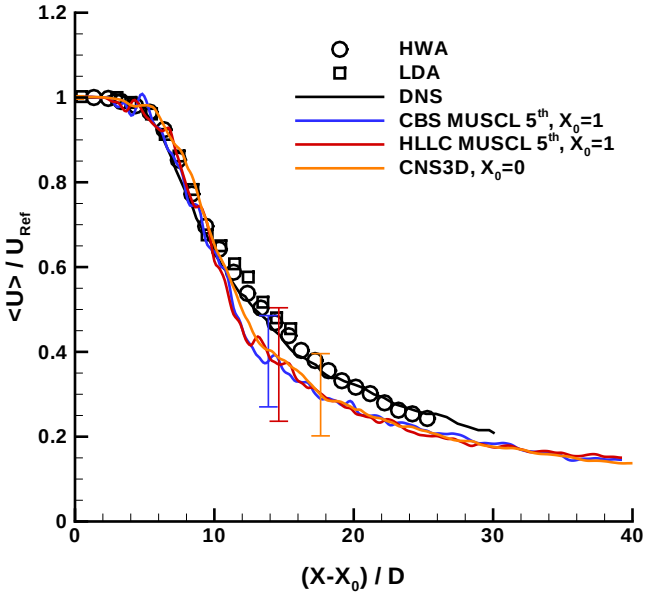

FIGURE E.2: Static Jet Central Line velocity distribution, **MUSCL** 5^{th}, p-study.

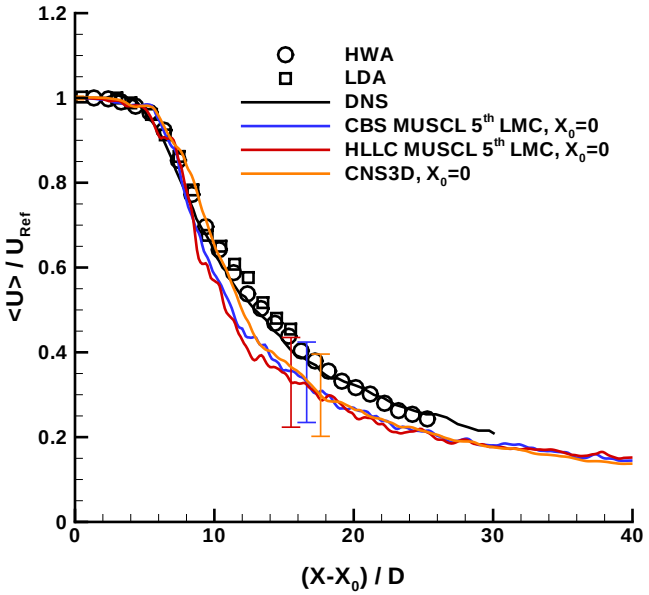

Figure E.3: Static Jet Central Line velocity distribution, **MUSCL** 5^{th} **LMC**, *p*-study.

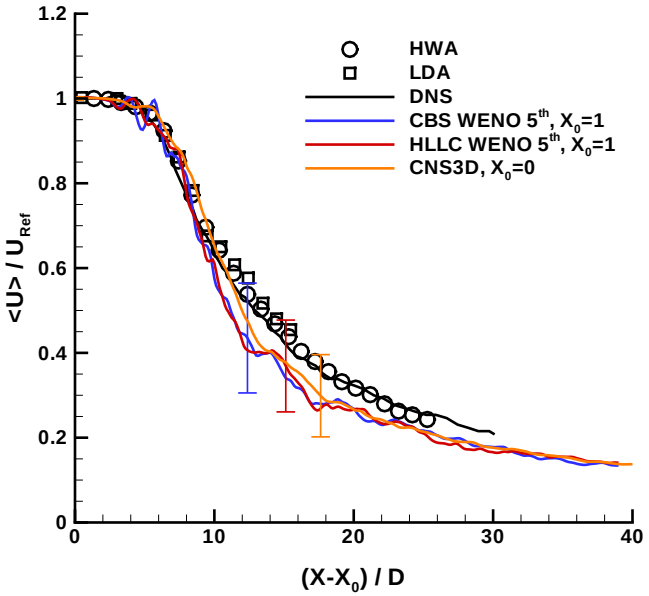

Figure E.4: Static Jet Central Line velocity distribution, **WENO** 5^{th}, *p*-study.

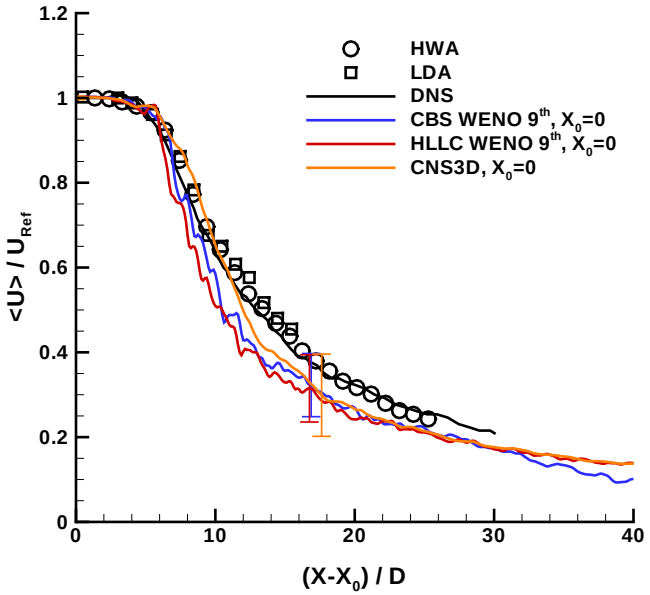

Figure E.5: Static Jet Central Line velocity distribution, **WENO** 9^{th}, *p*-study.

E.2 Co-flow Jet

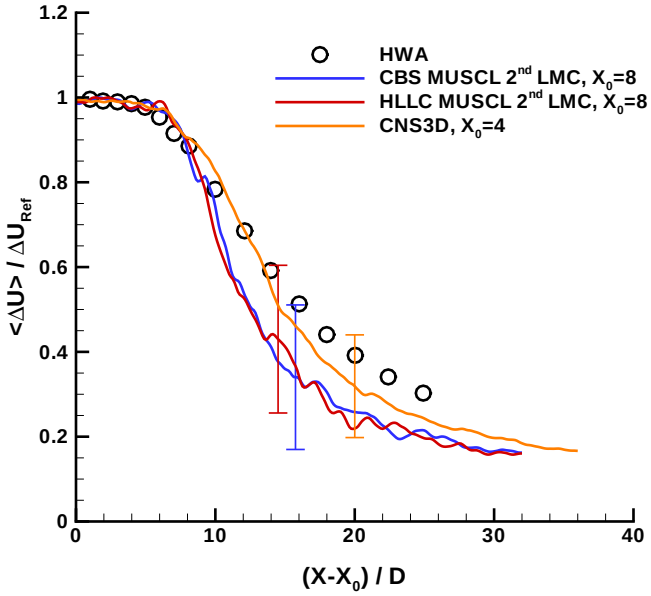

Figure E.6: Co-Flow Jet Central Line velocity distribution, **MUSCL** 2^{nd} **LMC**, *p*-study.

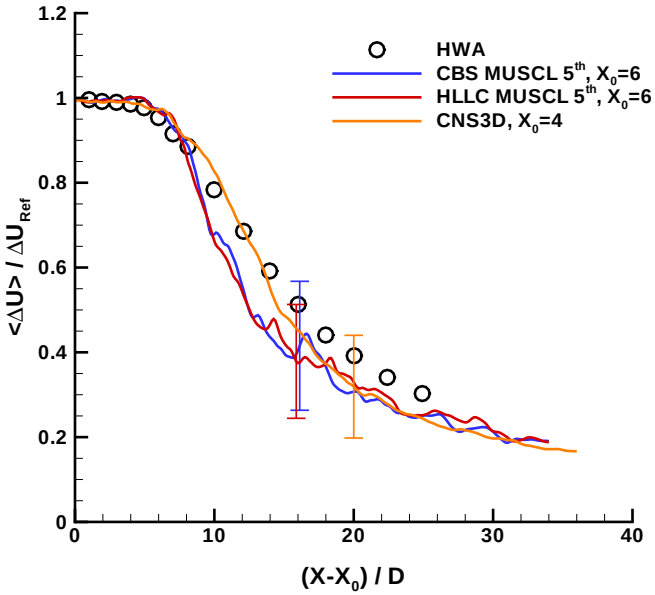

Figure E.7: Co-Flow Jet Central Line velocity distribution, **MUSCL** 5^{th}, *p*-study.

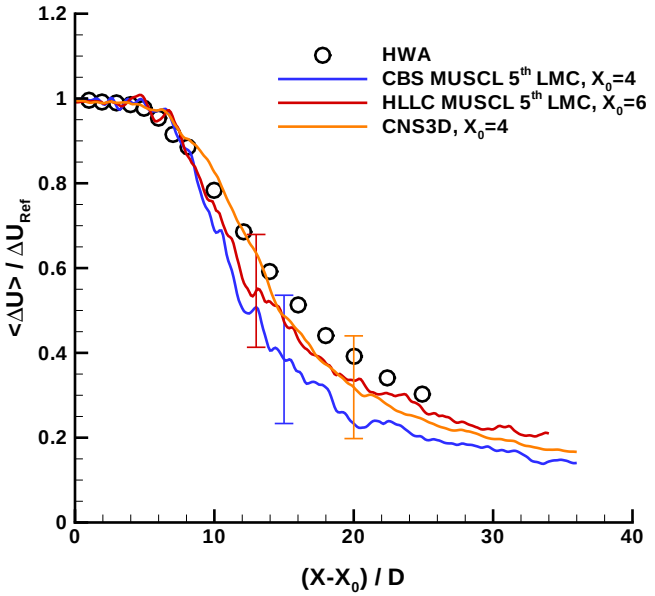

Figure E.8: Co-Flow Jet Central Line velocity distribution, **MUSCL** 5^{th} **LMC**, *p*-study.

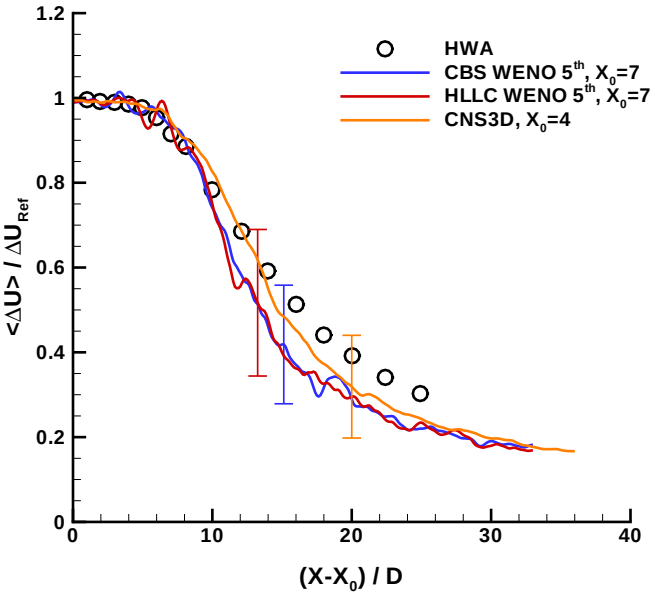

Figure E.9: Co-Flow Jet Central Line velocity distribution, **WENO** 5^{th}, p-study.

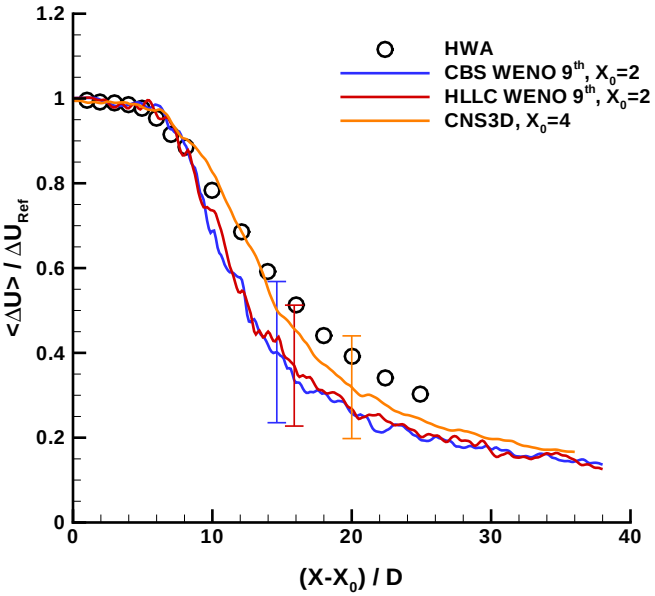

Figure E.10: Co-Flow Jet Central Line velocity distribution, **WENO** 9^{th}, p-study.

F

Mathematical and Physical Steady State

In this appendix, the statistical and similarity results of both jet cases are presented for all the selected methodologies employed in this thesis.

F.1 Static Jet

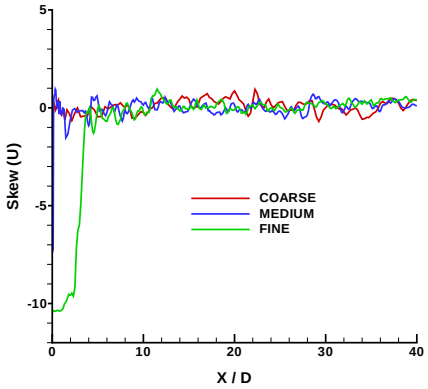

(a) Central Line final value.

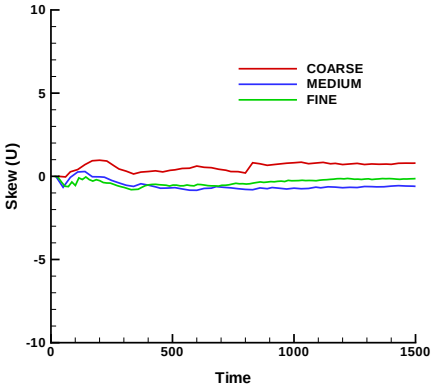

(b) Point $\frac{X}{D} = 20$.

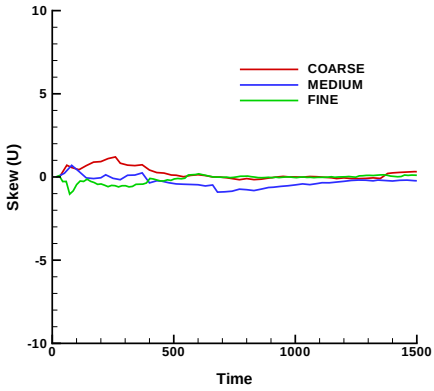

(c) Point $\frac{X}{D} = 25$.

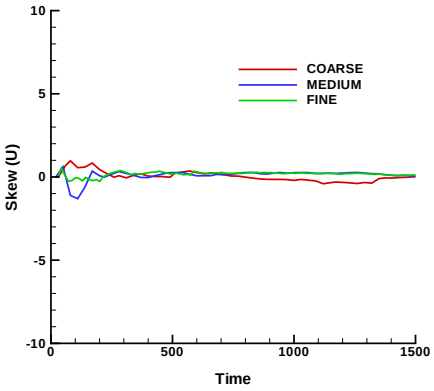

(d) Point $\frac{X}{D} = 30$.

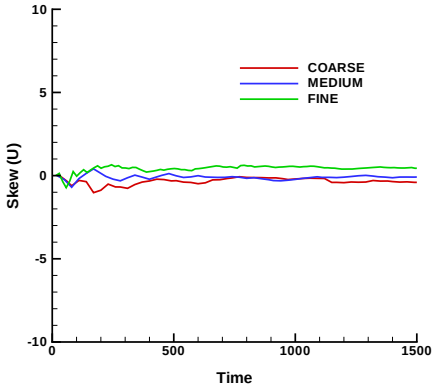

(e) Point $\frac{X}{D} = 35$.

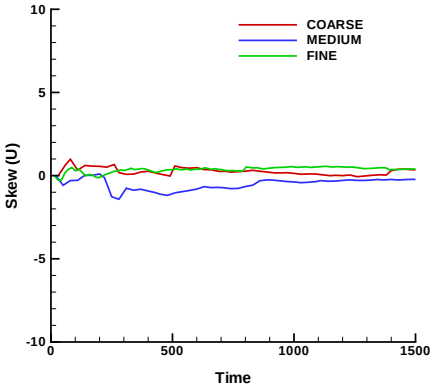

(f) Point $\frac{X}{D} = 40$.

Figure F.1: Skewness results, *h*-study.

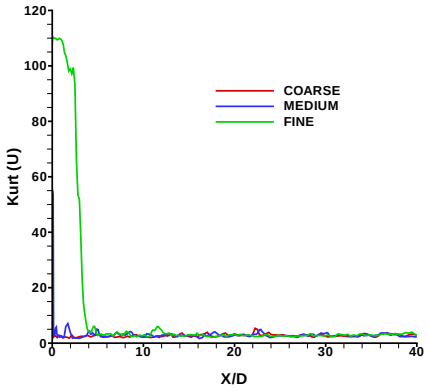

(a) Central Line final value.

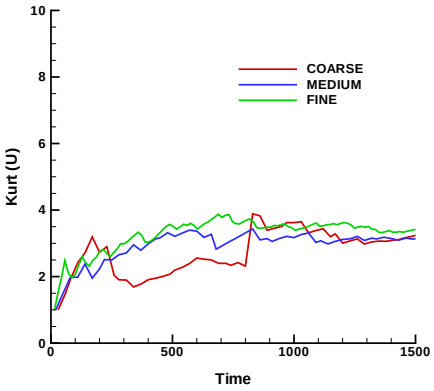

(b) Point $\frac{X}{D} = 20$.

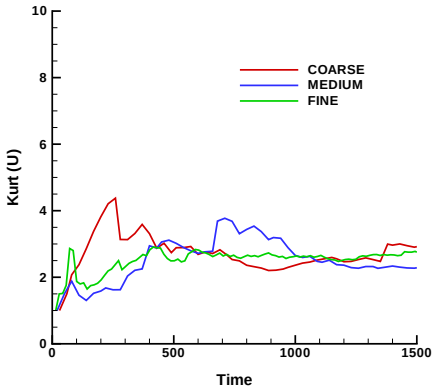

(c) Point $\frac{X}{D} = 25$.

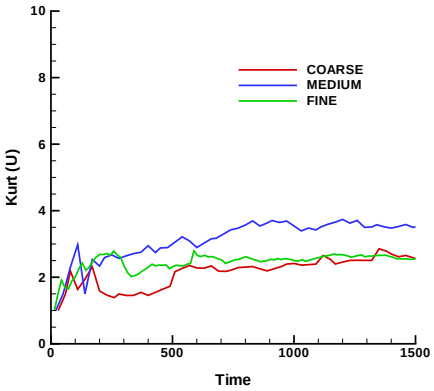

(d) Point $\frac{X}{D} = 30$.

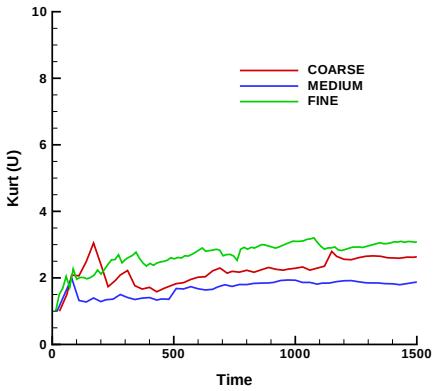

(e) Point $\frac{X}{D} = 35$.

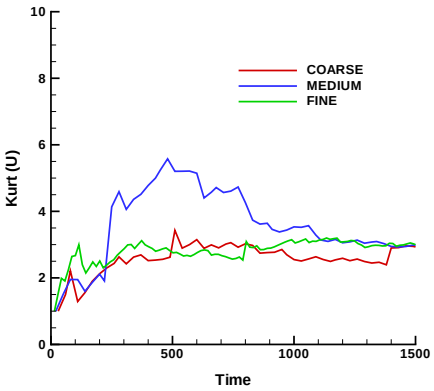

(f) Point $\frac{X}{D} = 40$.

Figure F.2: Kurtosis results, *h*-study.

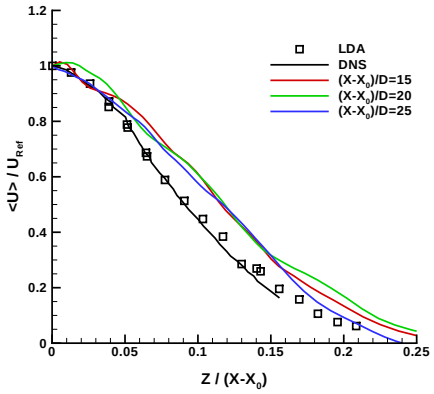

(a) **Coarse** mesh.

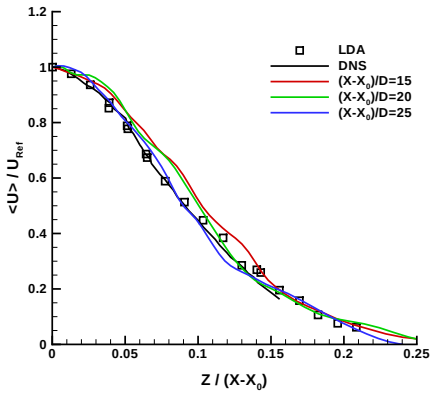

(b) **Medium** mesh.

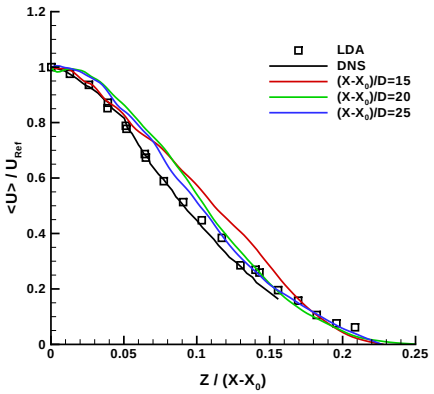

(c) **Fine** mesh.

Figure F.3: Similarity profiles, *h*-study.

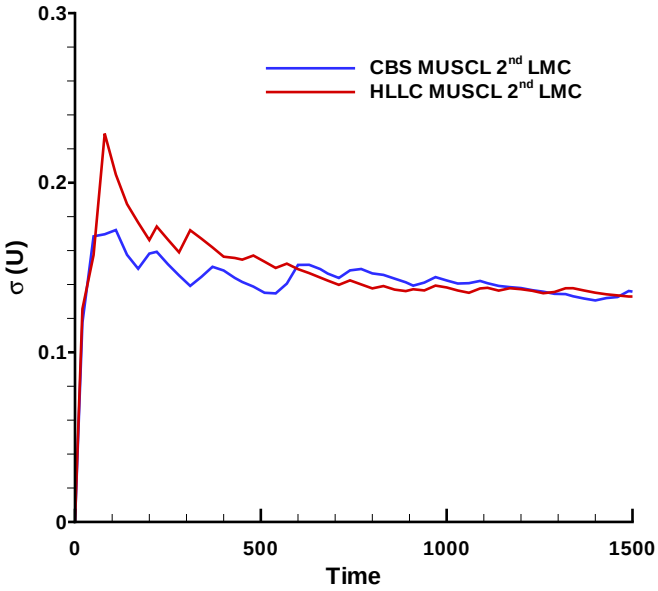

Figure F.4: Domains Maximum Standard Deviation, **MUSCL** 2^{nd} **LMC**, *p*-study.

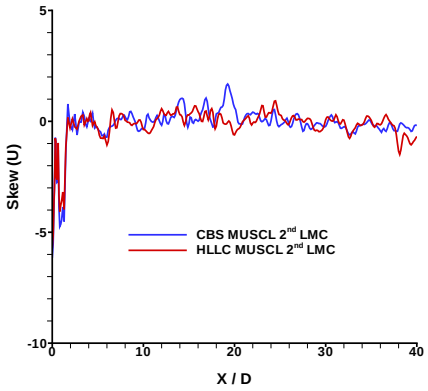

(a) Central Line final value.

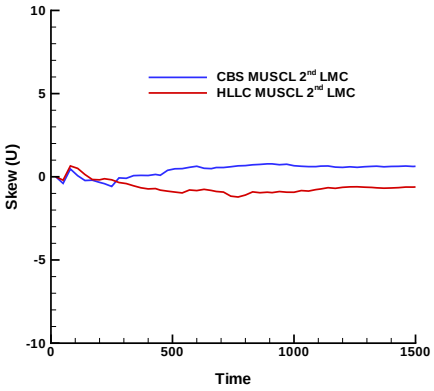

(b) Point $\frac{X}{D} = 20$.

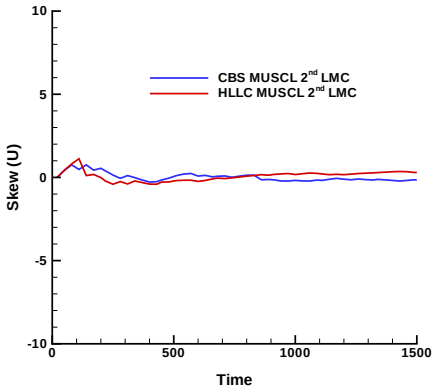

(c) Point $\frac{X}{D} = 25$.

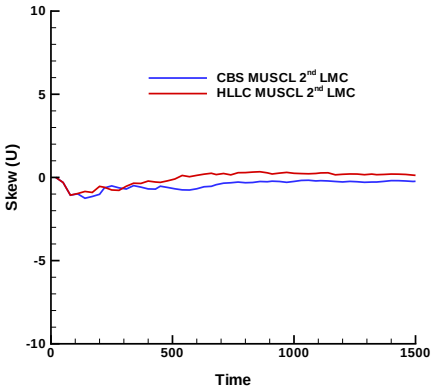

(d) Point $\frac{X}{D} = 30$.

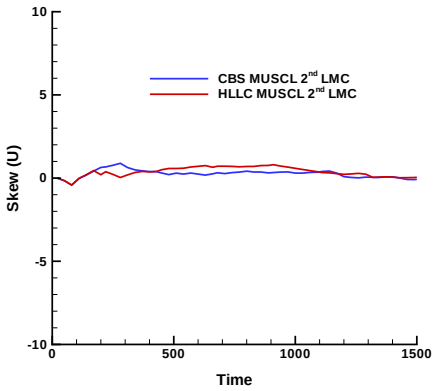

(e) Point $\frac{X}{D} = 35$.

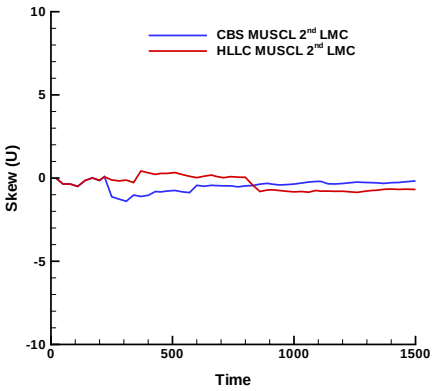

(f) Point $\frac{X}{D} = 40$.

Figure F.5: Skewness results, **MUSCL** 2^{nd} **LMC**, p-study.

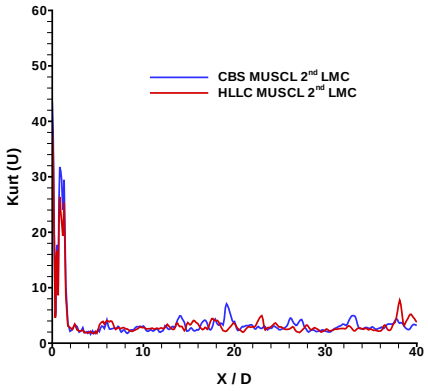

(a) Central Line final value.

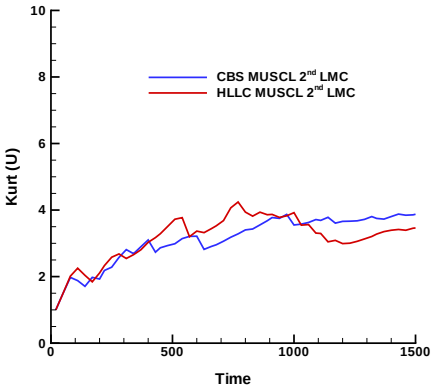

(b) Point $\frac{X}{D} = 20$.

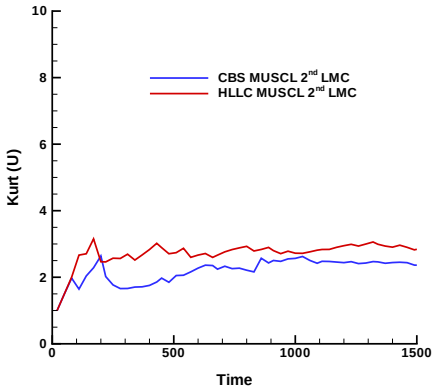

(c) Point $\frac{X}{D} = 25$.

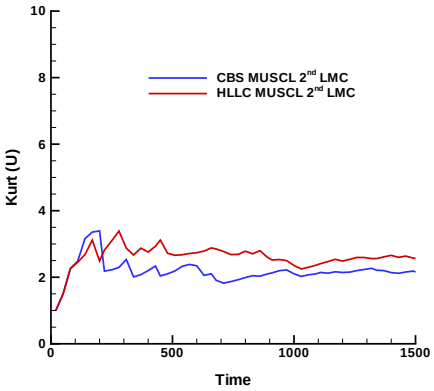

(d) Point $\frac{X}{D} = 30$.

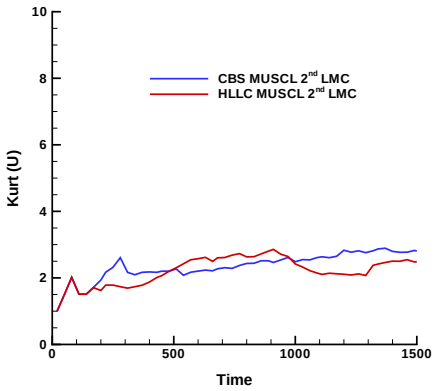

(e) Point $\frac{X}{D} = 35$.

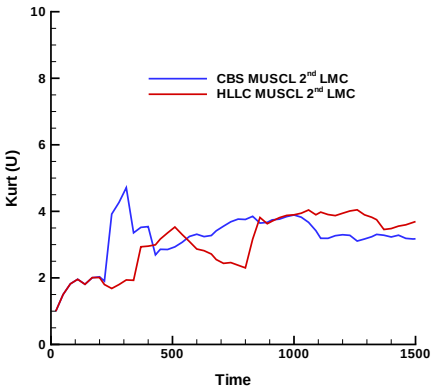

(f) Point $\frac{X}{D} = 40$.

Figure F.6: Kurtosis results, **MUSCL** 2^{nd} **LMC**, p-study.

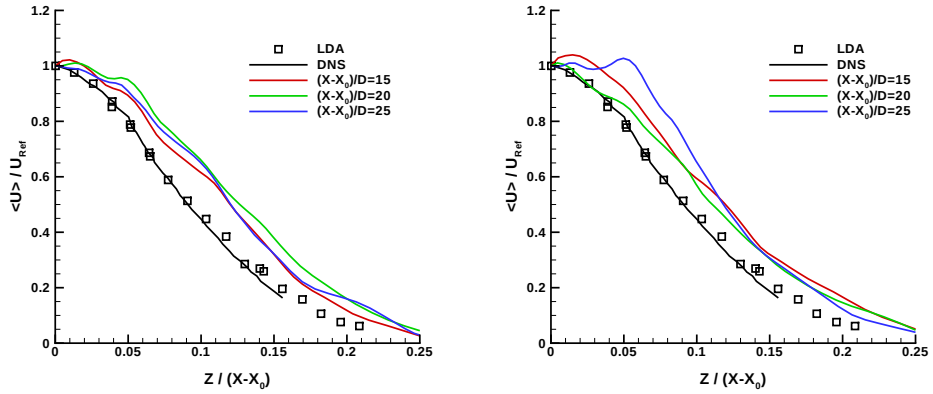

(a) **CBS**. (b) **HLLC**.

Figure F.7: Similarity profiles, **MUSCL** 2^{nd} **LMC**, p-study.

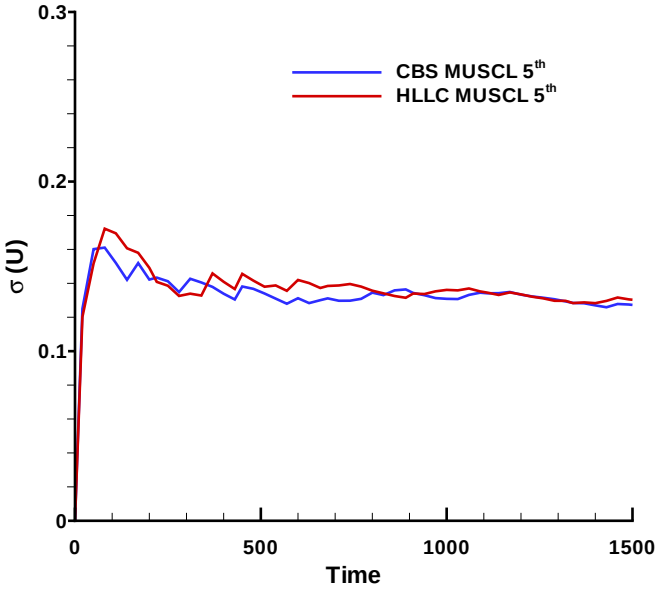

Figure F.8: Domains Maximum Standard Deviation, **MUSCL** 5^{th}, p-study.

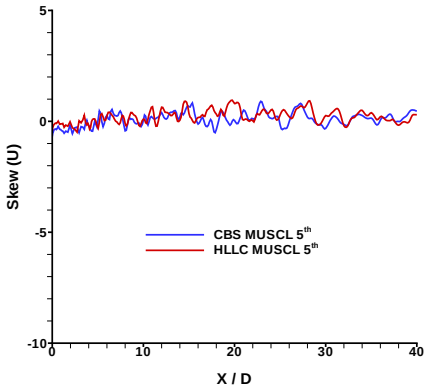

(a) Central Line final value.

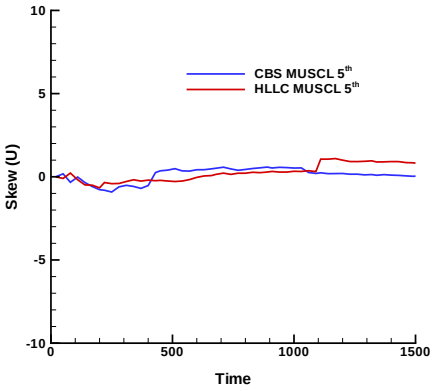

(b) Point $\frac{X}{D} = 20$.

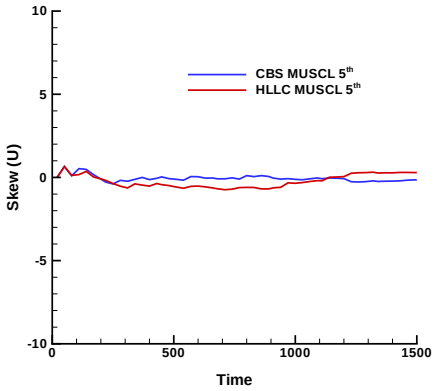

(c) Point $\frac{X}{D} = 25$.

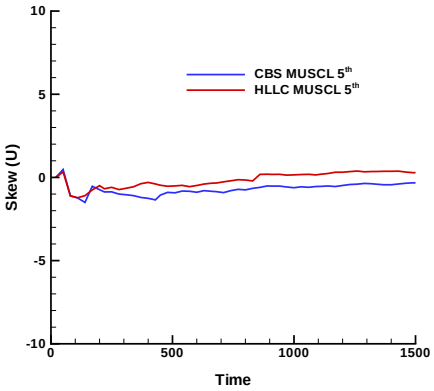

(d) Point $\frac{X}{D} = 30$.

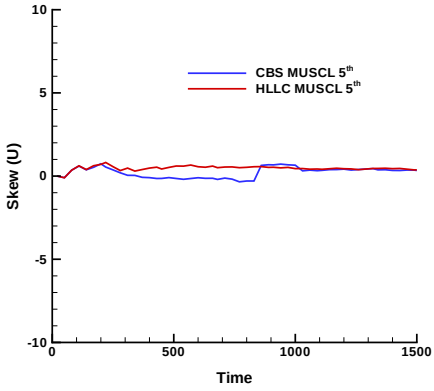

(e) Point $\frac{X}{D} = 35$.

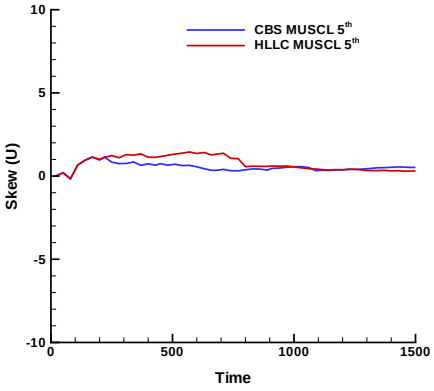

(f) Point $\frac{X}{D} = 40$.

Figure F.9: Skewness results, **MUSCL** 5^{th}, p-study.

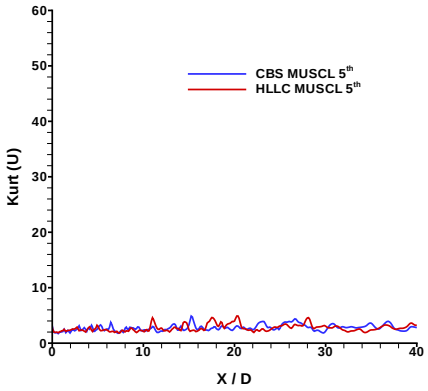

(a) Central Line final value.

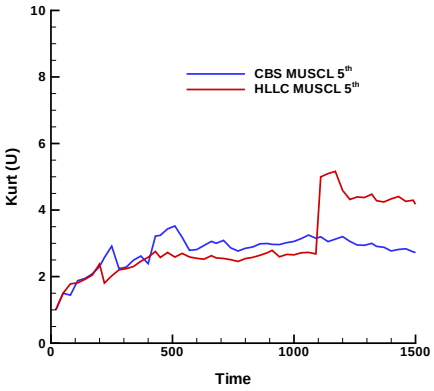

(b) Point $\frac{X}{D} = 20$.

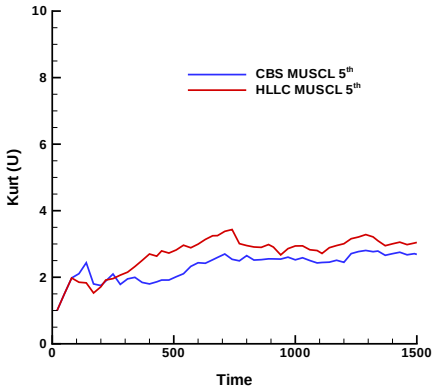

(c) Point $\frac{X}{D} = 25$.

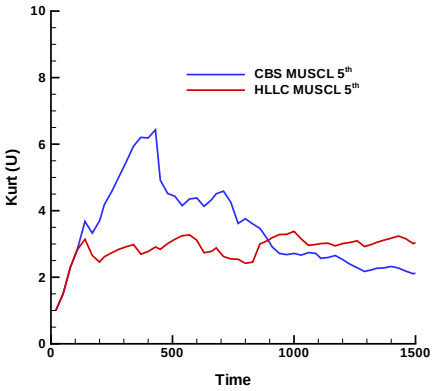

(d) Point $\frac{X}{D} = 30$.

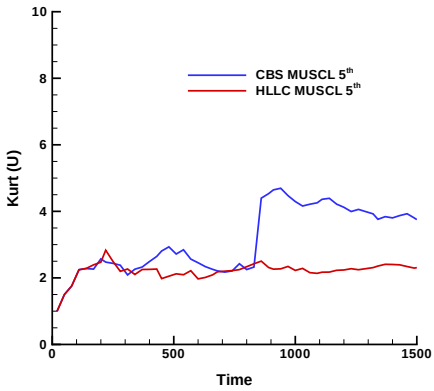

(e) Point $\frac{X}{D} = 35$.

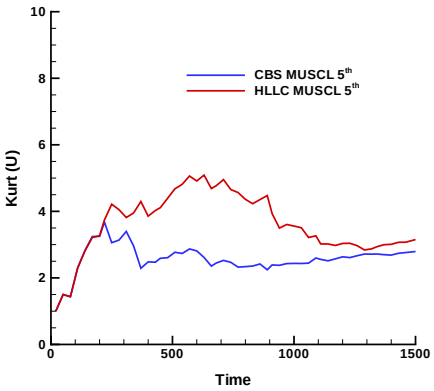

(f) Point $\frac{X}{D} = 40$.

Figure F.10: Kurtosis results, **MUSCL** 5^{th}, p-study.

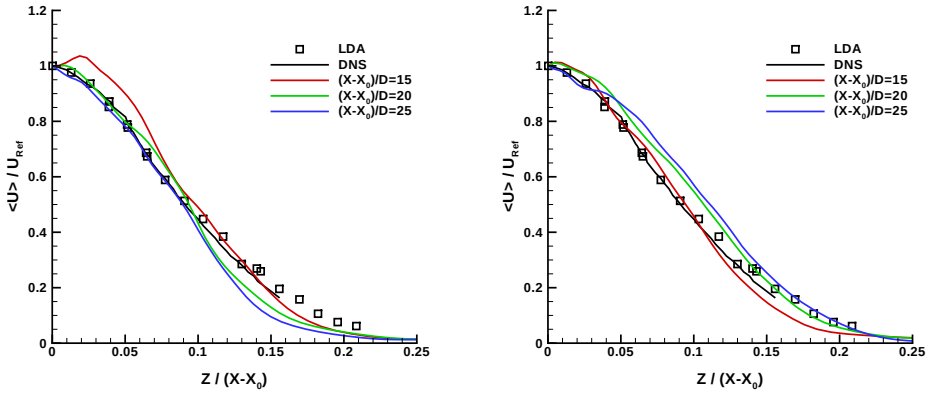

(a) **CBS**. (b) **HLLC**.

Figure F.11: Similarity profiles, **MUSCL** 5^{th}, p-study.

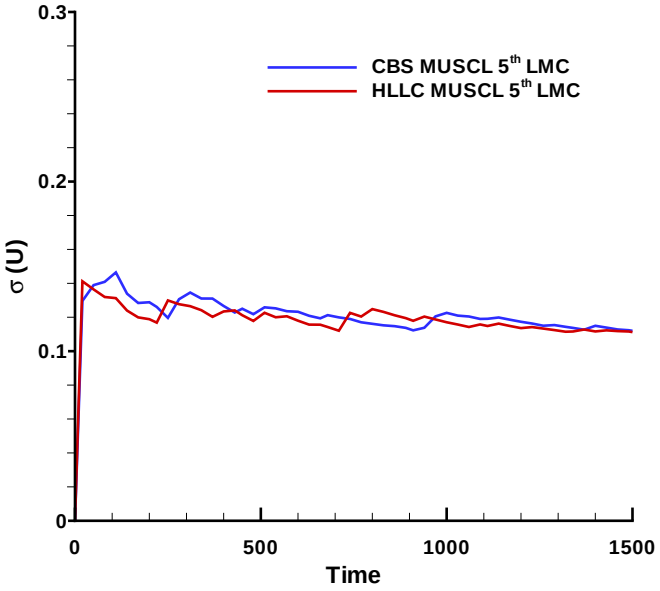

Figure F.12: Domains Maximum Standard Deviation, **MUSCL** 5^{th} **LMC**, p-study.

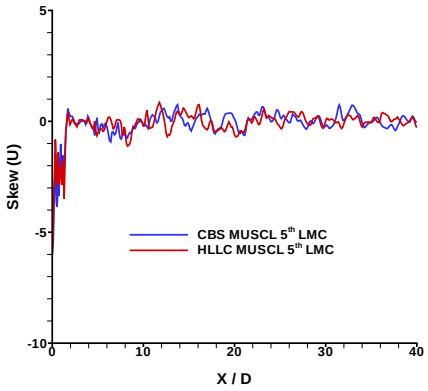

(a) Central Line final value.

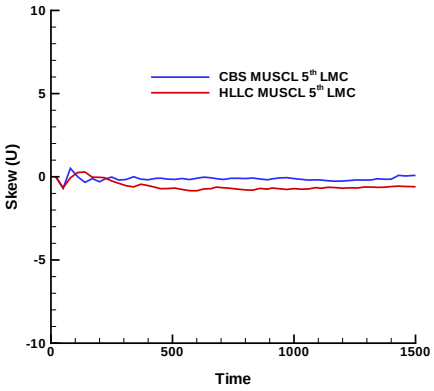

(b) Point $\frac{X}{D} = 20$.

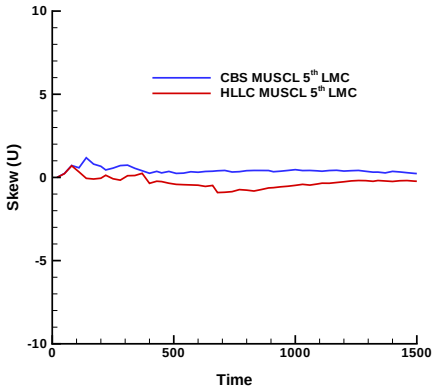

(c) Point $\frac{X}{D} = 25$.

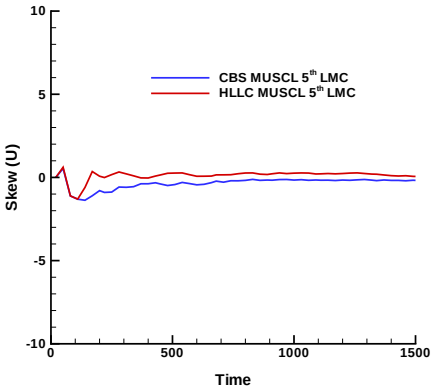

(d) Point $\frac{X}{D} = 30$.

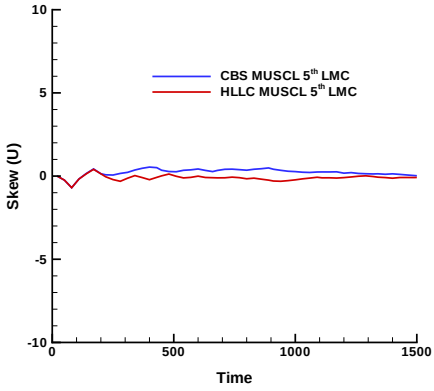

(e) Point $\frac{X}{D} = 35$.

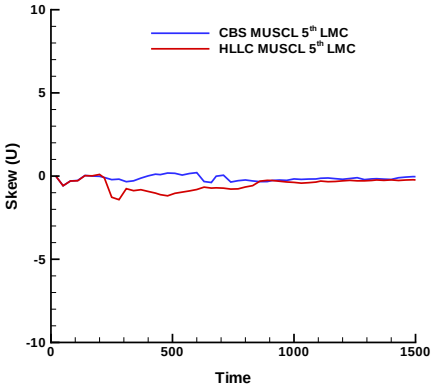

(f) Point $\frac{X}{D} = 40$.

FIGURE F.13: Skewness results, **MUSCL** 5^{th} **LMC**, p-study.

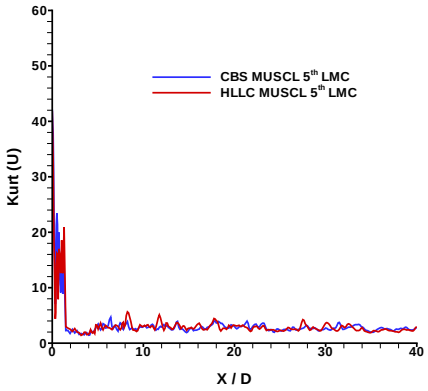

(a) Central Line final value.

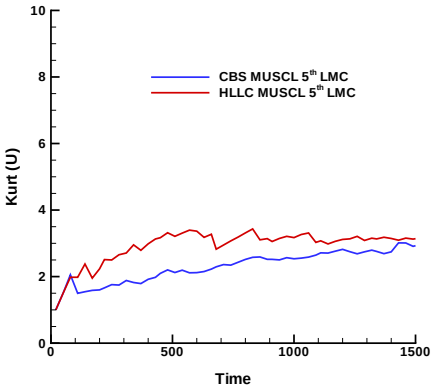

(b) Point $\frac{X}{D} = 20$.

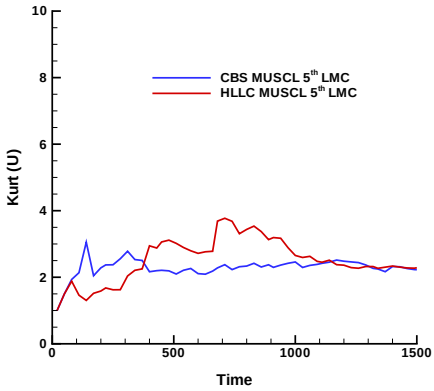

(c) Point $\frac{X}{D} = 25$.

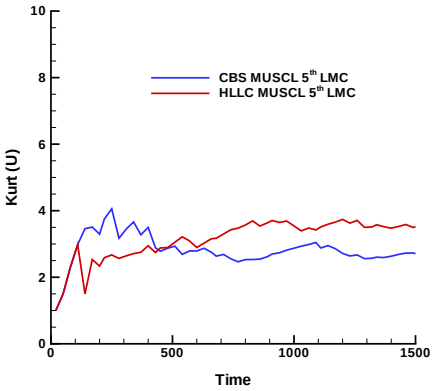

(d) Point $\frac{X}{D} = 30$.

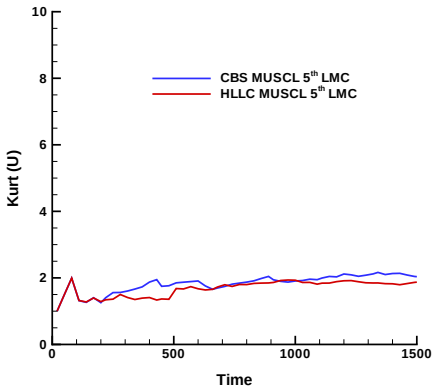

(e) Point $\frac{X}{D} = 35$.

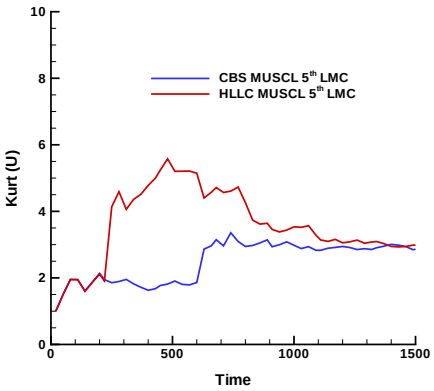

(f) Point $\frac{X}{D} = 40$.

FIGURE F.14: Kurtosis results, **MUSCL** 5^{th} **LMC**, p-study.

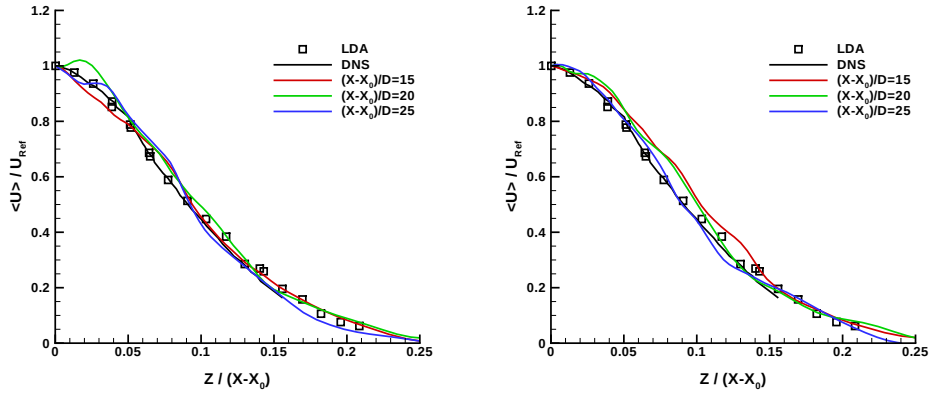

(a) **CBS**. (b) **HLLC**.

Figure F.15: Similarity profiles, **MUSCL** 5^{th} **LMC**, p-study.

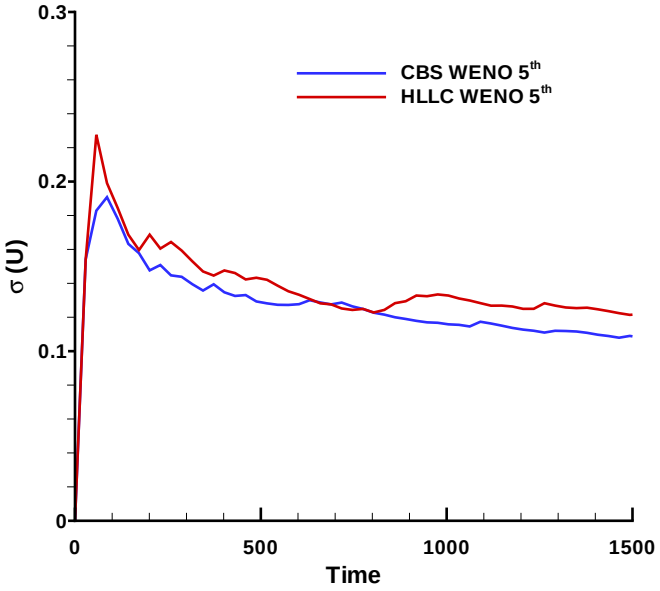

Figure F.16: Domains Maximum Standard Deviation, **WENO** 5^{th}, p-study.

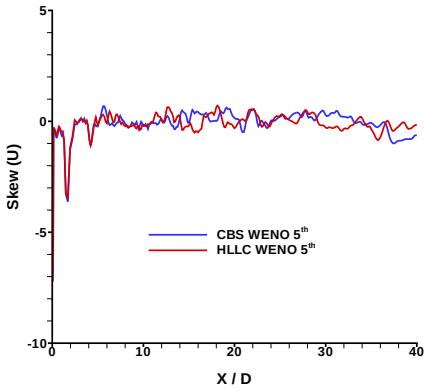

(a) Central Line final value.

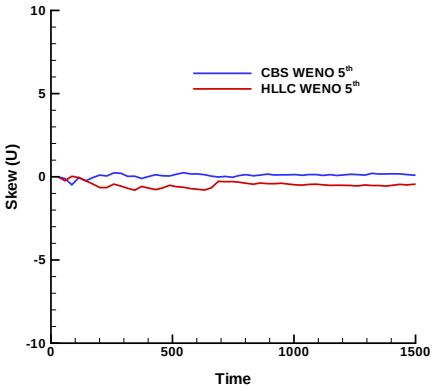

(b) Point $\frac{X}{D} = 20$.

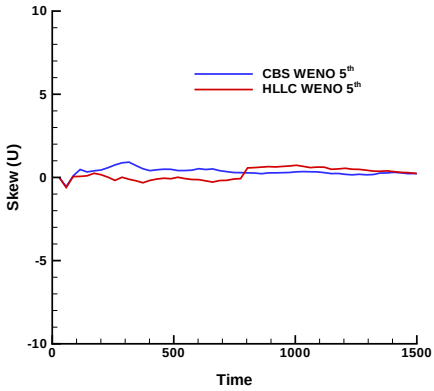

(c) Point $\frac{X}{D} = 25$.

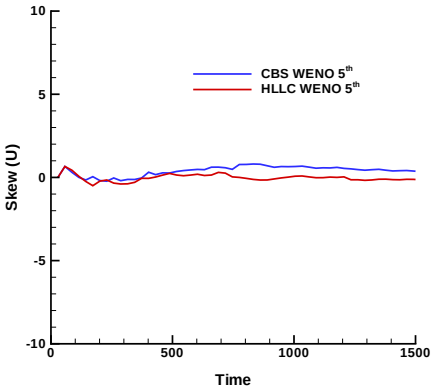

(d) Point $\frac{X}{D} = 30$.

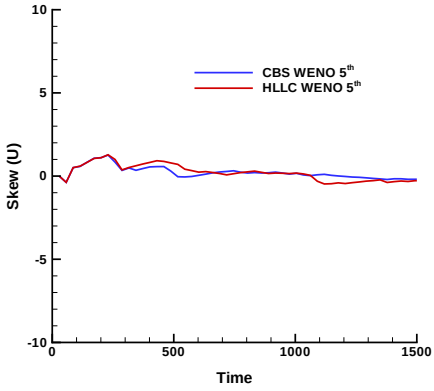

(e) Point $\frac{X}{D} = 35$.

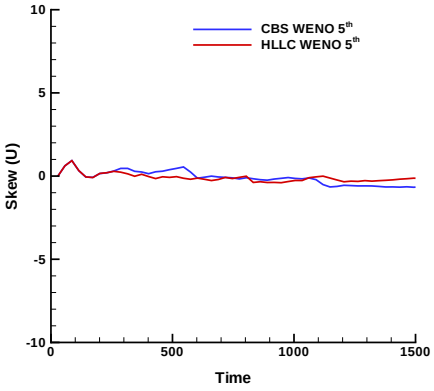

(f) Point $\frac{X}{D} = 40$.

FIGURE F.17: Skewness results, **WENO** 5^{th}, p-study.

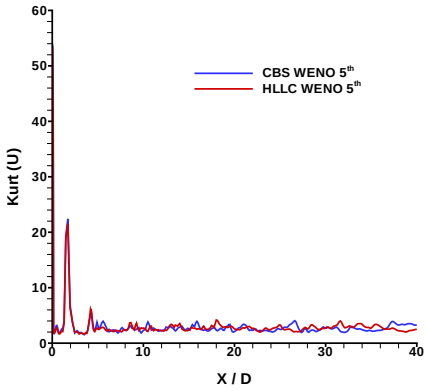

(a) Central Line final value.

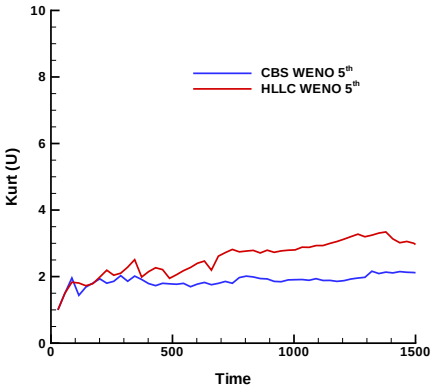

(b) Point $\frac{X}{D} = 20$.

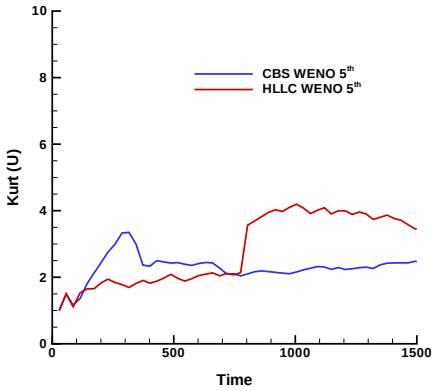

(c) Point $\frac{X}{D} = 25$.

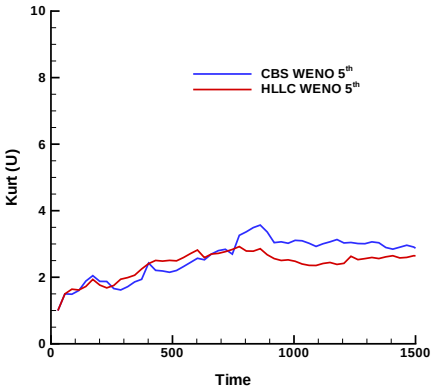

(d) Point $\frac{X}{D} = 30$.

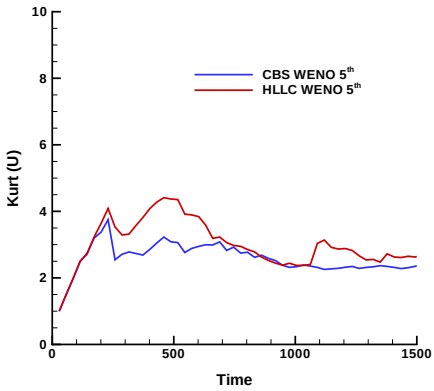

(e) Point $\frac{X}{D} = 35$.

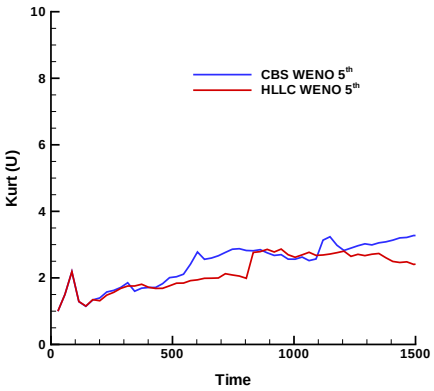

(f) Point $\frac{X}{D} = 40$.

FIGURE F.18: Kurtosis results, **WENO** 5^{th}, p-study.

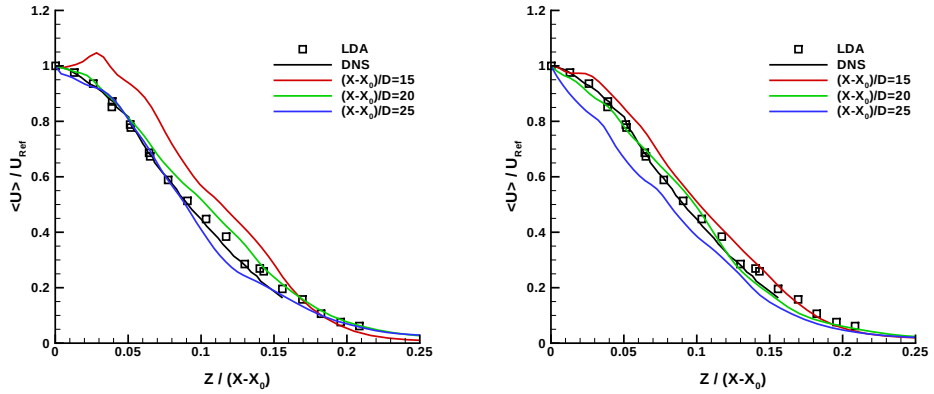

(a) **CBS**. (b) **HLLC**.

Figure F.19: Similarity profiles, **WENO** 5^{th}, p-study.

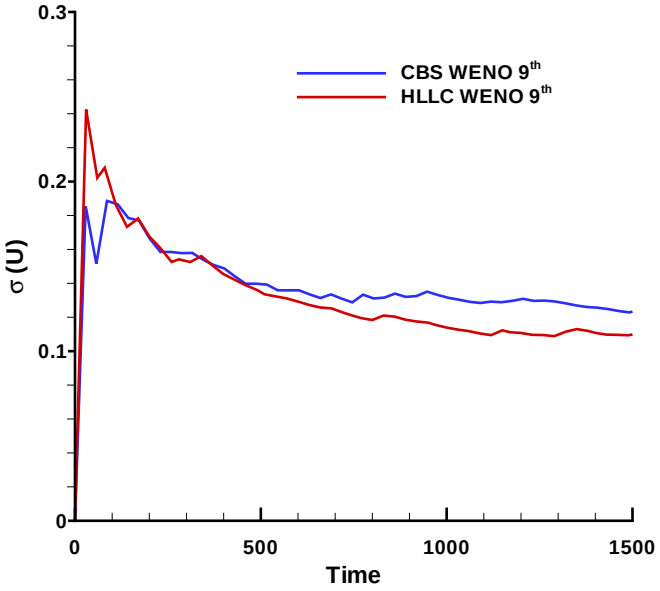

Figure F.20: Domains Maximum Standard Deviation, **WENO** 9^{th}, p-study.

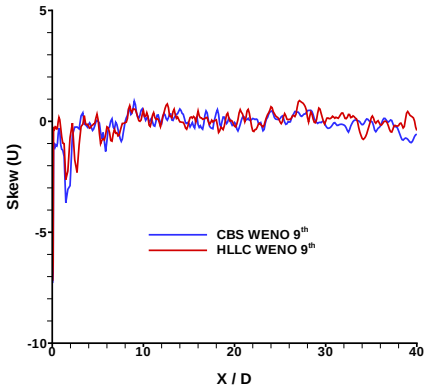

(a) Central Line final value.

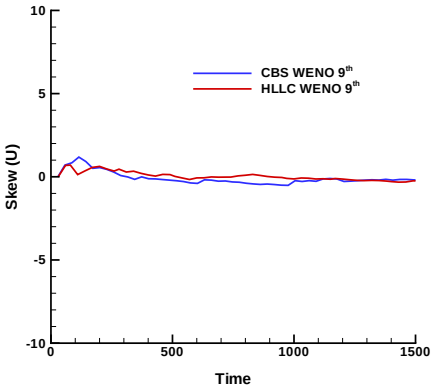

(b) Point $\frac{X}{D} = 20$.

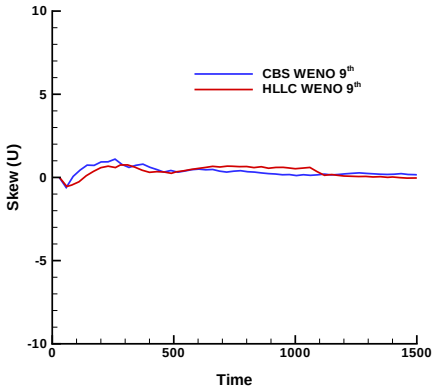

(c) Point $\frac{X}{D} = 25$.

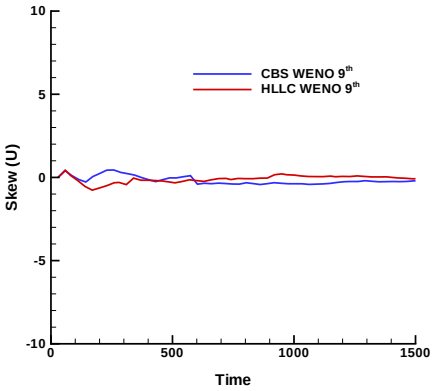

(d) Point $\frac{X}{D} = 30$.

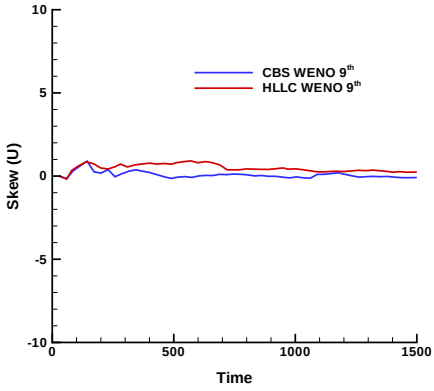

(e) Point $\frac{X}{D} = 35$.

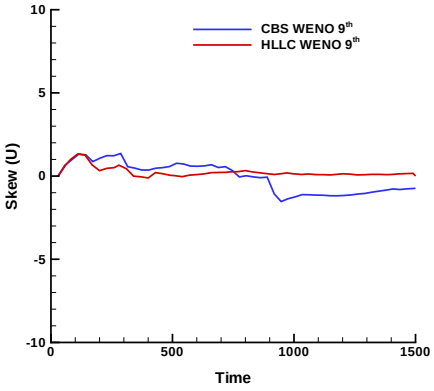

(f) Point $\frac{X}{D} = 40$.

FIGURE F.21: Skewness results, **WENO** 9^{th}, p-study.

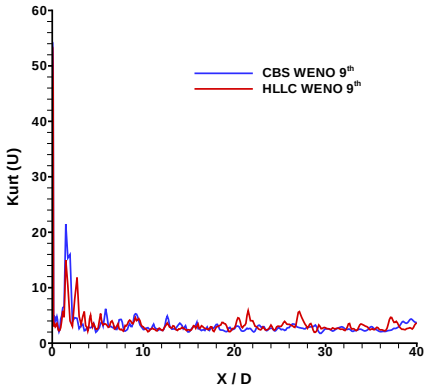

(a) Central Line final value.

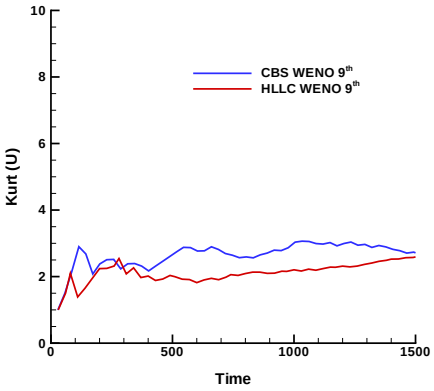

(b) Point $\frac{X}{D} = 20$.

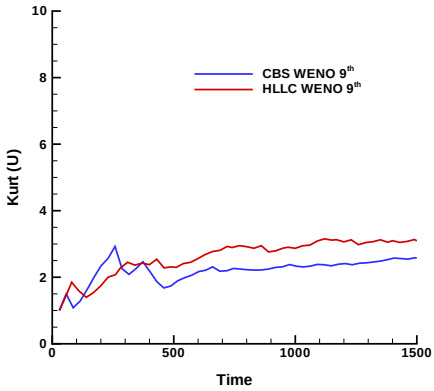

(c) Point $\frac{X}{D} = 25$.

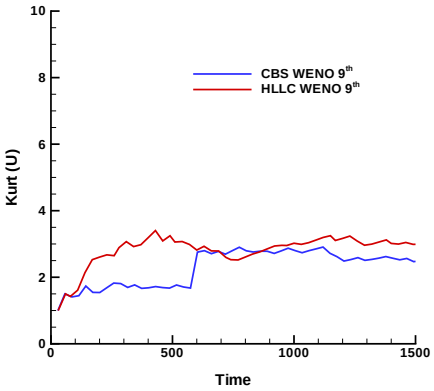

(d) Point $\frac{X}{D} = 30$.

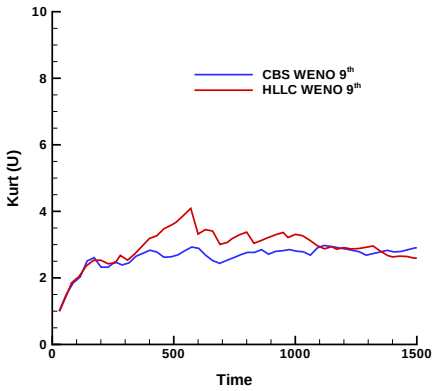

(e) Point $\frac{X}{D} = 35$.

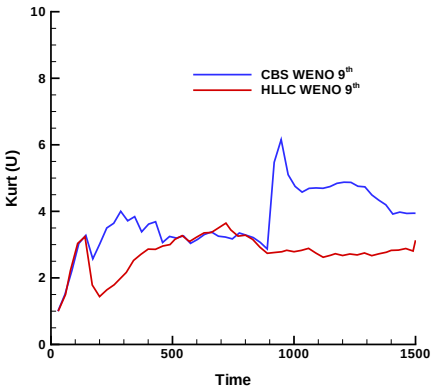

(f) Point $\frac{X}{D} = 40$.

Figure F.22: Kurtosis results, **WENO** 9^{th}, p-study.

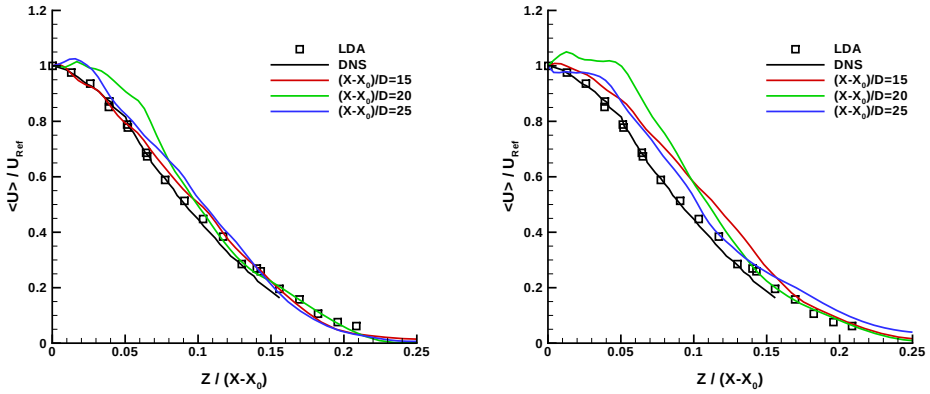

(a) **CBS**. (b) **HLLC**.

FIGURE F.23: Similarity profiles, **WENO** 9^{th}, p-study.

F.2 Co-flow Jet

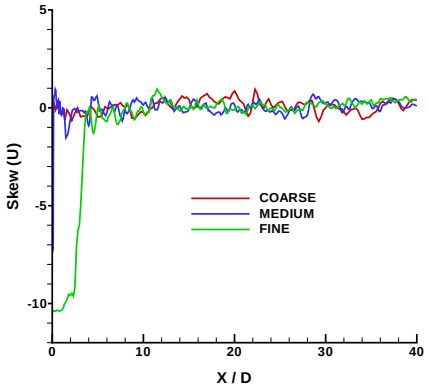

(a) Central Line final value.

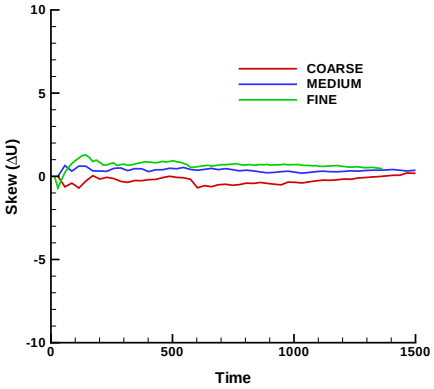

(b) Point $\frac{X}{D} = 20$.

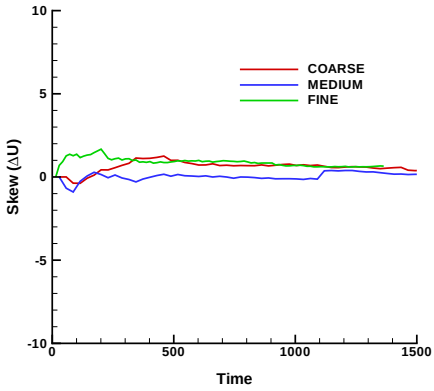

(c) Point $\frac{X}{D} = 25$.

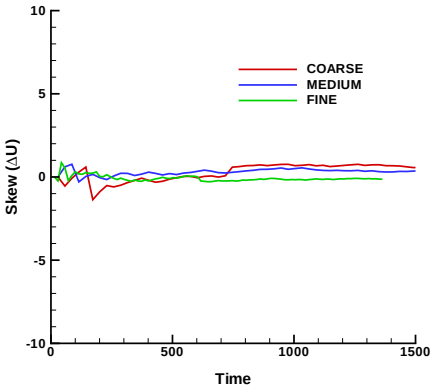

(d) Point $\frac{X}{D} = 30$.

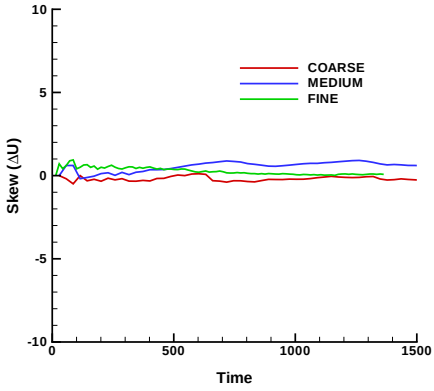

(e) Point $\frac{X}{D} = 35$.

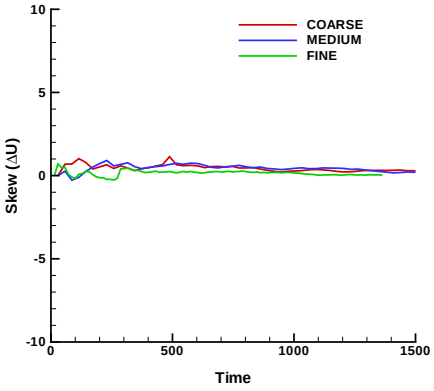

(f) Point $\frac{X}{D} = 40$.

FIGURE F.24: Skewness results, h-study.

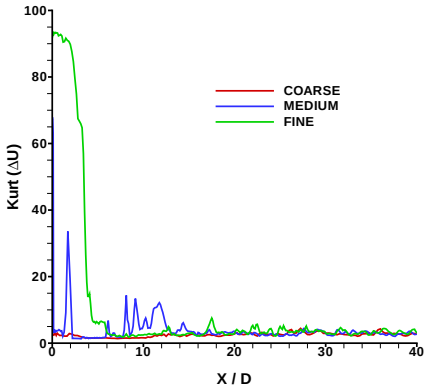

(a) Central Line final value.

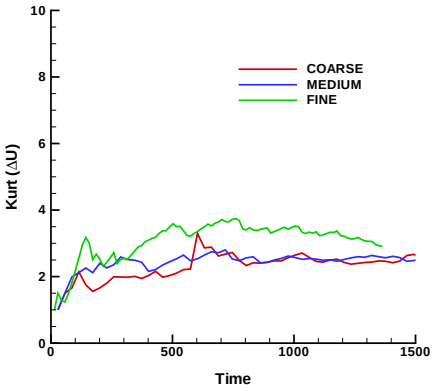

(b) Point $\frac{X}{D} = 20$.

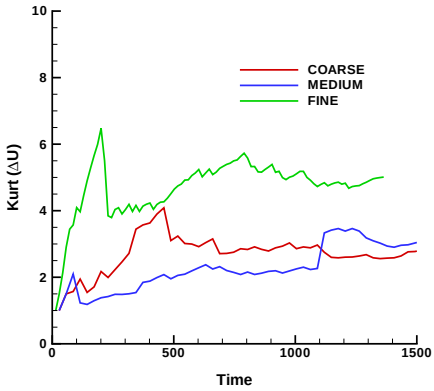

(c) Point $\frac{X}{D} = 25$.

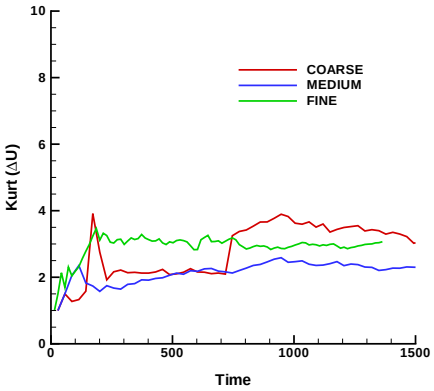

(d) Point $\frac{X}{D} = 30$.

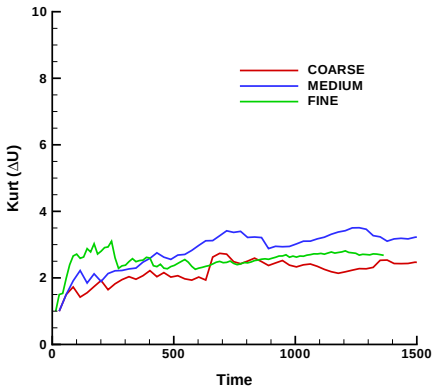

(e) Point $\frac{X}{D} = 35$.

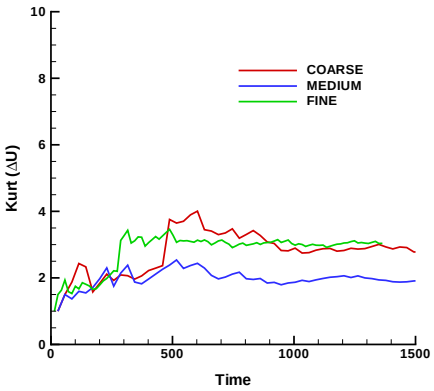

(f) Point $\frac{X}{D} = 40$.

Figure F.25: Kurtosis results, *h*-study.

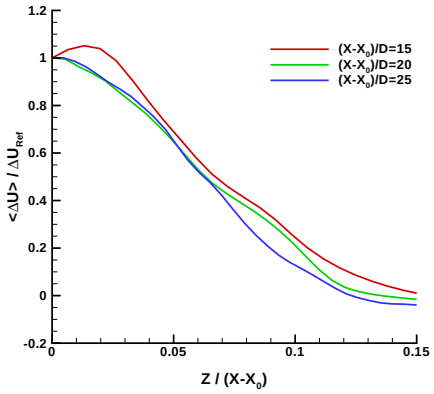

(a) **Coarse** mesh.

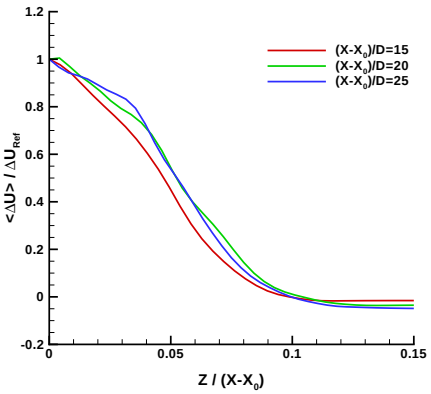

(b) **Medium** mesh.

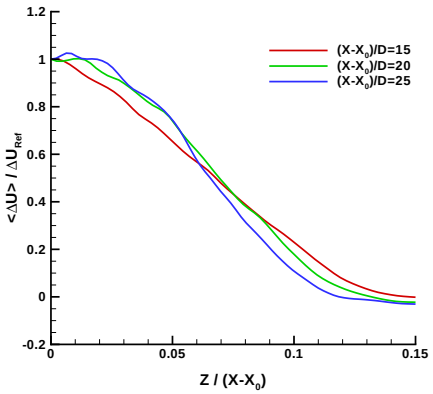

(c) **Fine** mesh.

Figure F.26: Similarity profiles, *h*-study.

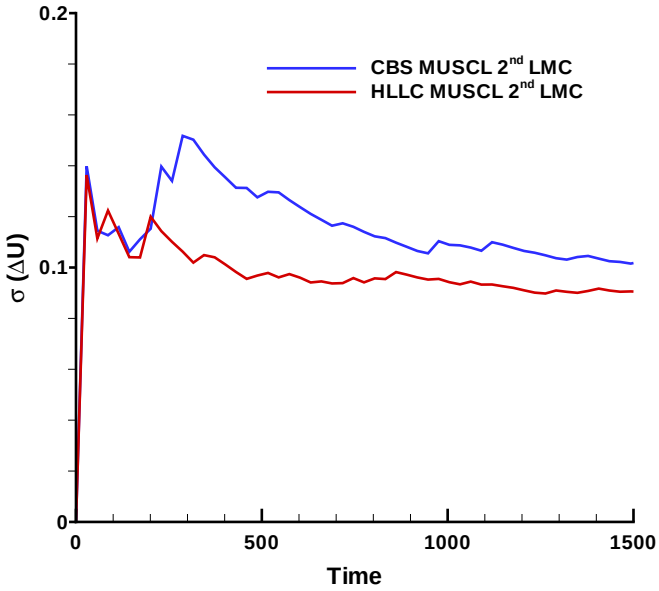

Figure F.27: Domains Maximum Standard Deviation, **MUSCL** 2^{nd} **LMC**, *p*-study.

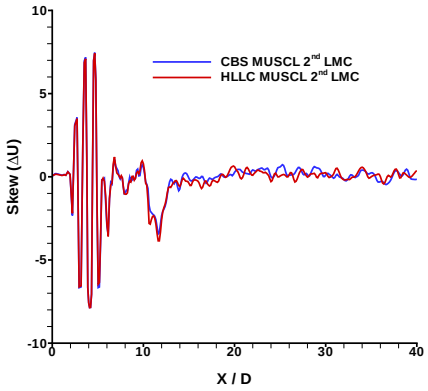

(a) Central Line final value.

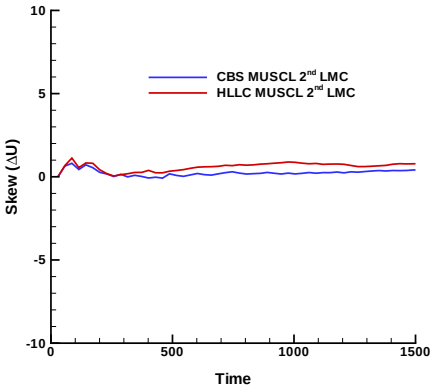

(b) Point $\frac{X}{D} = 20$.

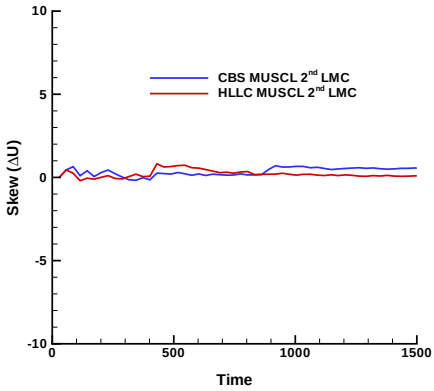

(c) Point $\frac{X}{D} = 25$.

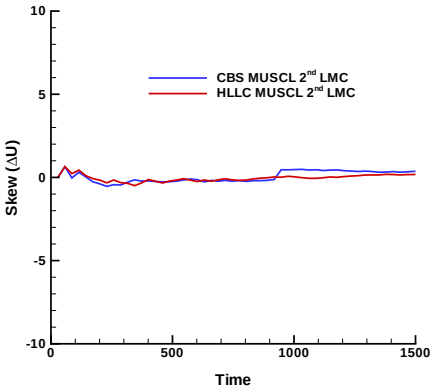

(d) Point $\frac{X}{D} = 30$.

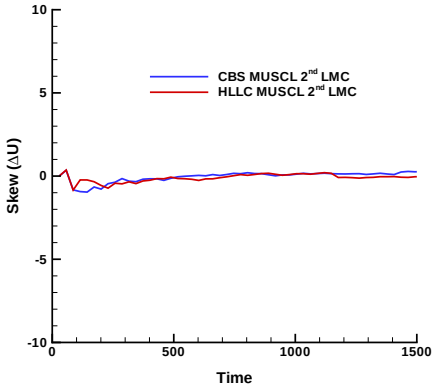

(e) Point $\frac{X}{D} = 35$.

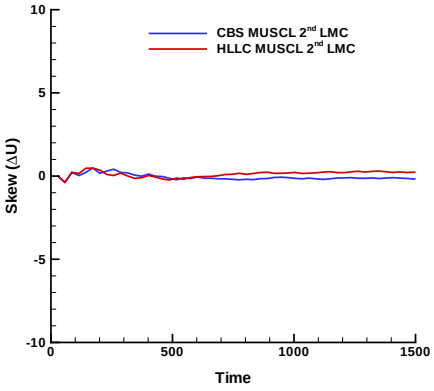

(f) Point $\frac{X}{D} = 40$.

Figure F.28: Skewness results, **MUSCL** 2^{nd} **LMC**, p-study.

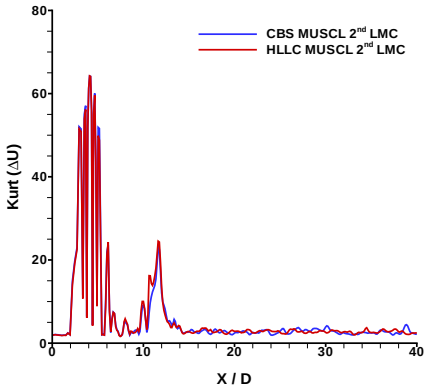

(a) Central Line final value.

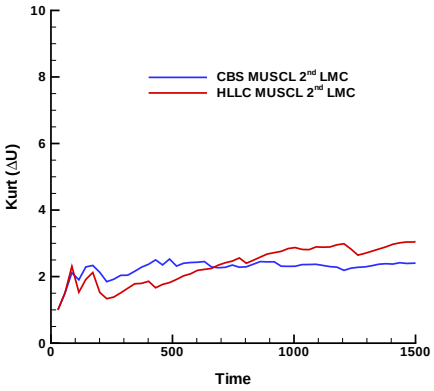

(b) Point $\frac{X}{D} = 20$.

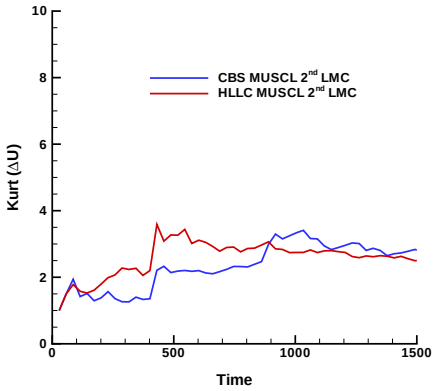

(c) Point $\frac{X}{D} = 25$.

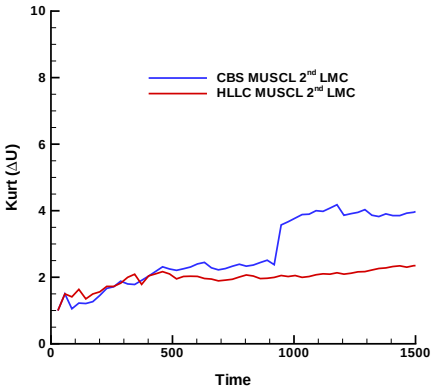

(d) Point $\frac{X}{D} = 30$.

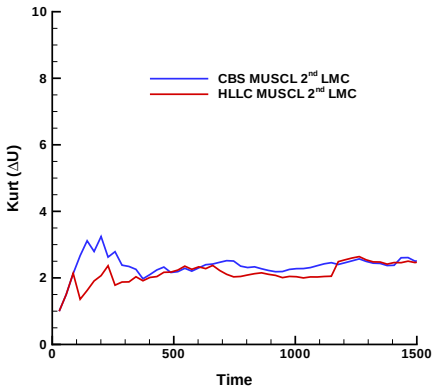

(e) Point $\frac{X}{D} = 35$.

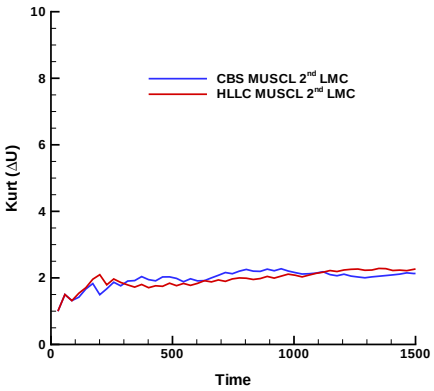

(f) Point $\frac{X}{D} = 40$.

Figure F.29: Kurtosis results, **MUSCL** 2^{nd} **LMC**, p-study.

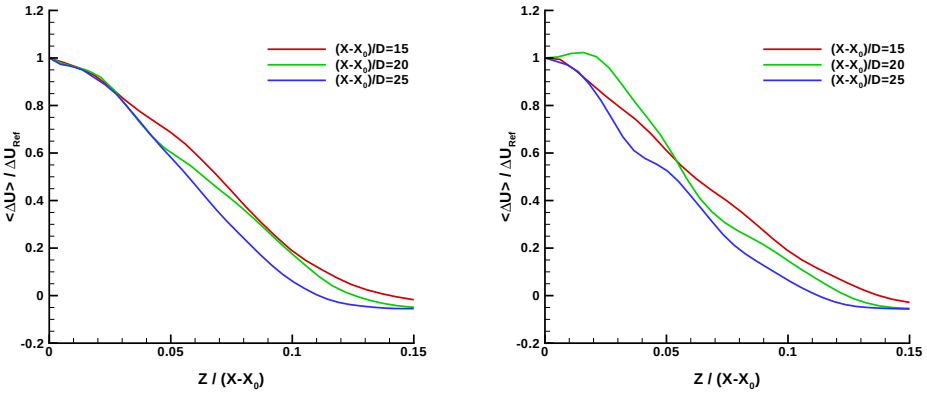

(a) **CBS**. (b) **HLLC**.

Figure F.30: Similarity profiles, **MUSCL** 2^{nd} **LMC**, *p*-study.

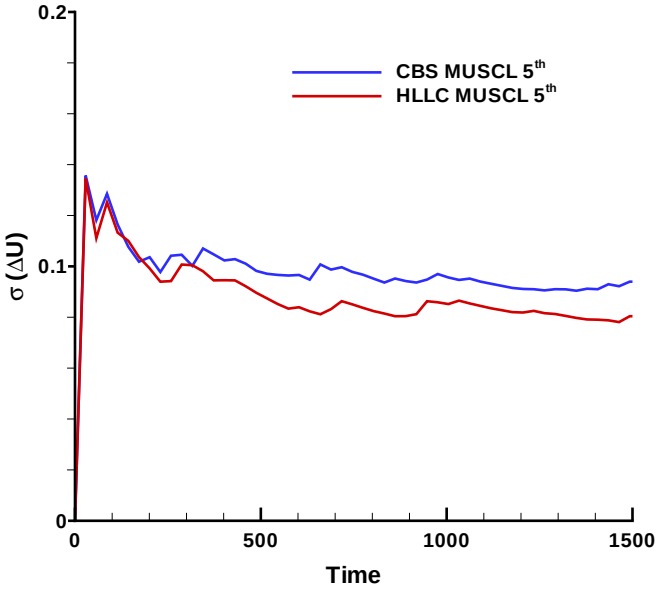

Figure F.31: Domains Maximum Standard Deviation, **MUSCL** 5^{th}, *p*-study.

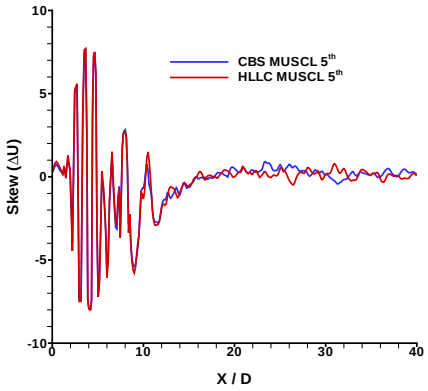

(a) Central Line final value.

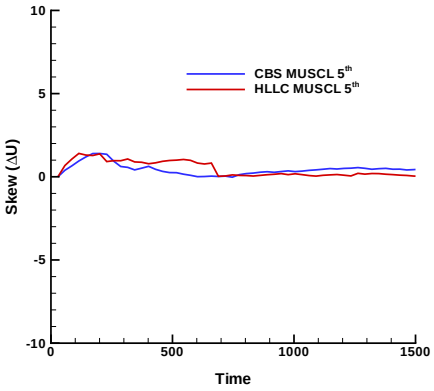

(b) Point $\frac{X}{D} = 20$.

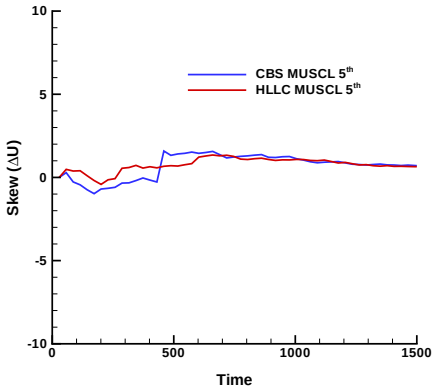

(c) Point $\frac{X}{D} = 25$.

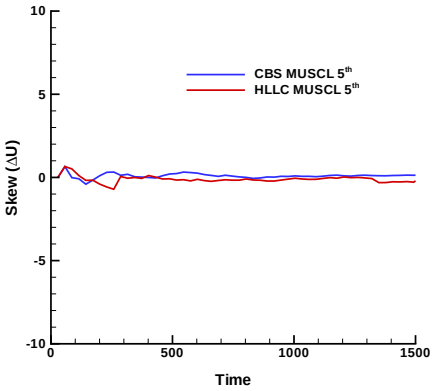

(d) Point $\frac{X}{D} = 30$.

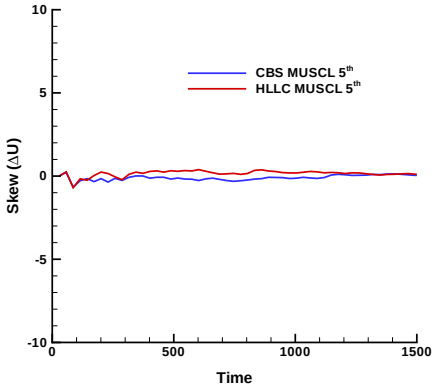

(e) Point $\frac{X}{D} = 35$.

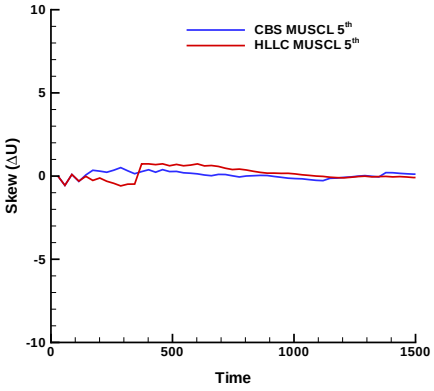

(f) Point $\frac{X}{D} = 40$.

Figure F.32: Skewness results, **MUSCL** 5^{th}, p-study.

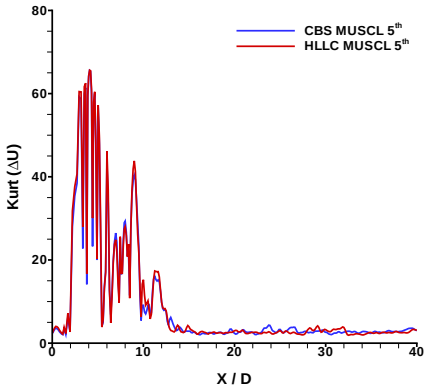

(a) Central Line final value.

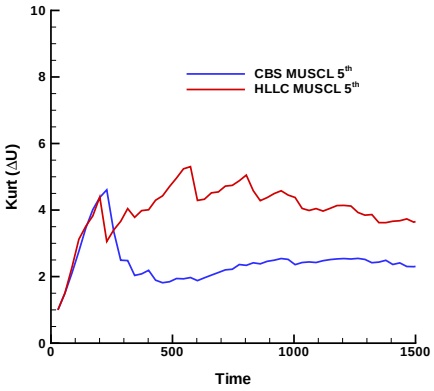

(b) Point $\frac{X}{D} = 20$.

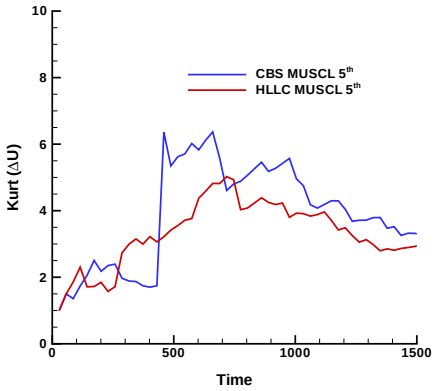

(c) Point $\frac{X}{D} = 25$.

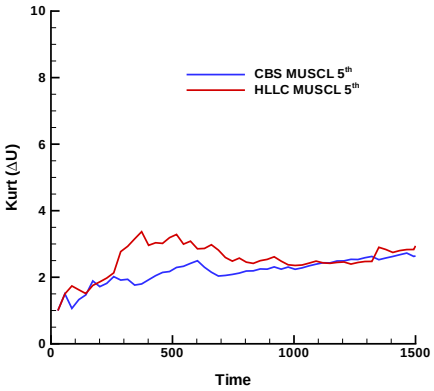

(d) Point $\frac{X}{D} = 30$.

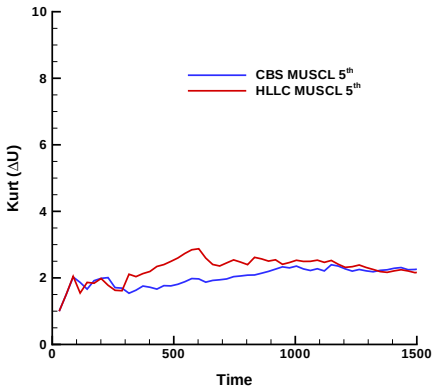

(e) Point $\frac{X}{D} = 35$.

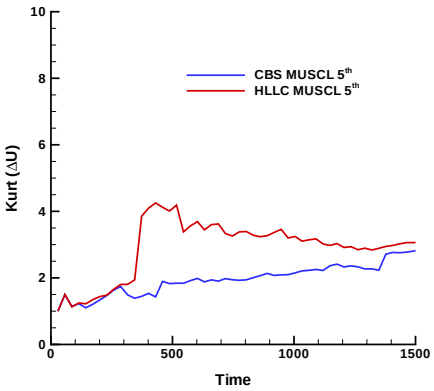

(f) Point $\frac{X}{D} = 40$.

Figure F.33: Kurtosis results, **MUSCL** 5^{th}, p-study.

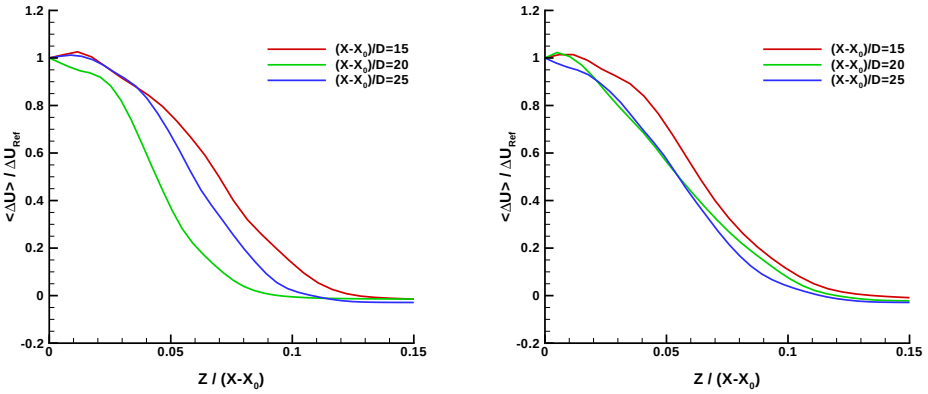

(a) **CBS**. (b) **HLLC**.

Figure F.34: Similarity profiles, **MUSCL** 5^{th}, *p*-study.

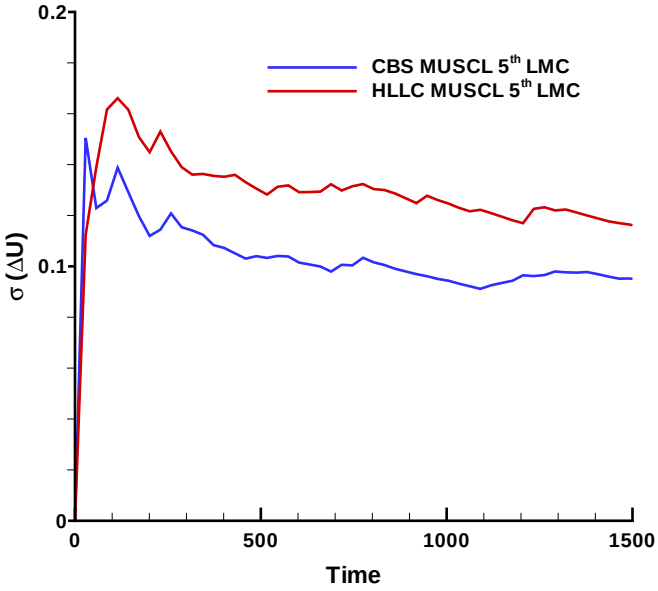

Figure F.35: Domains Maximum Standard Deviation, **MUSCL** 5^{th} **LMC**, *p*-study.

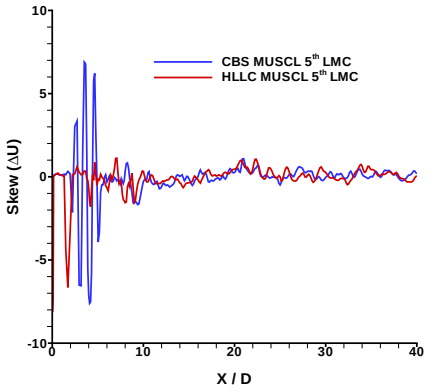

(a) Central Line final value.

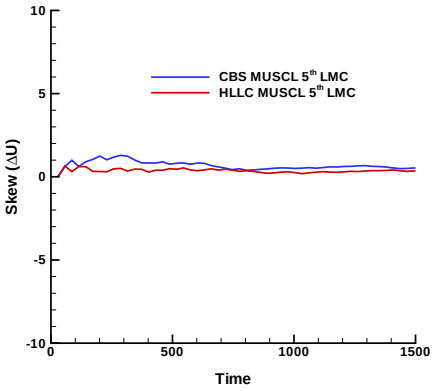

(b) Point $\frac{X}{D} = 20$.

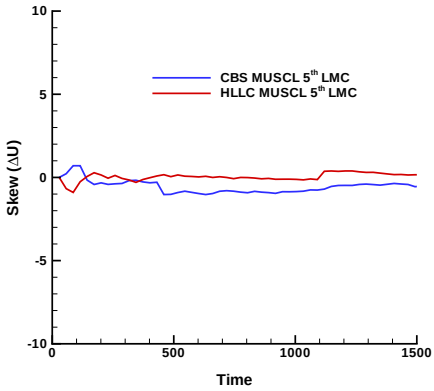

(c) Point $\frac{X}{D} = 25$.

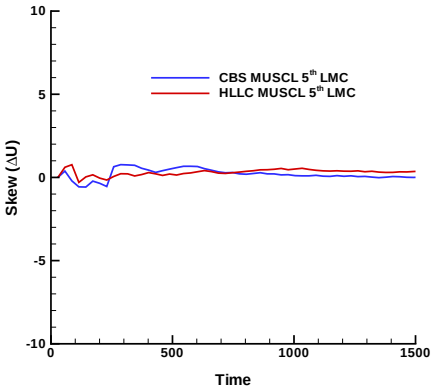

(d) Point $\frac{X}{D} = 30$.

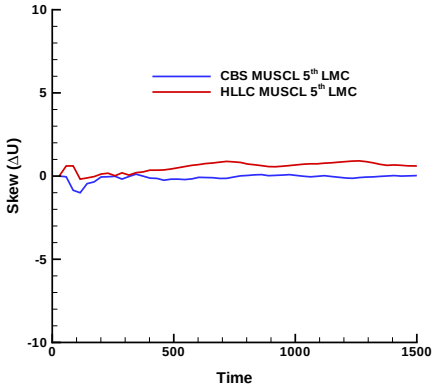

(e) Point $\frac{X}{D} = 35$.

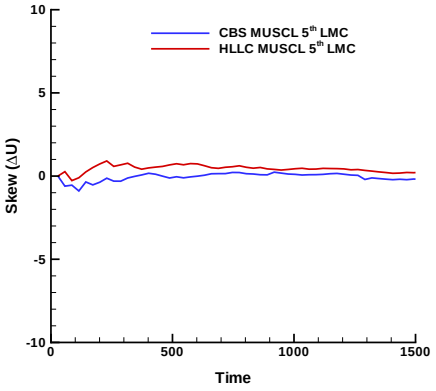

(f) Point $\frac{X}{D} = 40$.

Figure F.36: Skewness results, **MUSCL** 5^{th} **LMC**, p-study.

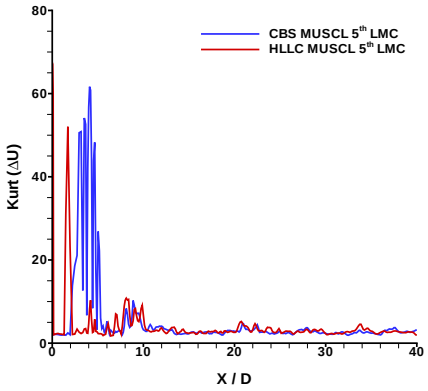

(a) Central Line final value.

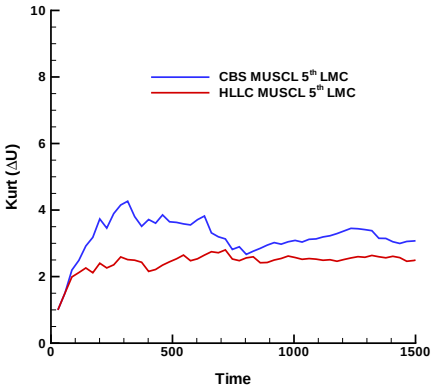

(b) Point $\frac{X}{D} = 20$.

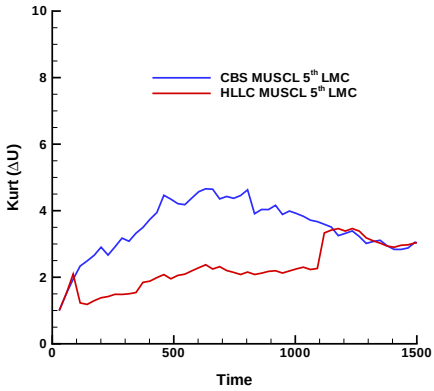

(c) Point $\frac{X}{D} = 25$.

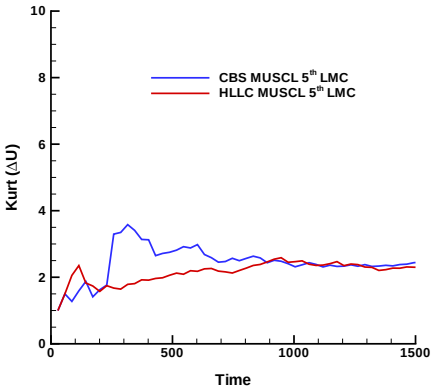

(d) Point $\frac{X}{D} = 30$.

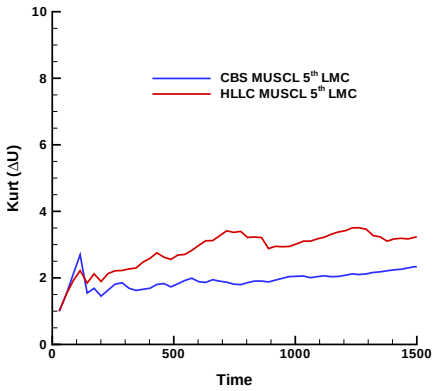

(e) Point $\frac{X}{D} = 35$.

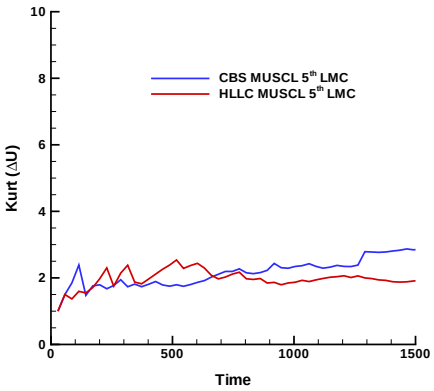

(f) Point $\frac{X}{D} = 40$.

Figure F.37: Kurtosis results, **MUSCL** 5^{th} **LMC**, p-study.

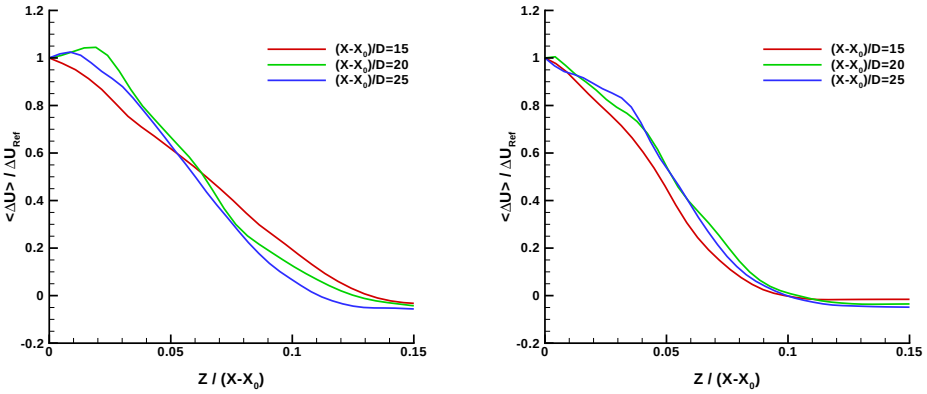

(a) **CBS**. (b) **HLLC**.

Figure F.38: Similarity profiles, **MUSCL** 5^{th} **LMC**, p-study.

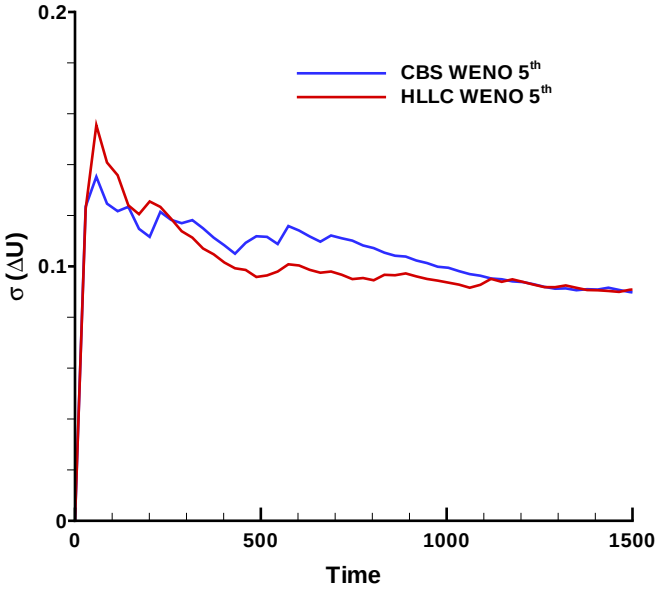

Figure F.39: Domains Maximum Standard Deviation, **WENO** 5^{th}, p-study.

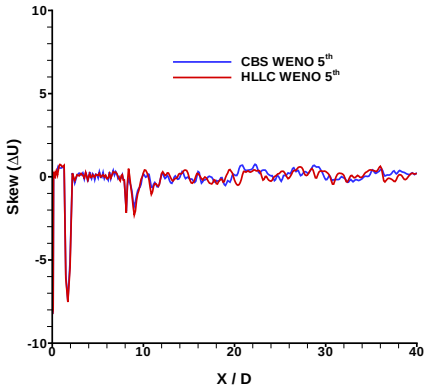

(a) Central Line final value.

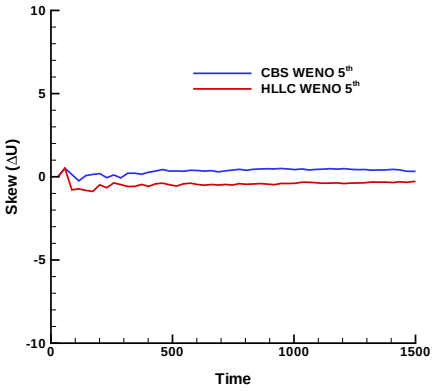

(b) Point $\frac{X}{D} = 20$.

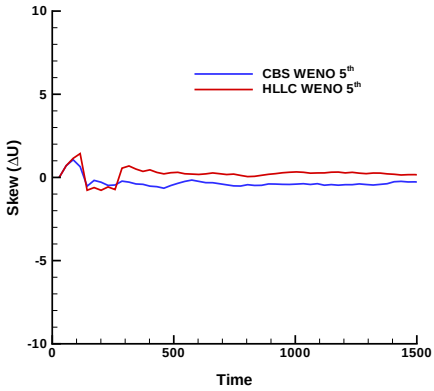

(c) Point $\frac{X}{D} = 25$.

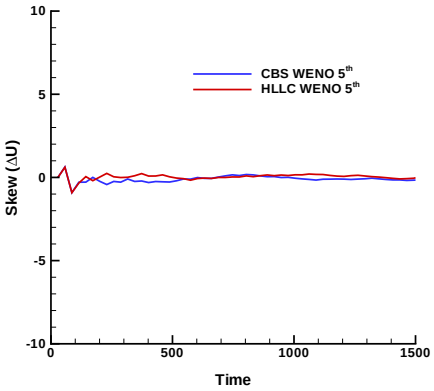

(d) Point $\frac{X}{D} = 30$.

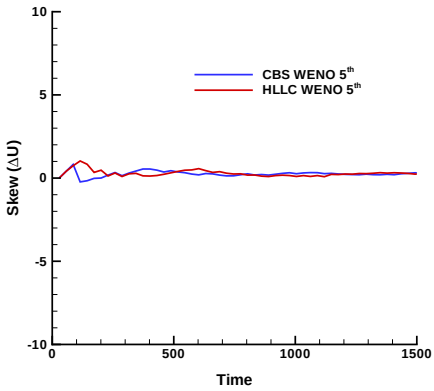

(e) Point $\frac{X}{D} = 35$.

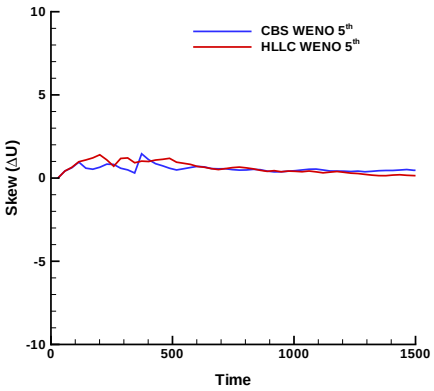

(f) Point $\frac{X}{D} = 40$.

Figure F.40: Skewness results, **WENO** 5^{th}, p-study.

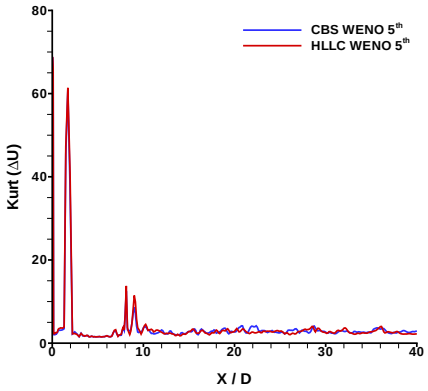

(a) Central Line final value.

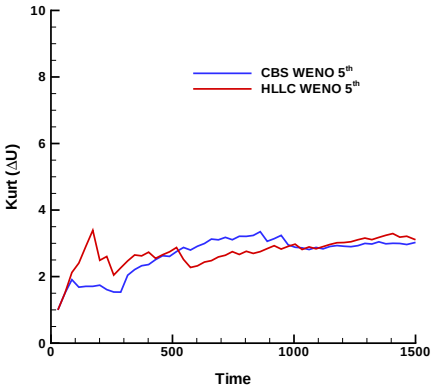

(b) Point $\frac{X}{D} = 20$.

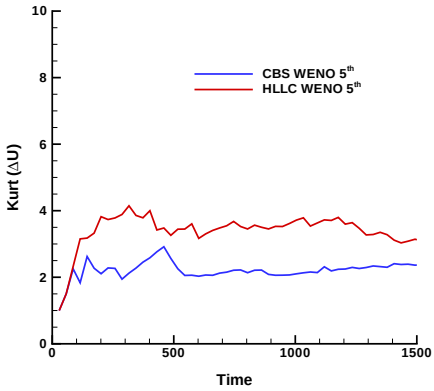

(c) Point $\frac{X}{D} = 25$.

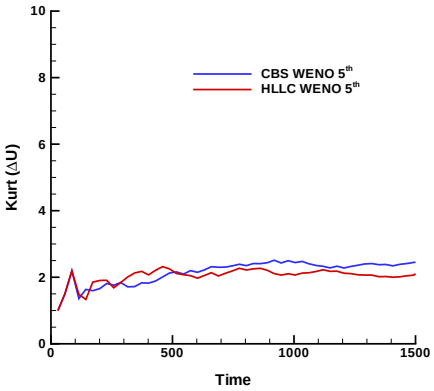

(d) Point $\frac{X}{D} = 30$.

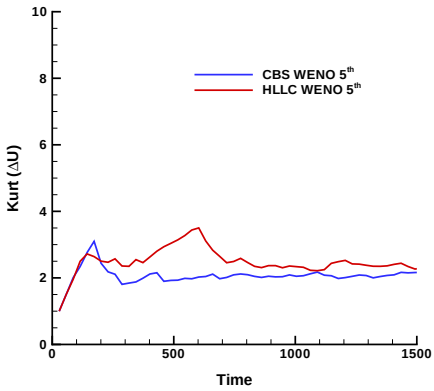

(e) Point $\frac{X}{D} = 35$.

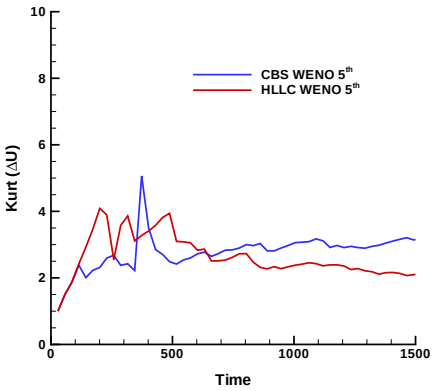

(f) Point $\frac{X}{D} = 40$.

Figure F.41: Kurtosis results, **WENO** 5^{th}, p-study.

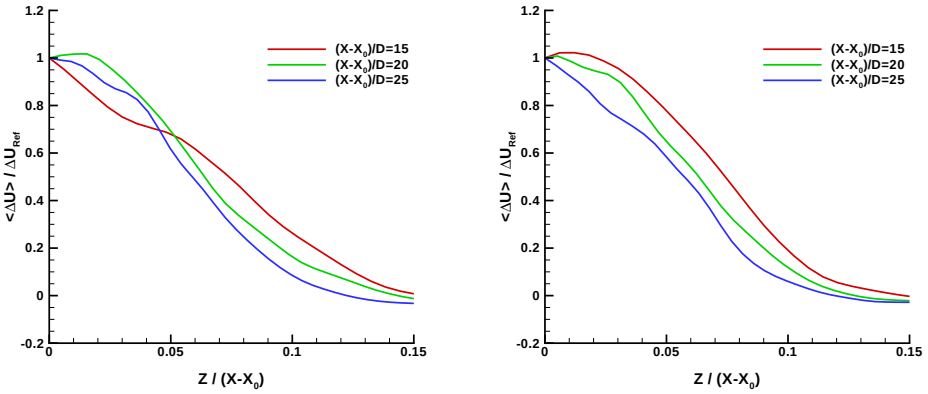

(a) **CBS**. (b) **HLLC**.

Figure F.42: Similarity profiles.

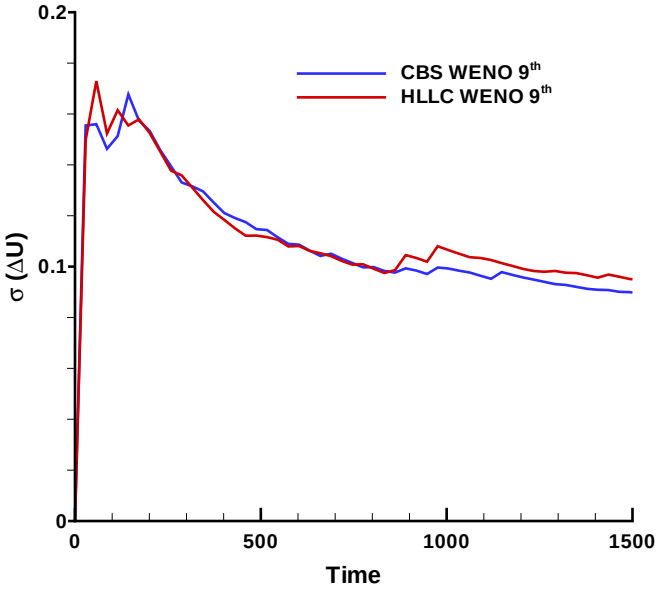

Figure F.43: Domains Maximum Standard Deviation, **WENO** 9^{th}, *p*-study.

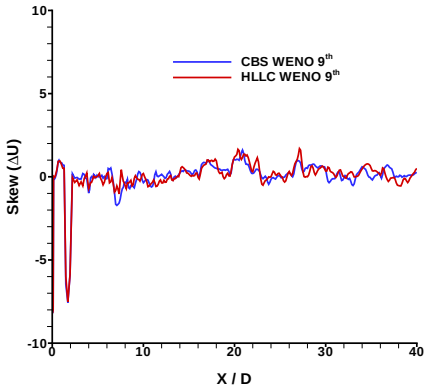

(a) Central Line final value.

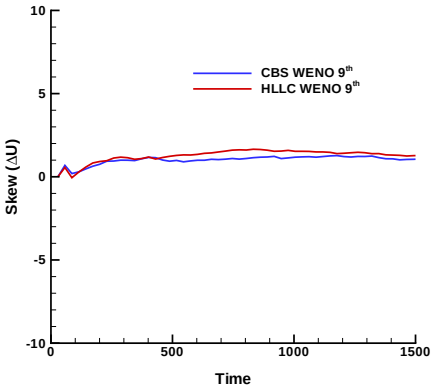

(b) Point $\frac{X}{D} = 20$.

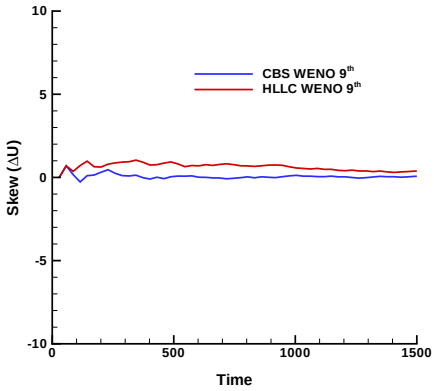

(c) Point $\frac{X}{D} = 25$.

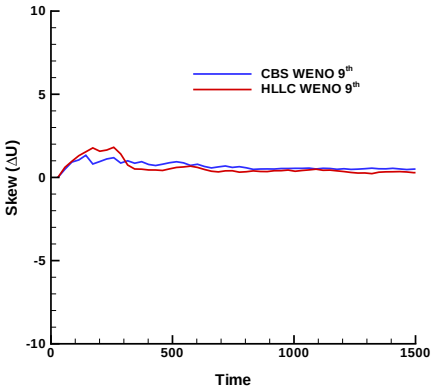

(d) Point $\frac{X}{D} = 30$.

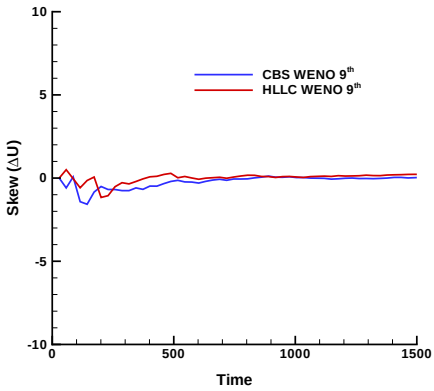

(e) Point $\frac{X}{D} = 35$.

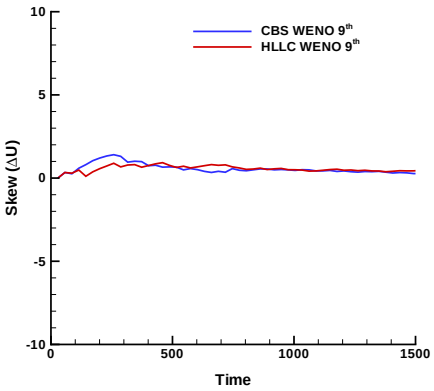

(f) Point $\frac{X}{D} = 40$.

Figure F.44: Skewness results, **WENO** 9^{th}, p-study.

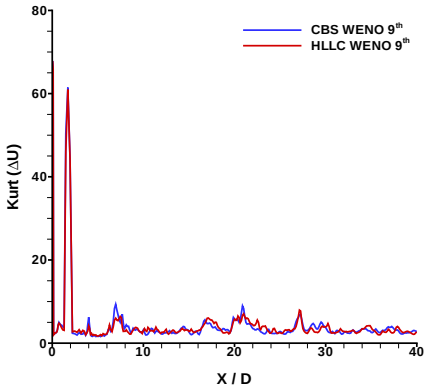

(a) Central Line final value.

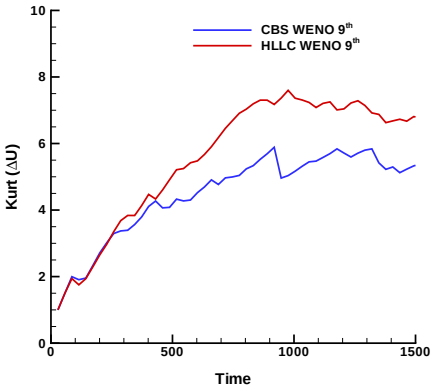

(b) Point $\frac{X}{D} = 20$.

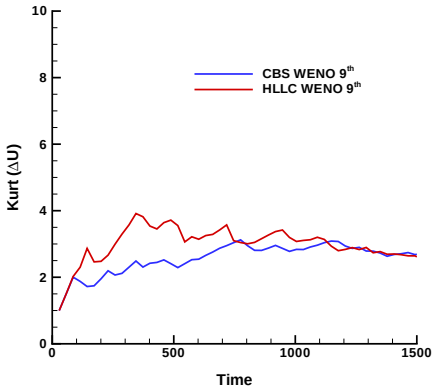

(c) Point $\frac{X}{D} = 25$.

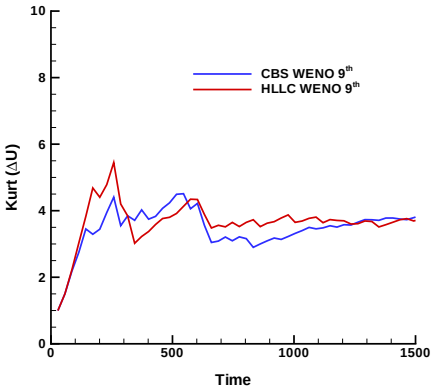

(d) Point $\frac{X}{D} = 30$.

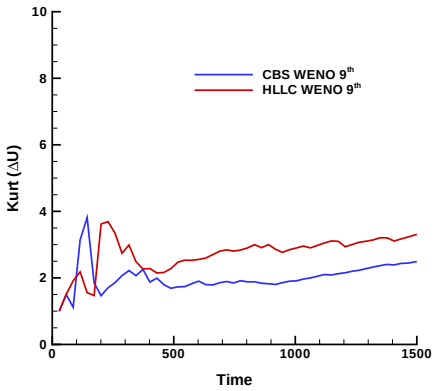

(e) Point $\frac{X}{D} = 35$.

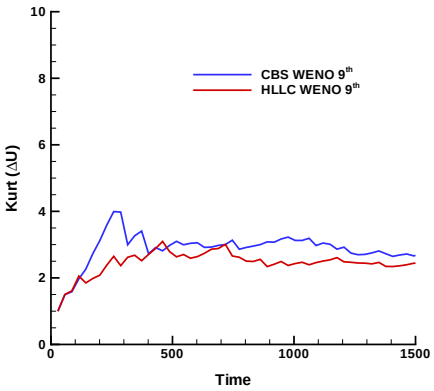

(f) Point $\frac{X}{D} = 40$.

Figure F.45: Kurtosis results, **WENO** 9^{th}, p-study.

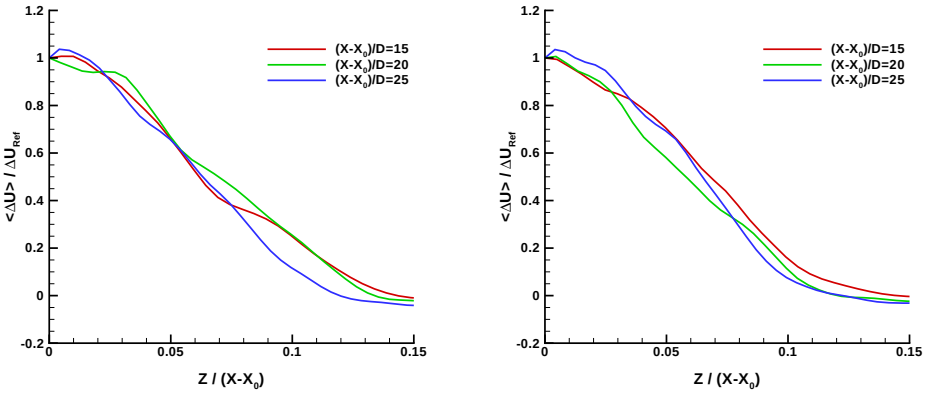

(a) **CBS**. (b) **HLLC**.

Figure F.46: Similarity profiles, **WENO** 9^{th}, p-study.

G

Spectral analysis

In this appendix, the temporal total kinetic energy and the correspondent phase diagrams for both jet cases are presented for the **CBS MUSCL** 5^{th}**-order LMC** (Static jet case) and **HLLC MUSCL** 5^{th}**-order LMC** (Co-Flow jet case) methodologies employed in this thesis. It can be observed, for the transition and far field regions of the jet's, the "stabilization" of the phase value around $\phi = \pm\frac{\pi}{2}$, that identifies the inertial scales. The importance of the phase value is then associated with the transformation from the Fourier Space to the Real Space, where the phase describe and completely identify each frequency/wave number of the energy decay spectrum.

G.1 Static Jet

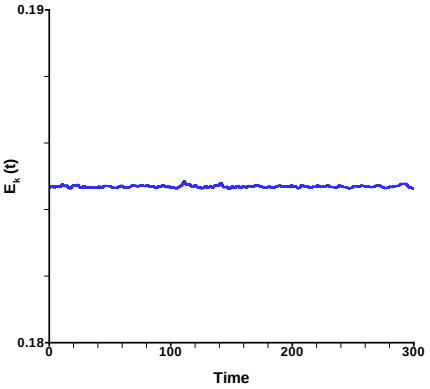

(a) Time Domain, $\frac{X}{D} = 0$.

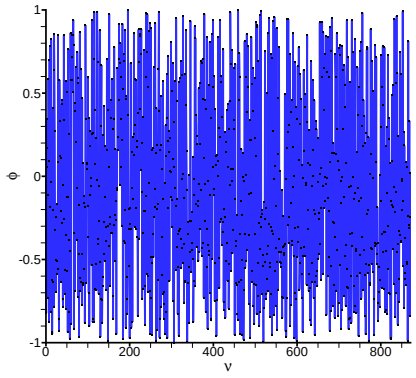

(b) Phase diagram, $\frac{X}{D} = 0$.

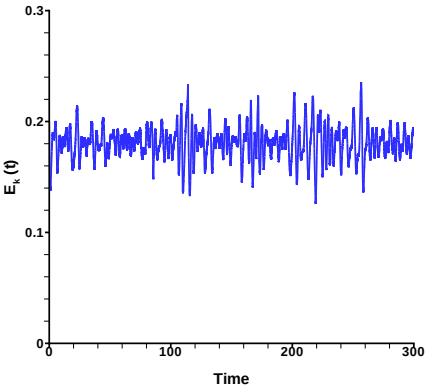

(c) Time Domain, $\frac{X}{D} = 5$.

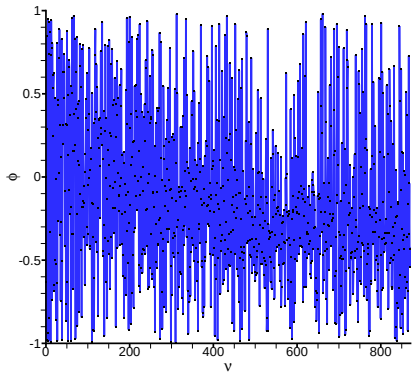

(d) Phase diagram, $\frac{X}{D} = 5$.

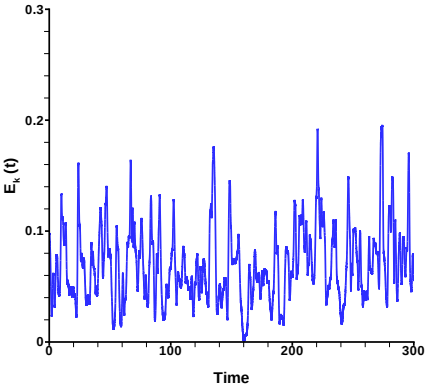

(e) Time Domain, $\frac{X}{D} = 10$.

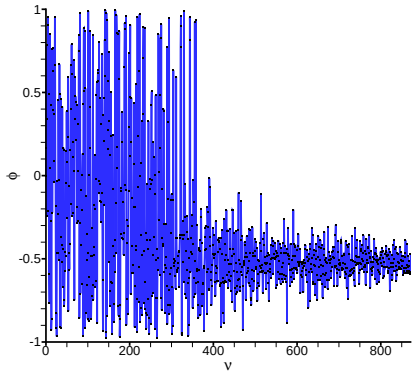

(f) Phase diagram, $\frac{X}{D} = 10$.

Figure G.1: Kinetic Energy, **CBS MUSCL** 5^{th} **LMC**.

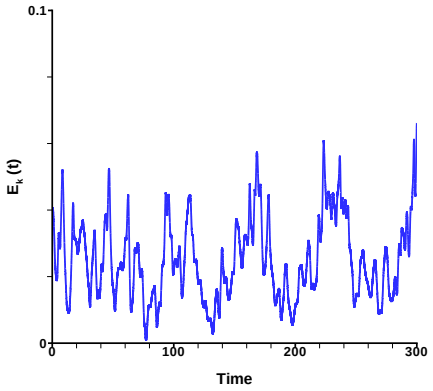

(a) Time Domain, $\frac{X}{D} = 15$.

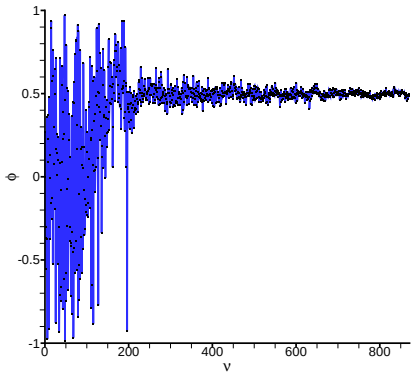

(b) Phase diagram, $\frac{X}{D} = 15$.

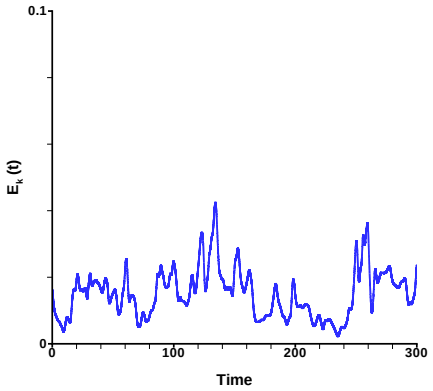

(c) Time Domain, $\frac{X}{D} = 20$.

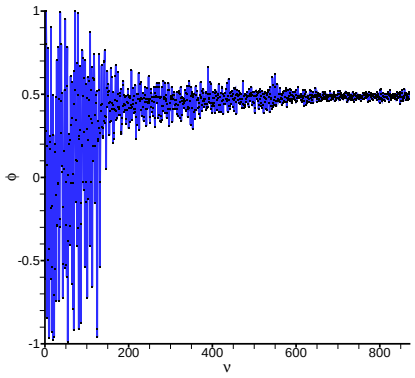

(d) Phase diagram, $\frac{X}{D} = 20$.

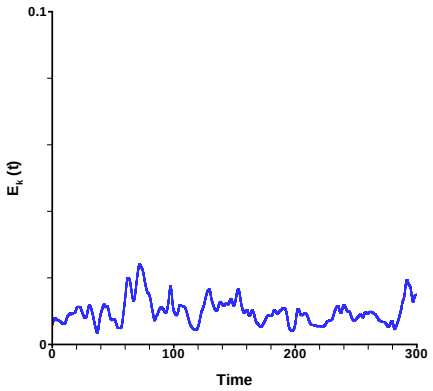

(e) Time Domain, $\frac{X}{D} = 25$.

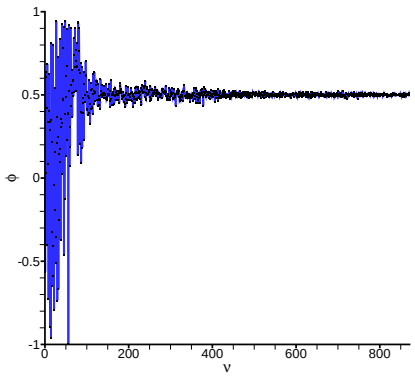

(f) Phase diagram, $\frac{X}{D} = 25$.

FIGURE G.2: Kinetic Energy, **CBS MUSCL** 5^{th} **LMC**.

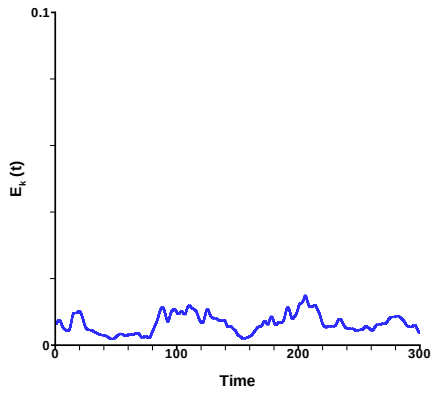

(a) Time Domain, $\frac{X}{D} = 30$.

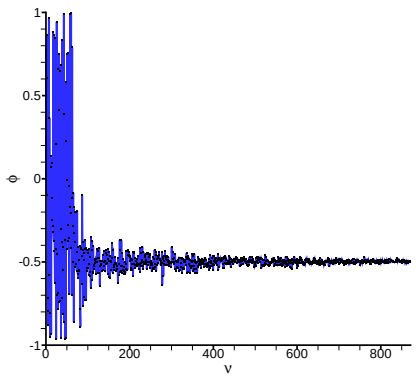

(b) Phase diagram, $\frac{X}{D} = 30$.

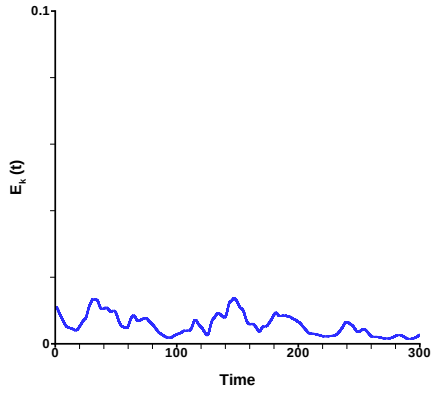

(c) Time Domain, $\frac{X}{D} = 35$.

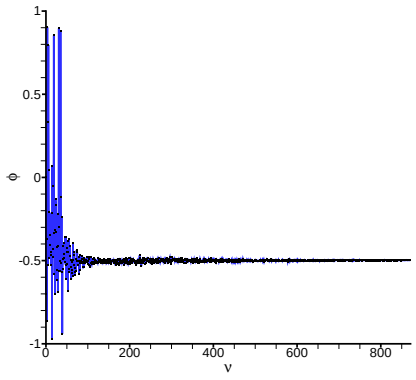

(d) Phase diagram, $\frac{X}{D} = 35$.

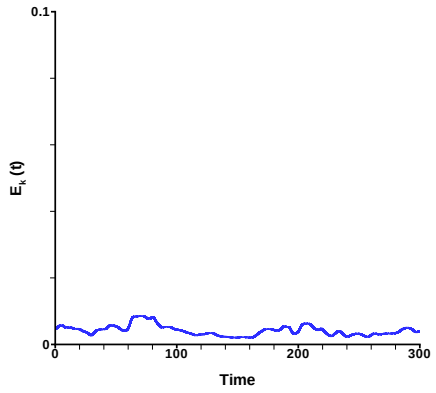

(e) Time Domain, $\frac{X}{D} = 40$.

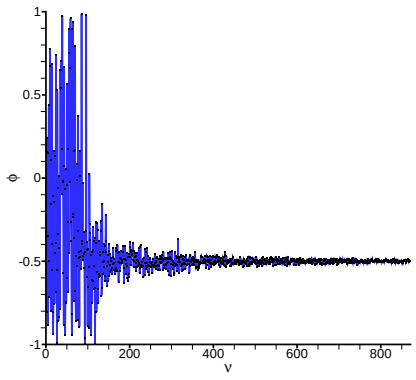

(f) Phase diagram, $\frac{X}{D} = 40$.

FIGURE G.3: Kinetic Energy, **CBS MUSCL** 5^{th} **LMC**.

G.2 Co-flow Jet

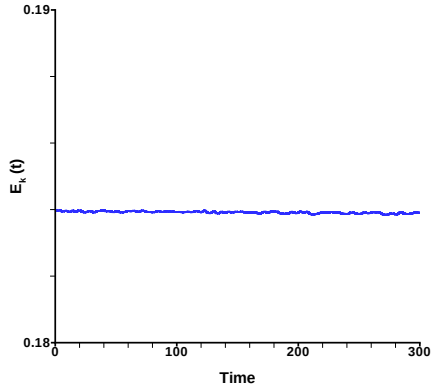

(a) Time Domain, $\frac{X}{D} = 0$.

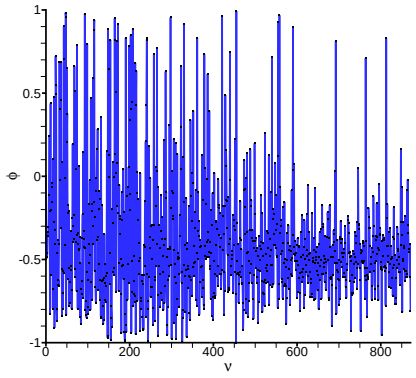

(b) Phase diagram, $\frac{X}{D} = 0$.

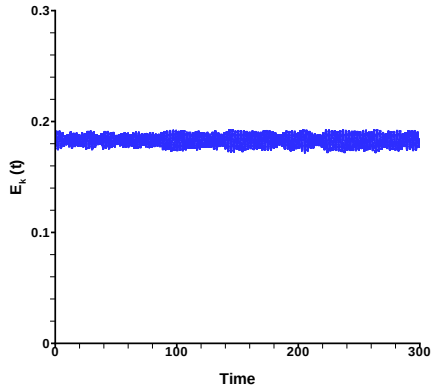

(c) Time Domain, $\frac{X}{D} = 5$.

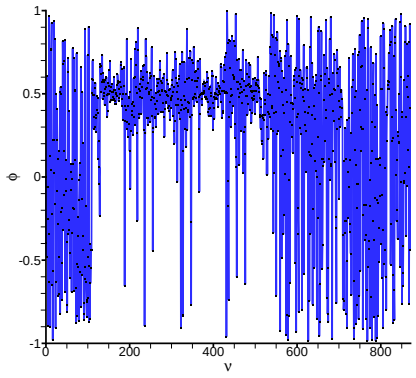

(d) Phase diagram, $\frac{X}{D} = 5$.

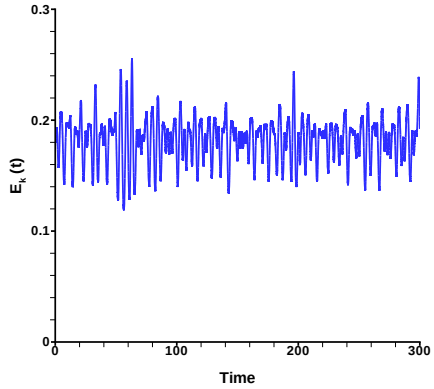

(e) Time Domain, $\frac{X}{D} = 10$.

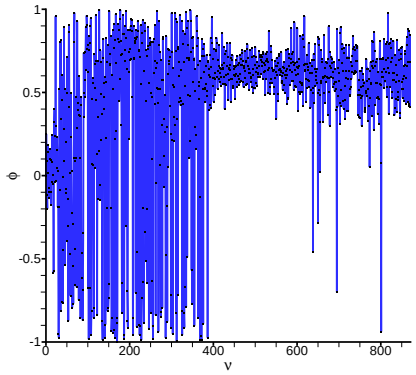

(f) Phase diagram, $\frac{X}{D} = 10$.

FIGURE G.4: Kinetic Energy, **HLLC MUSCL** 5^{th} **LMC**.

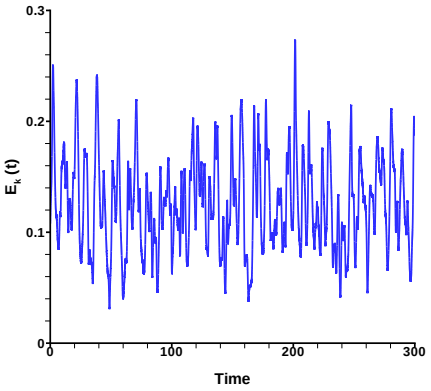

(a) Time Domain, $\frac{X}{D} = 15$.

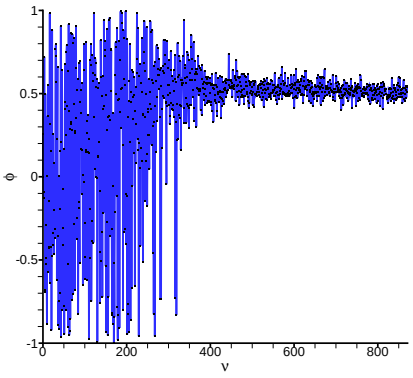

(b) Phase diagram, $\frac{X}{D} = 15$.

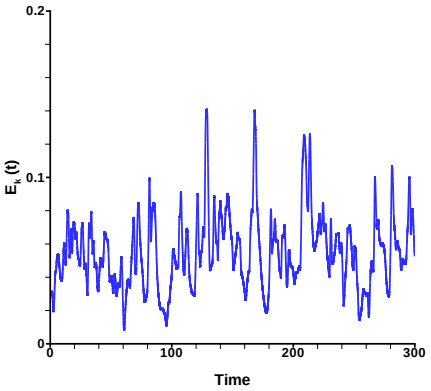

(c) Time Domain, $\frac{X}{D} = 20$.

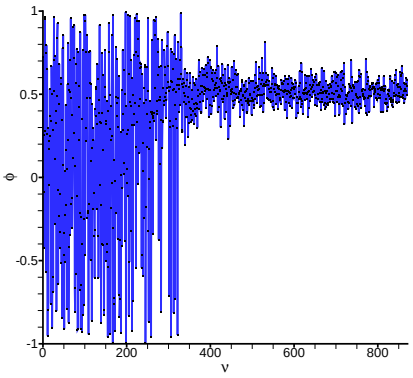

(d) Phase diagram, $\frac{X}{D} = 20$.

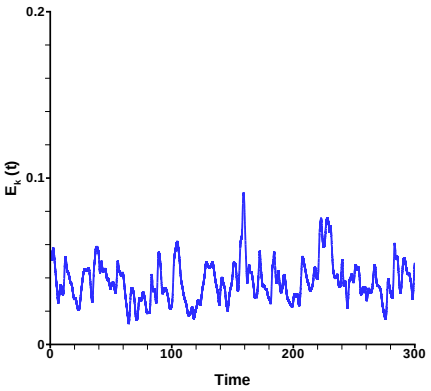

(e) Time Domain, $\frac{X}{D} = 25$.

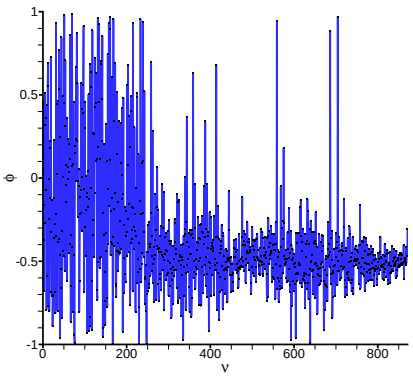

(f) Phase diagram, $\frac{X}{D} = 25$.

Figure G.5: Kinetic Energy, **HLLC MUSCL** 5^{th} **LMC**.

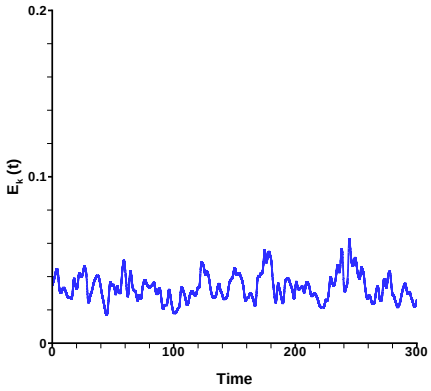

(a) Time Domain, $\frac{X}{D} = 30$.

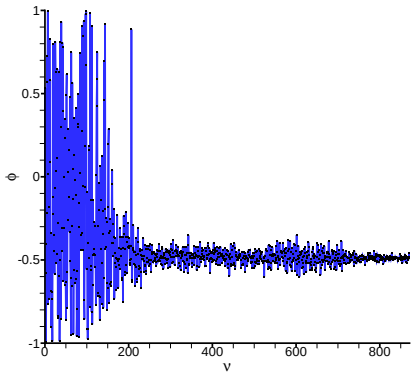

(b) Phase diagram, $\frac{X}{D} = 30$.

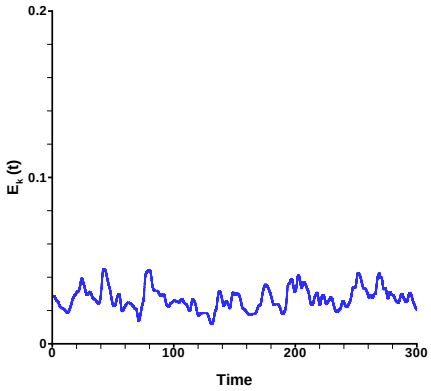

(c) Time Domain, $\frac{X}{D} = 35$.

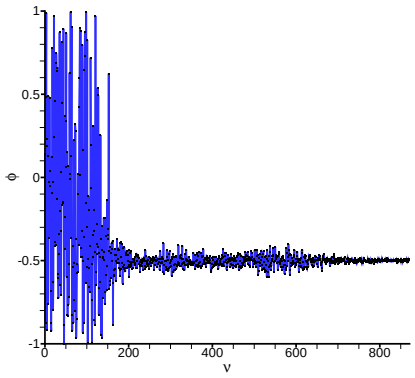

(d) Phase diagram, $\frac{X}{D} = 35$.

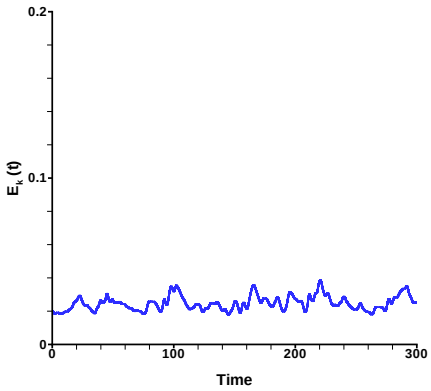

(e) Time Domain, $\frac{X}{D} = 40$.

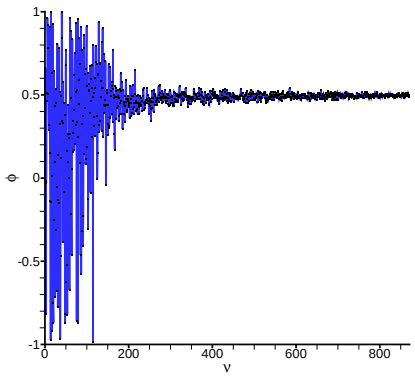

(f) Phase diagram, $\frac{X}{D} = 40$.

Figure G.6: Kinetic Energy, **HLLC MUSCL** 5^{th} **LMC**.

H

Final Results

In this appendix, the remaining results for the **CBS MUSCL** 5^{th}**-order LMC** (Static jet case) and **HLLC MUSCL** 5^{th}**-order LMC** (Co-Flow jet case) are presented, accordingly. This data can be used in future investigations as reference.

H.1 Static Jet

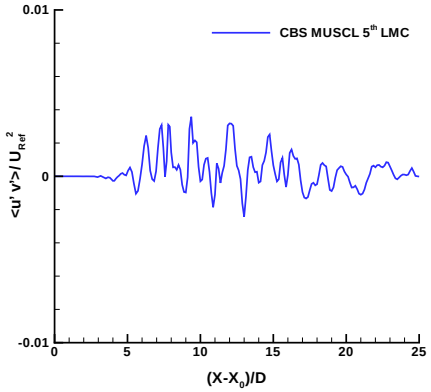

(a) Central line $\langle u'v' \rangle$ component.

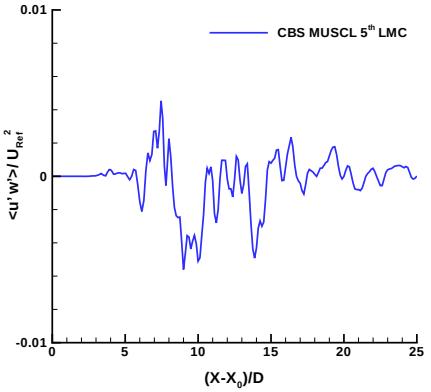

(b) Central line $\langle u'w' \rangle$ component.

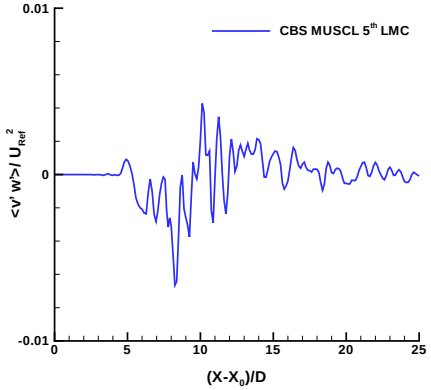

(c) Central line $\langle v'w' \rangle$ component.

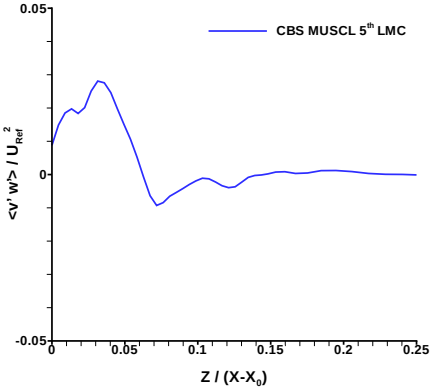

(d) Section $\frac{X-X_0}{D} = 15$ $\langle v'w' \rangle$ component.

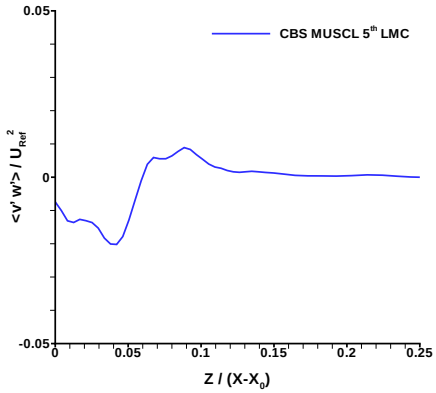

(e) Section $\frac{X-X_0}{D} = 20$ $\langle v'w' \rangle$ component.

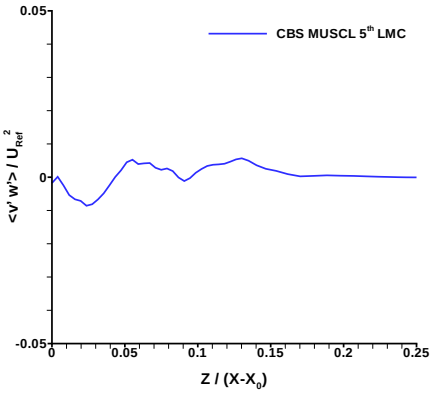

(f) Section $\frac{X-X_0}{D} = 25$ $\langle v'w' \rangle$ component.

FIGURE H.1: Central line and Sections Reynolds Stresses, Static jet case.

H.2 Co-flow Jet

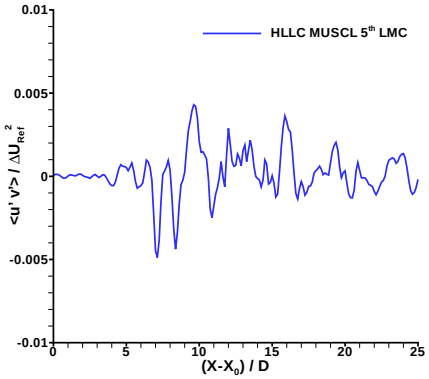

(a) Central line $\langle u'v' \rangle$ component.

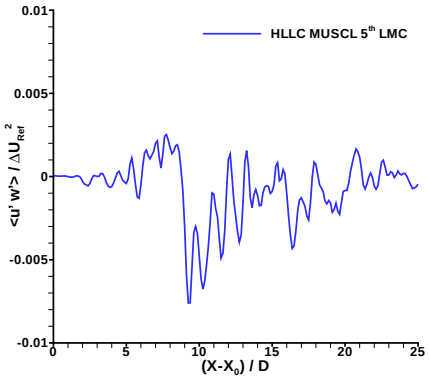

(b) Central line $\langle u'w' \rangle$ component.

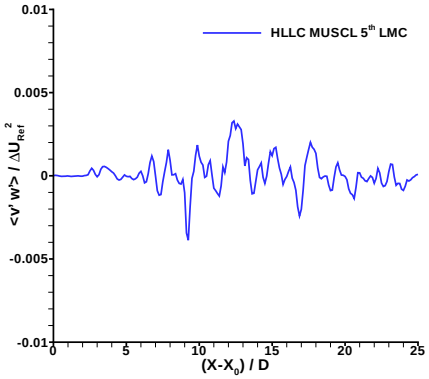

(c) Central line $\langle u'w' \rangle$ component.

FIGURE H.2: Central line Reynolds Stresses, Co-flow jet case.

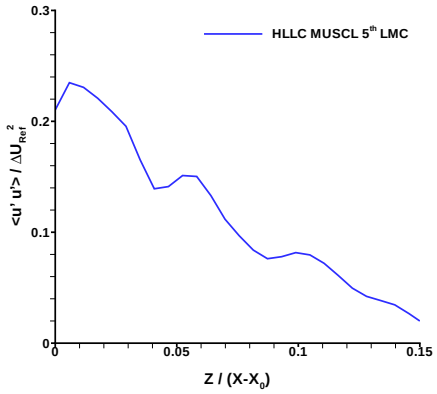

(a) $\langle u'u' \rangle$ component.

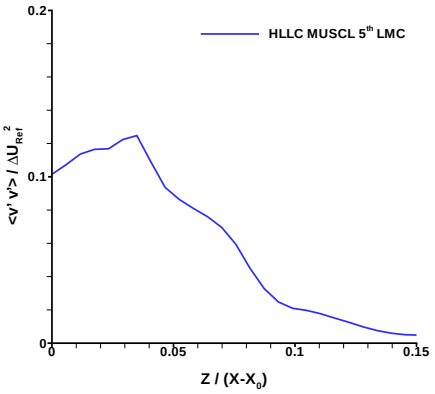

(b) $\langle v'v' \rangle$ component.

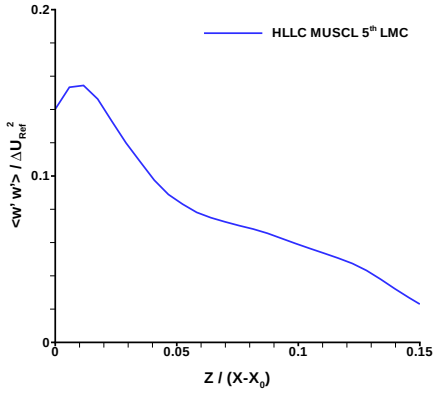

(c) $\langle w'w' \rangle$ component.

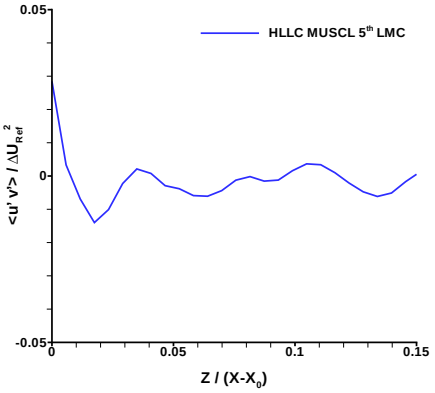

(d) $\langle u'v' \rangle$ component.

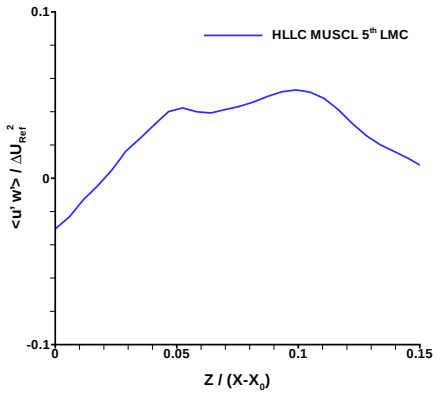

(e) $\langle u'w' \rangle$ component.

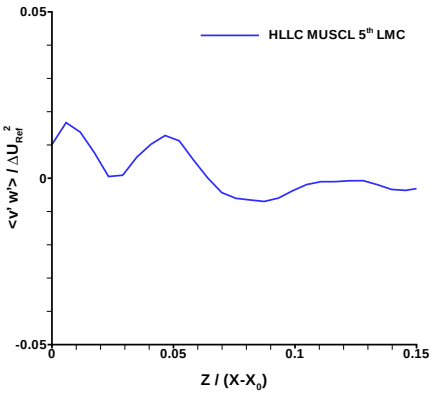

(f) $\langle v'w' \rangle$ component.

Figure H.3: Section $\frac{X-X_0}{D} = 15$ Reynolds Stresses, Co-flow jet case.

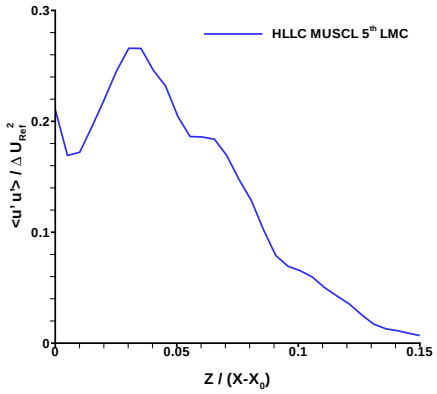

(a) $\langle u'u' \rangle$ component.

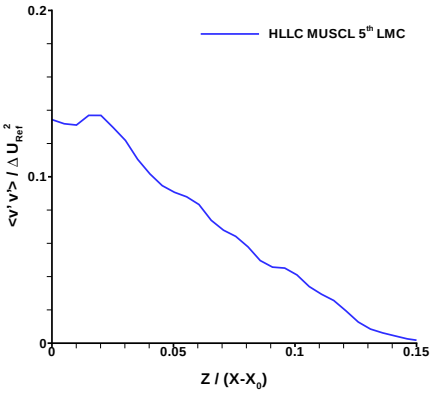

(b) $\langle v'v' \rangle$ component.

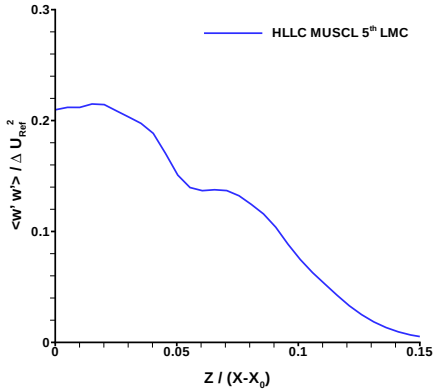

(c) $\langle w'w' \rangle$ component.

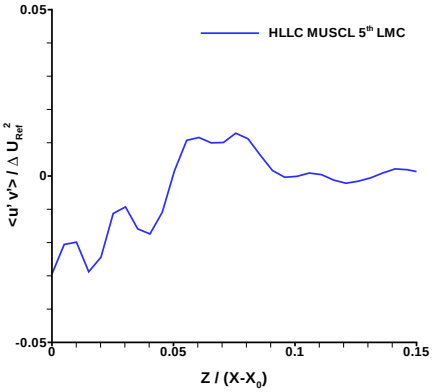

(d) $\langle u'v' \rangle$ component.

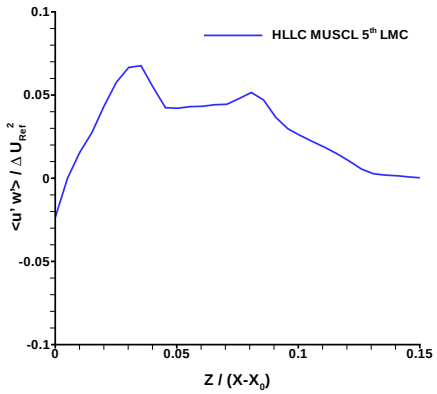

(e) $\langle u'w' \rangle$ component.

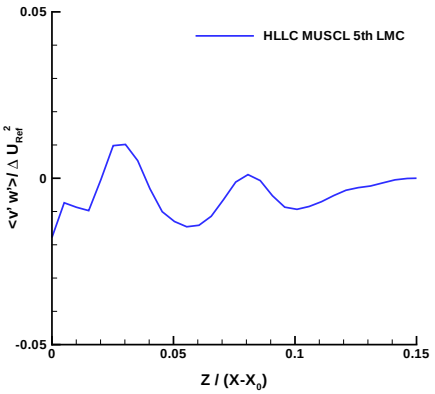

(f) $\langle v'w' \rangle$ component.

FIGURE H.4: Section $\frac{X-X_0}{D} = 20$ Reynolds Stresses, Co-flow jet case.

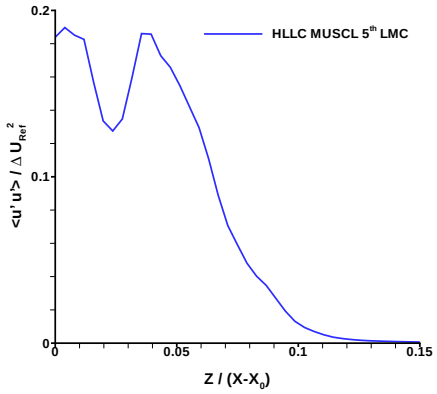

(a) $\langle u'u' \rangle$ component.

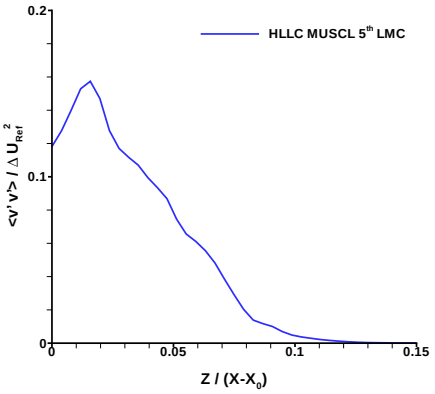

(b) $\langle v'v' \rangle$ component.

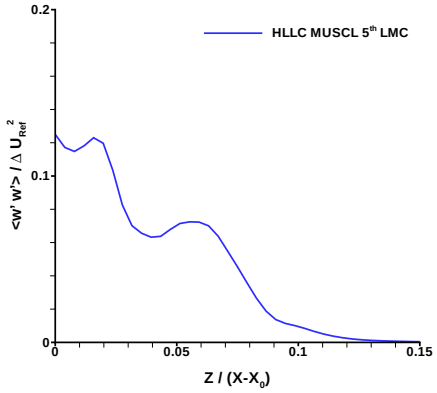

(c) $\langle w'w' \rangle$ component.

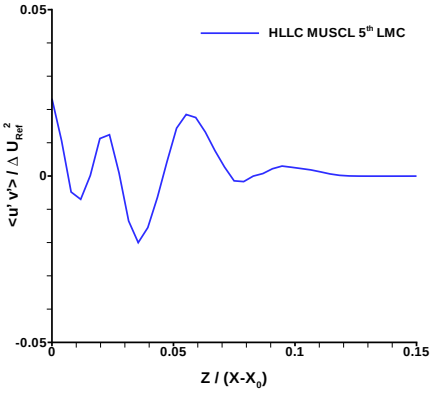

(d) $\langle u'v' \rangle$ component.

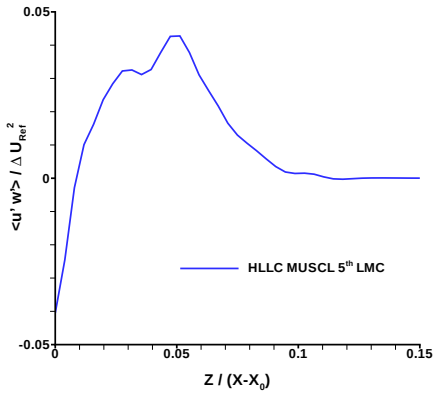

(e) $\langle u'w' \rangle$ component.

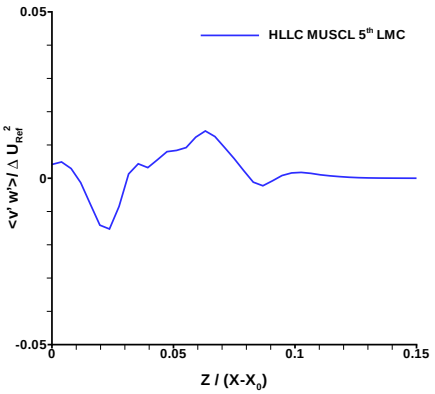

(f) $\langle v'w' \rangle$ component.

FIGURE H.5: Section $\frac{X-X_0}{D} = 25$ Reynolds Stresses, Co-flow jet case.